ABSTRACT

Title of Dissertation: AEROMECHANICS OF A DOUBLE ANHEDRAL TIP COMPOSITE ROTOR: EXPERIMENT AND MODELING

Cheng Chi
Doctor of Philosophy, 2022

Dissertation Directed by: Professor Anubhav Datta
Department of Aerospace Engineering

This thesis investigates the performance and loads on a double-anhedral tip modern composite rotor. Double anhedral tips are a recent introduction in rotors with no research data available for understanding their behavior or modeling them adequately. The objectives were to bridge these gaps. Both experimental and analytical methods were employed to fulfill the objectives systematically. Double anhedral blades of 5.6-ft diameter were designed and fabricated. The blades had a uniform VR-7 airfoil profile, a D-spar, -16° twist, a 5° dihedral from 80%R to 95%R and a 15° anhedral from 95%R to the tip. The blades were built in-house using IM7/8552 graphite/epoxy prepreg weave. They were instrumented for strains and structural loads measurement. A two-bladed hingeless hub was designed and fabricated for the vacuum chamber to measure rotating frequencies (fan plot). The hover tests were performed on the Alfred Gessow Rotorcraft Center Mach-scaled four-bladed hingeless rig. Tests were carried out up to tip Mach number of 0.6 over a collective range of 0° to 10°. The rotor performance, blade structural loads,

pitch link loads, and surface strains were measured. A double anhedral tip is a 3-D structure. Accordingly, a 3-D model was developed with CATIA (CAD), Cubit (hexahedral meshing), and X3D (aeromechanics). The 3-D CAD was constructed with guidance from Boeing to ensure the geometry was representative of a modern rotor yet generic enough to be open source for U.S. Gov-industry-academia joint study. The meshing used 27-node solid hexahedral elements, as needed by X3D. The pitch bearing was modeled with a joint commanded by control input. In total there were 3427 elements and approximately 100,000 degrees of freedom. Properties of the composite plies were acquired through in-house four-point bending coupon tests. The aerodynamic model used in-house CFD extracted C-81 decks and a lifting line with a refined free wake. The data acquired from tests were used to validate the model. A 3-D model of a straight blade was also developed as a baseline for comparison. These models have the same external and internal structure except for the tip. By comparing the behavior of the analytical models, insights were gained on the impacts of a double anhedral tip on the structural dynamics and aeromechanics in hover and forward flight. The local center of gravity offset at the tip appeared to make the blade softer. No performance gain was predicted in hover, however, the static flap, lag, and torsion moments at the root all decreased due to the vertical center of gravity offset in the tip portion. Strong 3-D strain patterns and multiple strain concentrations at the tip were predicted. In forward flight, the 4/rev vibratory vertical hub load and hub moments were predicted to increase by 15% and 100% respectively at tip speed ratio 0.1. Higher 1/rev oscillatory flap bending moment and 2/rev oscillatory lag bending moments were also predicted. The key

conclusion is that the vertical center of gravity of the double anhedral tip can have significant ramifications on blade loads - reducing the static loads while increasing oscillatory harmonics particularly vibratory harmonics in forward flight. Systematic wind-tunnel tests are needed in future to dissect these effects. This thesis laid the foundations of that future through blade fabrication, vacuum and hover testing.

AEROMECHANICS OF A DOUBLE ANHEDRAL TIP COMPOSITE ROTOR: EXPERIMENT AND MODELING

by

Cheng Chi

Dissertation submitted to the Faculty of the Graduate School of the
University of Maryland, College Park in partial fulfillment
of the requirements for the degree of
Doctor of Philosophy
2022

Advisory Committee:
Dr. Anubhav Datta, Chair/Advisor
Dr. Inderjit Chopra, Co-Advisor
Dr. James Baeder
Dr. Alison B. Flatau
Dr. Amr M. Baz

© Copyright by
Cheng Chi
2022

Acknowledgments

The graduate school experience at UMD has been the one that I will cherish forever. But the journey to complete this thesis would not be as pleasant and beneficial without the help and support of many people. First of all, I would like to express my sincere appreciation to my advisor, Anubhav Datta. Dr. Datta has expanded my knowledge in the field of rotorcraft research and has given me the opportunities to engage in meaningful research projects like the Mars Helicopter. Working with Dr. Datta, I am always motivated by his trust and expectation. And it's his guidance and encouragement that supported me to finish this thesis and pursue my helicopter pilot license. I would also like to thank Inderjit Chopra, who gave me the opportunity to join the Alfred Gessow Rotorcraft Center in the first place. Dr. Chopra also provided many opportunities for my research skills development, allowing me to find my field of interest. Whenever I encounter difficulties, Dr. Chopra always reminds me to trace my way back to an anchor point, which has become a beneficial habit of mine.

I would also like to thank the other members of my committee, James Baeder, Alison B. Flatau, and Amr M. Baz, for their expertise and guidance throughout my time in Maryland. It is an honor to have you on the committee. This work has been a collaborative effort of UMD and Boeing. Without the support from Boeing

and the guidance of Brahmananda Panda, Boeing technical fellow, this endeavor would not be possible. I owe many thanks to Vengalattore T. Nagaraj. Dr. VT is so knowledgeable about the rotorcraft industry. Every time I encountered questions in rotor design, he always pointed me in the right direction. And I could never thank him enough for inviting me to join the Vertical Flight Society student design competition team.

I learned from the senior students as much as I learned from the professors. I am very thankful to Ananth Sridharan who pointed me into the path of 3-D modeling, and Bharath Govindarajan and Vikram Hrishikeshavan who instilled me in a strong work ethic. I would also like to thank Will Staruk, Daniel Escobar, Tyler Sinotte, and Xing Wang for teaching me all of the necessary skills to tackle engineering problems. I am very grateful to have the company of Elena Shrestha, Fred Tsai, Brandyn Phillips, Vera Klimchenko, Seyhan Gul, Ravi Lumba, Mrinalgouda Patil, Shashank Maurya, James Sutherland, Abhishek Shastry, Wanyi Ng, Emily Fisler, Katie Krohmaly, Peter Ryseck, and Amy Morin.

Finally, I would like to thank my family. My parents, Jiangneng Chi and Yanjuan Lu, always support and encourage me unconditionally. My grandfather, Yongshen Chi, cared for me deeply and always had my best interests at heart. May he rest in peace and forgive me for not being near him in his last days. Thanks to my grandma, Qiuqun Liao, for her optimism and encouragement. Special thanks are due to my wife, Wei Huang, for her support and understanding, which I could not appreciate more. Thank you for supporting me in pursuing my dreams.

Table of Contents

Acknowledgements ii

Table of Contents iv

List of Tables vii

List of Figures viii

List of Abbreviations xiv

Chapter 1: Introduction 1
- 1.1 Background and Motivation . . . 1
  - 1.1.1 History of Anhedral Tip on Fixed-Wing . . . 6
  - 1.1.2 History of Anhedral Tip on a Rotor Blade . . . 7
  - 1.1.3 Rotor Testing . . . 10
  - 1.1.4 Rotor Comprehensive Analysis . . . 14
- 1.2 Objectives of the Thesis . . . 18
- 1.3 Organization of the Dissertation . . . 19

Chapter 2: Development of Double Anhedral Tip Composite Blade 21
- 2.1 Blade Design . . . 22
- 2.2 Blade Mold . . . 27
- 2.3 Internal Components Fabrication . . . 28
- 2.4 Spar and Skin Fabrication . . . 34
- 2.5 Blade Curing and Finishing . . . 36
- 2.6 Blade Instrumentation . . . 38
- 2.7 Material Elastic Property . . . 48
- 2.8 Blade Mass . . . 51
- 2.9 Summary . . . 53

Chapter 3: Development of Test Rigs 55
- 3.1 Vacuum Chamber Rig . . . 56
  - 3.1.1 Vacuum Chamber . . . 56
  - 3.1.2 Design of a New Vacuum Chamber Hub . . . 58
  - 3.1.3 Vacuum Chamber Hub Fabrication . . . 62
  - 3.1.4 Vacuum Chamber Hub Stiffness . . . 67
  - 3.1.5 Vacuum Chamber Instrumentation and Data Acquisition . . . 71

3.2 Hover Rig . . . 72
3.2.1 Hover Rig Components . . . 72
3.2.2 Hover Rig Instruments . . . 76
3.2.3 Hover Stand Data Acquisition . . . 80
3.3 Summary . . . 82

Chapter 4: Development of 3-D Blade Model 83
4.1 Blade Geometric Model . . . 84
4.2 Blade Mesh . . . 89
4.2.1 Clean-up . . . 90
4.2.2 Decomposition . . . 91
4.2.3 Imprinting and Merging . . . 94
4.2.4 Meshing . . . 95
4.2.5 Assignment of Blocks, Sidesets, and Nodesets . . . 99
4.3 Blade Aerodynamic Model . . . 107
4.4 Blade Structural Load Calculation . . . 110
4.5 Summary . . . 123

Chapter 5: Rotor Tests and Model Validation 124
5.1 Vacuum Chamber Test . . . 124
5.1.1 Test Procedure . . . 124
5.1.2 Data Processing . . . 127
5.1.3 Data Analysis and Model Validation . . . 129
5.2 Hover Test . . . 133
5.2.1 Test Procedure . . . 133
5.2.2 Data Processing . . . 138
5.2.3 Data Correlation with Prediction . . . 139
5.3 Summary . . . 148

Chapter 6: Comparison of Straight and Double Anhedral Blades 149
6.1 Blade Natural Frequencies and Mode Shapes . . . 150
6.2 Strains in Vacuum . . . 157
6.3 Hover Analysis . . . 161
6.3.1 Rotor Performance . . . 161
6.3.2 Blade Structural Loads . . . 163
6.3.3 Blade Strain/stress . . . 171
6.4 Forward Flight Analysis . . . 176
6.4.1 Rotor Performance . . . 176
6.4.2 Hub Vibratory Loads . . . 180
6.4.3 Blade Structural Loads . . . 185
6.4.4 Blade Strain/stress . . . 195
6.5 Summary . . . 207

Chapter 7: Summary and Conclusions 209
7.1 Summary . . . 209

7.2 Key Conclusions 210
7.3 Contributions 214
7.4 Recommendations for Future Work 215

Appendix A: Engineering Drawings 217
A.1 Vacuum Chamber Hub Central Block 218
A.2 Vacuum Chamber Hub End Block 219
A.3 Vacuum Chamber Hub Blade grip 220
A.4 Vacuum Chamber Hub Blade Adaptor 221
A.5 Vacuum Chamber Hub Pitch Horn 222
A.6 Vacuum Chamber Hub Pitch Link 223
A.7 Vacuum Chamber Hub Pitch arm 224
A.8 Vacuum Chamber Hub Shaker Housing 225

Appendix B: Test Data 226
B.1 Vacuum Frequency Test Data 226
B.2 Hover Performance Test Data 227

Bibliography 229

List of Tables

2.1 Blade parameters. 23
2.2 Elastic properties of IM7/8552 graphite/epoxy prepreg weave. 51
2.3 Elastic properties of the isotropic materials. 51
2.4 Measured weight of each component in gram. 52
2.5 Measured center of gravity location. 52
2.6 Measured density of each components in kg/m^3. 52

3.1 Aluminum beam frequencies in Hz. 71
3.2 Rotor parameters. 74

4.1 Primary variables of the parametric geometry. 85
4.2 Secondary variables of the parametric geometry. 85
4.3 Structural analysis representation. 89
4.4 Size of blade meshes. 98

B.1 Frequency test data. 226
B.2 Hover performance test data ($M_{tip} = 0.4$). 227
B.3 Hover performance test data ($M_{tip} = 0.5$). 228
B.4 Hover performance test data ($M_{tip} = 0.6$). 228

List of Figures

1.1 Rotorcraft with advance tip geometry. 2
1.2 Blade tip elementary parameters. 4
1.3 Winglet designed by Richard Whitcomb [21]. 7
1.4 Double vortex sytem [32]. 9
1.5 Boeing Advanced Chinook Rotor Blades. 10
1.6 Rabbott's wind tunnel rotor test in 1956 [50]. 11
1.7 UH-60A wind tunnel test in 2010 [51]. 11
1.8 Model rotor with anhedral tips in TDT wind tunnel [15]. 12
1.9 PF1 tip tested at ONERA [34]. 13
1.10 Double vortex system visualized by Muller [32]. 13
1.11 Aeroacoustic test of anhedral tip rotor at NUAA [46]. 14
1.12 Rigid anhedral tip blade tested by Uluocak [48]. 14

2.1 UMD Double Anhedral Tip Blade. 21
2.2 Boeing Advanced Chinook Rotor Blade [88]. 22
2.3 The airfoil layout. 23
2.4 Blade tip geometry and planform. 24
2.5 Types of blade spar. 25
2.6 Blade cross-section structure. 26
2.7 The layout of leading-edge weights. 26
2.8 Root insert design. 26
2.9 CAD model of each blade component. 27
2.10 CAD model of the mold. 27
2.11 Double anhedral tip blade mold. 28
2.12 Root inserts fabrication. 30
2.13 Foam sheet inside the mold. 31
2.14 Machining of the foam core. 32
2.15 Blade internal components. 33
2.16 Assembly of internal components. 33
2.17 The D-spar. 35
2.18 Blade core assembly. 35
2.19 Release film and skin. 36
2.20 Uncured blade. 37
2.21 Leading-edge of the blade in the mold. 37
2.22 Double anhedral tip composite blades. 38

2.23 Methods of strain gauge installation. . . . 39
2.24 Wires for instrumentation. . . . 40
2.25 Structural load sensors. . . . 41
2.26 Strain gauge configurations for structural load sensors. . . . 41
2.27 Structural load sensors calibration. . . . 45
2.28 Strain measurement. . . . 46
2.29 Strain rosette. . . . 47
2.30 Strain rosette on the blade. . . . 47
2.31 Four-point bending test. . . . 49
2.32 Composite coupons. . . . 50
2.33 Measurement of blade center of gravity. . . . 52
2.34 Final blades. . . . 53

3.1 Experimental tests. . . . 55
3.2 Vacuum chamber. . . . 56
3.3 Air Pump system. . . . 57
3.4 Vacuum chamber systems. . . . 58
3.5 Internal setup design of the chamber test. . . . 59
3.6 Hub central block on shaft. . . . 60
3.7 Connection of hub central block and end block. . . . 60
3.8 Connection of end block and blade grip. . . . 61
3.9 Connection of blade grip and blade adaptor. . . . 61
3.10 Connection of blade adaptor and blade. . . . 62
3.11 Connection of blade grip and pitch horn. . . . 62
3.12 Pitch mechanism. . . . 62
3.13 Machining of blade adaptor. . . . 63
3.14 Machining of central block. . . . 63
3.15 Machining of blade grip. . . . 64
3.16 Tension-torsion strap. . . . 64
3.17 Vacuum chamber hub components. . . . 65
3.18 Assemble of pitch bearings. . . . 65
3.19 Vacuum chamber hub assembly with shaker. . . . 66
3.20 Vacuum chamber hub assembly with fixed pitch. . . . 67
3.21 Vacuum chamber hub pitch stiffness test. . . . 68
3.22 Vacuum chamber hub pitch moment versus pitch deformation. . . . 68
3.23 Vacuum chamber hub flap and lag stiffness test. . . . 69
3.24 3-D model of the aluminum beam. . . . 69
3.25 Frequency spectrum of aluminum beam strain signal. . . . 70
3.26 Vacuum chamber hub instrumentation. . . . 72
3.27 Vacuum chamber test data acquisition system. . . . 72
3.28 Hover test stand. . . . 73
3.29 Hover test stand components. . . . 74
3.30 Hingeless hub. . . . 75
3.31 Swashplate. . . . 76
3.32 PCB on the hub cap. . . . 76

3.33 Hover stand slip ring. . . . 76
3.34 Hub balance. . . . 77
3.35 Torque sensor. . . . 77
3.36 Pitch link load sensors. . . . 78
3.37 Pitch Hall sensor. . . . 78
3.38 Pitch Hall sensor calibration. . . . 78
3.39 Encoder. . . . 79
3.40 Azimuth calibration. . . . 79
3.41 Optic sensor. . . . 80
3.42 Output of optic sensor and encoder. . . . 80
3.43 Hover test data acquisition system. . . . 81
3.44 LabVIEW program. . . . 81

4.1 Development of 3-D Blade Model. . . . 83
4.2 Parameterization models. . . . 86
4.3 Bodies in the geometric model. . . . 87
4.4 Leading edge weight body; the gaps are merged in geometry for smooth meshing but defined by material properties. . . . 87
4.5 Shared surfaces between bodies. . . . 88
4.6 Multi-section surface. . . . 89
4.7 Composite of sliver surfaces. . . . 91
4.8 Spanwise decomposition. . . . 92
4.9 Sectional decomposition; each volume has a different ply angle. . . . 93
4.10 Leading-edge weights decomposition. . . . 94
4.11 Cross-section selected to mesh. . . . 96
4.12 Cross-section mesh. . . . 96
4.13 Radial curve mesh. . . . 96
4.14 Root insert mesh. . . . 97
4.15 Tip portion mesh. . . . 97
4.16 Blade meshes. . . . 98
4.17 Blade meshes scale Jacobian quality. . . . 99
4.18 Blocks of isotropic material volumes. . . . 100
4.19 Blocks of spar volumes. . . . 100
4.20 Blocks of skin volumes. . . . 101
4.21 Aerodynamic segment sidesets (top view). . . . 102
4.22 Root boundary and strain gauge nodeset. . . . 103
4.23 Nodset for applying static loads. . . . 103
4.24 The 700 class nodesets 104
4.25 The 800 class nodesets. . . . 105
4.26 The 900 class nodesets. . . . 106
4.27 Hover free wake geometry. . . . 108
4.28 Aerodynamic panels corresponding to aerodynamic sideset. . . . 109
4.29 Aerodynamic node forces. . . . 109
4.30 Mesh and 800 class nodesets of a twisted aluminum beam. . . . 112
4.31 Axial strain on a twisted aluminum beam under tip loads. . . . 113

4.32 In-plane shear strain on a twisted aluminum beam under tip loads. . 113
4.33 Structural loads of a twisted aluminum beam under tip loads. 114
4.34 Axial strain on a rotating twisted aluminum beam. 115
4.35 In-plane shear strain on a rotating twisted aluminum beam. 115
4.36 Structural loads of a rotating twisted aluminum beam. 116
4.37 Mesh and 800 class nodesets of the straight twisted blade. 117
4.38 Axial strain on the straight blade under tip loads. 119
4.39 In-plane shear strain on the straight blade under tip loads. 119
4.40 Structural loads of the straight blade under tip loads. 120
4.41 Axial strain on the rotating straight blade. 121
4.42 In-plane shear strain on the rotating straight blade. 121
4.43 Structural loads of the rotating straight blade. 122

5.1 Final setup of the frequency test. 126
5.2 Frequency spectrum of strain signal at 200 RPM. 128
5.3 Raw strain signals. 129
5.4 Strain rosette diagram. 129
5.5 Fan plot of the double anhedral blade: symbols are measurements; solid lines are predictions. 130
5.6 Arms of the vacuum chamber hub. 131
5.7 Rotating strains on the top surface at 30%R: symbols are measurements; lines are predictions. 132
5.8 Hover stand hub balancing. 134
5.9 Reflective tapes for blade tracking. 136
5.10 Blade tracking. 136
5.11 Final setup of the hover test. 137
5.12 Fan plot of the hingeless rotor; the vertical lines are the RPM selected. 137
5.13 Hover test envelope. 139
5.14 Blade loading vs. collective. 140
5.15 Power coefficient vs. collective. 140
5.16 Power vs. Thrust. 141
5.17 Figure of Merit vs. blade loading. 142
5.18 Flap bending moment at 40%R (test vs. prediction). 143
5.19 Lag bending moment at 40%R. 143
5.20 Torsional moment at 40%R. 145
5.21 Pitch link load vs. collective. 145
5.22 Two version of 800 class nodesets. 146
5.23 Mean Strain on the top surface of 30%R. 147
5.24 Mean Strain on the bottom surface of 80%R. 147

6.1 Straight and double anhedral blades; same twist of $-16°$ 149
6.2 Fan plot of straight blade (solid lines) compared to double anhedral blade (dotted lines). Rigid root, $\theta_{75} = 0°$. 151
6.3 Straight blade mode 1; first flap (1.32/rev). 152
6.4 Double anhedral blade mode 1; first flap (1.29/rev). 152

6.5 Straight blade mode 2; first lag (2.62/rev). . . . 153
6.6 Double anhedral blade mode 2; first lag (2.32/rev). . . . 153
6.7 Straight blade mode 3; second flap (4.07/rev). . . . 154
6.8 Double anhedral blade mode 3; second flap (3.8/rev). . . . 154
6.9 Straight blade mode 4; third flap (8.9/rev). . . . 155
6.10 Double anhedral blade mode 4; third flap (8.12/rev). . . . 155
6.11 Straight blade mode 5; first torsion (11.07/rev). . . . 156
6.12 Double anhedral blade mode 5; first torsion (10.64/rev). . . . 156
6.13 Predicted axial strain ϵ_{xx} distribution in vacuum for straight blade (1522 RPM). . . . 158
6.14 Predicted axial strain ϵ_{xx} distribution in vacuum for double anhedral blade (1522 RPM). . . . 158
6.15 Predicted in-plane shear strain γ_{xy} distribution in vacuum for straight blade (1522 RPM). . . . 160
6.16 Predicted in-plane shear strain γ_{xy} distribution in vacuum for double anhedral blade (1522 RPM). . . . 160
6.17 Predicted out-of-plane strain ϵ_{zz} distribution in vacuum (1522 RPM; left: straight blade; right: double anhedral blade). . . . 161
6.18 Power versus blade loading. $M_{tip} = 0.4$. . . . 162
6.19 Figure of Merit versus blade loading. $M_{tip} = 0.4$. . . . 162
6.20 Comparison of axial force.$M_{tip} = 0.4$. . . . 163
6.21 Flap bending moment in hover. Straight blade versus double anhedral blade. $M_{tip} = 0.4$. . . . 165
6.22 Diagram of flap bending moment on the double anhedral blade. . . . 165
6.23 Lag bending moment in hover: Straight blade versus double anhedral blade. $M_{tip} = 0.4$. . . . 166
6.24 Diagrams of lag bending moment on the double anhedral blade. . . . 167
6.25 Torsion moment in hover. Straight blade versus double anhedral blade. $M_{tip} = 0.4$. . . . 168
6.26 Diagrams of torsion moment on the double anhedral blade. . . . 169
6.27 Pitch link load in hover. Straight blade versus double anhedral blade. $M_{tip} = 0.4$. . . . 170
6.28 Propeller moment direction of the straight and double anhedral blades. 170
6.29 Axial strain ϵ_{xx} distribution of straight blade. $C_T/\sigma = 0.117$, $M_{tip} = 0.4$. . . . 172
6.30 Axial strain ϵ_{xx} distribution of double anhedral blade. $C_T/\sigma = 0.117$, $M_{tip} = 0.4$. . . . 172
6.31 Internal axial stress σ_{xx} distribution. $C_T/\sigma = 0.117$, $M_{tip} = 0.4$. . . . 173
6.32 In-plane shear strain γ_{xy} distribution of straight blade. $C_T/\sigma = 0.117$, $M_{tip} = 0.4$. . . . 174
6.33 In-plane shear strain γ_{xy} distribution of double anhedral blade. $C_T/\sigma = 0.117$, $M_{tip} = 0.4$. . . . 174
6.34 Internal in-plane shear stress σ_{xy} distribution. $C_T/\sigma = 0.117$, $M_{tip} = 0.4$. . . . 175

6.35 Out-of-plane strain ϵ_{zz} distribution of straight blade and double anhedral blade. $C_T/\sigma = 0.117$, $M_{tip} = 0.4$. 175
6.36 Out-of-plane stress σ_{zz} distribution of straight blade and double anhedral blade. $C_T/\sigma = 0.117$, $M_{tip} = 0.4$. 176
6.37 Diagram of rotor in forward flight. 177
6.38 Rotor effective lift-to-drag ratio ($M_{tip} = 0.4$, $\alpha_s = 4°$, $C_T/\sigma = 0.1$). . . 178
6.39 Rotor propulsive force coefficient ($M_{tip} = 0.4$, $\alpha_s = 4°$, $C_T/\sigma = 0.1$). . 178
6.40 Rotor torque coefficient ($M_{tip} = 0.4$, $\alpha_s = 4°$, $C_T/\sigma = 0.1$). 179
6.41 Trimmed forward flight control ($M_{tip} = 0.4$, $\alpha_s = 4°$, $C_T/\sigma = 0.1$). . . 179
6.42 Hub 4/rev and 8/rev vibratory loads ($M_{tip} = 0.4$, $\alpha_s = 4°$, $C_T/\sigma = 0.1$).183
6.43 Non-dimensional hub 4/rev and 8/rev vibratory loads ($M_{tip} = 0.4$, $\alpha_s = 4°$, $C_T/\sigma = 0.1$). 185
6.44 Flap bending moment versus azimuth ($M_{tip} = 0.4$, $\alpha_s = 4°$, $C_T/\sigma = 0.1$). 187
6.45 Oscillatory flap bending moment versus tip speed ratio ($M_{tip} = 0.4$, $\alpha_s = 4°$, $C_T/\sigma = 0.1$). 188
6.46 Lag bending moment versus azimuth ($M_{tip} = 0.4$, $\alpha_s = 4°$, $C_T/\sigma = 0.1$).189
6.47 Oscillatory lag bending moment versus tip speed ratio ($M_{tip} = 0.4$, $\alpha_s = 4°$, $C_T/\sigma = 0.1$). 190
6.48 Torsion moment versus azimuth ($M_{tip} = 0.4$, $\alpha_s = 4°$, $C_T/\sigma = 0.1$). . 192
6.49 Oscillatory torsion moment versus tip speed ratio ($M_{tip} = 0.4, \alpha_s = 4°, C_T/\sigma = 0.1$). 193
6.50 Pitch link load versus azimuth ($M_{tip} = 0.4$, $\alpha_s = 4°$, $C_T/\sigma = 0.1$). . . 194
6.51 Oscillatory pitch link load versus tip speed ratio ($M_{tip} = 0.4$, $\alpha_s = 4°$, $C_T/\sigma = 0.1$). 195
6.52 Axial strain ϵ_{xx} distribution of straight blade ($M_{tip} = 0.4$, $\alpha_s = 4°$, $C_T/\sigma = 0.1$, $\mu = 0.3$). 198
6.53 Axial strain ϵ_{xx} distribution of double anhedral blade ($M_{tip} = 0.4$, $\alpha_s = 4°$, $C_T/\sigma = 0.1$, $\mu = 0.3$). 200
6.54 In-plane shear strain γ_{xy} distribution of straight blade ($M_{tip} = 0.4$, $\alpha_s = 4°$, $C_T/\sigma = 0.1$, $\mu = 0.3$). 202
6.55 In-plane shear strain γ_{xy} distribution of double anhedral blade ($M_{tip} = 0.4$, $\alpha_s = 4°$, $C_T/\sigma = 0.1$, $\mu = 0.3$). 204
6.56 Out-of-plane strain ϵ_{zz} distribution comparison ($M_{tip} = 0.4$, $\alpha_s = 4°$, $C_T/\sigma = 0.1$, $\mu = 0.3$). 206

List of Abbreviations

ACRB	Advanced Chinook Rotor Blade
AGRC	Alfred Gessow Rotorcraft Center
BVI	Blade Vortex Interaction
CAD	Computer Aided Design
CFD	Computational Fluid Dynamics
CNC	Computer Numerical Control
CSD	Computational Structural Dynamics
EMI	Electro Magnetic Interference
FEM	Finite Element Method
FFT	Fast Fourier Transform
FM	Figure of Merit
GF	Gauge Factor
IGES	International Graphics Exchange Specification
NASA	National Aeronautics and Space Administration
NUAA	Nanjing University of Aeronautics and Astronautics
PCB	Printed Circuit Board
PIV	Particle Image Velocimetry
RCAS	Rotorcraft Comprehensive Analysis System
RPM	Revolutions Per Minute
SAM	Structural Analysis Model
SAR	Structural Analysis Representation
STEP	Standard for the Exchange of Product
STL	Stereolithography

TDT	Transonic Dynamics Tunnel
UMARC	University of Maryland Advanced Rotorcraft Code
UMD	University of Maryland
VABS	Variational Asymptotical Beam Sectional Analysis
3−D	three dimensional
c	blade chord
C.G.	center of gravity
C_{d0}	drag coefficient at zero angle of attack
C_M	hub moment coefficient
C_P	power coefficient
C_Q	torque coefficient
C_T	thrust coefficient
C_X	propulsive force coefficient
E	Young's modulus
G	shear modulus
L/D_e	rotor effective lift-to-drag ratio
K_θ	pitch stiffness
K_β	flap stiffness
K_ζ	lag stiffness
M_{tip}	tip Mach number
r	spanwise location
R	blade radius
t	ply thickness
α_s	shaft tilt angle
γ_{xy}	in-plane shear engineering strain
ϵ_{xx}	axial normal strain
ϵ_{yy}	chordwise normal strain
ϵ_{zz}	out-of-plane strain
θ_0	collective
θ_{1S}	longitudinal cyclic
θ_{1C}	lateral cyclic
θ_{tw}	built-in twist
Λ_A	Anhedral angle
μ	tip speed ratio or Poisson ratio
σ	rotor solidity
σ_{xx}	axial stress

σ_{xy}	in-plane shear stress
σ_{zz}	out-of-plane stress
ϕ	azimuth angle

Chapter 1: Introduction

1.1 Background and Motivation

As a special air vehicle that has the ability to take-off and land vertically, hover and fly slowly in any direction, rotorcraft has been an important part of the aviation community since it was invented. Over the last century, higher cruise speed, larger payload, and better handling qualities have been the primary pursuits of rotorcraft designers. These design goals have been mutually exclusive to some extent historically. Therefore, design compromises between high lift-to-drag ratio, high Figure of Merit, and low vibration level have to be made. These design compromises were eased as the rotor aeromechanic behavior was better understood, and new rotor technologies were developed.

The main rotor, as the source of lift, propulsion, and control all combined, naturally became the focus of research. Due to the slender and flexible nature of the blade structure, the blade tip, that has the highest dynamic pressure and complex flow also has the maximum deformation, and hence has the most powerful impact on performance, noise, loads, and vibration. Meanwhile, due to the design flexibility introduced by advanced composite materials and fabrication methods, the design of blade tips became more and more innovative. The goal of these tip

designs is to alleviate the problems of loads, acoustics, and vibration while enhancing performance. The objective of this thesis is to study one such special tip profile.

For decades, engineers and researchers tried various tip geometries to design better rotor blades. Figure 1.1 shows examples of advanced tip geometries on rotorcraft. It shows the swept tip on Sikorsky UH-60, the anhedral tip on Sikorsky S-92, the double swept tip (Blue Edge tip) on Airbus H160, and the double anhedral tip on Boeing CH-47, and the paddle tip (BERP tip) on AgustaWestland Merlin Mk3.



(a) UH-60 with swept tip



(b) S92 with anhedral tip



(c) H160 with double swept tip (Blue Edge tip)



(d) CH-47 with double anhedral tip



(e) Merlin Mk3 with paddle tip (BERP tip)

Figure 1.1: Rotorcraft with advance tip geometry.

All of these advanced tip geometries can be condensed into three canonical parameters or a combination of them [1], which are planform-taper, sweep, and anhedral (Figure 1.2). The tapered tip is the small outboard portion of the blade that has a significant variation in chord length. According to the tests reported by Stroub et al [2], McVeigh and McHugh [3], and Althoff and Noonan [4], a properly designed tapered tip can improve the maximum rotor Figure of Merit in hover and the rotor effective lift-to-drag ratio in forward flight. This effect is due to the reduction in outboard profile drag [5, 6]. However, the tapered tip can also be prone to premature stall and increase in vibration due to the low Reynolds number on the retreating side as well as present difficulty in inserting tip weights for autorotation [7].

A swept tip shifts (shears/or rotates) the blade cross-sections toward the trailing edge. This type of tip geometry is driven by the pursuit of high forward flight speed by delaying the drag divergence Mach numbers. The sweep back can delay the onset of compressibility effects on the advancing side, which reduce drag and unsteady pitching moments [8–12]. This can be explained by the reduction of Mach number normal to the tip leading-edge, or equivalently by the rotated cross-sections having a lower thickness-to-chord ratio which performs better at high Mach numbers. However, this advantage on the advancing side may be reduced by the early flow separation on the retreating side. More importantly, the rearward shift of the center of gravity and aerodynamic center on the swept tip introduces aerodynamic and inertial couplings that have significant impacts on pitch links and blade structural loads. [13, 14].

Anhedral tips rotate the cross-sections up or down away from the plane of rotation. An important effect is the change in the position of the tip vortex and hence the induced velocity field in the plane of rotation. An anhedral tip can show improvement in hover performance, as reported by Weller [15] and Mueller [16]. The change of tip vortex release location also changes Blade-Vortex Interaction (BVI) which is a major source of vibration and noise [17].

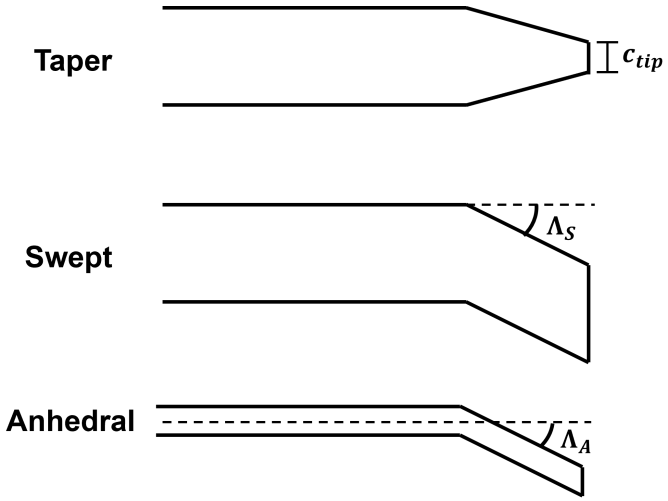

Figure 1.2: Blade tip elementary parameters.

Among these three canonical geometries, the anhedral tip has seen less in-depth investigations, and the few that were carried out all focused on aerodynamics and noise. Recently, there have been attempts to improve hover performance by using an anhedral tip on a production rotor. The inertial couplings may be lowered by having both dihedral and anhedral in the tip region (called the double anhedral) to bring the effective C.G. close to the rotating plane. Though it was reported that this attempt has the potential of increasing the payload, excessive vibrations occurred in forward flight. High vibrations shorten the fatigue life of key components,

degrade ride qualities, and are major detriments for a new design, particularly when discovered late in the design cycle. This vibration problem shows that accompanying performance and acoustic benefits are structural and aeromechanical behavior that are not fully understood.

In order to understand the behavior of double anhedral tips, test data from realistic rotor blades are vital. Good test data requires systematic step-by-step investigation with clear documentation of not only data by also rotor properties. The model rotor should be Mach-scaled and representative of real aircraft, so the phenomena measured are relatable to the flight vehicles. Good research data should be open-source, allow peer review, and open to assessment by other investigators. None of the existing data sets satisfied these criteria. Most of the important tests are either proprietary or documented with insufficient details to be admissible as a benchmark for fundamental understanding or model validation.

Precise modeling is equally critical to capturing and understanding basic phenomena. The aerodynamics of even a straight blade tip is complex as it is subjected to rapidly varying conditions under unsteady 3-D transonic flow. An anhedral tip is expected to add more complexity. The structural dynamics do not conform to the basic assumptions of a 1-D beam near the tip. Therefore, structural models that are not limited to beams are needed to investigate the impact of 3-D aerodynamics on blade stresses.

In this work, Mach-scale double anhedral tip composite rotors were fabricated, hover tested and modeled with 3-D structures to validate with test data. The aerodynamic model was still lifting line with free wake. Once validated, the analysis

was extended to forward flight. Since the Glenn L. Martin wind tunnel remained closed, the high-fidelity 3-D analysis took its place instead for the best assessment of blade stress/strain. Ultimately the prediction will need to be validated with test data, which remains a task for the future.

1.1.1 History of Anhedral Tip on Fixed-Wing

The concept of a non-planar endplate, or a winglet, on a lifting device to improve aircraft performance can be traced to Frederick W. Lanchester's patent in 1897. Later, Nagel (1924) [18], Hemke (1928) [19], and Mangler (1938) [20] carried out theoretical investigations on lift and induced drag. One of the first applications was carried out by Richard Whitcomb of NASA Langley Research Center [21, 22]. Whitcomb installed a fin extending both upwards and downward (Figure 1.3) of a semi-span wing to reduce induced drag and increase the lift-to-drag ratio. This kind of tip extension can be seen on many commercial jets today.

Theoretical analysis by Jones and Lasinski of NASA Ames Research Center [23] confirmed that reduction of induced drag can be achieved by extending the tip vertically. One of the more recent studies was that of Eppler, in 1997, who showed that a dihedral angle is more beneficial than anhedral [24]. A similar conclusion was drawn by Boeing and Aviation Partners Inc. since they developed what they called a blended winglet [25]. A blended winglet is simply a continuous smooth structure without a sharp edge. In 2000, Herrick designed what he called a raked wingtip [28]. The increase in the effective span is the main target since it reduces

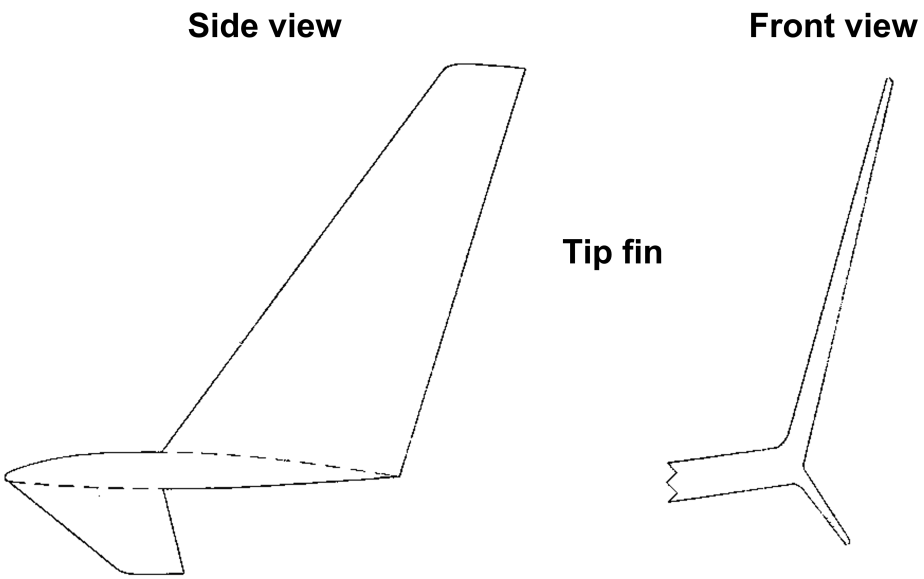

Figure 1.3: Winglet designed by Richard Whitcomb [21].

induced drag [29].

The induced power benefit of the winglets is derived from the reduction in the strength of wingtip vortices. These are moved further away from the wing [30]. There is a secondary benefit. A component of the winglet aerodynamic force can be pointed forward if suitably designed. This component is an additional counter to the drag. Mary variants of winglets can be found today, including canted winglet, vortex diffuser, blended split, sharklet, spiroid winglet, downward canted winglet, active winglets, and tip sails [30, 31].

1.1.2 History of Anhedral Tip on a Rotor Blade

The success of winglets on fixed-wing aircraft cannot be simply carried over to rotor blades. Rotor blades have g-loading of nearly 1000 at the tip, so structural pieces cannot be installed without taking into consideration other effects. Moreover,

the induced power loss is not due to the vortex right at the tip but from the vortices of all blades. The rapid variation of local flow, plunge, and pitch of the blade section, and stronger tip vortex make blade tips on the rotor significantly different from fixed-wings. The lessons learned from fixed-wing, while providing a basis, do not transfer directly to rotors. Nevertheless, motivated by the potential benefit of non-planar tips, researchers have conducted some investigations in the past.

The development of advanced blade tips was made possible by metal, and then by the advent of composite materials. The discussion of advanced blade tips on rotors can be found in an early work by Spivey in 1968 [8]. Thereafter, no tests or studies were conducted on anhedral tips in the next ten years until Weller [15] and Mantay and Yeager [11] considered it again in 1979 and 1983. Both studies showed the hover performance could be improved by an anhedral tip.

At the time, the mechanism behind the performance improvement was not clear. A study by Muller [16, 17] found there might be a double vortex system formed by the anhedral tip (Figure 1.4), which reduces Blade Vortex Interaction (BVI) by smoothing the vortex core and lowering the initial location of the tip vortex [32]. More recently, anhedral tip aerodynamic studies were conducted by Desopper et al [33, 34], Vuillet et al [35], and Tung et al [36] in the 90s. In 2001, McAlister et al also considered the anhedral tip to reduce BVI [37]. The aeroelastic impact of the anhedral tip on helicopter rotor blade and tilt-rotor blade was studied by Kim and Chopra [13] and Srinivas, Chopra and Nixon [38], respectively. These were all analyses with no data to verify or validate. Some of the analyses were too approximate to even capture the expected 3-D effects near the tip.

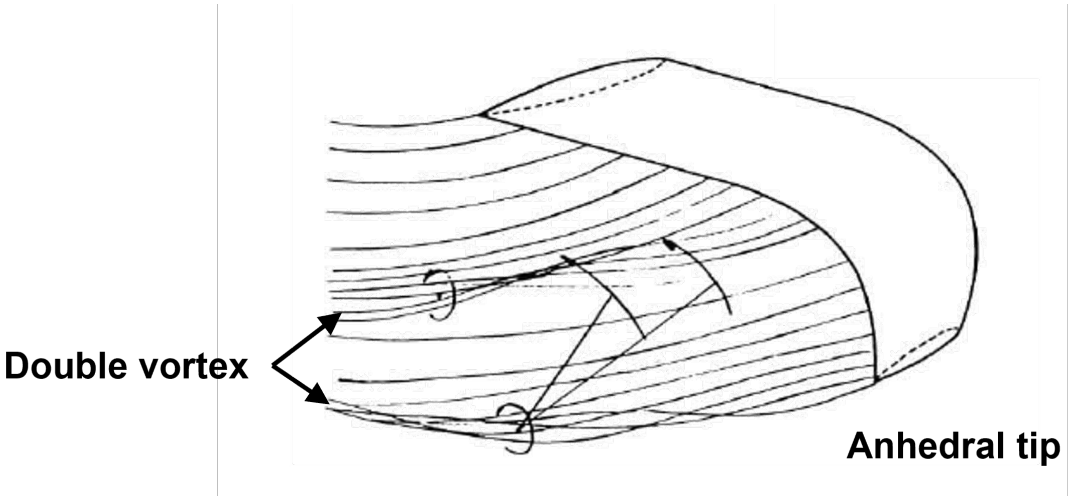

Figure 1.4: Double vortex sytem [32].

The maturation of Computational Fluid Dynamics (CFD) for rotors in the past 20 years [39, 40] has opened the avenue to a better understanding of anhedral tip. Some sample optimization attempts can be found in Refs. 41–44. Interest in anhedral tips has transitioned from performance to acoustics and flight dynamics [45–48]. So far, there are far fewer variants of anhedral tips envisioned on rotors due to the natural hesitation of introducing discontinuities at the tip. Boeing adopted the double anhedral tips on Chinook CH-47 (Figure 1.5), and some analyses were carried out jointly by Boeing and Army. However, there is limited to no data available in public.



Figure 1.5: Boeing Advanced Chinook Rotor Blades.

1.1.3 Rotor Testing

There is a long and rich history of full-scale helicopter rotor tests in the US. Bousman, in his Nikolsky Lecture [49], traced this history beginning with the pioneering Langley 15.3-ft diameter teetering rotor wind tunnel tests in 1956 (Figure 1.6) [50] to the modern NASA Ames 26.8-ft diameter UH-60A Black Hawk articulated rotor tests in 2010 (Figure 1.7) [51]. The Bousman review focused on tests that measured airloads—the most difficult of all tests. However, there were no anhedral tips in any of them.

There is also a vast literature on model-scale rotor tests and the story is somewhat better there. A few cases had anhedral tips. These were: 1) the 2.743 m radius four-bladed articulated rotor model tested by Weller at the Langley Transonic Dynamics Tunnel (TDT) (Figure 1.8) measuring rotor performance and blade flap and lag bending moments [15]; 2) the 0.857 m radius rotor model with PF1 tips

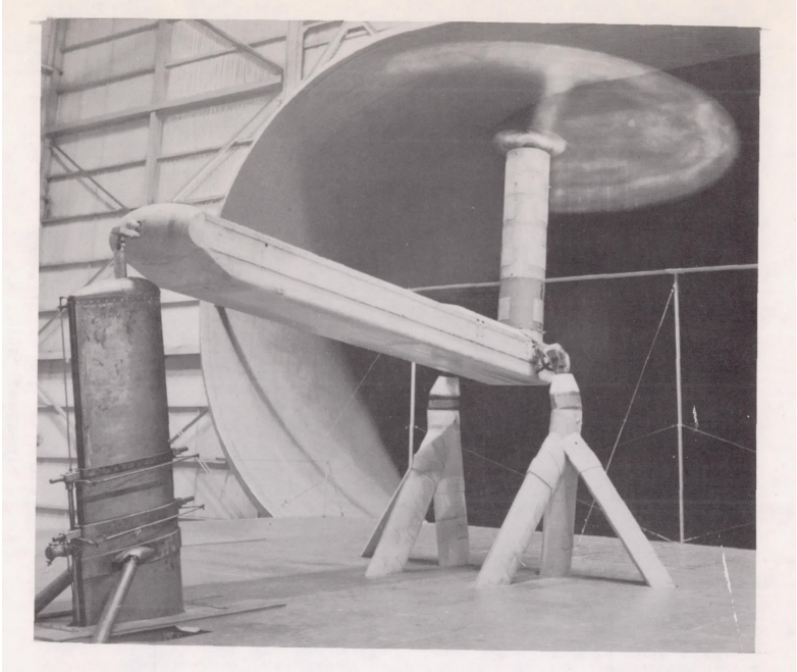

Figure 1.6: Rabbott's wind tunnel rotor test in 1956 [50].



Figure 1.7: UH-60A wind tunnel test in 2010 [51].

(Figure 1.9) tested by Desopper at the ONERA S2 Chalais-Heudon wind tunnel measuring rotor performance [34]; 3) the 0.5 m radius rotor model tested by Muller at Associazione Industrie Aerospaziali wind tunnel [16] and FIBUS Research Institute

water tunnel [32] measuring the vortex system (Figure 1.10); 4) the 1 m radius rotor model tested by Huang at Nanjing University of Aeronautics and Astronautics (NUAA) acoustic chamber (Figure 1.11) measuring sound pressure level [46]; and 5) the 0.65 m radius five-bladed rigid rotor model tested by Uluocak at Middle East Technical University (Figure 1.12) measuring flow field with Particle Image Velocimetry (PIV) technique [48]. None of these measured blade dynamics or loads — the fundamental barrier of anhedral blades. None of these were double anhedral blades.

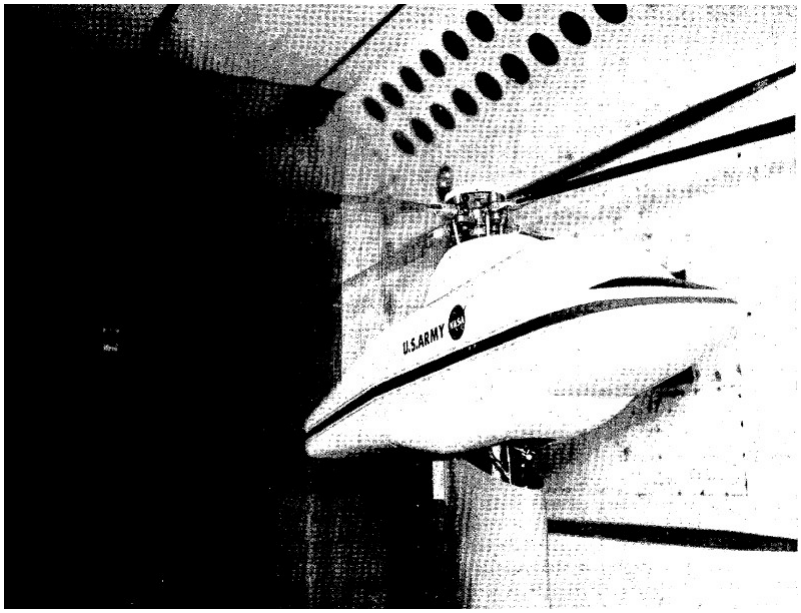

Figure 1.8: Model rotor with anhedral tips in TDT wind tunnel [15].

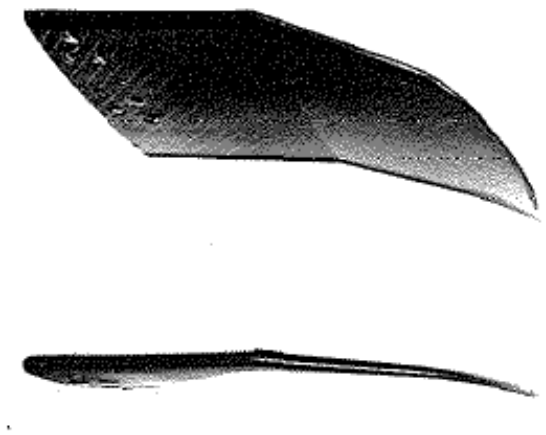

Figure 1.9: PF1 tip tested at ONERA [34].

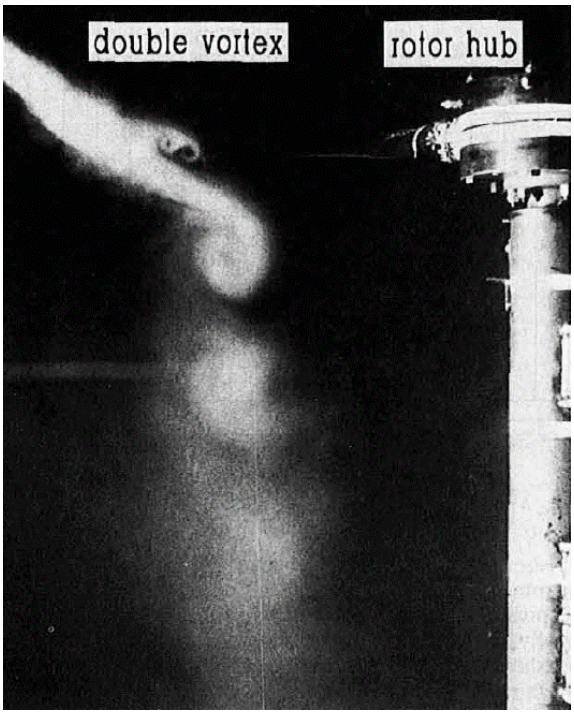

Figure 1.10: Double vortex system visualized by Muller [32].



Figure 1.11: Aeroacoustic test of anhedral tip rotor at NUAA [46].

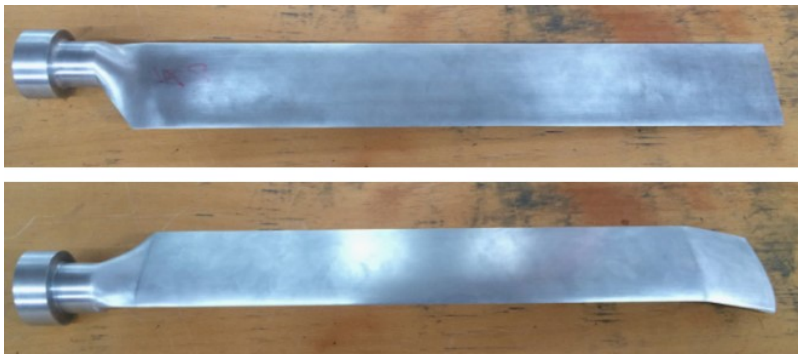

Figure 1.12: Rigid anhedral tip blade tested by Uluocak [48].

1.1.4 Rotor Comprehensive Analysis

The early helicopters had articulated or teetering rotors. And the blades are considerably rigid due to their metal spars. So the elastic motion of the blades was not the main consideration in engineering design at that time. It was not until 8 years after the successful maiden flight of Sikorsky's first helicopter, the VS-300,

that the first elastic flap bending blade model was proposed by Flax [52]. Next, through the efforts of Yuan and Diprima et al. [53, 54], an elastic blade model with lag and torsion degrees of freedom was conjured. Eventually, the seminal work of Houbolt and Brooks established the flap, lag, and torsion linear dynamic model (the nonlinear effect of the centrifugal force was reduced through tension) with a built-in twist in 1957 [55]. The linear model dropped many flap-lag-torsion coupling terms, consistent with the small deformation assumption. Hodges and Dowell derived nonlinear flap-lag-torsion coupled equations in 1974 [56]. An ordering scheme was used in that model to obtain manageable analytical expressions. Concurrently, Kvaternik [57], Johnson [58], and Rosen [59] also built models of equal accuracy by expanding on Houbolt and Brooks. Most comprehensive codes still use these models or their more refined geometrically exact versions. The University of Maryland Advanced Rotorcraft Code (UMARC) was also developed based on these models [60].

Later, Crespo da Silva [61] and Hodges [62] developed a large deformation beam model that does not depend on the ordering scheme. The strains are still small, but the rotations are exact. Concurrently, Johnson [63] also extended the beam model and unified multibody dynamics to allow exact rotation.

Next, researchers turned attention to the modeling of composite blades. From the isotropic material to the anisotropic material, the constitutive relationship of the material and the warping of the beam cross-section are the two aspects that change the most. Hong and Chopra [64] studied the effect of composite laminate structure on the blade stiffness coupling by replacing the isotropic material constitutive relation in Hodges and Dowell nonlinear blade model with that of the laminate structure.

Bauchau et al [65–67] focused on adding degrees of freedom for section warping to the beam model. Hong [68] and Smith [69] combined the above two aspects of work and carried out research on the modeling and analysis of composite blades. Benquet [70] and Celi et al [71–73] analyzed the complex geometry blades with swept and dihedral tips via coordinate system transformation and special finite element matrix assembly method. With the development of the new rotor structural designs, the drawbacks of simplifying the model based on the rotor system characteristics were exposed. Whenever there was a new structural design, the model needed to be re-derived and validated. Bauchau and Ghiringhelli [74–76] showed how general-purpose multi-body dynamics can be used to build up systems of blades, hubs, and pitch links while avoiding repeated re-derivation of the equations. However, all of these models were limited to beams. The blades must be uniform and slender. The composite formulation was applied to the cross-section. The computational power available at the time would not allow 3-D models for rotor dynamics.

Thus, for decades, the rotor blades were analyzed by a combination of two-dimensional cross-sectional analysis and one-dimensional beams. However, it is obvious that when the blade profile, internal structure, and material properties have discontinuities, the blade should be regarded as a three-dimensional structure. Parts of the rotor that are near the hub are not even slender structures. These parts absorb stresses and determine weight. These parts provide kinematic couplings that determine stability. The growth of active rotors revealed further drawbacks and limitations of analyses. Damaged blades or blades with live fire hit could not be modeled as beams. Chordwise deformations or spanwise discontinuities like flaps

and slats are also hard to model. The beam models became more and more reliant on empirical measurements made after the rotor is built and fell short of providing a true first principal prediction.

Epps [14] studied the effect of the swept tip on the natural frequency of a rotating beam. By comparing the experimental data and the analysis results, it was found that when the sweep angle of the tip section increases, the error of the beam model also increases, and the error in the higher-order frequencies are more prominent. In 2005, Truong et al [77] attempted to compare the blade analysis results of the beam model and the 3-D finite element model. In this study, the beam model and the 3-D model in the commercial program MSC/Marc were used. The results indicated that the difference between the natural frequencies of the blade obtained by the 3-D finite element model and the experimental value is lower than that of the beam model. Then Yeo et al carried out further systematic comparison [78]. The beam model, in this study, adopted the geometric accurate composite beam model and Variational Asymptotical Beam Sectional Analysis (VABS) method in the Rotorcraft Comprehensive Analysis System (RCAS), while the 3-D finite element model was still MSC/Marc. The comparison of natural frequencies shows that this beam model has good accuracy for beams with a small aspect ratio. However, when a swept tip is present, whether it is a metal beam or a composite blade, the difference between the beam model and the 3-D finite element model increases with the swept angle. Even though these models were elementary and included none of the complexities of a modern rotor that called for 3-D, these findings reveal the value of developing 3-D structural finite element models for blades.

In 2008, NASA [79] identified 3-D structures as one of the requirements of future comprehensive analysis. Datta and Johnson [80] proposed a 3-D finite element structural analysis method for rotor blades in 2009. In 2010, they unified multi-body dynamics with 3-D formulation [81]. But these were idealized rotors. From 2014 to 2017 Staruk et al established the analysis process and tools based on Computer-aided Design (CAD) [82]. Ward et all established material modeling techniques for 3-D [84]. These ultimately opened the door to application on real rotors. NASA provided the 1/4 scale V-22 model geometry to the University of Maryland to assist in the creation of a showcase problem [83]. The 3-D methodology has matured since then [85–87], and it is now available within the X3D solver.

1.2 Objectives of the Thesis

The objectives of this thesis are to: 1) fabricate and test a double anhedral tip composite rotor to investigate its impact on structural dynamics and loads; 2) develop a state-of-art 3-D model and validate it with test data.

The first objective aims to fill the lack of basic understanding of loading on the rotor with anhedral tips. A set of Mach-scaled double anhedral composite blades were designed in consultation with Boeing to ensure that the geometry and structure are realistic enough to be representative of a modern rotor and yet be open source. An in-house fabrication methodology was developed for these blades. A special-purpose hingeless hub was designed and fabricated in-house to excite the rotating blades in vacuum, and allow the measurement of rotating frequencies. Hover tests

were carried out with a hingeless rig as well.

Three-dimensional models were developed from the same CAD used in fabrication. Then they were meshed in Cubit and analyzed with X3D. A lifting line aerodynamic model with free wake was used with particular attention paid to the aero-structure interface. The correlation of the test data and the analysis not just laid the foundation for studying the double anhedral tip, but reproduced the 3-D workflow, and validated the 3-D model on a realistic advanced rotor. A straight blade model was also developed as a baseline control case to explore the impact of the double anhedral tip in forward flight. The straight blade was not fabricated, however. Nor were forward flight tests carried out in the wind tunnel. These remain work for the future.

1.3 Organization of the Dissertation

This dissertation contains seven chapters. These chapters are organized as follows. Chapter one presented the background and motivation of the investigation of the double anhedral composite blade. Prior work in fixed-wing aircraft and rotary-wing was reviewed. The objective of the current thesis was described. Chapter two describes the development of the double anhedral composite blade. Chapter three covers the test rigs used in vacuum tests and hover tests. Chapter four introduces the development of the 3-D blade model. Chapter five validates the 3-D double anhedral composite rotor with the test data acquired from the vacuum test and hover test. Chapter six contains the fundamental understanding of the double anhedral tip. A

straight blade 3-D model is used as a baseline. Chapter seven summarizes the work and draws key conclusions. It ends with recommendations for future work.

Chapter 2: Development of Double Anhedral Tip Composite Blade

This chapter presents the development of the double anhedral tip composite blades (Figure 2.1). The double anhedral tip was designed with a superficial resemblance to the Boeing CH-47F like Advanced Chinook Rotor Blade (ACRB), as shown in Figure 2.2, with a similar but simplified tip shape. The cross-section, twist, and structural properties are otherwise generic. Thus, in essence it is an open-source academic research blade. The blade geometry, structure, and materials are representative of any modern scaled composite rotor, and they are detailed in this chapter.

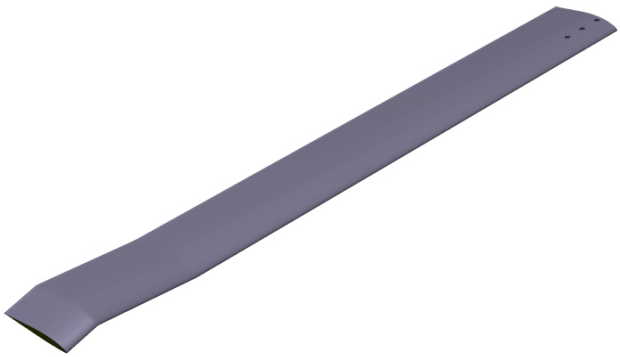

Figure 2.1: UMD Double Anhedral Tip Blade.



Figure 2.2: Boeing Advanced Chinook Rotor Blade [88].

2.1 Blade Design

The overall parameters of the blade are shown in Table 2.1. The blade has a span of 0.713 m and a uniform chord of 0.08 m. There is a linear built-in twist of -16° over the radius and a non-symmetric VR-7 airfoil. The layout of the airfoil across the span is shown in Figure 2.3. The anhedral angles are defined by a curved quarter chord line with respect to the rotational plane. The airfoil always remains perpendicular to the local quarter chord line. Moreover, the blade cross-sections are rotated about the local quarter chord line to form the built-in twist.

The blade design has three main sections and two transition regions, as shown in Figure 2.4. The straight portion extends from the root to 80%R connecting to a 5° dihedral portion over $80 - 95$%R. The last portion has an anhedral of 15° over the last 5%R. Two transition regions are designed at the beginning of each anhedral portion to ensure a smooth aerodynamic contour. Each transition region occupies the first 0.5%R of its portion. The quarter chord lines are linear outside

the transition region. These geometric attributes were decided in consultation with Boeing and based on the hover tower and the Glenn L. Martin wind tunnel test section at Maryland.

Table 2.1: Blade parameters.

Parameters	English	Metric
Span	28 inch	0.713 m
Chord	3.15 inch	0.08 m
Airfoil	VR-7	
Twist	$-16°$/radius	
Taper	Untapered	

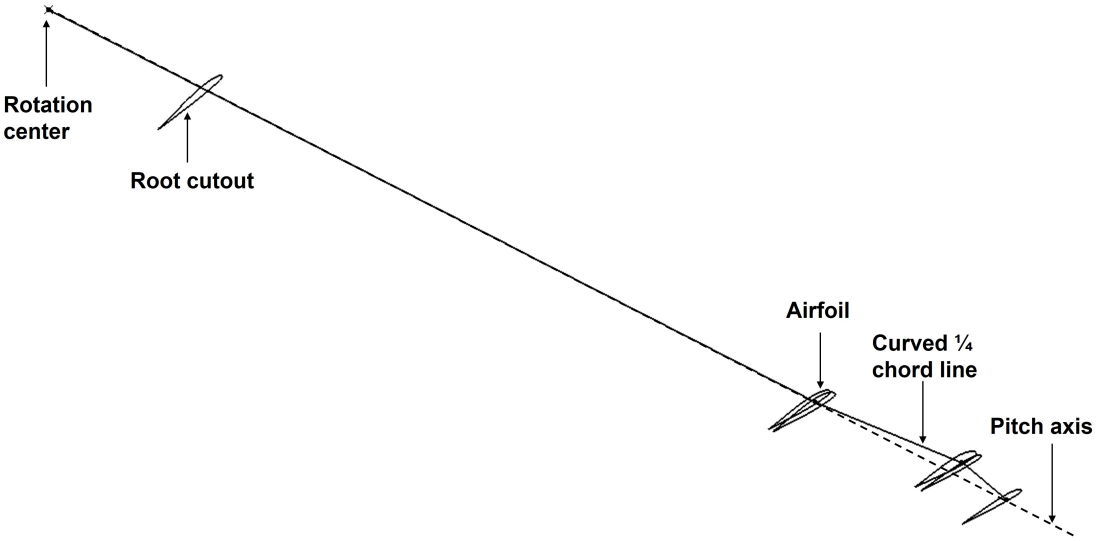

(a) Isotropic view of the airfoil layout.



(b) Rear view of the airfoil layout.

Figure 2.3: The airfoil layout.

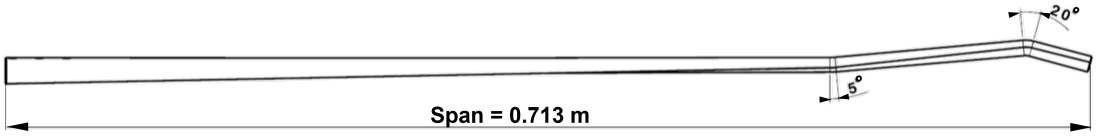

(a) Rear view of the blade geometry.

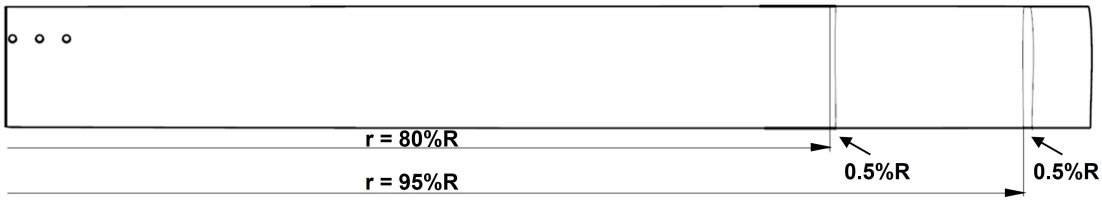

(b) Top view of the blade geometry.

Figure 2.4: Blade tip geometry and planform.

As for the internal structure, the cross-section is mainly determined by the spar type since it is the main structural member of a blade. Figure 2.5 shows four spars considered for this design: C-spar, D-spar, box spar, and solid spar. The D-spar was selected. Compared to the C-spar and the solid spar, the D-spar is a closed section and therefore has a higher torsion stiffness which is beneficial to prevent instabilities such as flap-pitch flutter and divergence. Compared to the box spar, the D-spar provides better support for the leading-edge shape with fewer ply layups and more space for leading-edge weights which are required for small-scale rotors. Furthermore, the D-spar structure is a good representative of the Chinook blade internal structure [89]. Therefore, the D-spar was chosen to be the main structural member of the blade.

The final internal structure is shown in Figure 2.6. The width of the D-spar is 26.8 mm (33.5%c) starting at the leading-edge. The parameter is mainly affected by the location and size of the blade root insert. It comprises two layers of $\pm 45°$

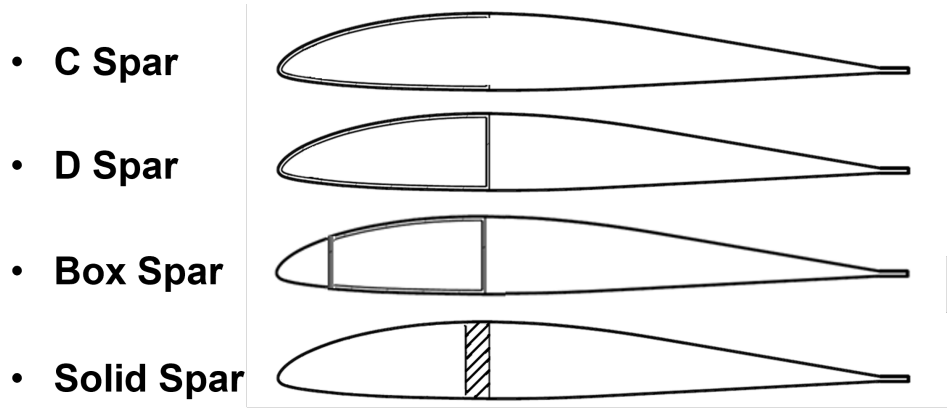

Figure 2.5: Types of blade spar.

IM7/8552 graphite/epoxy prepreg weave throughout the span. Besides the D-spar, another main structural member is the skin. The same composite material is shared between the spar and the skin. The skin is made of one layer instead of two. A 3.6 mm long trailing edge tab is designed to obtain a better bond between the upper and lower skins at the trailing edge. As shown in Figure 2.6, there is a leading-edge weight inside the D-spar to bring the cross-sectional center of gravity (C.G.) to the nominal aerodynamic center at the quarter chord. To minimize the mass and size of leading-edge weight, it is better to use dense material and place it as close to the leading-edge as possible. Hence, tungsten alloy was chosen. However, placing the leading-edge weight against the internal surface of the spar requires the leading-edge weight to have an airfoil profile, which is hard to machine in-house. Based on these considerations, tungsten alloy rods of 13.2 mm diameter are used as leading-edge weights, and they have located 16.1 mm ahead of the quarter chord. Instead of a single continuous rod, there are 16 discrete rods to limit their effect on the blade structural stiffness (Figure 2.7). Each tungsten alloy rod has a length of 38.1 mm

which can fit inside the 5%R anhedral tip portion of the blade. An aluminum root insert was designed as shown in Figure 2.8 for blade connection. All of the blade features discussed are individually modeled and are parts of a 3-D Computer-Aided Design (CAD) model built in CATIA (Figure 2.9).

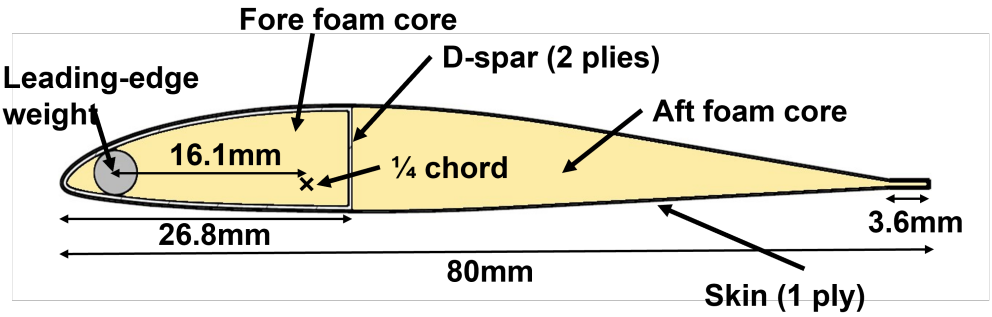

Figure 2.6: Blade cross-section structure.

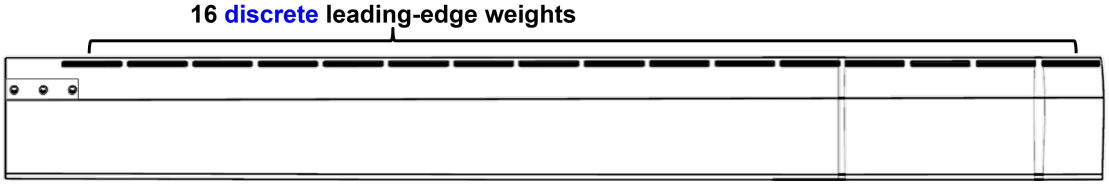

Figure 2.7: The layout of leading-edge weights.



(a) Top view of the root insert.

(b) Side view of the root insert.

Figure 2.8: Root insert design.

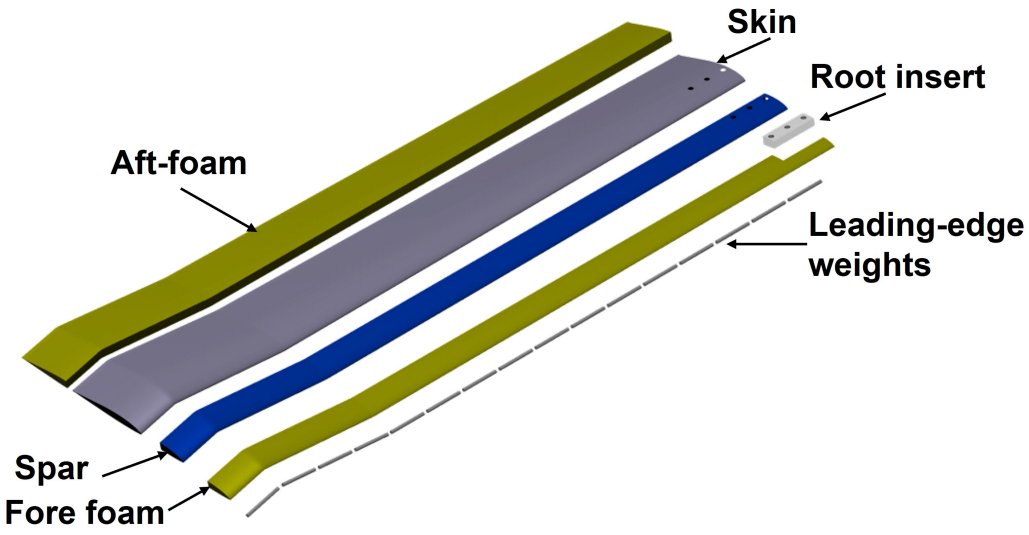

Figure 2.9: CAD model of each blade component.

2.2 Blade Mold

Based on the blade CAD model, a blade mold was designed (Figure 2.10) and fabricated (Figure 2.11) by Xcentric Mold & Engineering Inc. The mold is made of aluminum 5083 selected to limit the deformation due to the temperature change.

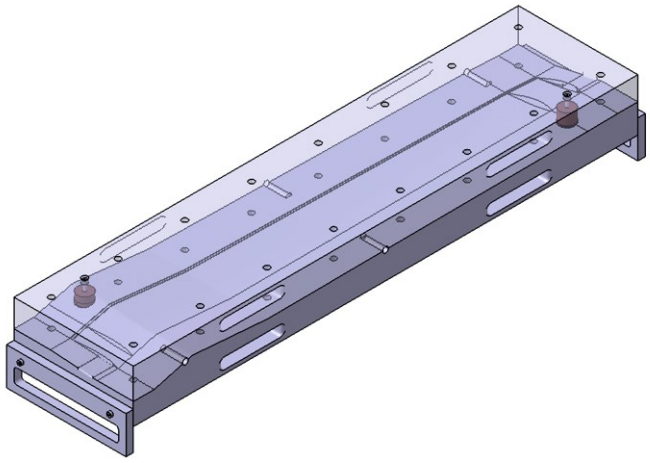

Figure 2.10: CAD model of the mold.

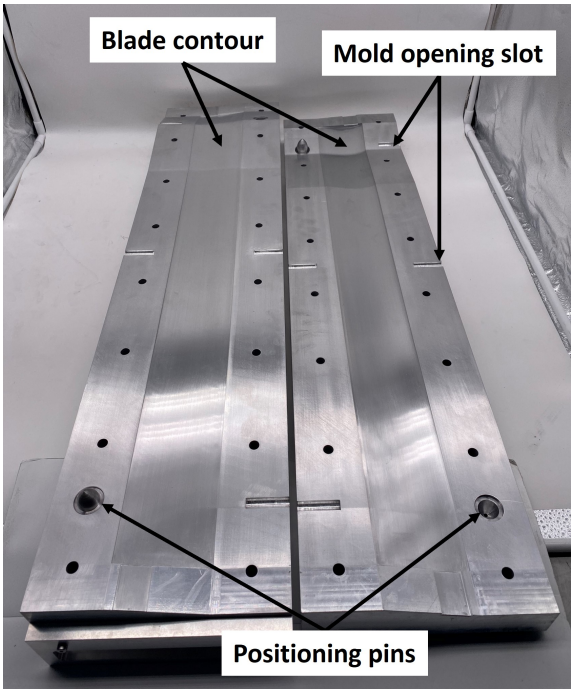

Figure 2.11: Double anhedral tip blade mold.

The mold can be separated into a top and a bottom part. Two pairs of ogive-shaped positioning pins were designed to help the top and bottom surface of the blade match precisely when the mold is closed. The length of the internal space is longer than the blade, and the extra internal space was designed to allow the epoxy to flow freely at the root and the tip portion. Sixteen through holes distributed evenly on the mold are used to apply uniform pressure on the blade via bolts and nuts. There are two opening slots on the side of the mold to help open the mold after the curing process.

2.3 Internal Components Fabrication

The blade fabrication process essentially follows the standard University of Maryland process [90] but is refined here for advanced blade geometry. The internal

components of the blade include: 1) root insert, 2) leading-edge weights, 3) fore core, and 4) aft-core. Their fabrication is documented here.

The root insert transfers loads from the blade to the blade grip by providing attachment points to three bolts. It was machined out from an aluminum 7075 plate that is slightly thicker than the root insert. Its fabrication process involves drilling and Computer Numerical Control (CNC) machining. Because the top surface of the root insert is not flat but follows the airfoil profile (Figure 2.4(b)), the blade grip holes need to be drilled before CNC machining to ensure the quality of the holes (Figure 2.12(a)). The alignment and orientation of these holes are critical to the blade as they determine if the blade has any unintentional pre-pitch and pre-lag angles.

The G-code for CNC machining was generated via a CAM program–SprutCAM [91] based on the root insert CAD model. As shown in Figure 2.12(b), the CNC machining was done by Tormach PCNC1100 [92]. It is recommended that a batch of root inserts are fabricated at the same time to reduce dissimilarity among blades and time consumed (Figure 2.8(b)). The same is true for the other internal components.

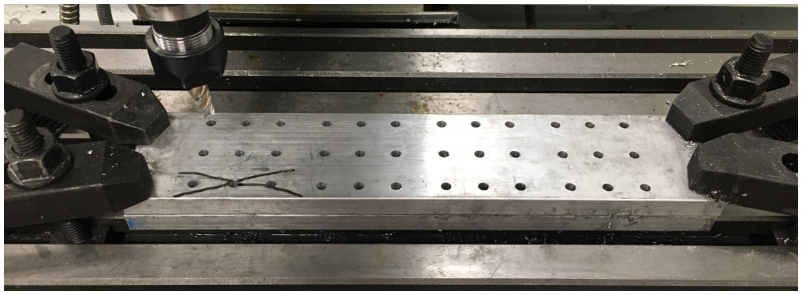

(a) Root insert holes drilling.

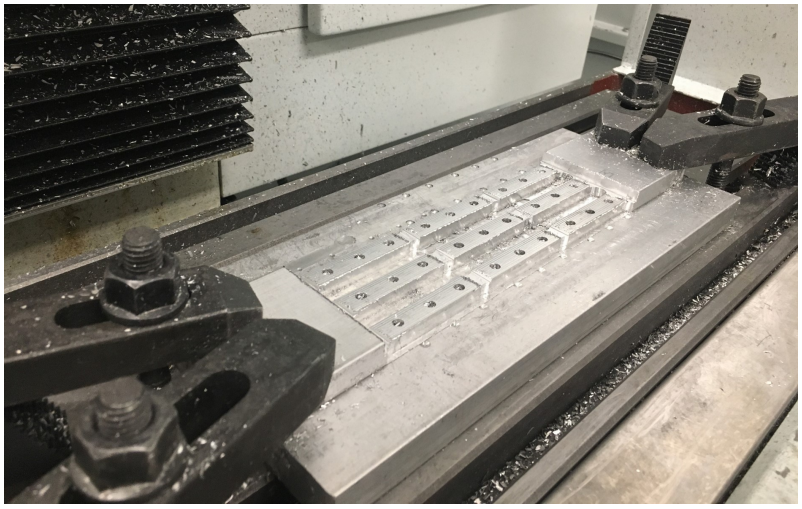

(b) Root insert machining.



(c) Root inserts.

Figure 2.12: Root inserts fabrication.

The next step is the fabrication of the foam core. The primary function of the foam core is to support the aerodynamic shape and hold the leading-edge weights in place. Typically, foam with a high density is better for holding the internal components. However, the denser foam the harder it is to work with. Rohacell 31 IG-F [93] 12.75 mm thick sheet is used as the raw material of the foam core. A rectangular foam piece that is slightly larger than the blade contour was cut out from the foam sheet. This prevents manual adjustment of the foam shape later and ensures a consistent core density. The tip of the blade has a 20° bend which exceeds

the maximum allowable bending curvature of the foam sheet. Therefore, a separate piece of foam is needed for the tip.

The airfoil contour of the core is formed by the mold pressure. It is challenging to precisely set the foam pieces into the mold since this blade has a highly twisted and curved tip geometry. Double-sided tape was used to ensure the foam stays in a secured place. While closing the mold, it is important to make sure the leading and trailing sides of the foam are caught by the leading and trailing edge of the mold (Figure 2.13). This can be checked by looking from the side of the mold with a flashlight. As long as the foam is fully caught by the mold, the internal space of the mold will be fully filled by the foam and form a precise blade contour. The bolts and nuts should be tightened manually, and slowly, beginning in a star pattern to minimize the chances of relative motion between the foam and the mold. The star pattern also helps to apply pressure evenly across the blade. Finally, an impact wrench was used to tighten the bolts and close the mold completely.



Figure 2.13: Foam sheet inside the mold.

After closing the mold, the aerodynamic contour is formed on the foam core. However, this is only temporary. The foam core needs to be heated to solidify the

shape. The oven (FREAS 645) is heated up to 177°C before the mold is put inside and held at the same temperature for 90 minutes. After cooling down, the foam core is removed from the mold, and the excess material at the leading-edge and trailing-edge are trimmed and lightly sanded. Particular care should be taken while treating the leading-edge to make sure the airfoil profile is preserved smoothly. The leading-edge is critical for airfoil performance.

The splitting of the foam core into fore and aft-core pieces (Figure 2.9), milling of the circular slots for leading-edge weights, and creating the space for root insert also require CNC machining. A 3-D printed base with an internal airfoil profile is used to untwist and level the foam core during the machining process (Figure 2.14). The foam core is secured in the base using double-sided tape. By splitting the foam into the fore and aft-core, a gap is created in between which accommodates the D-spar. The leading-edge weight slots are milled from the bottom surface of the core. The entire machining process can be done automatically and precisely by generating a G-code based on the foam core CAD model.

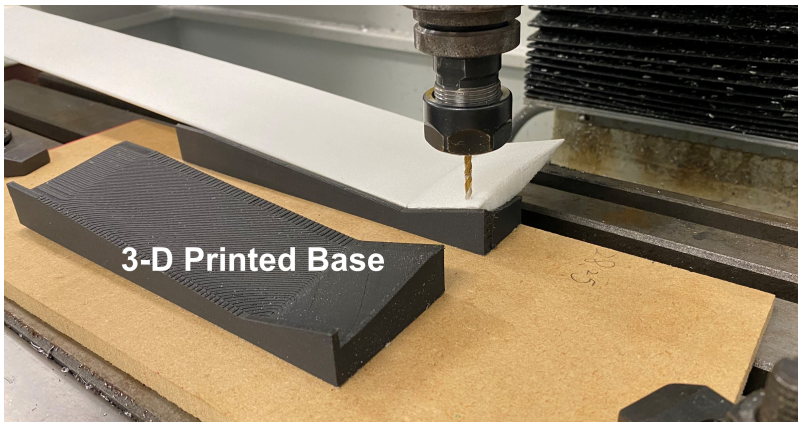

Figure 2.14: Machining of the foam core.

At this stage, the fabrication of internal components is complete and they are ready to be assembled (Figure 2.15). The next step is to wrap the leading-edge weight rods with a ply of film adhesive (Cytec FM300 [94]) before inserting them into the circular slots in the fore core. After covering the root insert with a ply of film adhesive to enhance structural integrity, the fore foam core and the root insert are assembled and wrapped with one additional ply of film adhesive. This assembly becomes the mandrel of the D-spar. Similarly, the aft-core is also wrapped by a layer of film adhesive (Figure 2.16).

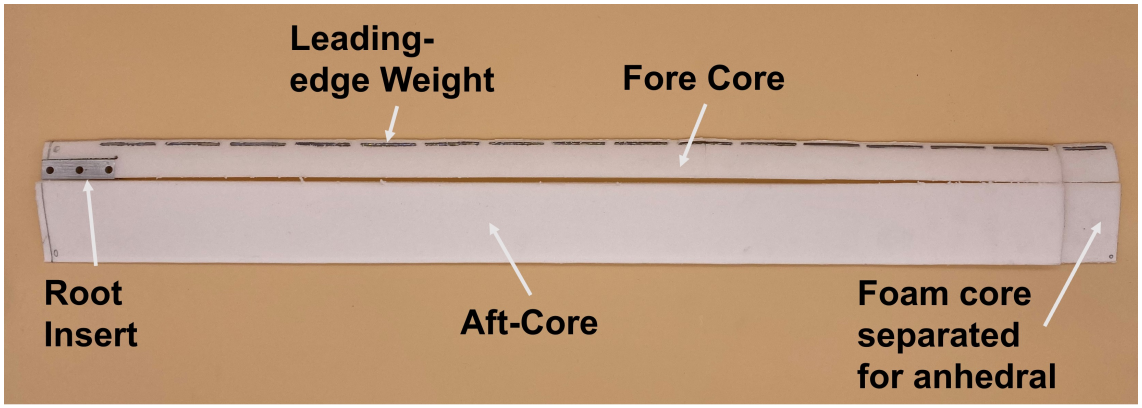

Figure 2.15: Blade internal components.

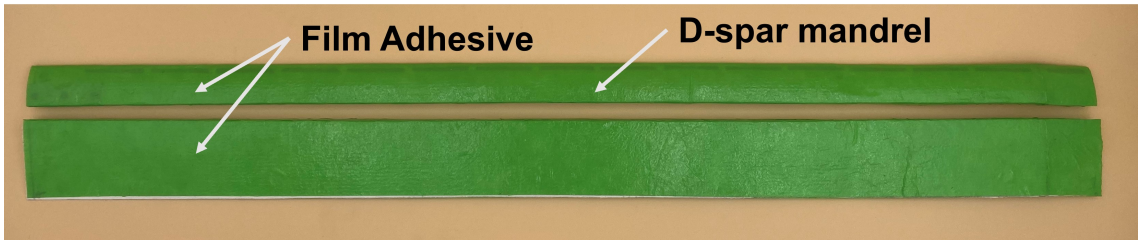

Figure 2.16: Assembly of internal components.

2.4 Spar and Skin Fabrication

A ±45° IM7/8552 graphite/epoxy prepreg weave is the material of the main structural members: spar and skin. This composite material is donated by Boeing. Prior to working with carbon fabric material, gloves are required to protect the specimen and the fabricator. Acetone is needed to clean the tools and mold. A release film (Wrightlon 5200) cover is needed on the workspace to create a clean dust-free environment.

In order to have precise cuts on composite sheets, a new X-ACTO blade is used. Both the size and fabric orientation are crucial considerations. The exact size of the composite sheet needed for the spar and skin can be extracted from the CAD model. Instead of having a slightly larger sheet, then trim after wrapping, an exact size allows better control over the weight. As for the ±45° fabric orientation, it is recommended to use the white fabric bundle as a reference. Using a metal cutting template, the composite sheets can be cut efficiently and accurately. All of the composite sheets cut out for spar and skin should be preserved in the fridge and the temperature kept under −18° to prevent dehydration of the epoxy and breakage of the fabric.

The final step of the D-spar fabrication is to wrap the mandrel with ±45° IM7/8552 graphite/epoxy prepreg weave. The prepreg sheet is wrapped around the mandrel twice to form the double layers starting at the back surface of the mandrel. As the sheet wraps around the mandrel, a rubber roller is used to compress the composite sheet to the mandrel. The wrapping should be done as tightly as possible

(Figure 2.17). At the anhedral tip, the mandrel is straightened and wrapped the sheet as if it was a straight blade, then let the mold bend the blade later. As shown in Figure 2.18, the assembly of the D-spar and the aft-core now becomes the core of the blade.

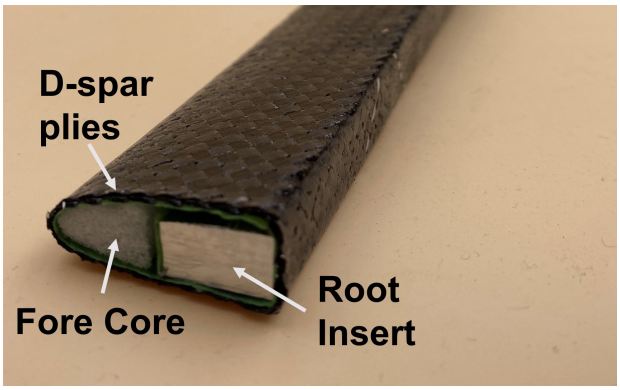

Figure 2.17: The D-spar.

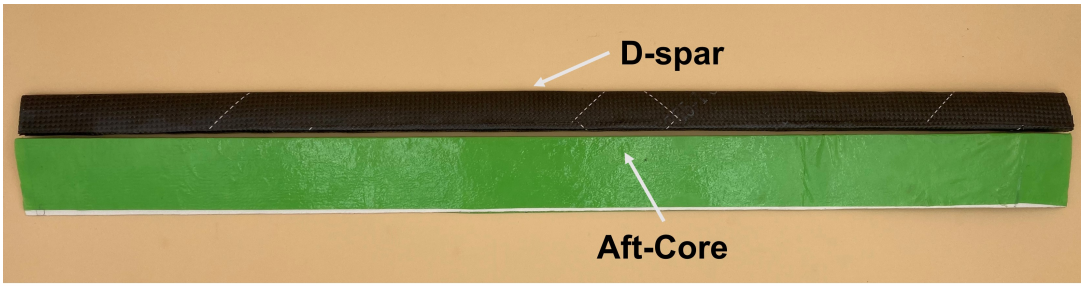

Figure 2.18: Blade core assembly.

To prevent the blade from sticking inside the mold after curing, one layer of release film (Wrightlon 5200) is used to cover the blade and separate the blade from the mold. To ensure the smoothness of the skin, the release film is attached to the skin before wrapping the skin to the blade core assembly. As shown in Figure 2.19, the skin is covered by an oversized release film. This step must be performed carefully to remove any wrinkles and bubbles. Then the skin is flipped

and the trailing-edge of the blade core is pressed against the long edge of the skin. While laying down the rest of the blade core, a roller is used to press and remove the trapped air. By lifting the blade core and pressing it against the table, a good bond between the D-spar and the skin can be achieved. Now the rest of the skin is pulled across the top surface of the blade core. The trailing-edge of the top and bottom skin needs to be bound firmly by the roller pressure. It is critical to keep the skin smooth in this process.

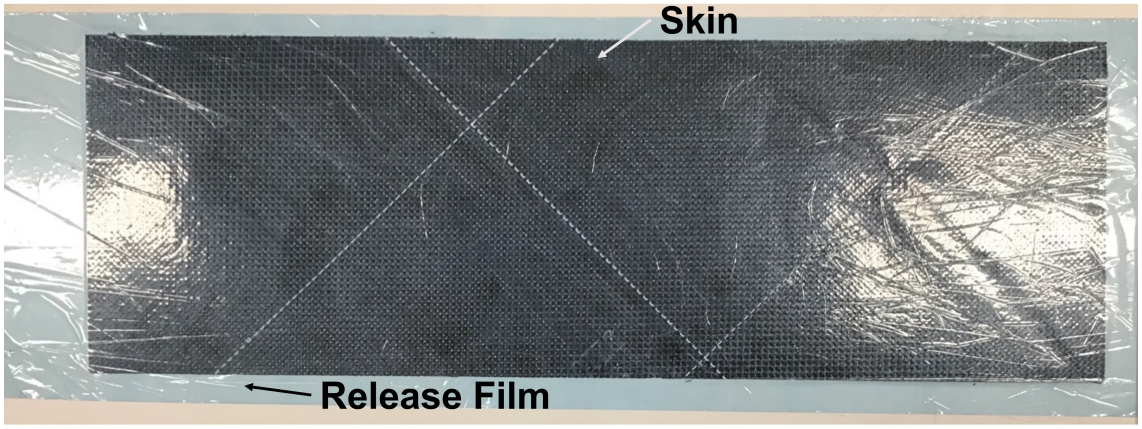

Figure 2.19: Release film and skin.

2.5 Blade Curing and Finishing

The uncured blade assembly is shown in Figure 2.20. Similar to the foam core fabrication process, double-sided tape is needed to secure the blade in the right place inside the mold. As the mold is closing, it is vital to keep the leading-edge of the blade aligned with the leading-edge of the mold (Figure 2.21).

The 8552 epoxy is a toughened resin that must be cured under high temper-

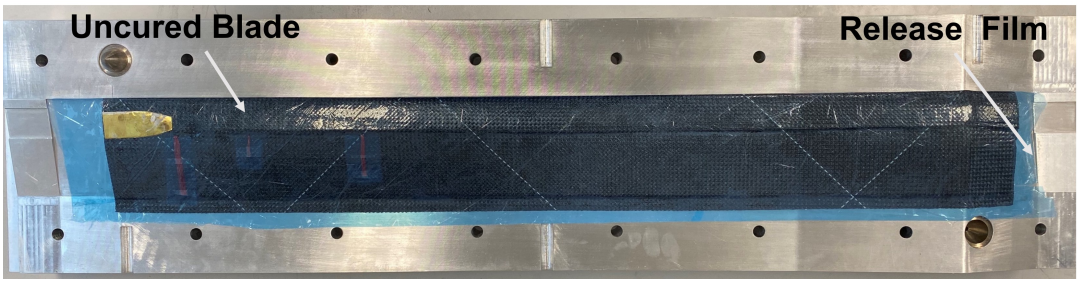

Figure 2.20: Uncured blade.

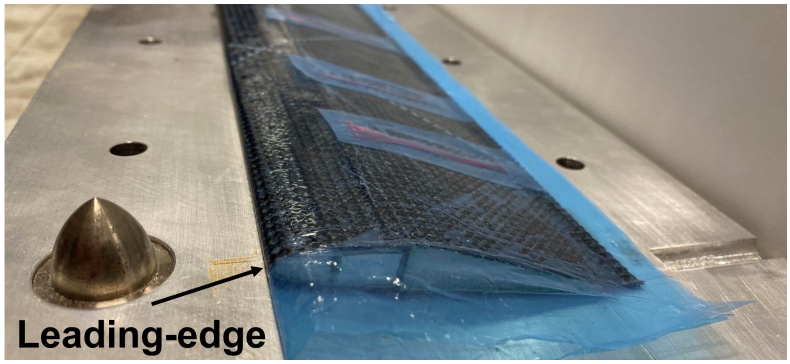

Figure 2.21: Leading-edge of the blade in the mold.

ature and high pressure. Therefore, the curing of the blade is effectively the curing of the epoxy. Similarly to the foam core fabrication, the oven is heated up to 177°C, then the mold is heated up from room temperature to 177°C and then held the temperature for 150 minutes. The double anhedral tip geometry was formed by the mold pressure.

After curing, the resin beads and unnecessary extrusions are trimmed out by a grinder. The leading-edge is sanded manually for a smooth finish. Drilling the bolt holes at the root is the final step. The root insert holes are covered by spar and skin. These holes can be found by using a relatively small drill bit. Then gradually increase the size of the drill bit until the holes are fully opened. In this study, a total of six blades were fabricated (Figure 2.22).

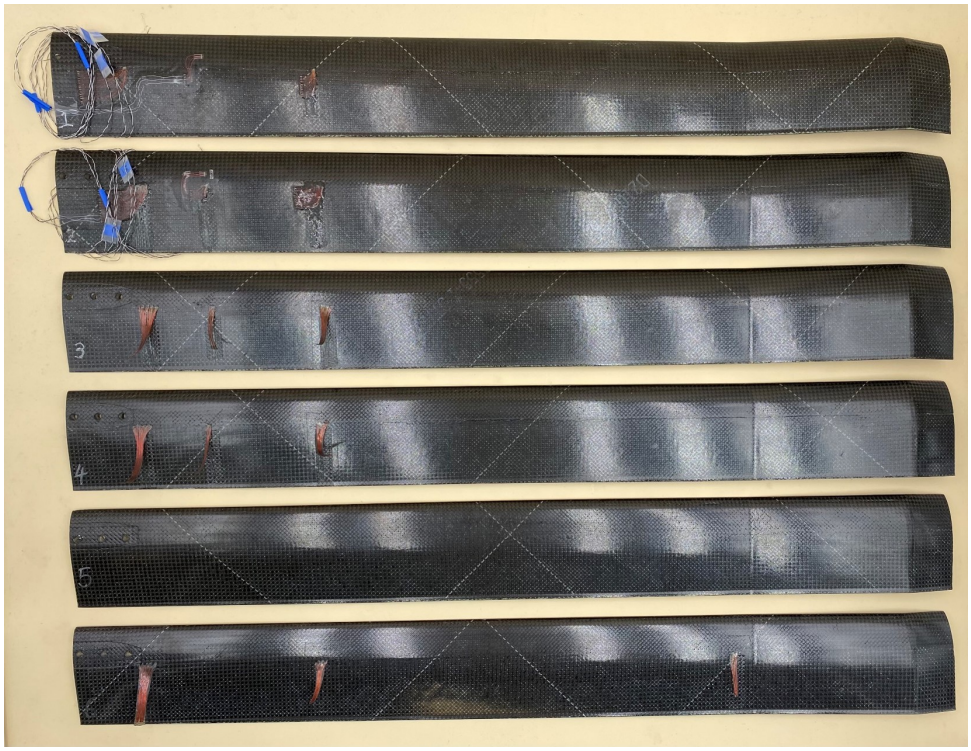

Figure 2.22: Double anhedral tip composite blades.

2.6 Blade Instrumentation

Strain gauges are needed to measure blade structural loads. The installation of gauges should be such that there is minimal change to structural integrity, sectional mass, stiffness, and aerodynamic properties. To this end, multiple ways of strain gauge installation were investigated, as shown in Figure 2.23. Method-1 binds the strain gauge on the surface of the blade and then protects it with a layer of epoxy. This method is easy to implement and has the minimum impact on blade structure. However, it changes the airfoil shape. Method-2 creates an indentation on the blade skin before curing using a thin metal shim. After installing the strain gauge, the indentation is filled with epoxy to recover the aerodynamic shape. In contrast to

method-1, this method has minimum impact on airfoil shape. However, it indents the structure. Method-3 embeds the strain gauge on the inner surface of the skin. In this method, the strain gauge neither indents the structure nor changes the aerodynamic shape. But the strain gauge must be installed before curing. It is hard to find a strain gauge that can survive the heat and pressure in the curing process. Since this study focuses on the structural loads and strain/stress of the blade, method-1 is chosen to keep the blade structure intact.

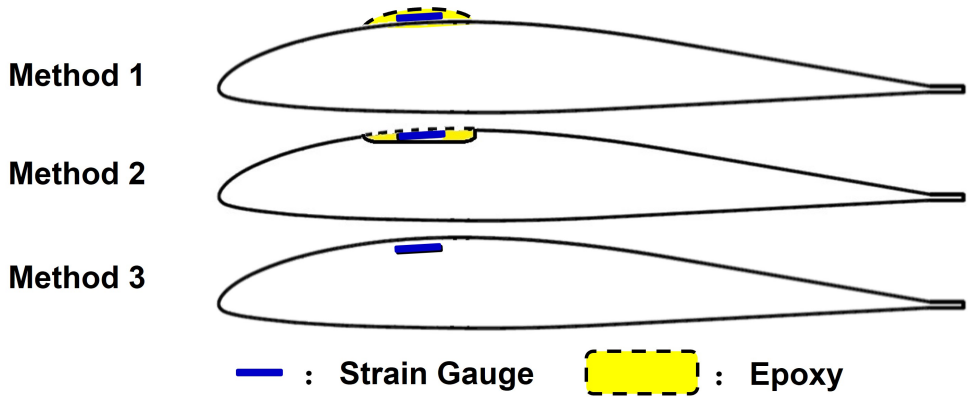

Figure 2.23: Methods of strain gauge installation.

To limit the impact of instrumentation, the wiring of the sensor is embedded inside the blade. As shown in Figure 2.24(a), copper wires were embedded in the aft-core. Due to the skin being made of prepreg weave material, existing holes allow the wires to pierce through the skin. The exposed wires are wrapped by release film to separate them from the outer surface of the skin during curing. Then they are trimmed to the right length and protected by epoxy (Figure 2.24(b)).

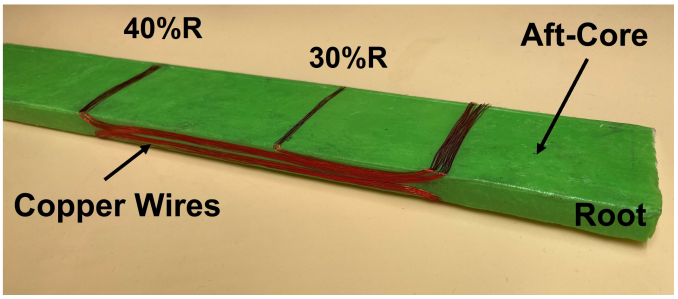

(a) Wires embedded in foam core.

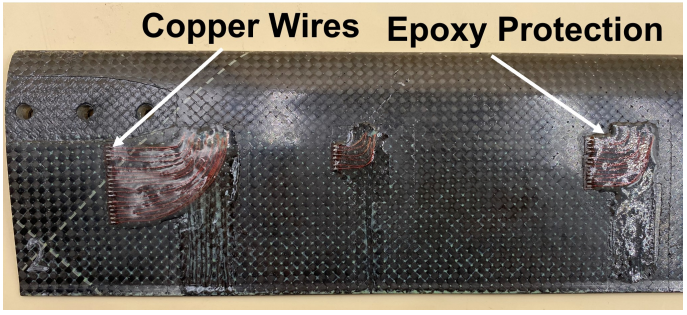

(b) Wires pierced through the skin.

Figure 2.24: Wires for instrumentation.

There are three sets of structural load sensors on each blade to measure flap bending, lag bending, and torsional moment at 40%R (Figure 2.25). Full Wheatstone bridge (Figure 2.26(a)) is used to build the sensors. V_{EX} is the excitation voltage, and V_C is the signal voltage. This kind of circuit has a good temperature compensation feature and the ability to amplify the signal of the target load while suppressing others. Figure 2.26 shows the strain gauge configurations for the measurement of each load. Two parallel grid gauges (Micro-measurements, N2A-13-S5092N-350/E5) near the quarter chord measure flap bending moment; four 1-axis linear gauges (Omega engineering, SGD-3/350-SY43) at leading and trailing-edge measure lag bending moment; two dual shear gauges (Omega engineering, SGT-3JS/350-SY41) near the quarter chord measure torsional moment.

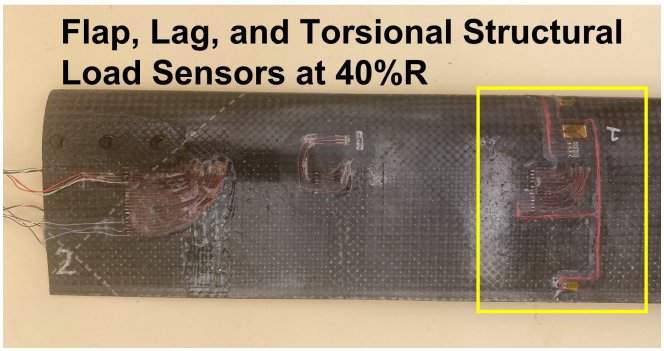

Figure 2.25: Structural load sensors.

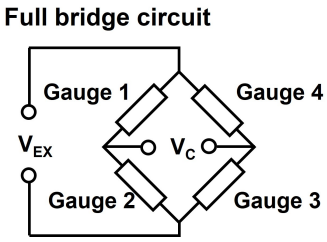

(a) Full Wheatstone bridge circuit.

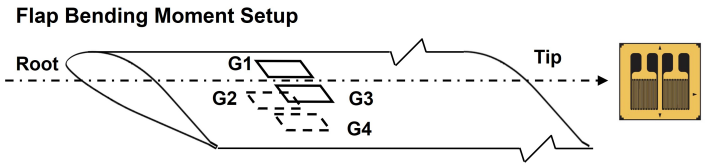

(b) Flap bending moment configuration.

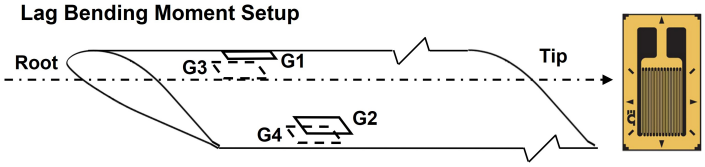

(c) Lag bending moment configuration.

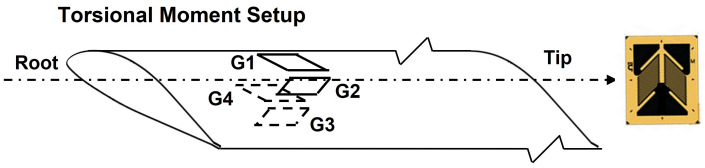

(d) Torsional moment configuration.

Figure 2.26: Strain gauge configurations for structural load sensors.

All of these sensors are calibrated carefully. A static loading frame is built out of 80-20 frames to perform the calibration. Figure 2.27 shows the setup for each load. For flap and lag bending moment, the blade root is clamped in a vise, and static weights are hung via a pulley to create the bending moment. An in-house fabricated load cell is used to measure the applied load accurately. For torsional moment calibration, the torsional moment is applied by a pair of the weight-pulley system and a moment arm. As each type of load (flap, lag, and torsion) is applied, the moment and the voltage signals from all three sets of sensors are recorded. This process resulted in a calibration matrix for each blade to convert analog voltage to moment. Equation (2.1) can be used to calculate the calibration matrix K. M_T, M_F, and M_L are torsional, flap, and lag bending moments; V_T, V_F, and V_L are voltage signals from the torsional, flap, and lag bending sensors. This method allows three sensors to be calibrated together and account for structural coupling. Due to the built-in twist, it is important to define the reference frame of the measured structural loads precisely. During the calibration, the flap bending moment was applied by a force normal to the chord line of the blade root. Hence, the measured flap bending moment references the root chord line. Similarly, the lag bending moment references the root insert bolt hole axis, and the torsional moment is about the quarter chord line of the straight portion of the blade. This means the structural loads were measured in an undeformed blade frame that rotates with the blade pitch control angle during testing.

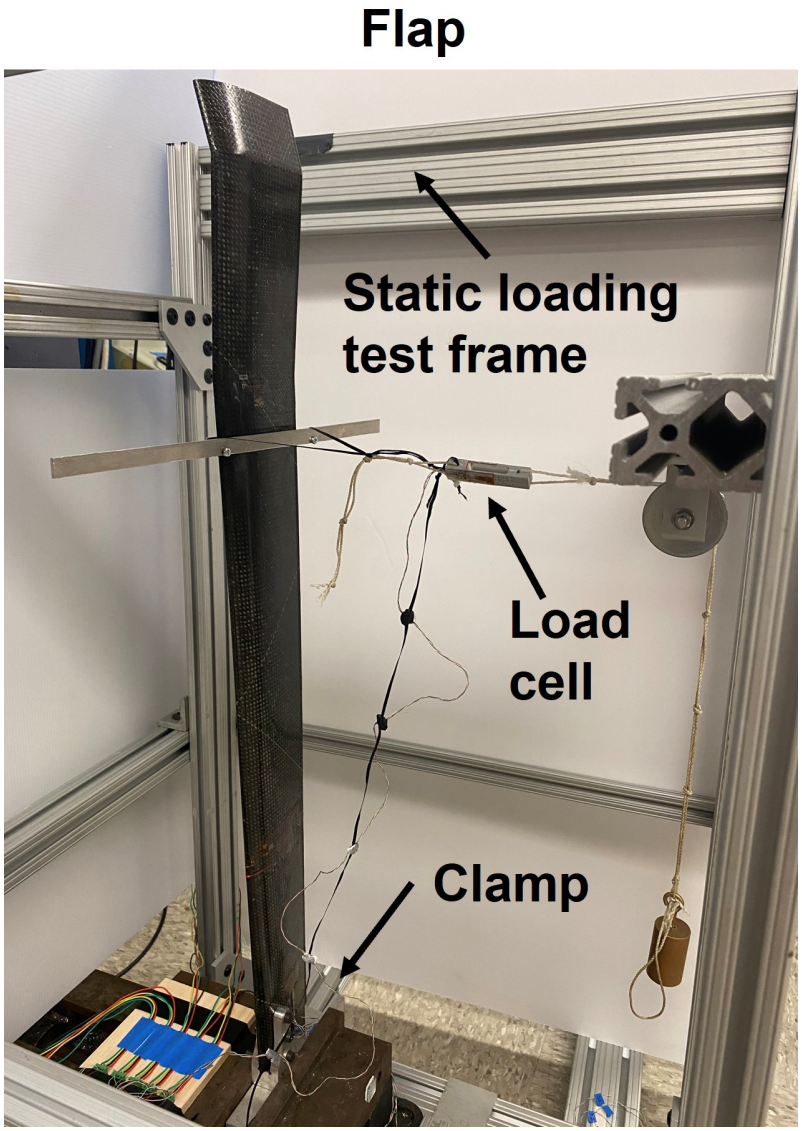

(a) Flap bending moment calibration.

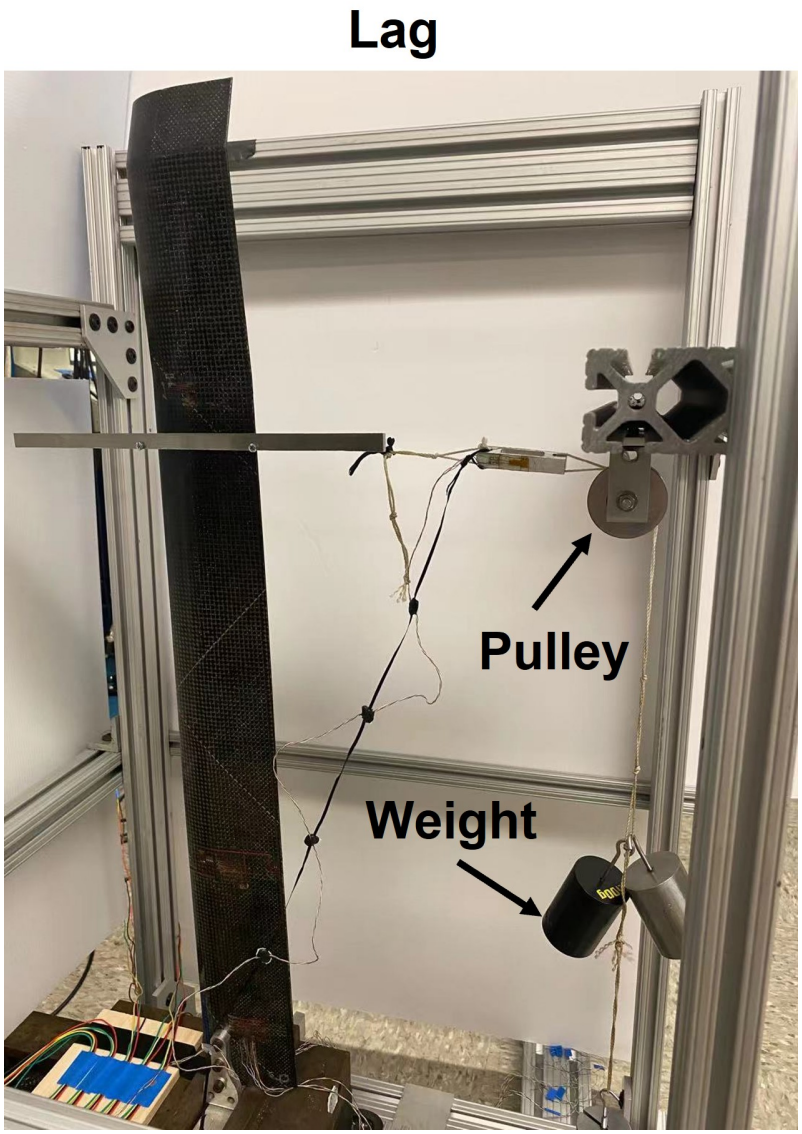

(b) Lag bending moment calibration.

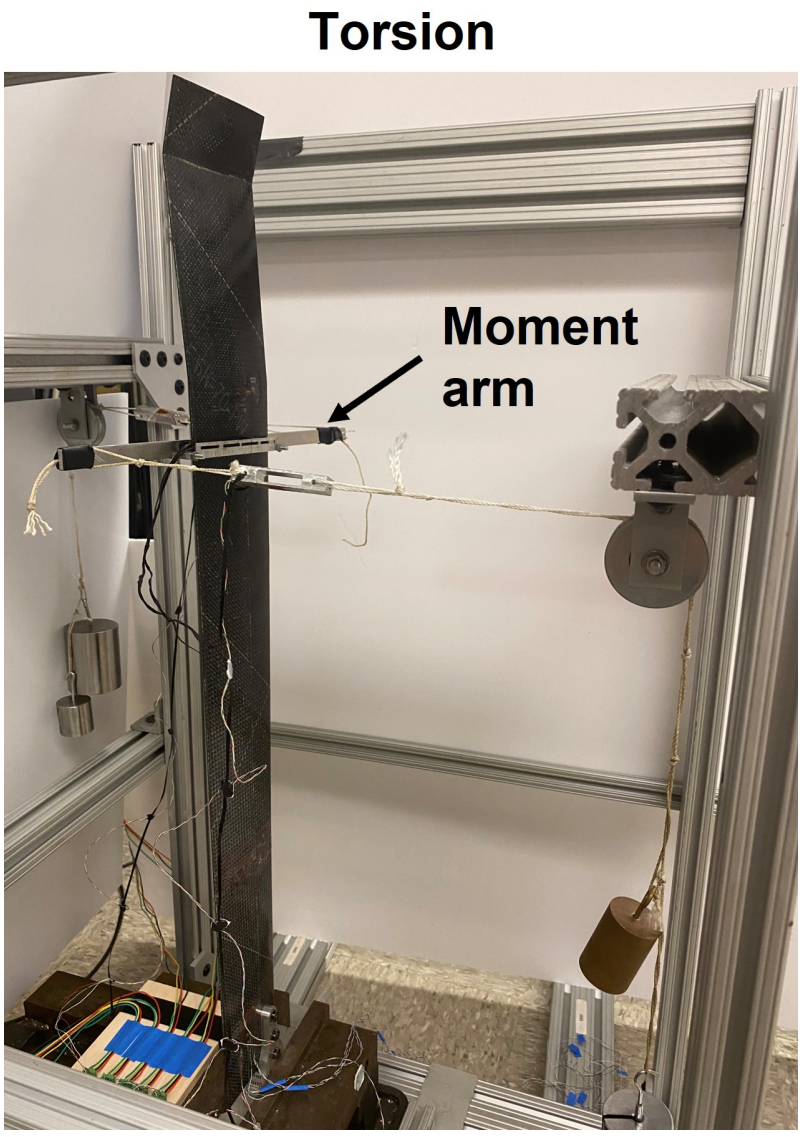

(c) Torsional moment calibration.

Figure 2.27: Structural load sensors calibration.

$$\begin{bmatrix} V_T & V_T & V_T \\ V_F & V_F & V_F \\ V_L & V_L & V_L \end{bmatrix} \begin{bmatrix} K_{11} & K_{21} & K_{31} \\ K_{21} & K_{22} & K_{32} \\ K_{31} & K_{32} & K_{33} \end{bmatrix} = \begin{bmatrix} M_T & 0 & 0 \\ 0 & M_F & 0 \\ 0 & 0 & M_L \end{bmatrix} \tag{2.1}$$

As for surface strain, there are two monitoring points: the top surface at 30%R near the root and the bottom surface at 80%R at the first anhedral junction. A diagram is shown in Figure 2.28. Both of the measurement points are on the quarter chord line. Metal foil strain gauge rosettes (Figure 2.29) with a relatively small footprint are used (Micro-measurements, C5K-09-S5198-350-33F). The gauges are protected by an epoxy coating (Figure 2.30). There are three linear strain gauges in a rosette.

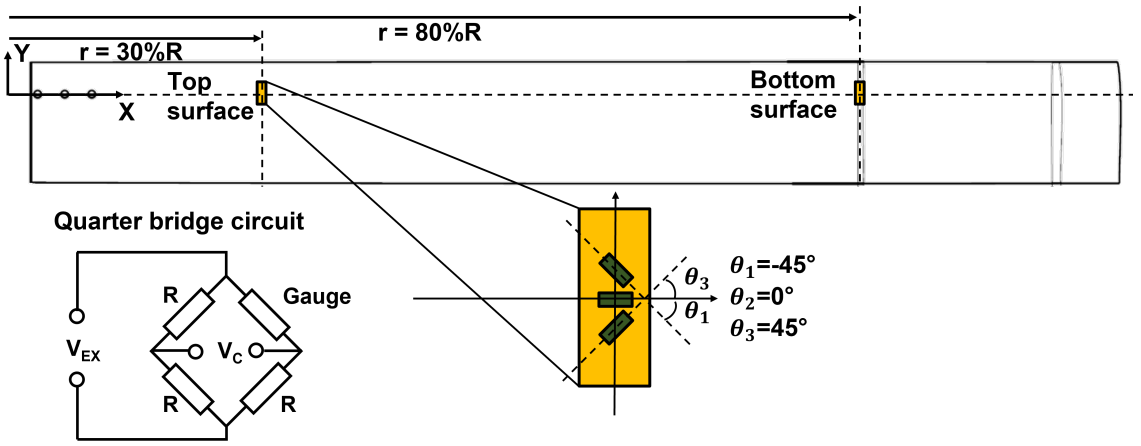

Figure 2.28: Strain measurement.

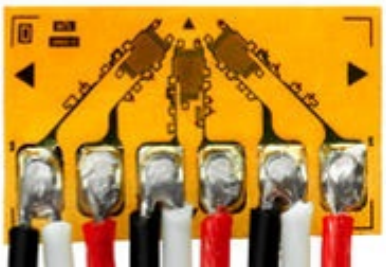

Figure 2.29: Strain rosette.

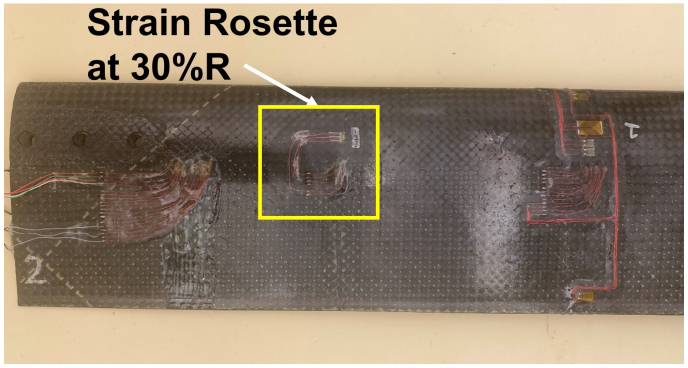

(a) Strain rosette at 30%R.

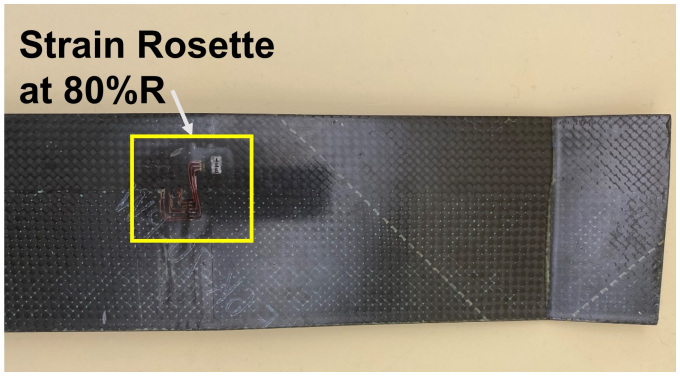

(b) Strain rosette at 80%R.

Figure 2.30: Strain rosette on the blade.

Quarter Wheatstone bridge (only one active element) is used to measure the strain ϵ, and it is given by Equation (2.2). GF is the gauge factor. For the rosette used in this study, the gauge factors are 1.86, 1.79, and 1.86 for each gauge, respectively. Strain rosette allows the access of axial normal strain ϵ_{xx}, chordwise normal strain ϵ_{yy}, and in-plane engineering shear strain γ_{xy}. Equation (2.3) is used

to transform the measured strains into strains in the global blade coordinate. θ_1, θ_2, and θ_3 are the orientation angles of the strain gauge with respect to the blade X axis.

$$\varepsilon = \frac{4\frac{V_C}{V_{EX}}}{GF\left(1 - 2\frac{V_C}{V_{EX}}\right)} \tag{2.2}$$

$$\begin{pmatrix} \epsilon_{xx} \\ \epsilon_{yy} \\ \gamma_{xy} \end{pmatrix} = \begin{bmatrix} \cos^2\theta_1 & \sin^2\theta_1 & \cos\theta_1 \sin\theta_1 \\ \cos^2\theta_2 & \sin^2\theta_2 & \cos\theta_2 \sin\theta_2 \\ \cos^2\theta_3 & \sin^2\theta_3 & \cos\theta_3 \sin\theta_3 \end{bmatrix}^{-1} \begin{pmatrix} \epsilon_1 \\ \epsilon_2 \\ \epsilon_3 \end{pmatrix} \tag{2.3}$$

2.7 Material Elastic Property

To build a reliable 3-D blade structural model, the material elastic properties and density of each component are necessary. They are documented in the next two sections.

The blade consists of four materials: IM7/8552 graphite/epoxy weave for spar and skin, tungsten alloy for leading-edge weight, Rohacell 31 IG-F for foam core, and aluminum 7075 for root insert. The elastic properties of IM7/8552 graphite/epoxy weave are important since it is the material of the main structural member (spar and skin). A standard four-point bending test is performed to measure the elastic properties (Figure 2.31). The four-point bending test creates constant bending moment and surface strain at the middle section of the beam, which is easier to

measure accurately.

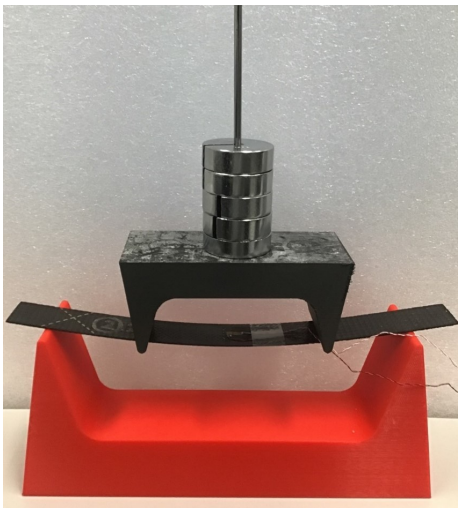

(a) Four-point bending test setup.

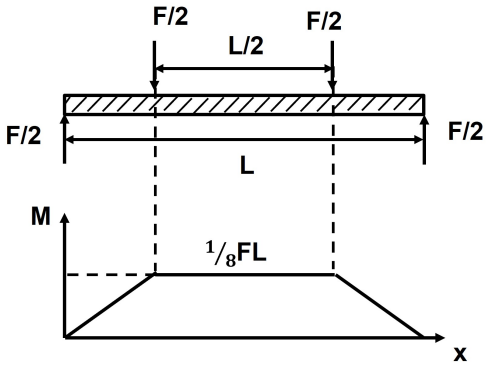

(b) Loading analysis of four-point bending test.

Figure 2.31: Four-point bending test.

As per ASTM D7264 [96], sample coupons were fabricated with layups of $[0/90]_6$, $[90/0]_6$, $[\pm 45]_6$, and $[\mp 45]_6$ to determine tensile moduli E_1 and E_2, in-plane shear modulus G_{12}, and major Poisson ratio μ_{12}. The subscripts (1 and 2) correspond to the fiber axis, and their definition is shown in Figure 2.32(a). Strain gauges are instrumented at the mid-section of the coupon along the longitudinal x and lateral y axis of the coupon to measure strains ϵ_{xx} and ϵ_{yy} (Figure 2.32(b)). Three coupons for each layup were fabricated and tested. Equations (2.4)-(2.7) are derived based on beam static load-strain relation, and then used for the elastic properties calculation.

Coupon $[0/90]_6$:

$$E_1 = \frac{6M}{bh^2\epsilon_{xx}} \tag{2.4}$$

$$\mu_{12} = \frac{-\epsilon_{yy}}{\epsilon_{xx}} \tag{2.5}$$

Coupon $[90/0]_6$:

$$E_2 = \frac{6M}{bh^2\epsilon_{xx}} \tag{2.6}$$

Coupon $[\pm 45]_6$ and $[\mp 45]_6$:

$$G_{12} = \frac{3M}{bh^2(\epsilon_{xx} - \epsilon_{yy})} \tag{2.7}$$

where M is the bending moment; b the width of the cross-section; h the height of the cross-section; ϵ_{xx}, and ϵ_{yy} are strains along its corresponding axis.

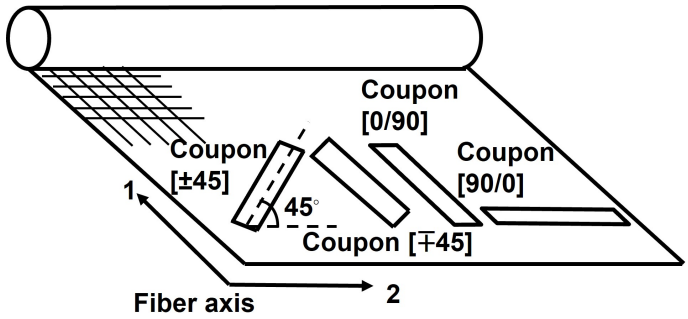

(a) Definition of fiber axis.

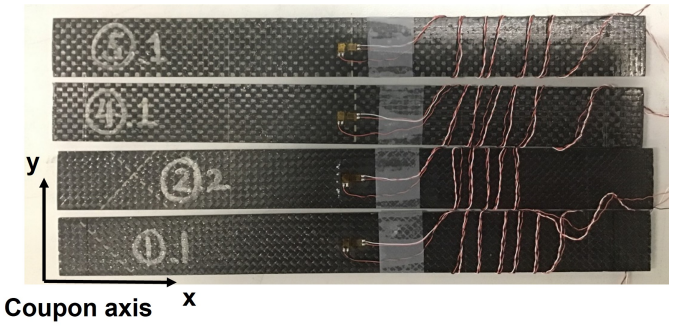

(b) Sample coupons.

Figure 2.32: Composite coupons.

The measured properties are shown in Table 2.2. The measured values show some differences with the product specification. The Poisson ratio μ_{12} and shear modulus G_{12} are not supplied at all. The differences are mainly due to the difference

in the curing cycle. The measured properties were used in modeling. The properties of the isotropic materials are taken from product specifications as they are fairly standard. They are listed in Table 2.3.

Table 2.2: Elastic properties of IM7/8552 graphite/epoxy prepreg weave.

Properties	Hexcel Corporation [95]	Present measurement
E_1, GPa	85	81.45
E_2, GPa	80	72.85
μ_{12}		0.0755
G_{12}, GPa		5.45
Cured ply thickness, mm	0.131	0.23

Table 2.3: Elastic properties of the isotropic materials.

Properties	Tungsten alloy	Rohacell 31 IG-F	Aluminum 7075
E, GPa	650	0.036	68.9
μ	0.2	0.3846	0.33

2.8 Blade Mass

The weights of the individual blade components were documented during fabrication for every blade. The weights are listed in Table 2.4. Blades 2, 3, 4, and 6 were then down selected as they were the most similar. The chordwise and span-wise center of gravity locations were also measured (Figure 2.33, Table 2.5). Based on the component weights from measurement, and the volumes extracted from the CAD, the density of each component can be calculated (Table 2.6). Thus, the weights of film adhesive and compressed foam are accounted for in these density data, which is important to reduce the uncertainties in the 3-D model. Figure 2.34 shows the final instrumented double anhedral tip composite blades.

Table 2.4: Measured weight of each component in gram.

ID	Root insert*	Fore core*	LEW*	Aft-core*	Spar	Skin	Mass	Total Discrepancy (%)
1	11.45	19.43	73.77	37.57	31.47	38.49	212.18	0.19
2	11.59	19.8	73.78	37.45	31.81	36.99	211.42	-0.17
3	11.33	19.67	73.77	37.56	31.6	37.77	211.7	-0.04
4	11.39	19.44	73.77	37.7	31.62	37.67	211.59	-0.09
5	12.34	19.68	73.77	37.21	32.19	37.17	212.36	0.28
6	11.53	19.66	73.78	37.78	30.85	37.79	211.39	-0.18

(*) including film adhesive

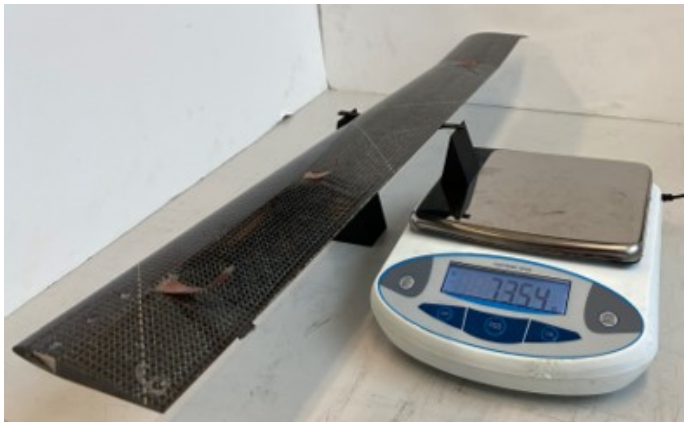

Figure 2.33: Measurement of blade center of gravity.

Table 2.5: Measured center of gravity location.

ID	Chordwise C.G. (%c)	Spanwise C.G. (%R)
2	29.8	40.2
3	30	40.6
4	28.9	40.6
6	29	40.9

Table 2.6: Measured density of each components in kg/m^3.

Component	Density
Skin	1415.2
Spar	1524.8
Fore foam	187.3
Aft-foam	193.2
Leading-edge weight	15287
Root insert	2750



Figure 2.34: Final blades.

2.9 Summary

This chapter presented the detailed design and fabrication of the double anhedral tip composite blade and the development of a corresponding 3-D CAD model. The fabricated blades were gauged and calibrated for structural loads. Material elastic properties were measured with coupon tests. The densities of each component were measured. Finally, six blades were fabricated of which four most similar were picked for testing. The key conclusions are:

1. Possible to create double anhedral tip blades with pressure molding alone.

2. Two spanwise internal cores are needed for the straight-dihedral section and the anhedral section.

3. The strain gauges can be mounted on the blade surface, but they should be connected to wires embedded in the foam core.

4. Reliable calibration is obtained by accounting for coupling.

5. Reliable component densities are acquired by weight measurement during fabrication and CAD model volume.

6. The composite material properties are different from the product specification. So in-house measurements are necessary.

Chapter 3: Development of Test Rigs

Vacuum tests and hover tests were carried out to obtain high-quality validation data and gain insights into the aeromechanics of the double anhedral tip composite rotor. Vacuum chamber rig (Figure 3.1(a)) was developed from scratch. The hover rig (Figure 3.1(b)) was repurposed from the existing test stand. This chapter presents the details of these two rigs.



(a) Vacuum test. (b) Hover test.

Figure 3.1: Experimental tests.

3.1 Vacuum Chamber Rig

3.1.1 Vacuum Chamber

A vacuum chamber test allows the elimination of aerodynamic couplings, and only the structural and kinematic couplings retain. Therefore, the blade structural integrity can be confirmed, and the rotating natural frequencies and surface strains can be measured. These data provide insights into pure structural dynamic characteristics. The vacuum chamber at UMD is shown in Figure 3.2. It is made of 1-in thick cast iron and has a cylindrical internal diameter of 10-ft and height of 3-ft.



Figure 3.2: Vacuum chamber.

The air inlet/outlet of the chamber allows the pressure to be controlled by an electric air pump (Figure 3.3). An analog gauge is used to monitor the chamber pressure. As the chamber is fully sealed, the pressure can be reduced to and

maintained at 99% vacuum, approximately 0.3 inch Hg.

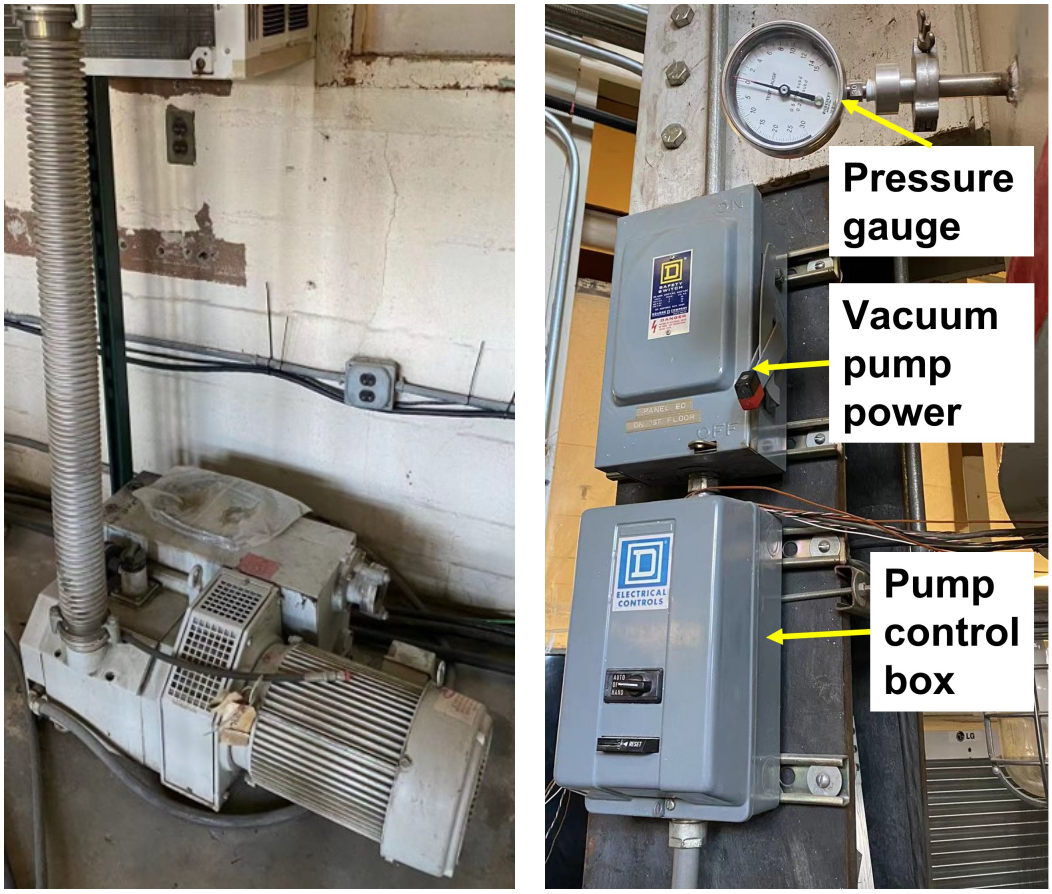

(a) Air pump. (b) Pump accessories.

Figure 3.3: Air Pump system.

The entire chamber is mounted on a steel structure and lifted 6 ft above the floor. This setup creates room for the rotor drive system, data acquisition system, and an entrance for the operator to access the rotor. As shown in Figure 3.4, the drive system and the instruments are mounted under the rotor shaft. The rotor is driven by an electric motor via a 1-to-1 ratio belt-pulley system. The rotor speed is set manually by the motor controller and monitored by optic sensors. The output voltage of the optic sensor changes every time a gear-tooth passes by, which results in a square wave signal. The rotor speed is acquired by analyzing the frequency

of the signal. A 64-channel slip ring is used to control the actuator on the rotor hub and communicate the sensor signal from the rotating frame to the non-rotating frame. It is connected to the rotor shaft through a shaft coupling to allow for some shaft misalignment and reduce vibration.

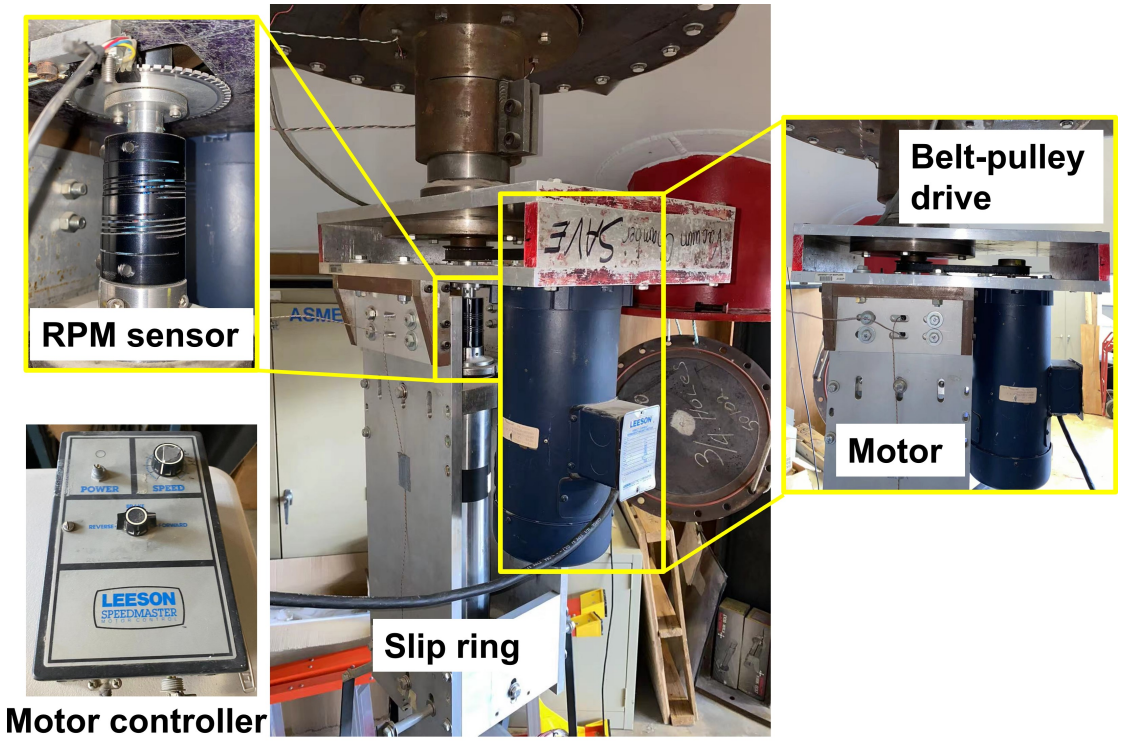

Figure 3.4: Vacuum chamber systems.

3.1.2 Design of a New Vacuum Chamber Hub

A new vacuum chamber hub is required to measure rotating frequencies. The design was performed in CATIA based on the CAD of the blade and the vacuum chamber as shown in Figure 3.5. The hub is two-bladed and hingeless. There is no swashplate. This configuration is chosen to limit the structural complexity, improve compactness, and obtain clean frequencies uncontaminated with complications of

the control system dynamics.

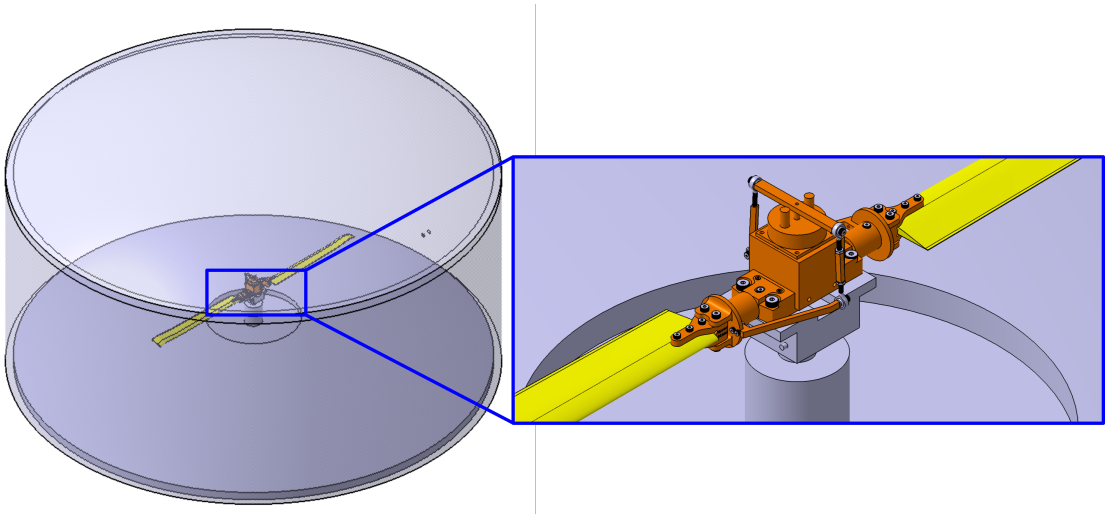

Figure 3.5: Internal setup design of the chamber test.

The details of the hub are described in Figures 3.6-3.11. The hub central block is mounted on the vacuum chamber rotor shaft (Figure 3.6). Then the end block is held in the central block. Ideally, the central and end blocks should be made in one piece. However, considering the workspace of the Tormach PCNC 1100 CNC milling machine, the design is separated into four pieces, two central blocks and two end blocks, that are feasible to machine yet can be assembled as one structure easily. The concave-convex shape (Figure 3.7) is designed to withstand the centrifugal force naturally.

As shown in Figure 3.8, the blade grip connects to the end block through a tension-torsion strap. The tension-torsion strap is designed to be flexible in torsion to allow twist deformation induced by pitch motion. The blade grip tube slips on the end block tube as a sleeve, and there are three pitch bearings between the two tubes. Moving outboard, the blade grip and the blade adaptor are connected by two

shoulder bolts (Figure 3.9). The blade adapter is used to connect the test blade to the hub (Figure 3.10). The blade adaptor in this design is interchangeable, which means the vacuum chamber hub can test blades other than the blades in this study. The current blade adaptor is designed to keep the radius and root cutout of the vacuum test rotor the same as the hover test rotor.

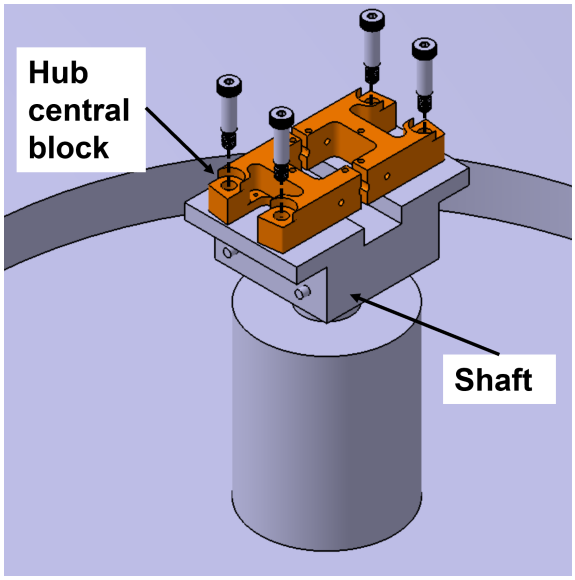

Figure 3.6: Hub central block on shaft.

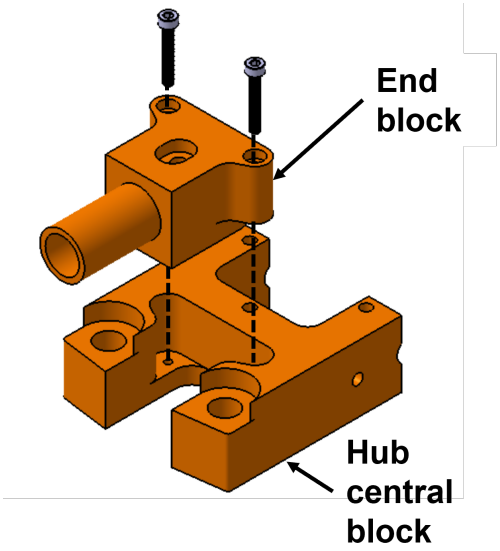

Figure 3.7: Connection of hub central block and end block.

In order to measure rotating frequency, the blade needs to be excited during rotation. Hence, a pitch mechanism is used to excite the blade in pitch motion. As shown in Figure 3.11, the pitch horn is mounted on the side of the blade grip. The other end of the pitch horn is connected to a pitch link via a ball-bearing rod. The ball-bearing allows free rotation and transfer of the linear translations. The pitch horn dimension is designed to keep the location of the pitch link close to the hub. There is another ball-bearing rod connecting the pitch link to the pitch arm, which is fixed on the actuator of the shaker. This pitch horn-link-arm mechanism

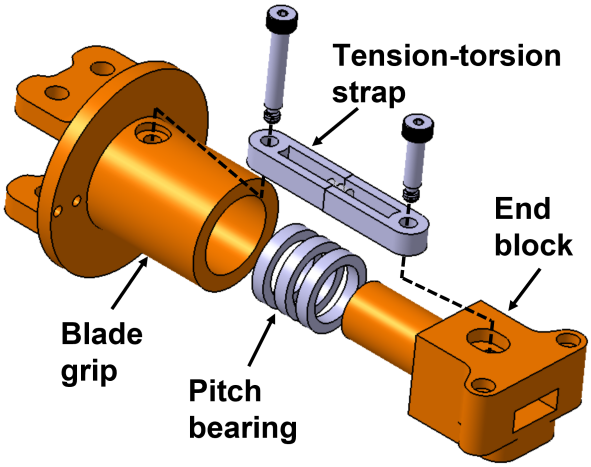

Figure 3.8: Connection of end block and blade grip.

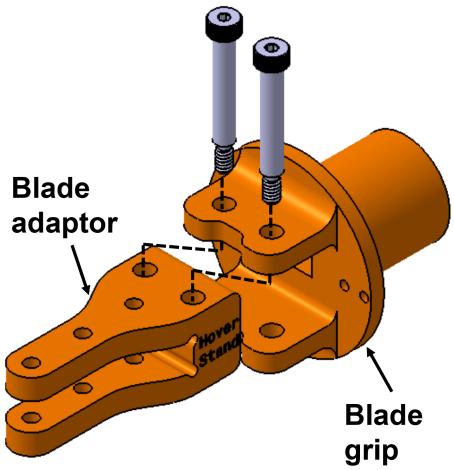

Figure 3.9: Connection of blade grip and blade adaptor.

(Figure 3.12) transforms the linear motion of the shaker into the pitch motion of the blade. Because only collective pitch input is needed, the shaker is mounted in the shaker housing on the hub, which rotates with the rotor. So the linear motion is imported directly in the rotating frame, and no swashplate is necessary. The shaker housing also connects two central blocks to strengthen the structure. Engineering drawings of each component are given in Appendix A. The material of the hub central block, end blocks, blade grips, blade adaptors, pitch horns, and pitch links is aluminum 7075.

There are three independent load paths on this hub design. The tension-torsion strap inside the end block tube carries the centrifugal force and passes it on to the end block and central block. Since the tension-torsion strap allows twist deformation and the blade grip can rotate freely about the pitch axis with the help of the pitch bearings on the end block tube, the majority of the pitch moment is transferred via the pitch mechanism and ends up at the shaker. The bending moments and shear

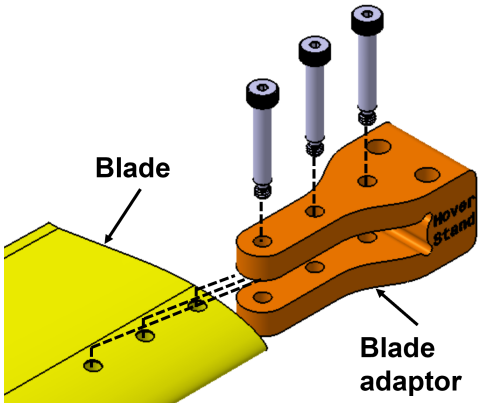

Figure 3.10: Connection of blade adaptor and blade.

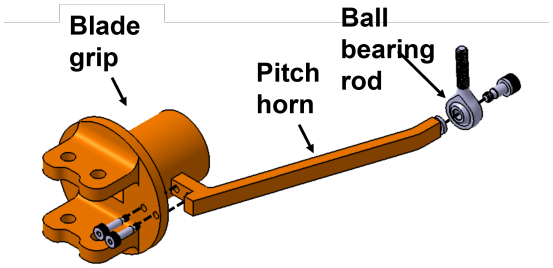

Figure 3.11: Connection of blade grip and pitch horn.

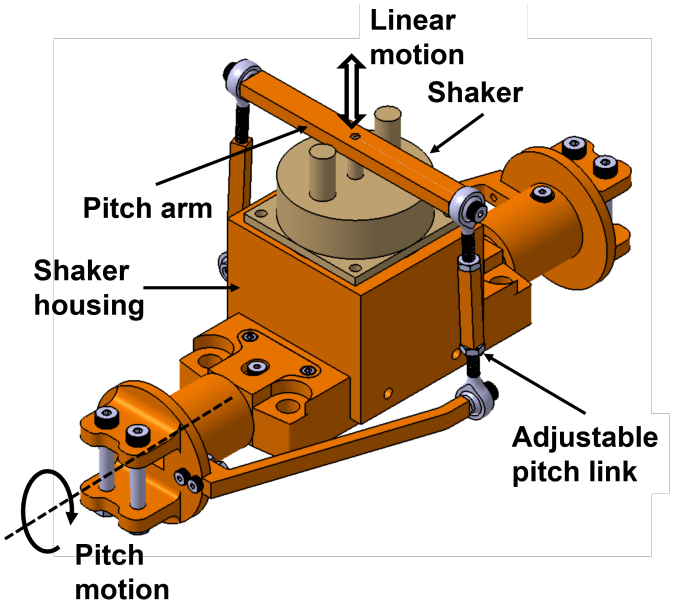

Figure 3.12: Pitch mechanism.

forces are carried by the pitch bearings and the end block tube. These bearings also help keep the blade grip tube and the end block tube aligned.

3.1.3 Vacuum Chamber Hub Fabrication

The vacuum chamber hub was fabricated in-house. Drilling, milling, and lathing were involved in the fabrication process of most of the components (Figure 3.13

and 3.14). Though the fabrication process is similar to the blade root insert, it is much more complicated. Due to the complexity of these components, milling of more than one side of the metal block is needed to fabricate them. The sequence of different machining methods (drill, milling, and lathing) and ways of securing the part on the workspace (vice clamping, fixture, etc.) were taken into consideration when generating the G-code in SprutCAM. Furthermore, the entire machining process was simulated virtually in SprutCAM to check for collision, tool travel limit, and stock removing rate. The simulation also allows the estimation of the machining time.

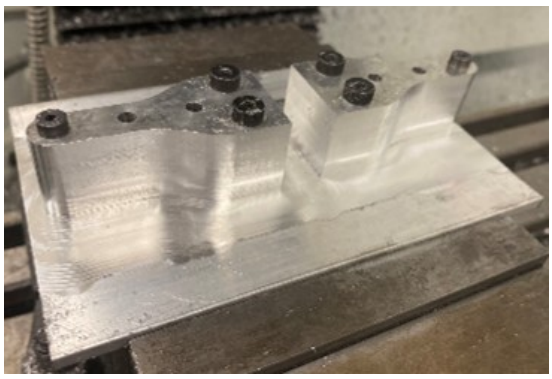

Figure 3.13: Machining of blade adaptor.

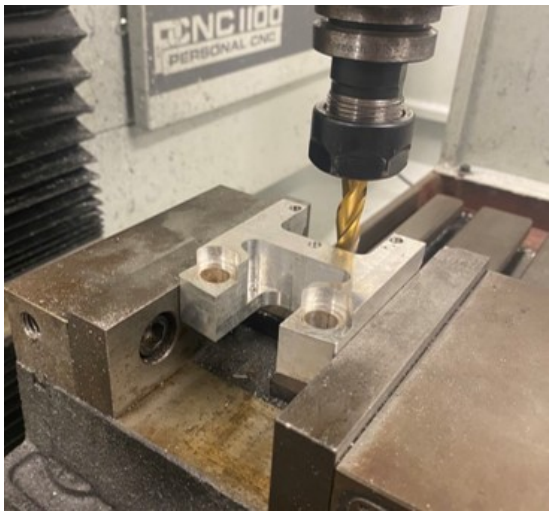

Figure 3.14: Machining of central block.

For components like the blade grip and blade adaptor that have cylinder features, the fabrication should start with a cylinder billet and lathing (Figure 3.15). It is because concentricity is very important for those components. This ensures the concentricity of the end block tube and blade grip tube, which aligns the pitch axis with the blade quarter chord axis.

The tension-torsion strap used in the vacuum chamber hub was designed and

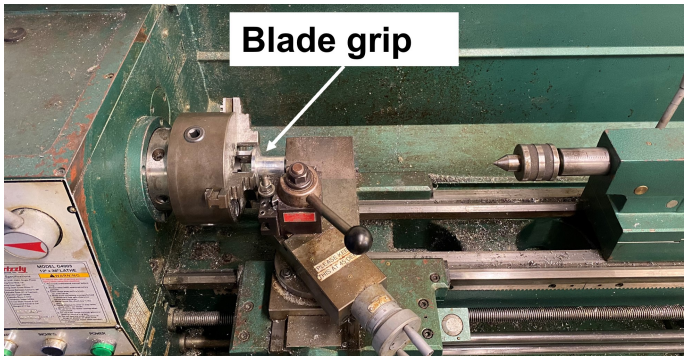

Figure 3.15: Machining of blade grip.

fabricated by Anand Saxena [97]. The tension-torsion strap (Figure 3.16) is designed for the Mach-scale model rotor hub, which can withstand a centrifugal force as high as 14000 N. The maximum rotational speed provided by the vacuum chamber motor (1500 RPM) is much lower than the hover stand rotor speed (2400 RPM) for which the strap was designed for. Therefore, the magnitude of safety in the vacuum chamber is sufficient.

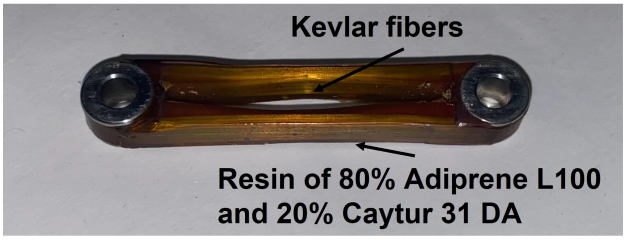

Figure 3.16: Tension-torsion strap.

The components of the vacuum chamber hub are laid out in Figure 3.17. Most of the assembly steps are elaborated in the hub design section. However, a few steps require more care during the assembly process. As shown in Figure 3.18, two types of 3-D printing sleeves were designed to keep the pitch bearings in place. The radius of the larger sleeve is the same as the radius of the pitch bearing outer ring, and the smaller sleeve corresponds to the inner ring. This arrangement is critical during

the assembly of the end block and the blade grip. It ensures the pitch bearings on each side of the hub have equal distances to the hub center. Lock tie glue was applied to both the outer and inner ring of the pitch bearing to fill all the gaps due to the machining tolerance. The length of the pitch link was designed to be adjustable. Since blade pitch has an influence on the rotating frequency and strain, it is necessary to set the pitch of both blades the same by adjusting the length of the pitch link.

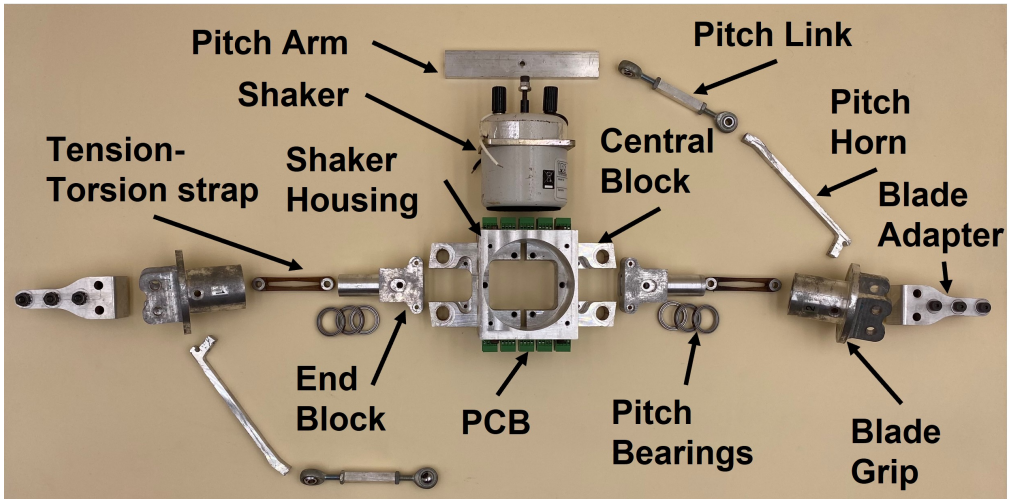

Figure 3.17: Vacuum chamber hub components.

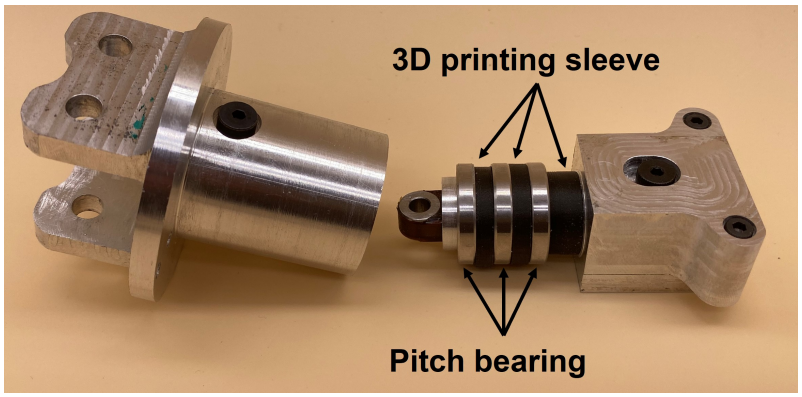

Figure 3.18: Assemble of pitch bearings.

Figure 3.19 shows the vacuum chamber hub assembly mounted inside the chamber. This setup was designed to excite and measure rotor blade rotating frequencies. As for rotating strains, the setup was modified slightly to fix the blade pitch. An aluminum block was designed to replace the shaker, and the pitch arm was mounted on top of it (Figure 3.20). Due to the vacuum environment, there is no need to perform tracking. But balancing the rotor is still critical to eliminate any undesired vibration. The hub was balanced separately from the blades by carefully measuring the weight of each component.

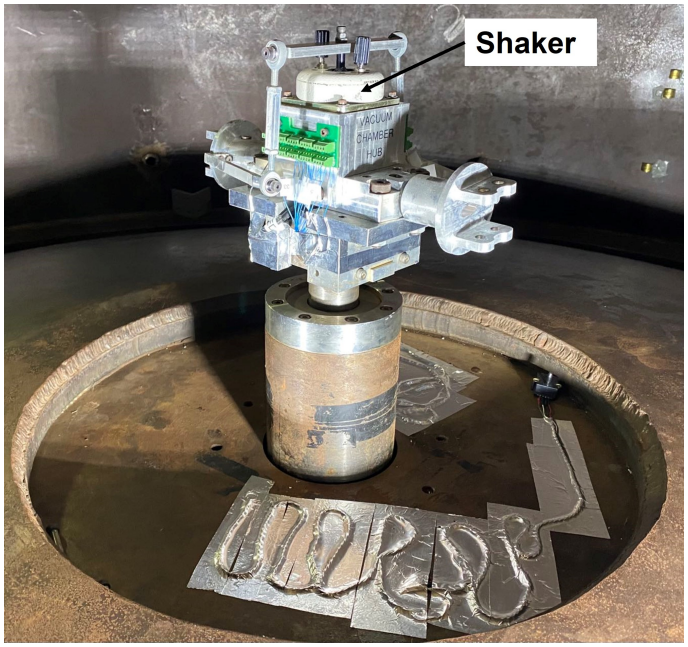

Figure 3.19: Vacuum chamber hub assembly with shaker.

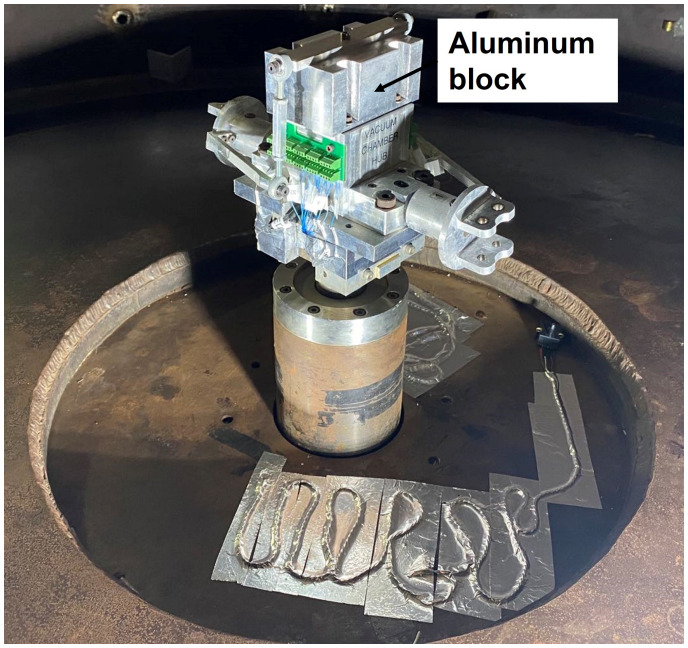

Figure 3.20: Vacuum chamber hub assembly with fixed pitch.

3.1.4 Vacuum Chamber Hub Stiffness

Identifying the blade root boundary condition is critical for performing analysis later. Therefore, static load tests and non-rotational frequency tests were performed to measure the pitch stiffness, flap stiffness, and lag stiffness of the hub. The test setup and diagram for measuring the pitch stiffness are shown in Figure 3.21. Static load F was applied on the pitch link via a pulley and measured by an in-house fabricated load cell. The deformation of the pitch horn Δ was measured by a laser sensor. Based on the distance h between the end of the pitch horn and the pitch axis, the pitch moment applied, and the rotational deflection about the pitch axis were determined (Figure 3.22), and then the pitch stiffness K_θ can be calculated by Equation (3.1).

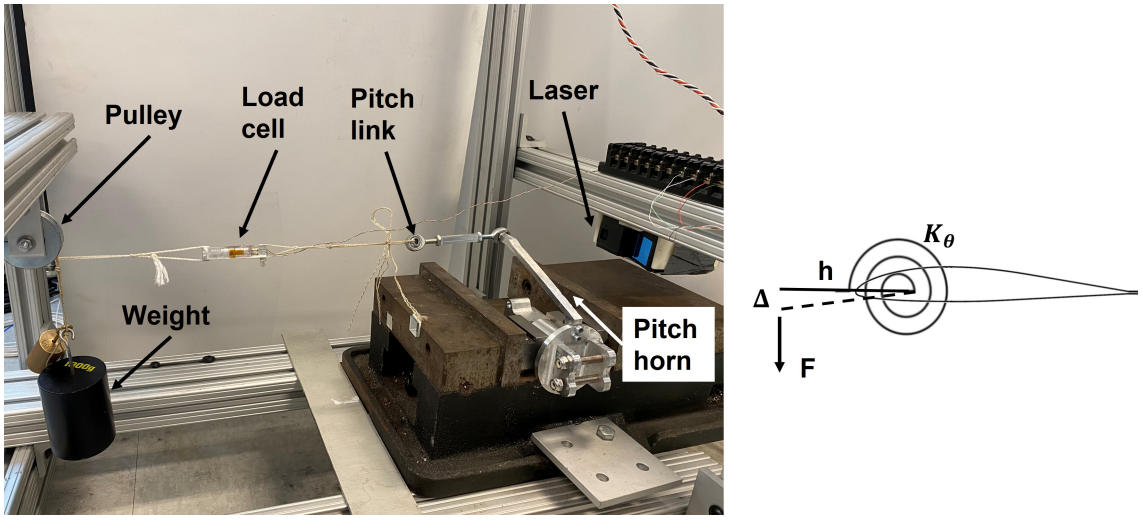

Figure 3.21: Vacuum chamber hub pitch stiffness test.

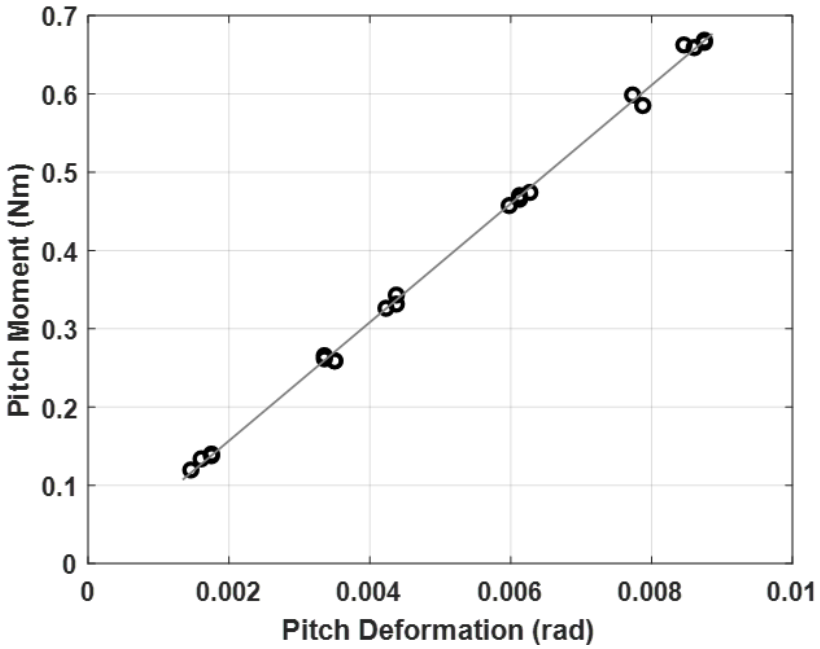

Figure 3.22: Vacuum chamber hub pitch moment versus pitch deformation.

$$K_\theta = \frac{Fh}{\sin^{-1}(\Delta/h)} \tag{3.1}$$

Direct measurement of the flap and lag root stiffness is error-prone as, unlike in pitch, the stiffness is much higher. Hence, a non-rotating frequency test was carried out, as shown in Figure 3.23. A rectangular aluminum beam was mounted on the vacuum chamber hub. The beam response was recorded by the laser sensor and strain gauge. Both shake tests and hammer tests were performed to measure the beam frequency. The frequency spectrum of the beam response is shown in Figure 3.25. The narrow peaks at the power supply frequency of 60 Hz and its integer multiples are discarded. The remaining peaks are the beam frequencies. Multiple tests were performed, and the measured frequencies were cross-referenced to identify the repeated results until repeatable results were obtained.

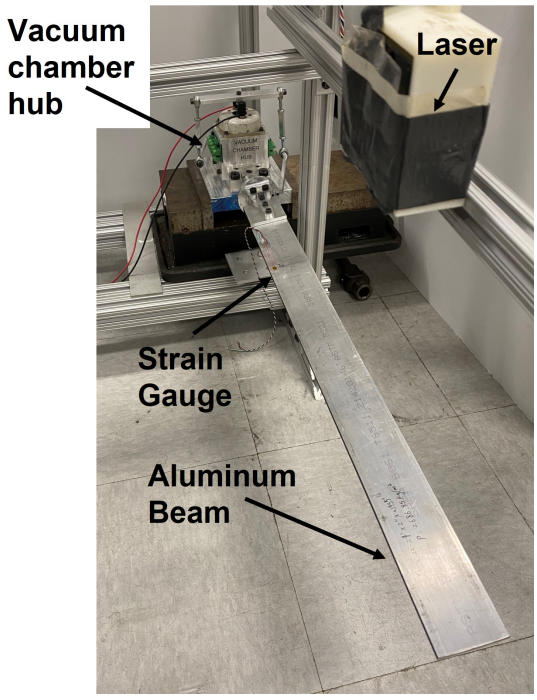

Figure 3.23: Vacuum chamber hub flap and lag stiffness test.

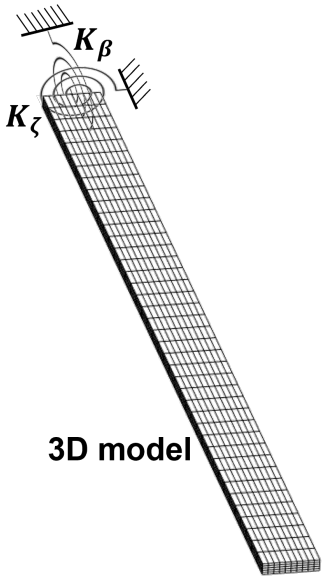

Figure 3.24: 3-D model of the aluminum beam.

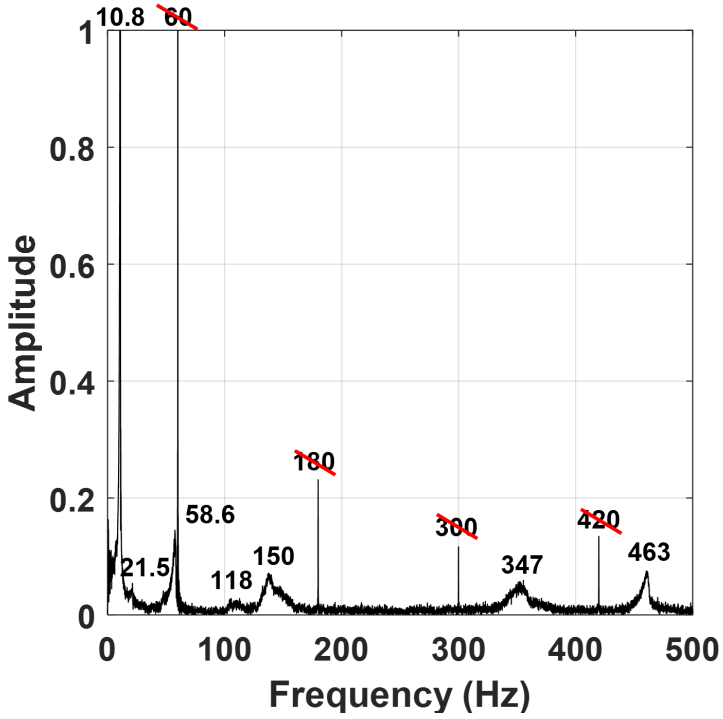

Figure 3.25: Frequency spectrum of aluminum beam strain signal.

Then a 3-D structural model (Figure 3.24) was developed for the aluminum beam using X3D. Due to the simple and well-defined structure, the beam can be modeled very accurately. The only parameter that can be varied in the model is the root stiffness. The root flap and lag bending stiffnesses were varied until the predicted frequencies matched the measured frequencies. The measured and predicted frequencies are listed in Table 3.1. The frequencies predicted with a clamped root are also presented to show the impact of the root stiffness. The outer tube on the blade grip and the inner tube on the end block are the main components that affect the flap and lag bending stiffness. Flap and lag directions have the same stiffness due to the circular cross-section of these two components. The final root stiffness values are pitch stiffness of 75 Nm/rad, flap and lag stiffness of 900 Nm/rad.

Table 3.1: Aluminum beam frequencies in Hz.

Measurement	Prediction (K_θ=75 Nm/rad, K_β=K_ζ=900 Nm/rad)	Prediction (clamped root)
10.8 (Flap)	10.8	12.7
21.5 (Flap)	20.8	79.5
58.6 (Lag)	66.5	117
118 (Torsion)	123 (used K_θ)	224
150 (Flap)	184	259
347 (Flap)	358	441
463 (Torsion)	486 (used K_θ)	720

3.1.5 Vacuum Chamber Instrumentation and Data Acquisition

A hub excitation frequency sensor is built into the rotating frame. As shown in Figure 3.26, a single linear strain gauge is used. For this purpose, a Printed Circuit Board (PCB) was designed and mounted on the side of the hub for the connection of sensors and slip ring. The PCB is also a checkpoint for system debugging.

Figure 3.27 shows the function generator to power and control the shaker. The frequency and magnitude of the shaker linear motion are determined by the output signal of this function generator. National Instruments PXIe is used as the data acquisition system in the vacuum chamber test. The 8-slot PXIe-1082 chassis provides housing to the PXIe-8840 controller, PXIe-6365 multifunction I/O module for rotor speed input and function generator output, PXIe-4331 8-Channel strain/bridge input module for blade strain outputs. A LabVIEW program was developed for this test to interface with the PXIe hardware.

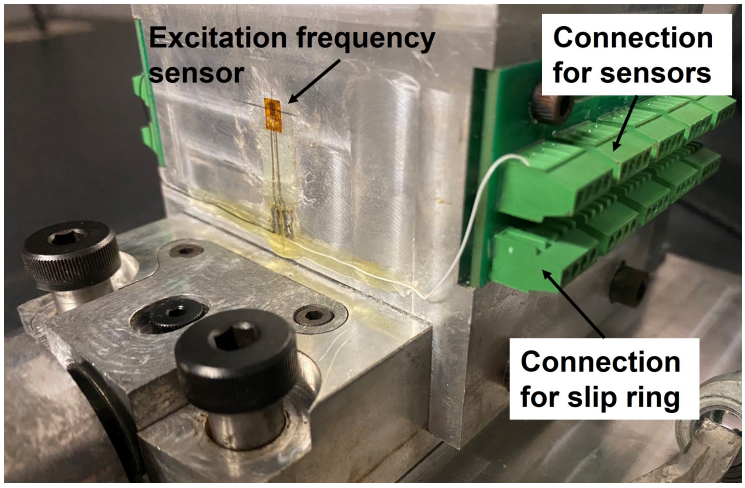

Figure 3.26: Vacuum chamber hub instrumentation.

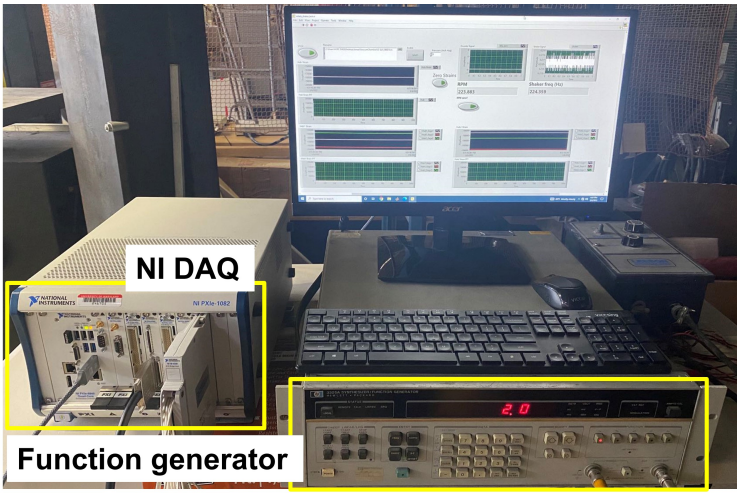

Figure 3.27: Vacuum chamber test data acquisition system.

3.2 Hover Rig

3.2.1 Hover Rig Components

Unlike vacuum chamber tests, there is aerodynamic forcing in hover tests. The test data can be used to validate the aerodynamic model for complex tips and the aero-structural interface.

The hover test was carried out on the hover stand at Alfred Gessow Rotorcraft Center (AGRC), shown in Figure 3.28. The stand is mounted on the hover tower, which raises the rotor hub two rotor diameters away from the ground to keep the rotor out-of-ground effect. In the present work, the blades were mounted on a four-bladed hingeless hub. The overall parameters of the rotor are summarized in Table 3.2. The rotor solidity is 0.1 with a root cutout of 16.4%R. The maximum rotational speed is 2282 RPM, allowing the blade tip speed to reach a Mach number of 0.6. The components, instruments, and data acquisition system are detailed in the following sections.



Figure 3.28: Hover test stand.

Figure 3.29 shows the main components of the hover stand. The rotor is driven by a hydraulic motor and a 2:1 ratio belt-pulley system. The hydraulic drive system is chosen to prevent Electro-Magnetic Interference (EMI) and improve the signal-to-noise ratio. The details of the drive system can be found in Ref [97].

Table 3.2: Rotor parameters.

	Parameters
Number of Blades	4
Radius	0.853 m
Root cutout	16.4%R
Solidity	0.1
Max tip Mach number	0.6
Hub type	Hingeless
Rotation direction	Counter-clockwise

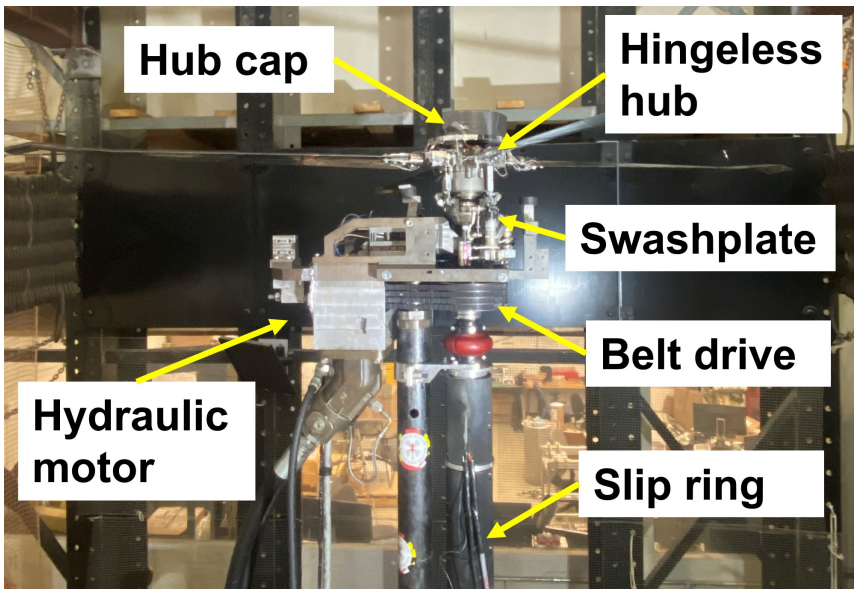

Figure 3.29: Hover test stand components.

The structure of the hingeless blade grip is similar to the vacuum chamber hub. As shown in Figure 3.30, the end block is clamped by two hub plates. The blade grip is connected to the end block via a tension-torsion strap. The end block tube is set inside the blade grip tube. The flap and lag motions are eliminated, and the pitch bearings between the end block tube and the blade grip tube enable the torsion degree of freedom. The pitch horn is fixed to the blade grip and connected with the pitch link to control the pitch input. There are no kinematic couplings since the pitch link is located inboard of any equivalent hinge of elastic flap and lag

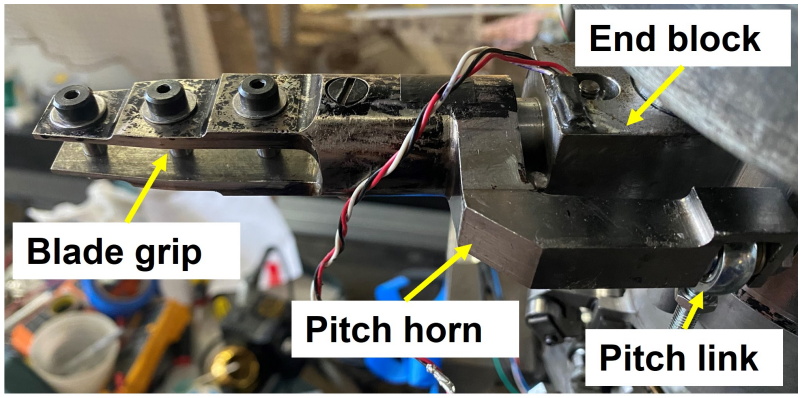

Figure 3.30: Hingeless hub.

motion. All of these components are made of steel. Therefore, the hingeless hub is stiff enough to be considered rigid.

The blade pitch is controlled by a swashplate (Figure 3.31) which influences the rotor tip path plane. Three electric actuators are used to tilt and or translate the non-rotating swashplate. Then the orientation and position of the non-rotating swashplate are transferred to the rotating swashplate via a spherical bearing, which decouples the rotation motion. A scissor connects the rotating swashplate and the shaft to ensure the rotating swashplate has the same rotational speed as the rotor. The rotating swashplate connects four pitch links that change the collective and cyclic inputs.

There are multiple sensors in the rotating frame (strain gauges, pitch sensors, pitch link load sensors, and shaft torque sensors), which are connected to a PCB in the hub cap (Figure 3.32). The bottom of the PCB is wired with a 150-channel slip ring to communicate the signals between the rotating and non-rotating frames. A shaft coupling is installed between the rotor shaft and the slip ring for protection (Figure 3.33). Aligning the slip ring with the shaft is very important. Any

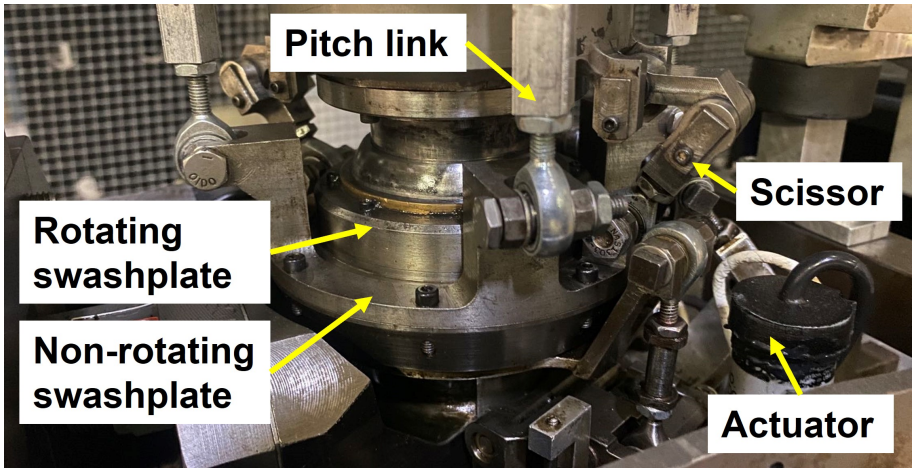

Figure 3.31: Swashplate.

misalignment can result in undesired vibration, noisy signal, and potential slip ring damage.

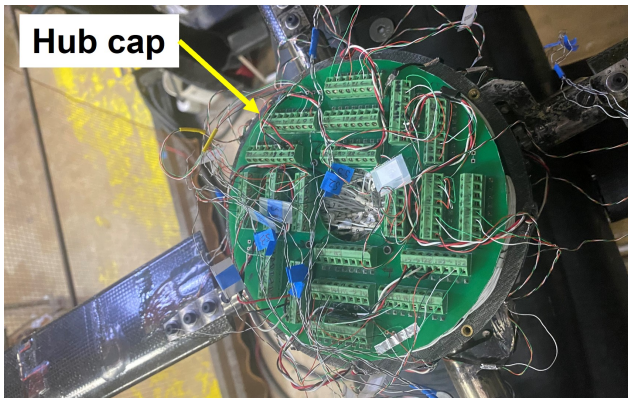

Figure 3.32: PCB on the hub cap.

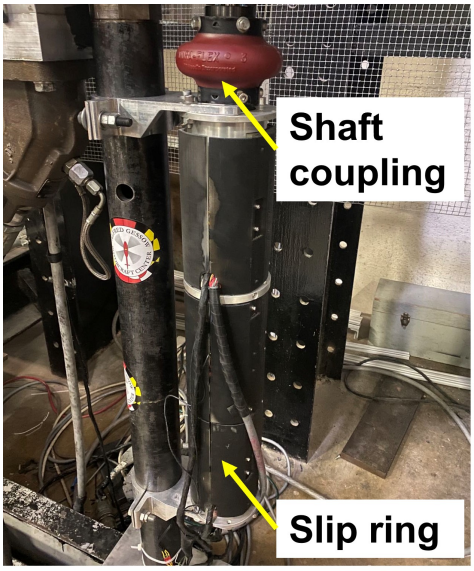

Figure 3.33: Hover stand slip ring.

3.2.2 Hover Rig Instruments

The base of a 6-component balance is installed on the test stand (Figure 3.34). The rotor shaft is held by the other end of the balance. A single load path ensures all hub loads are captured by the balance. Calibration was done in-house to account

for the vertical and axial offset of the hub from the center of the balance. The details of the static load calibration are documented by Wang [98].

The yaw moment measured by the hub balance is a fixed frame moment from shaft friction. The rotor torque is measured in the rotating frame. As shown in Figure 3.35, a torque sensor is installed on the shaft. This torque sensor consists of four shear strain gauges and a full-bridge circuit. The calibration process of this sensor is similar to that of the blade torsional moment sensor. The pitch link loads are also measured in the rotating frame. The pitch links are instrumented to measure the axial load for pitch moment estimation (Figure 3.36).



Figure 3.34: Hub balance.

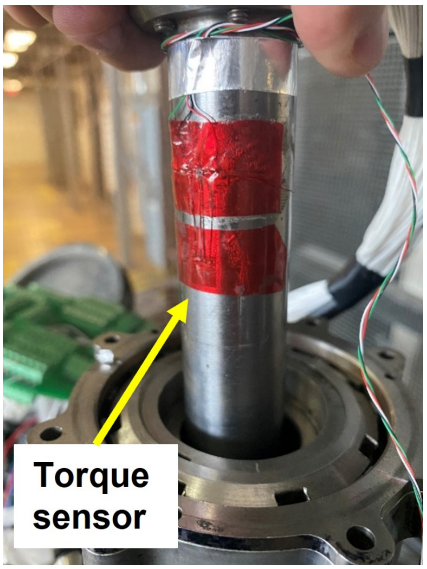

Figure 3.35: Torque sensor.

The root pitch angle of each blade is measured directly by Hall effect sensors. As shown in Figure 3.37, a Hall effect sensor is installed on the top surface of the end block, with a magnet on the pitch horn near the blade grip. As the blade grip rotates about the pitch axis, the magnet moves along with the blade grip, which changes the voltage of the Hall effect sensor output signal. To calibrate the Hall

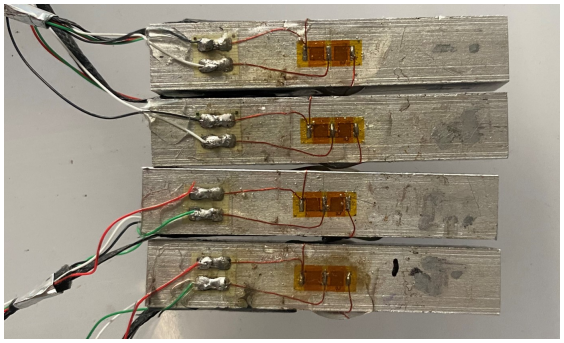

Figure 3.36: Pitch link load sensors.

effect sensors, an inclinometer was used to monitor the blade pitch angle while the collective or cyclic was adjusted to vary it. Since the blades are highly twisted, the inclinometer was clamped at 75%R to account for the slight difference in the orientation of the blade root insert. Figure 3.38 shows the calibration data of each blade. A third-order polynomial curve fit is used to generate the function for pitch measurement during the hover test.

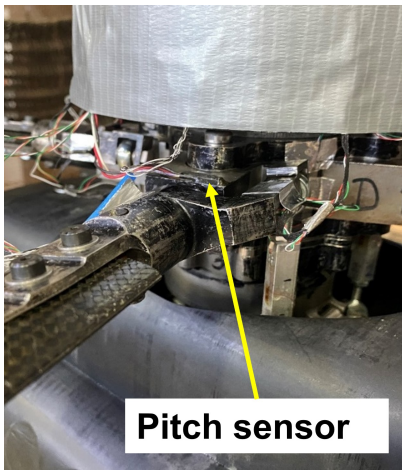

Figure 3.37: Pitch Hall sensor.

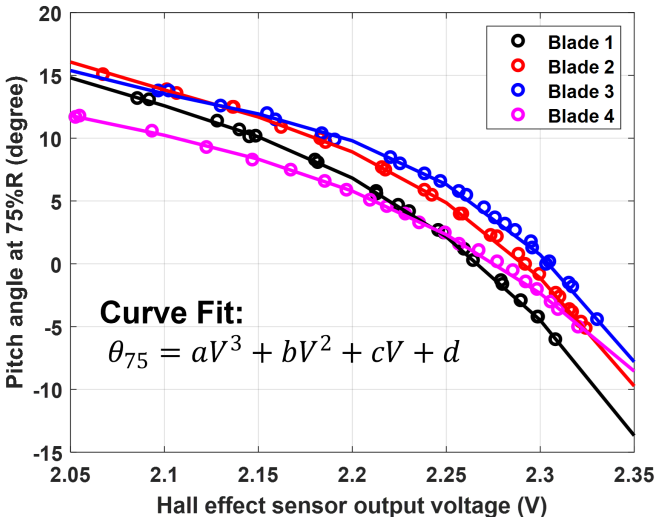

Figure 3.38: Pitch Hall sensor calibration.

The blade pitch angles are also needed to derive the control angles. Equations (3.2)-(3.4) can be used to calculate collective θ_0, longitudinal θ_{1S}, and lateral

θ_{1C} pitch given by the swashplate input. θ_i is the pitch angle at 75%R of blade i, and ϕ is the azimuth angle of blade one. The azimuth angle is measured by an encoder installed at the bottom of the slip ring (Figure 3.39). The magnitude of the encoder output signal varies linearly with azimuth angle, as shown in Figure 3.40.

$$\theta_0 = \frac{\theta_1 + \theta_2 + \theta_3 + \theta_4}{4} \tag{3.2}$$

$$\theta_{1s} = \frac{(\theta_1 - \theta_3)\sin(\phi) - (\theta_2 - \theta_4)\cos(\phi)}{2} \tag{3.3}$$

$$\theta_{1c} = \frac{(\theta_1 - \theta_3)\cos(\phi) + (\theta_2 - \theta_4)\sin(\phi)}{2} \tag{3.4}$$

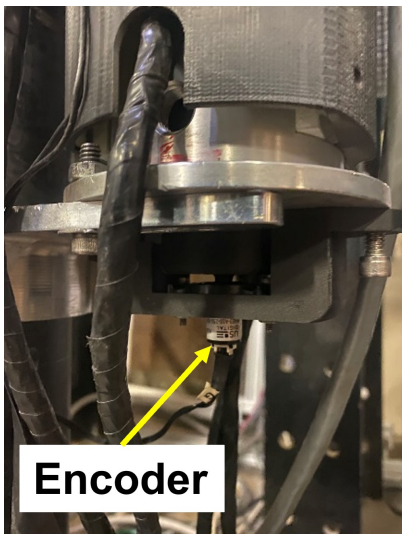

Figure 3.39: Encoder.

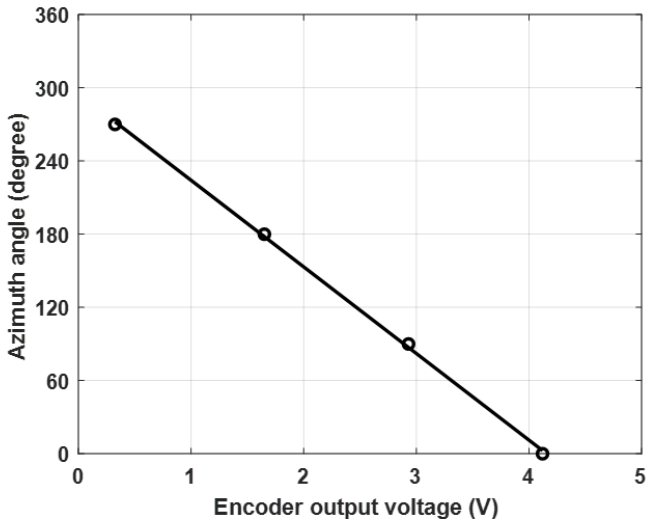

Figure 3.40: Azimuth calibration.

The rotor speed can be estimated with the sawtooth wave signal generated by the shaft encoder. The optic sensor (Figure 3.41) is also used to monitor rotor speed as a backup. As shown in Figure 3.42, the frequency of the optic sensor and

the shaft encoder is consistent, which indicates reliable rotor speed measurement.

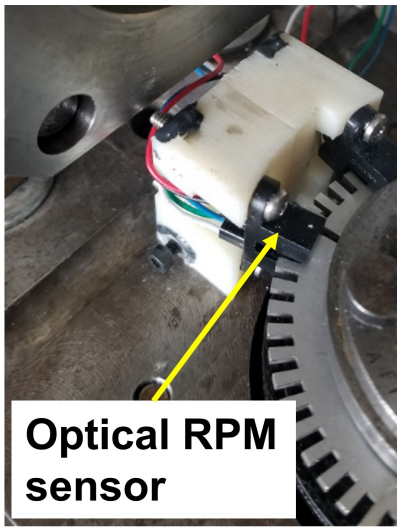

Figure 3.41: Optic sensor.

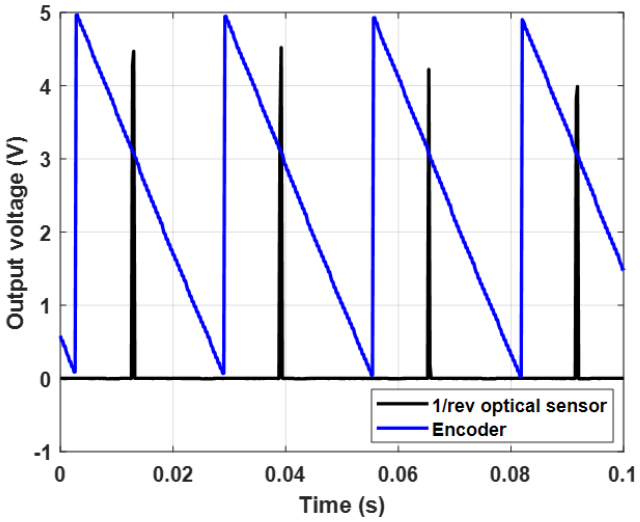

Figure 3.42: Output of optic sensor and encoder.

3.2.3 Hover Stand Data Acquisition

Figure 3.43 shows the hardware that controls the test system, provides power for sensors, as well as records the data. A motor control box is used to adjust the rotor speed and monitor the motor temperature. The control sticks are for collective/cyclic control. National Instruments SCXI system is for data acquisition, which is detailed in Ref [97]. Due to the emphasis on blade structural loads in this test, a LabVIEW program (Figure 3.44) is developed to store as well as process loads data in real-time for review. The program also allows access to the hub and structural load frequency spectrum to monitor resonance and safety of flight. The raw data from all instruments are stored in a time array.

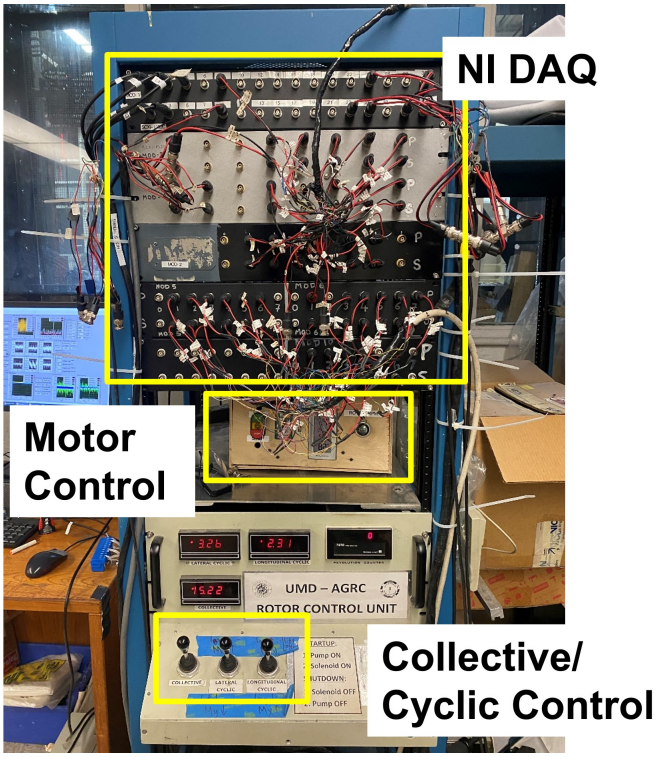

Figure 3.43: Hover test data acquisition system.

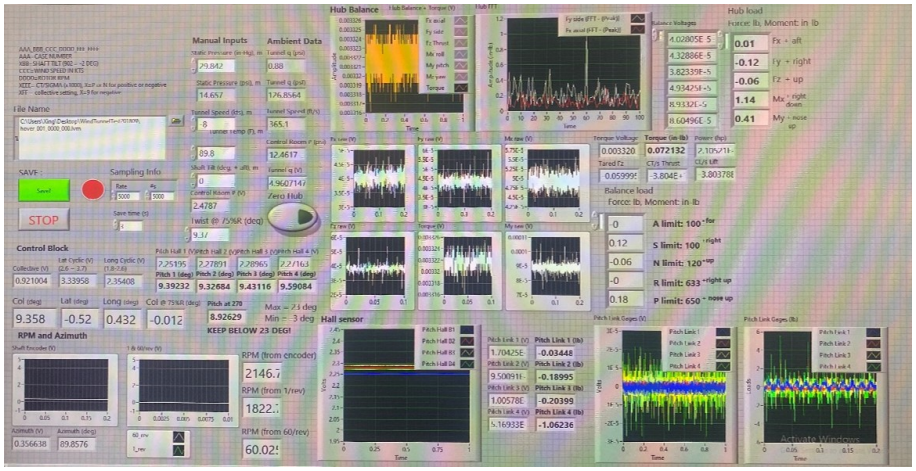

Figure 3.44: LabVIEW program.

3.3 Summary

This chapter described the test rigs used for vacuum chamber and hover tests. A two-bladed hingeless hub was designed and fabricated for the vacuum chamber as a part of this work. Benchtop tests were performed to determine the blade root stiffness in flap, lag, and torsion for this new hub. The existing four-bladed hingeless hub was needed for hover tests.

Chapter 4: Development of 3-D Blade Model

This chapter presents the development of the 3-D blade aeromechanic model, starting from the creation of CAD geometry to 3-D solid meshing to the aeroelastic model, to finally 3-D stresses. An overview is presented picturization in Figure 4.1.

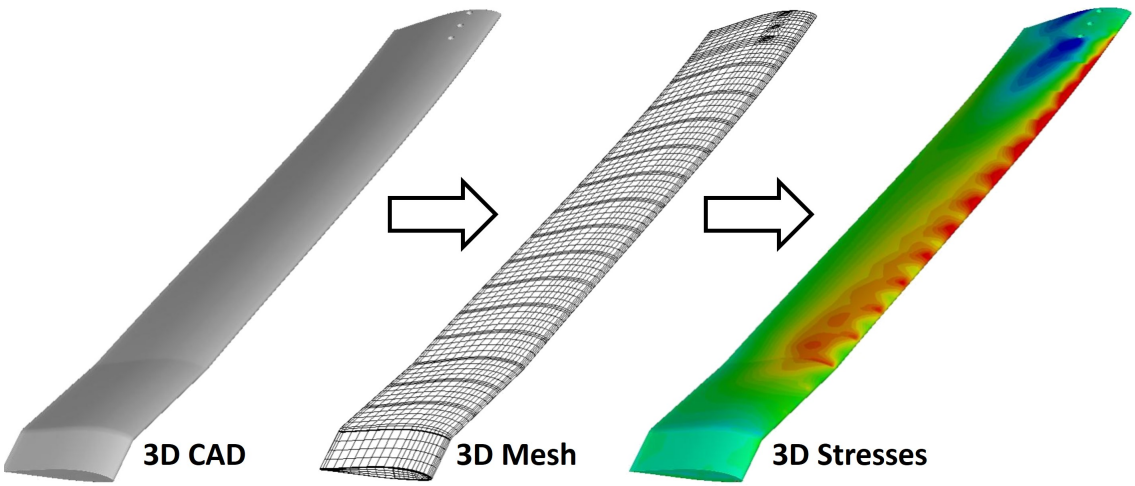

Figure 4.1: Development of 3-D Blade Model.

The X3D solver is used for aeroelastic predictions. X3D is a 3-D structural dynamics solver developed specifically for next-generation Integrated 3-D analysis of rotors [99]. X3D uses a multibody analysis framework in which flexible components are analyzed using 3-D brick finite elements and connected by multibody joints. The combination of the 3-D FEM with multibody dynamics, trim solution, and aerodynamics make X3D unique. The basic 3-D blade modeling process is documented by

Staruk in detail [100]. Therefore, only the specific steps for modeling the double anhedral tip and the special refinements are discussed here.

4.1 Blade Geometric Model

To create a 3-D blade aeroelastic model, 3-D CAD geometry with accurate internal structure is essential. Not every detail is essential to begin with, but the geometry should be consistent with the principal shapes and materials identified. The standard file formats for storing geometry are Stereolithography (STL), International Graphics Exchange Specification (IGES), and Standard for the Exchange of Product (STEP). The STEP format is considered to be the most suitable and portable for sharing 3D geometric models. Therefore, as long as the geometric model can be saved in a STEP format, it can be created with any CAD software. In this work, the CATIA V5R20 software is used.

A systematic study requires control over the variables of the subject. Parameterization of the geometric model allows the designer to have complete control of all the key shapes and features, thereby enabling precise variable control for subsequent structural analysis. Such a geometric model also minimizes the time required for analysis as well as subsequent mesh development. Table 4.1 lists the primary parameterized structural variables, and Table 4.2 shows the secondary variables which relate to the primary variables via analytical formulae. All dimensions are in the SI unit and angles in degrees.

A straight blade model is also developed as a baseline to analyze the impact

of the double anhedral tip. These two models fall out of the same parameterized CAD model. As shown in Figure 4.2, the only difference between the two models is the dihedral/anhedral angle. Both of them have the same twist about the local quarter chord.

Table 4.1: Primary variables of the parametric geometry.

Variable	Notation	Straight	Double anhedral tip
Radius	R	0.853 m	0.853 m
Root cutout	r_{root}	16.4%R	16.4%R
Chord	c	0.08 m	0.08 m
Spar width	w_{spar}	33.5%c	33.5%c
Skin layer thickness	t_{skin}	0.19 mm	0.19 mm
Number of skin layer	n_{skin}	1	1
Spar layer thickness	t_{spar}	0.19 mm	0.19 mm
Number of spar layer	n_{spar}	2	2
Location of 1st anhedral	$r_{\Lambda_{A1}}$	80%R	80%R
1st anhedral angle	Λ_{A1}	$0°$	$5°$
Location of 2nd anhedral	$r_{\Lambda_{A2}}$	95%R	95%R
2nd anhedral angle	Λ_{A2}	$0°$	$-15°$
Twist rate over radius	θ_{tw}	$-16°$	$-16°$

Table 4.2: Secondary variables of the parametric geometry.

Variable	Notation
Transition length	$l_{trans} = 0.5\%R$
Root pitch	$\theta_{root} = \theta_{tw}(r_{root}/R - 0.75)$
1st transition pitch	$\theta_{trans1} = \theta_{tw}(r_{\Lambda_{a1}}/R - 0.75)$
2st transition pitch	$\theta_{trans2} = \theta_{tw}(r_{\Lambda_{a2}}/R - 0.75)$
Tip pitch	$\theta_{tip} = \theta_{tw}(1 - 0.75)$

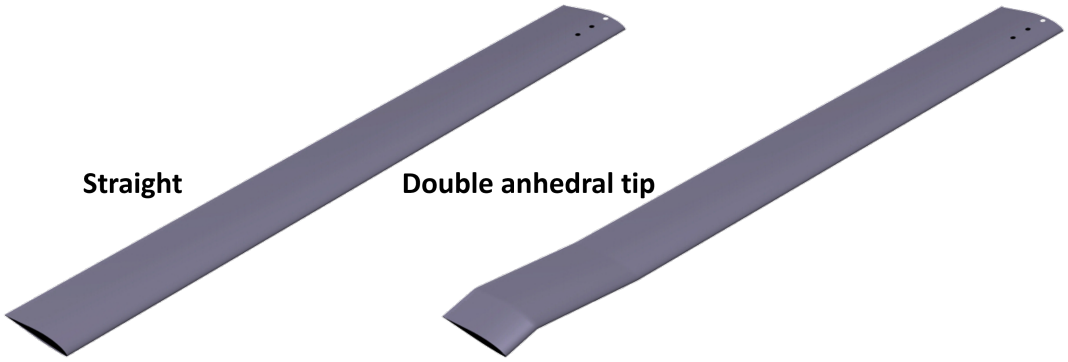

Figure 4.2: Parameterization models.

As the geometric model is created, the same parts can be generated in multiple ways. However, some are not beneficial for the finite element meshing process. The 3-D structural dynamics model, X3D, uses hexahedral brick finite elements. Hence, the familiarity with 3-D meshing with hexahedral brick elements is helpful for the creation of the geometric model. Although modifications of the geometry can be done later in the meshing software, it is not desired. Creating a geometric model upfront that is suitable for meshing later will significantly simplify the process. It is likely that iterations between CAD and meshing would be needed. The characteristics of a good CAD model are described as follows.

1. The internal structure of the blade is composed of as many parts as materials. "Bodies" in CATIA are used to create these parts. Ideally, each body is defined with a single material. For the double anhedral blade (Figure 4.3), skin, spar, fore core, aft-core, and root insert have their own bodies. However, for parts that are repeated in discrete intervals like the leading edge weights, it is beneficial to model all the leading edge weights including the foam in

between as one body (Figure 4.4). This reduces the number of bodies and unnecessary complexity in the geometric model. They can then be separated into multiple volumes by the meshing process. More details related to this step will be clarified in section 4.2.

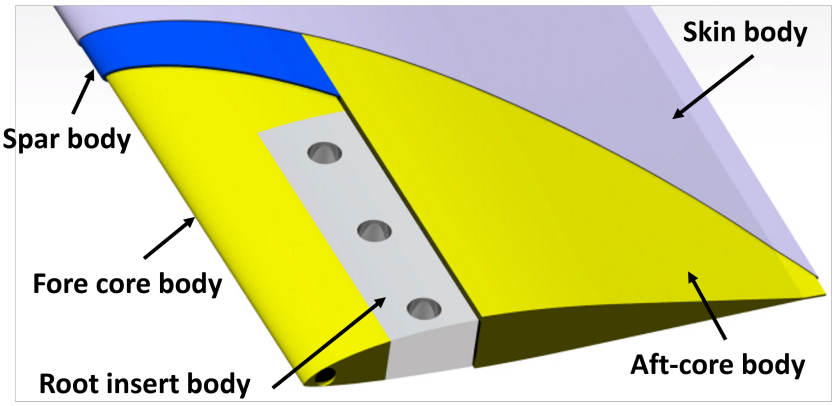

Figure 4.3: Bodies in the geometric model.

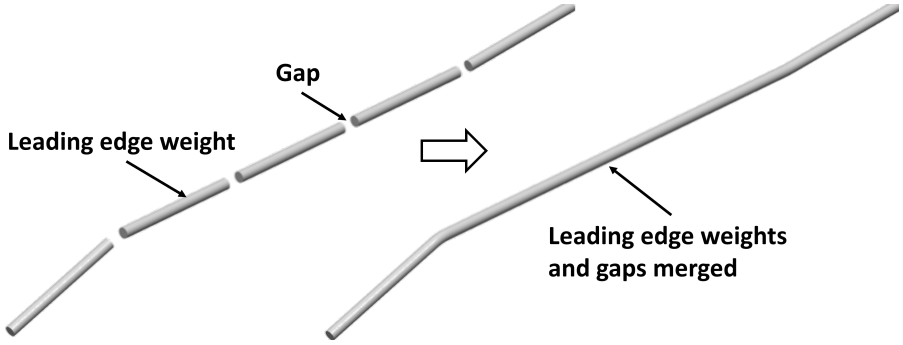

Figure 4.4: Leading edge weight body; the gaps are merged in geometry for smooth meshing but defined by material properties.

2. There should be no artificial gaps or overlaps between the internal structures. In other words, interfaces should be consistent. The definition of geometric elements such as points, lines, and surfaces between adjacent bodies should

be identical. For example, Figure 4.5 shows the surfaces used to construct the skin body, spar body, fore core body, and aft-core body. The skin inner and spar outer surfaces are the same surface, similarly, the spar inner and fore core surfaces are the same surfaces, so their definition is identical.

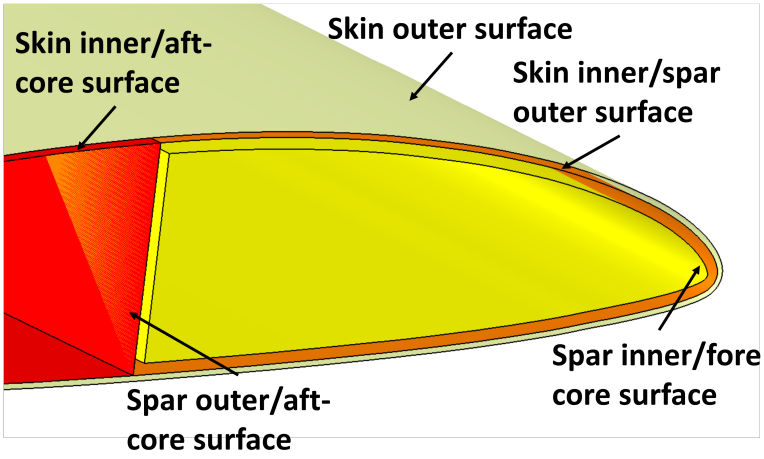

Figure 4.5: Shared surfaces between bodies.

3. The helicopter rotor blade is a structure with a long radial dimension in general. For such structures, a multi-section surface is a convenient way to construct bodies. In order to control the geometry between the cross-sections, it is necessary to define suitable guidelines, as shown in Figure 4.6. For highly twisted blades, the guidelines should be defined using helix. Using a straight line as a guideline will make the blade chord between two cross-sections shorter than the actual value.

The 3-D blade geometric model is used both in mold fabrication, as well as analysis. These two critical activities of the research are sourced from the same geometric model thus ensuring consistency.

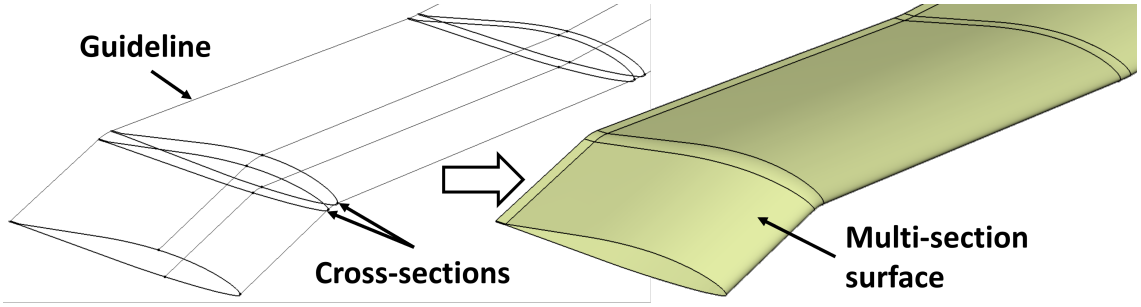

Figure 4.6: Multi-section surface.

4.2 Blade Mesh

Prior to meshing the blade, a Structural Analysis Representation (SAR) is needed to determine whether a component is modeled by a flex part or a joint. The SAR is simply a definition on paper along with a load path diagram. Because the vacuum chamber rotor hub and the hover tower rotor hub are both hingeless, the system can be simplified as a single flex part and a root joint. Additionally, a tip joint is assigned for blade structural loads. The position, orientation, and connections in the SAR are summarized in Table 4.3.

Table 4.3: Structural analysis representation.

Part ID	Part type	Name	Position (m)			Orientation (°)			Connections
			x	y	z	α_x	α_y	α_z	
1	Joint	Root holes	0	0	0	0	0	0	2
2	Flex part	Blade	0	0	0	0	0	0	1, 3
3	Joint	Tip connection	0.682	0	0	0	0	0	2

The Cubit v15.2 software [101] is chosen to mesh the flex part. In this study, the blade is the only flex part. The meshing process starts with importing the STEP file of the geometric model into Cubit. Then steps for clean-up, decomposition,

imprint, merge, mesh, and mesh quality estimation follow. The steps follow the sequence alone in general, but can also be combined when necessary. These steps are described next.

4.2.1 Clean-up

The first step in the meshing process is cleaning the geometric model. As the geometric model is imported into Cubit, geometric elements like vertices, curves, surfaces, and volumes (terms used in Cubit) are identified. Among these elements, there might be sliver elements that will lead to failure in mesh generation or a low-quality mesh. The "Remove small features" operation in Cubit can be used to detect the sliver elements. Normally, the smallest dimension in the geometric model is a suitable threshold for the operation to identify sliver elements. For a composite rotor blade, the threshold will be the thickness of a single ply of the composite material. There are mainly two types of sliver elements that require cleaning. The first type is created during the development of the geometric model. These sliver elements might be too small for the designer to check with naked eyes. Removing this type of sliver element by modifying the geometric model and then re-starting the meshing process all over again is recommended. The second type of sliver element is created by Cubit during STEP file import, particularly when the geometric model is complicated. This is usually the case for rotor blades. This type of sliver element does not exist in the geometric model. And it breaks up the continuous element. The "composite" function in Cubit can be used to clean this

type of sliver element. As shown in Figure 4.7, two sliver surfaces on the leading edge weights can be composited into a larger surface which allows better control of meshing in the following steps. This clean-up step might need to be performed multiple times in the entire mesh process, particularly after decomposition, imprint, and merge.

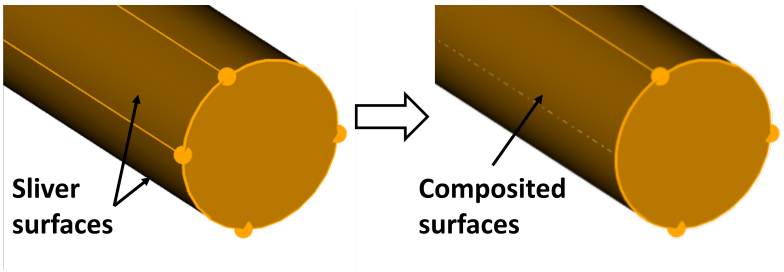

Figure 4.7: Composite of sliver surfaces.

4.2.2 Decomposition

Decomposing the volumes is a critical step in the meshing process. The purpose is not only to separate the existing geometries into meshable volumes but also to separate regions of different material properties and help control mesh quality. Since the double anhedral blade has two distinguish tip portions, the blade geometry is first decomposed into three main portions: straight, dihedral, and anhedral, and two transition portions as shown in Figure 4.8. The sectional geometry of each portion is the same, so, the geometries in each portion have two topologically similar opposite faces connected by curved surfaces. This kind of volume is easily meshable and can be meshed with the "sweeping" algorithm.

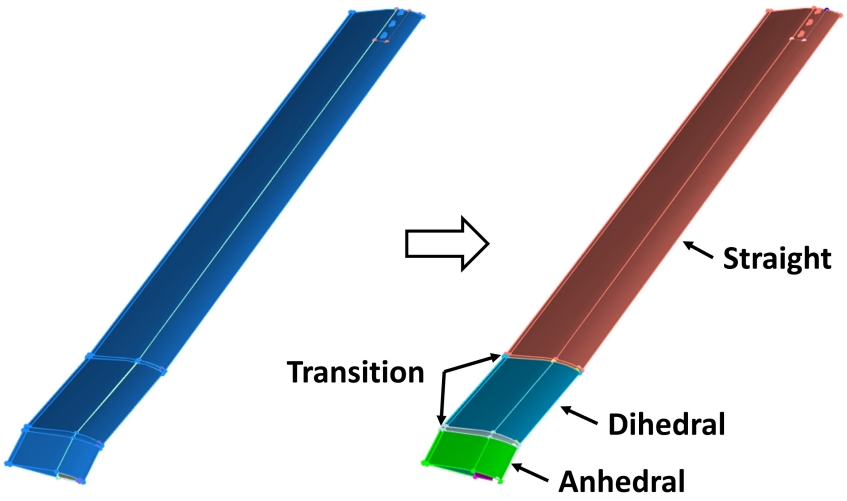

Figure 4.8: Spanwise decomposition.

As mentioned previously, the skin and spar consist of composite material, and the material property varies with the orientation of the layer. Therefore, the skin and spar needed to be decomposed further to apply layups with different orientations. This is done by the sectional decomposition in each portion. As shown in Figure 4.9, the skin is decomposed into three top volumes and three bottom volumes. The spar is decomposed similarly into two top, two bottom, and one web volume. The "Webcutting" (Cubit decomposition operation) surface should be created using the original vertices and curves to decompose sectional geometry efficiently. Such a surface can decompose volume accurately without generating additional sliver elements. An example is decomposing the highly twisted skin into a top and a bottom volume. The "Webcutting" surface should be created based on the leading-edge guide curves on the inner and outer surfaces of the skin volume as they share the same twist rate as the blade. This is also an aspect that the designer should keep in mind when defining the guidelines of the geometric model.

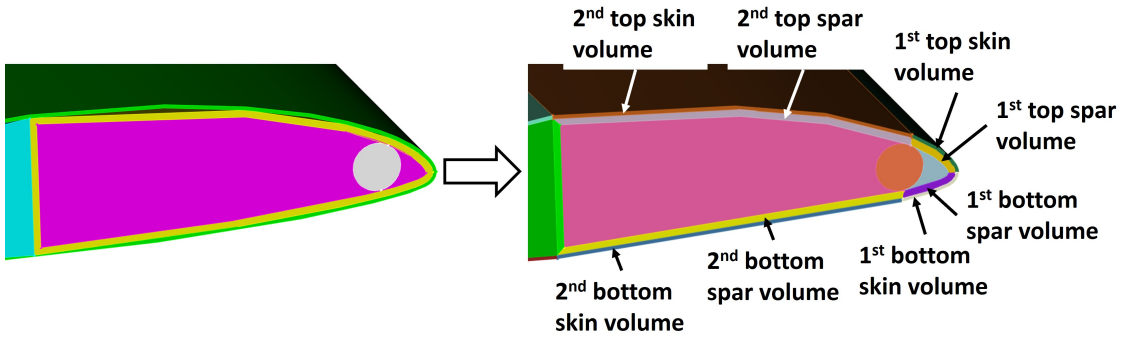

(a) Leading-edge.

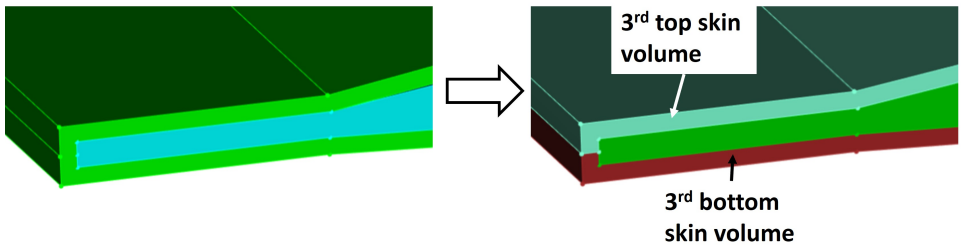

(b) Trailing-edge.

Figure 4.9: Sectional decomposition; each volume has a different ply angle.

Recalling the leading-edge weight body created in the geometric model is a continuous structure combining the leading-edge weights with the foam, further decomposition is needed now to separate them. Based on the spanwise location of the start and end of each leading-edge weight, the entire blade geometry can be further decomposed into smaller volumes (Figure 4.10). By decomposing the skin, spar, and foam core along with the leading-edge weights, more authority of mesh node placement is gained.

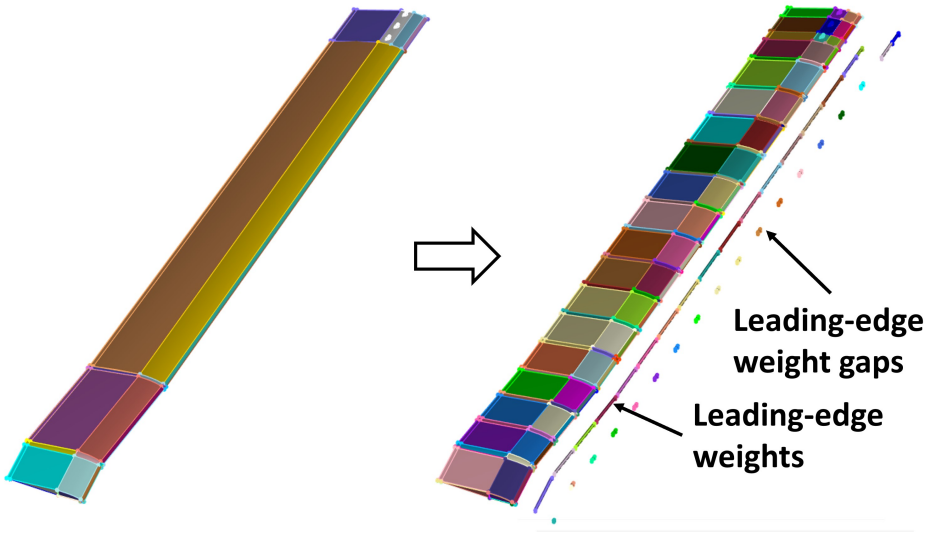

Figure 4.10: Leading-edge weights decomposition.

4.2.3 Imprinting and Merging

After decomposition, each volume is more or less independent. Even if the geometric elements (vertices, curves, and surfaces) between adjacent volumes are completely coincident, they are not connecting the adjacent volumes. A continuous geometry is needed to generate a continuous finite element mesh later. In order to join the adjacent geometric elements together, the step of imprinting and merging is needed. Imprinting refers to the identification of the common geometric elements between adjacent volumes and the generation of the missing elements. Merging refers to completing the fusion of adjacent and identical geometric elements. For a complex geometry like the double anhedral tip, it is not recommended to rely on the commands "imprint all" and "merge all" to perform this step automatically. Imprinting and merging are better performed along with decomposition. Every time a volume is separated into two, the interfaces should be imprinted and merged. For

the radial decomposition, which is relatively clean, the imprinting can be skipped and merge performed directly. The "Connect volumes" operation can identify the geometric element that fails to merge successfully. Then the geometries are ready for mesh generation.

4.2.4 Meshing

The majority of the blade volume can be meshed with the "sweeping" algorithm. A 2-D sectional surface mesh and radial curve meshes are needed to apply the "sweeping" algorithm. The selection of a suitable cross-section has a significant influence on the mesh quality. The best practice is to search for the cross-section with the most complex internal structure. For the present blade, that will be the cross-section at 5.58%R shown in Figure 4.11. This cross-section includes all the internal structures of the blade: skin, spar, leading-edge weight, fore core, aft-core, and root insert. The surfaces in this cross-section can be categorized into three types. The first type is a logical rectangle (four edges and four corners), and it is suitable for the "map" algorithm. The second type is a circle, which has its own specific algorithm "circle". The third type is a non-rectangle, which can be meshed by the "pave" algorithm. The meshing of radial curves is straightforward. The leading-edge curves are selected and meshed as shown in Figure 4.13. The cross-section mesh becomes the source of the "sweeping" algorithm to mesh the volume, whereas the curve mesh becomes the guile.

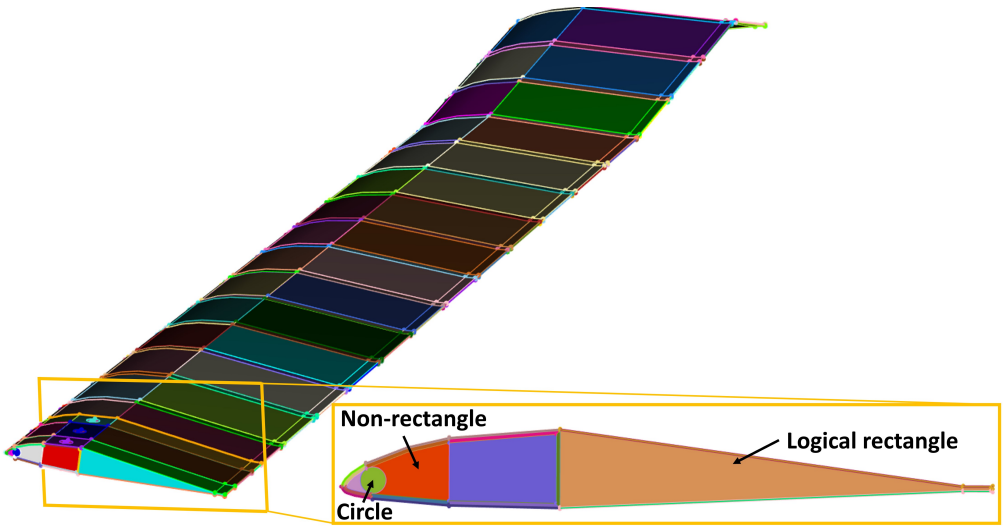

Figure 4.11: Cross-section selected to mesh.

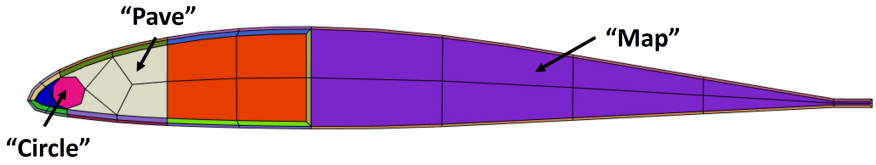

Figure 4.12: Cross-section mesh.

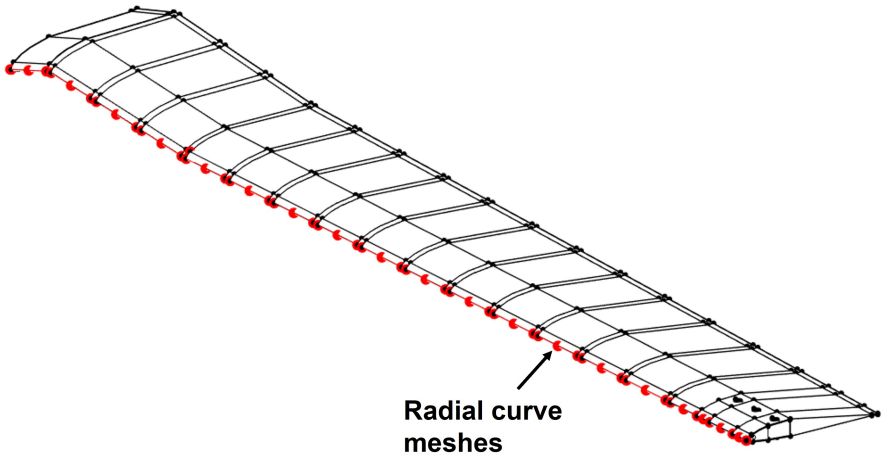

Figure 4.13: Radial curve mesh.

The cross-sectional mesh is swept inboard and outboard of 5.58%R to form the volume mesh. For sweeping the cross-section inboard, special treatment is required

to account for the root insert holes. The top surface of the root insert is meshed using the "hole" algorithm and then the surface meshes are swept vertically (Figure 4.14). The rest of the inboard volumes are meshed by sweeping the cross-section mesh inboard to the root. As for the outboard portion, the cross-section mesh is simply swept to the tip. Because of the special tip, it is crucial to ensure the tip mesh matches the airfoil. The double anhedral tip airfoils are always perpendicular to the local curved quarter chord line. Hence, the cross-section mesh in the tip should be perpendicular to the curved quarter chord line as well (Figure 4.15). This is determined by the aero-structural interface method, which will be detailed in section 4.3.

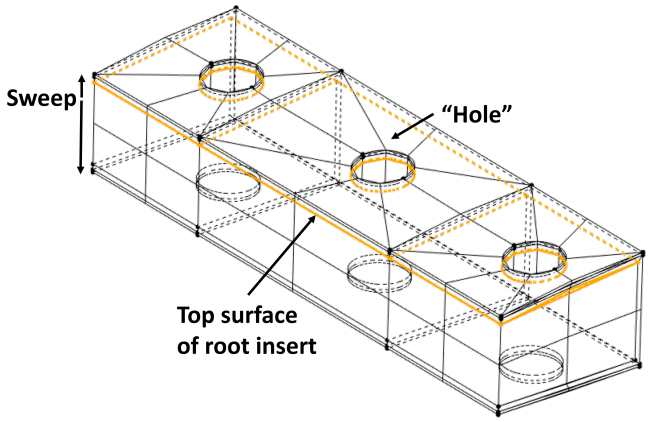

Figure 4.14: Root insert mesh.

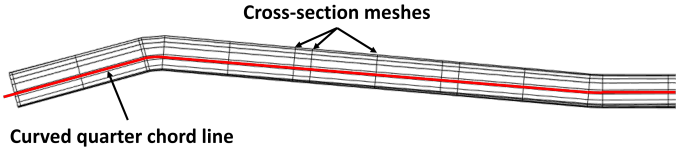

Figure 4.15: Tip portion mesh.

The meshes of the double anhedral blade and the straight blade are shown in Figure 4.16. All of the elements are converted from 8-noded hexahedral elements (in Cubit) to higher-order 27-noded hexahedral elements needed by X3D. It can be seen in Table 4.4 that two blade meshes have comparable sizes.

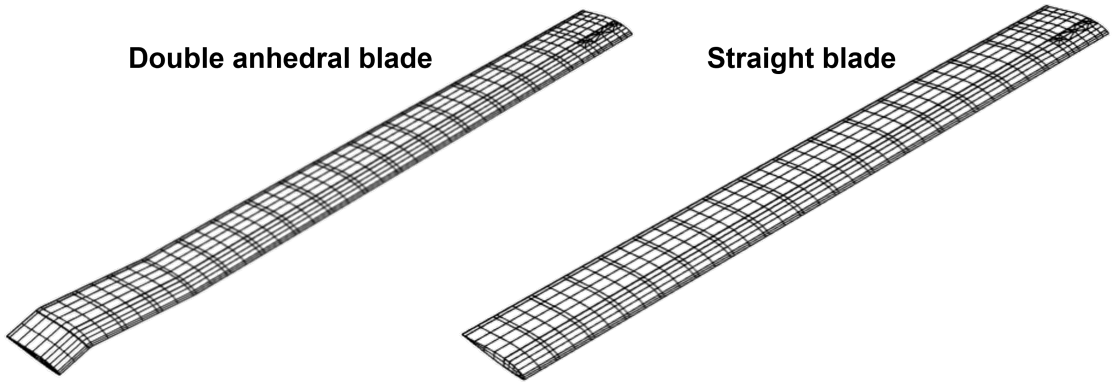

Figure 4.16: Blade meshes.

Table 4.4: Size of blade meshes.

	Double anhedral blade	Straight blade
No. of elements	3427	3305
No. of nodes	30,756	29,680
Degrees of freedom	$\approx 100,000$	$\approx 100,000$

It is necessary to evaluate the quality of the mesh. If the mesh quality is poor, the FEM model will generate inaccurate solutions or even be ill-conditioned. For 27-noded hexahedral elements, the scaled Jacobian is a useful metric of quality. This metric measures the proximity of each edge to the normal vector of its adjacent surface. The FEM model can be solved successfully if only all elements have scaled Jacobian greater than zero. Generally, for an 8-noded hexahedral mesh, a scaled Jacobian greater than 0.7 is desired for good accuracy. But when converted to 27-noded element values lower than 0.7 can be sufficient. The precise value for a 27-noded hexahedral mesh is not well-established generally and requires detailed

study outside the scope of this thesis. For the present blade, it was observed that a scaled Jacobian greater than 0.25 would provide an accurate solution. The mesh quality of both blade meshes is shown in Figure 4.17. The majority of the mesh elements have a scaled Jacobian close to 1, and the minimum value occurs at the root insert but remains higher than 0.25.

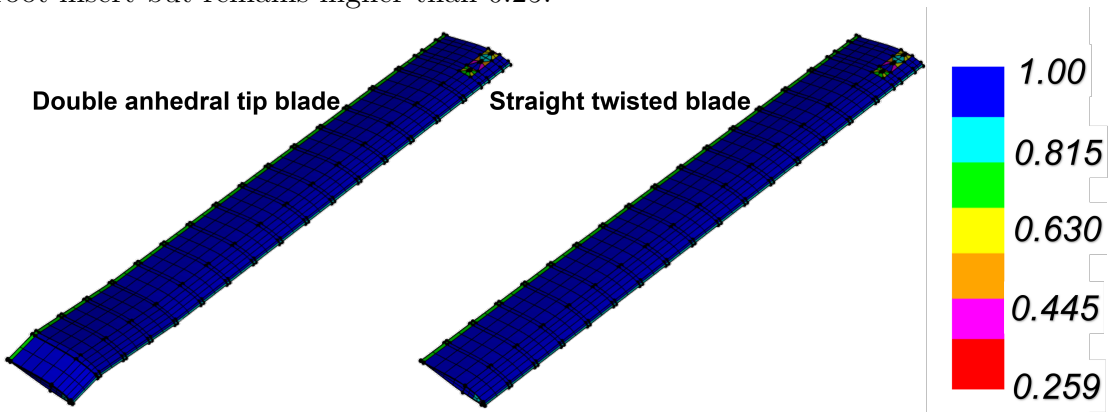

Figure 4.17: Blade meshes scale Jacobian quality.

4.2.5 Assignment of Blocks, Sidesets, and Nodesets

The assignment of material properties in X3D requires Blocks. Volumes with the same material properties are assigned to one block. As shown in Figure 4.18, the root insert, leading-edge weights, the fore core, and the aft-core are assigned to blocks 201-204 respectively. Though the fore and aft-core are both made of foam, they are assigned to different blocks to account for the density variation due to the film adhesive and compressed foam. For the spar and the skin, which consist of composite plies, the material properties in the global coordinate change with the volume orientation. So the spar or the skin cannot be assigned to one block. The spar volumes are assigned to 12 blocks (block 205-216, Figure 4.19), four for each portion (straight, dihedral, and anhedral). In each portion, top, leading-edge,

bottom, and web volumes are assigned to four blocks, respectively. The volumes in each block are assumed to have the same orientation. Similarly, the skin volumes are assigned to 15 blocks (block 217-231, Figure 4.20).

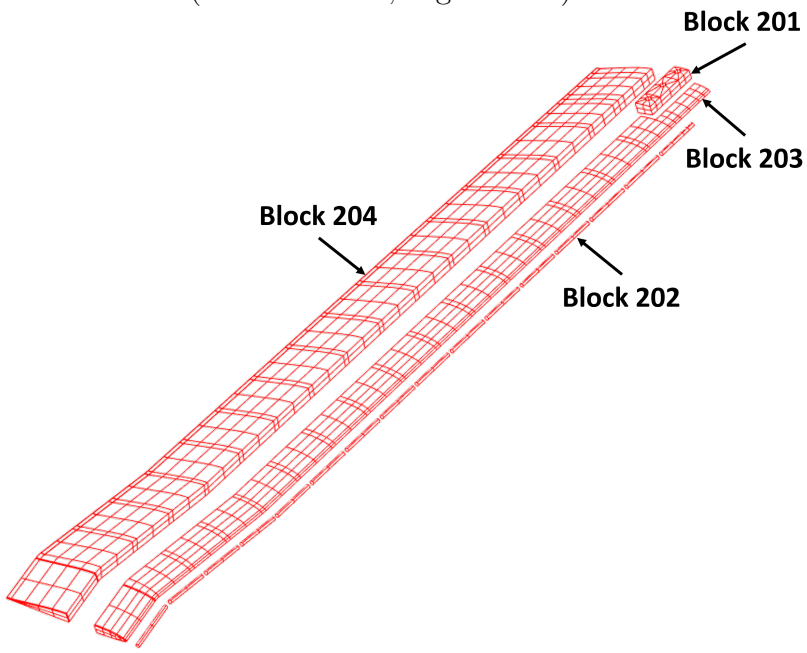

Figure 4.18: Blocks of isotropic material volumes.

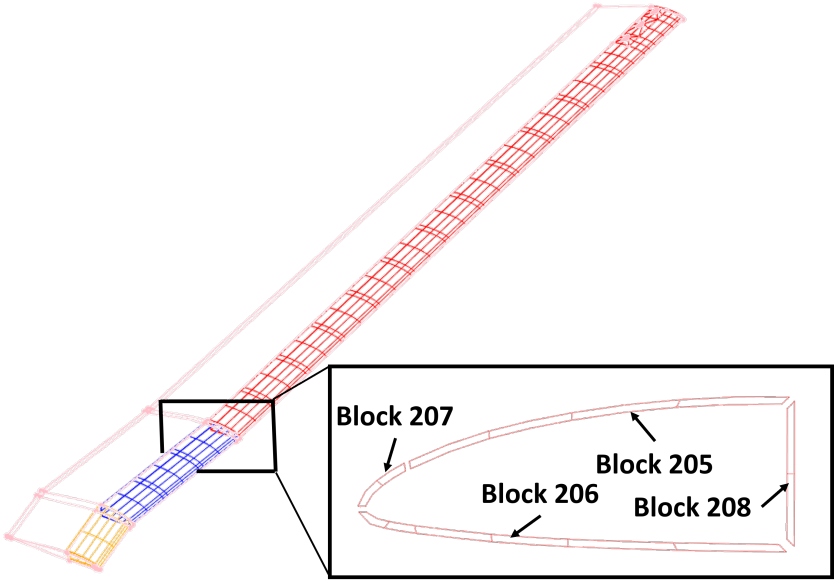

Figure 4.19: Blocks of spar volumes.

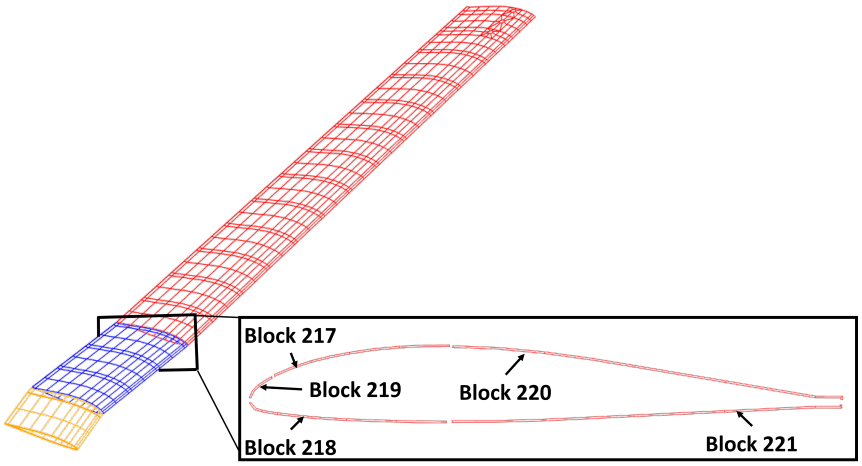

Figure 4.20: Blocks of skin volumes.

Since the block orientation impacts the composite properties in the global frame, it is important to extract the block orientation with respect to the X3D global coordinate system. These angles are extracted for each block and used as inputs later when building the Structural Analysis Model (SAM) input file. Currently, this step is done with an excel sheet.

The only kind of sideset used in this model is the 900 class sideset. This kind of sideset consists of the nodes on the external faces exposed to airflow (aerodynamic surface nodes). As shown in Figure 4.21, sixteen 900 class sidesets (SS901-SS916) are assigned. Each sideset is an aerodynamic segment. The aerodynamic forces and moments on each segment are distributed into nodal forces and applied to the nodes of this sideset.

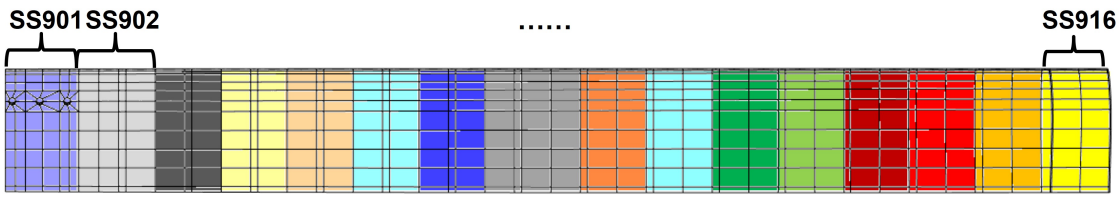

Figure 4.21: Aerodynamic segment sidesets (top view).

Compared to sidesets, nodesets have more functions. There are four types of nodesets defined on this blade. The first type is two 400 class nodesets identified as NS401 and NS402. These are used to define a joint. The solution process relates the degrees of freedom at these nodes to the joint degrees of freedom. The nodal degrees of freedom are then eliminated. Nodeset 401 are nodes on the inner surface of blade root holes (Figure 4.22). These are connected to the root joint for boundary conditions and pitch control input. Nodeset 402 are nodes near the quarter chord line in the cross-section of the first dihedral junction (Figure 4.23). A joint is defined with this nodeset, and it is used to apply static loads for structural load calibration. This nodeset can be placed at any radial location as long as it is outboard of the desired load inspection point. For the double anhedral blade, placing nodeset 402 at the end of the straight portion simplifies the calibration process. Note that unlike the root joint this joint is not a physical bearing but rather a load sensor.

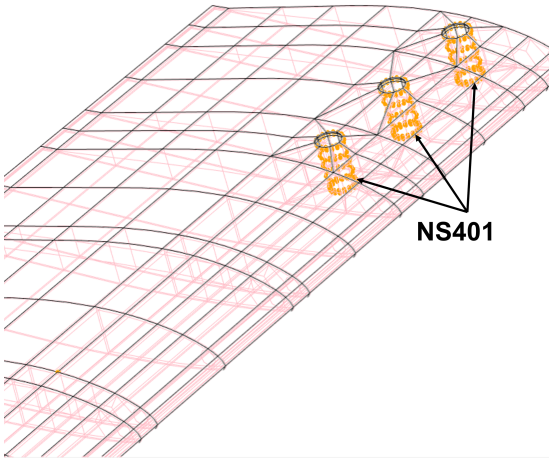

Figure 4.22: Root boundary and strain gauge nodeset.

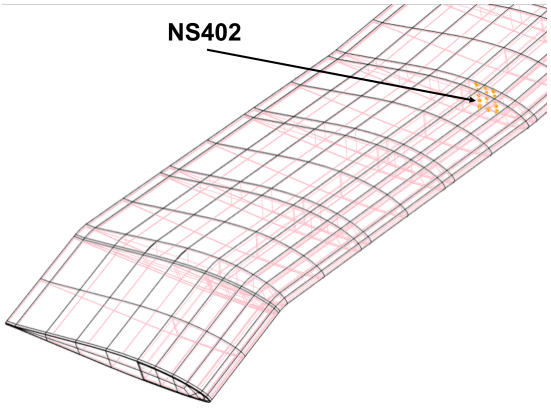

Figure 4.23: Nodset for applying static loads.

The second type of nodeset is the 700 class nodeset. As shown in Figure 4.24, the nodeset 701 is defined by nodes on the leading-edge curve, nodeset 702 for the trailing-edge curve, nodeset 703 for the top surface, and nodeset 704 for the bottom surface. The motions of these nodes are used to determine a beam-like cross-sectional deformation. It is critical to place the leading-edge nodes and trailing edge nodes precisely because these two nodesets define the chord lines. However, the placement of the top and bottom nodeset is not as strict. They define the thickness line loosely. When placing them, there are only two requirements: 1) the nodes are in the same cross-section as the chord nodeset, and 2) the vector joining them is not parallel to the chord line. The number of nodes in these four nodesets must be the same. Otherwise, there will be orphan nodes without any cross-sections.

The third type of nodeset is the 800 class nodeset. It is for structural load

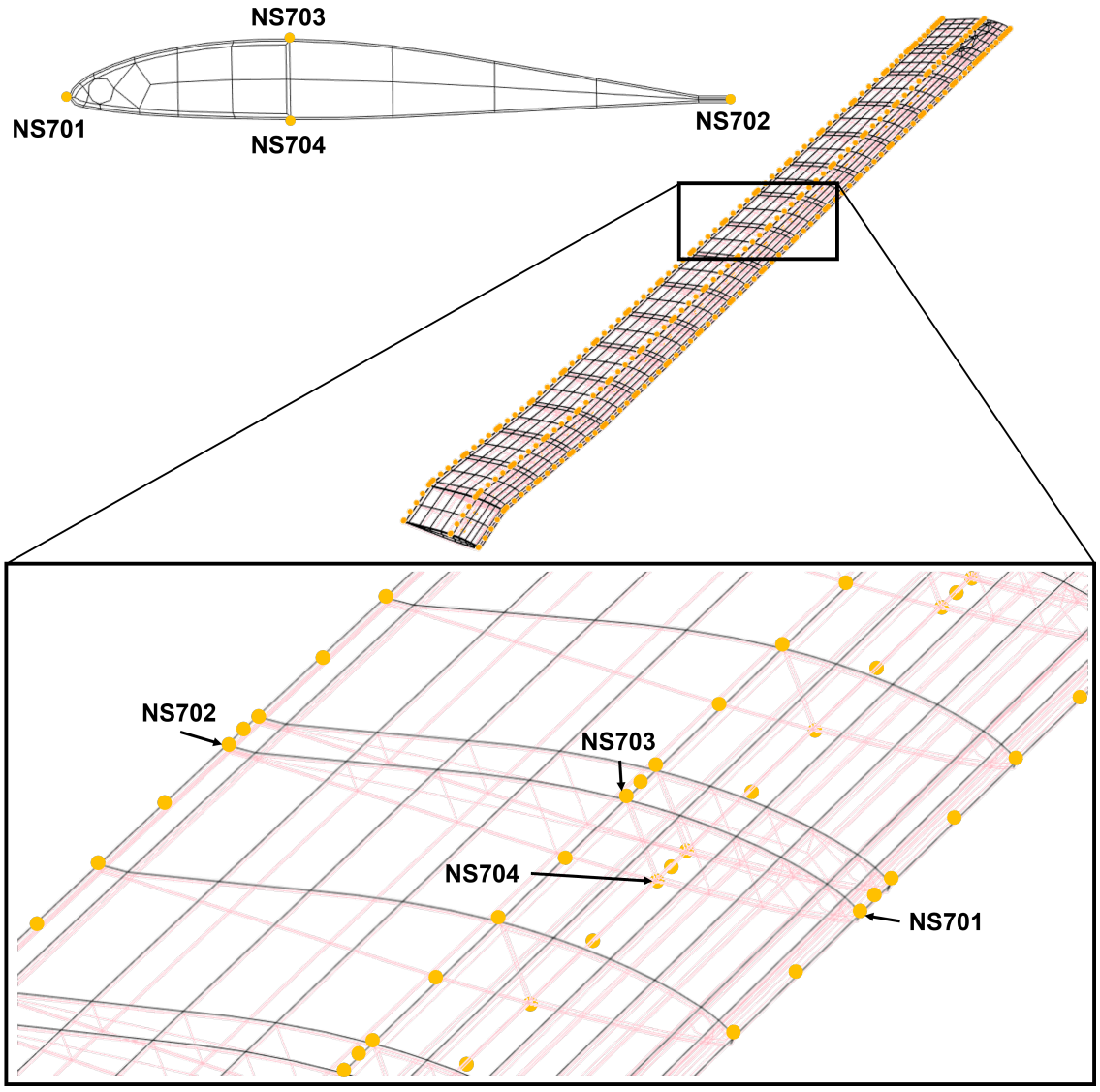

Figure 4.24: The 700 class nodesets .

calculation. The sectional blade structural loads (axial force, flap bending moment, lag bending moment, and torsional moment) can be calculated base on the 3-D strain of the selected nodes in the 800 class nodesets. As shown in Figure 4.25, this class of nodeset is also composed of four nodesets (NS801, NS802, NS803, and NS804). The rule of placement is that NS801 and NS802 are put on the top surface, whereas NS803 and NS804 are put on the bottom surface. Moreover, NS801 and

NS803 should be in front of NS802 and NS804. The specific node selection varies with the structure, and it is further discussed in section 4.4.

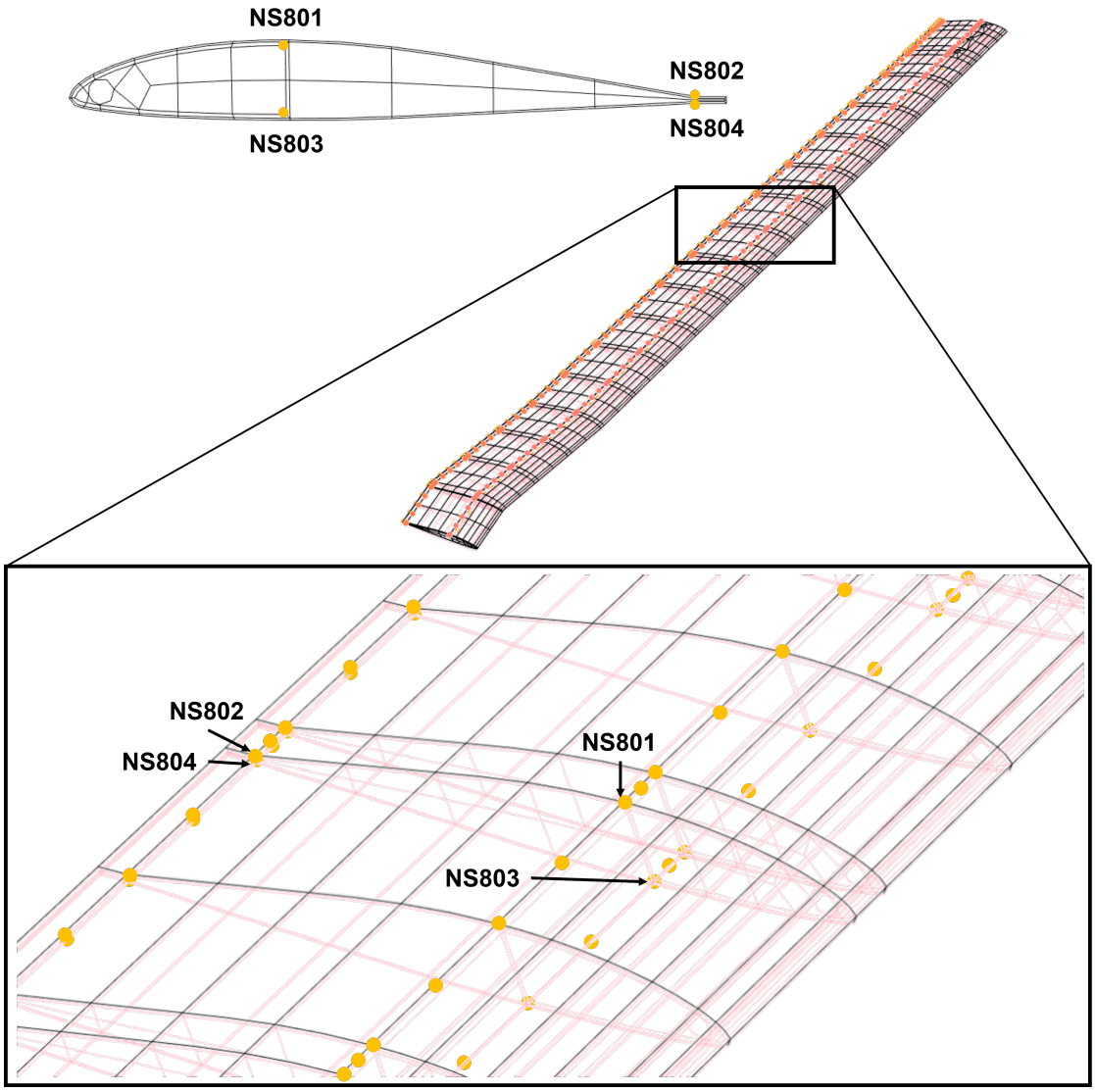

Figure 4.25: The 800 class nodesets.

The last type of nodeset is the 900 class nodeset. It is defined based on the 700 class nodeset (chord and thickness line) and 900 class sideset (aerodynamic surface). The locations of NS901-NS904 are shown in Figure 4.26. Essentially these nodes

are the 700 class nodesets at the beginning and end of 900 class sidesets. This type of nodeset is used to identify the sectional dynamic pressure and angles of attack for aerodynamic force and moment calculation of the corresponding segment (a 900 class sideset).

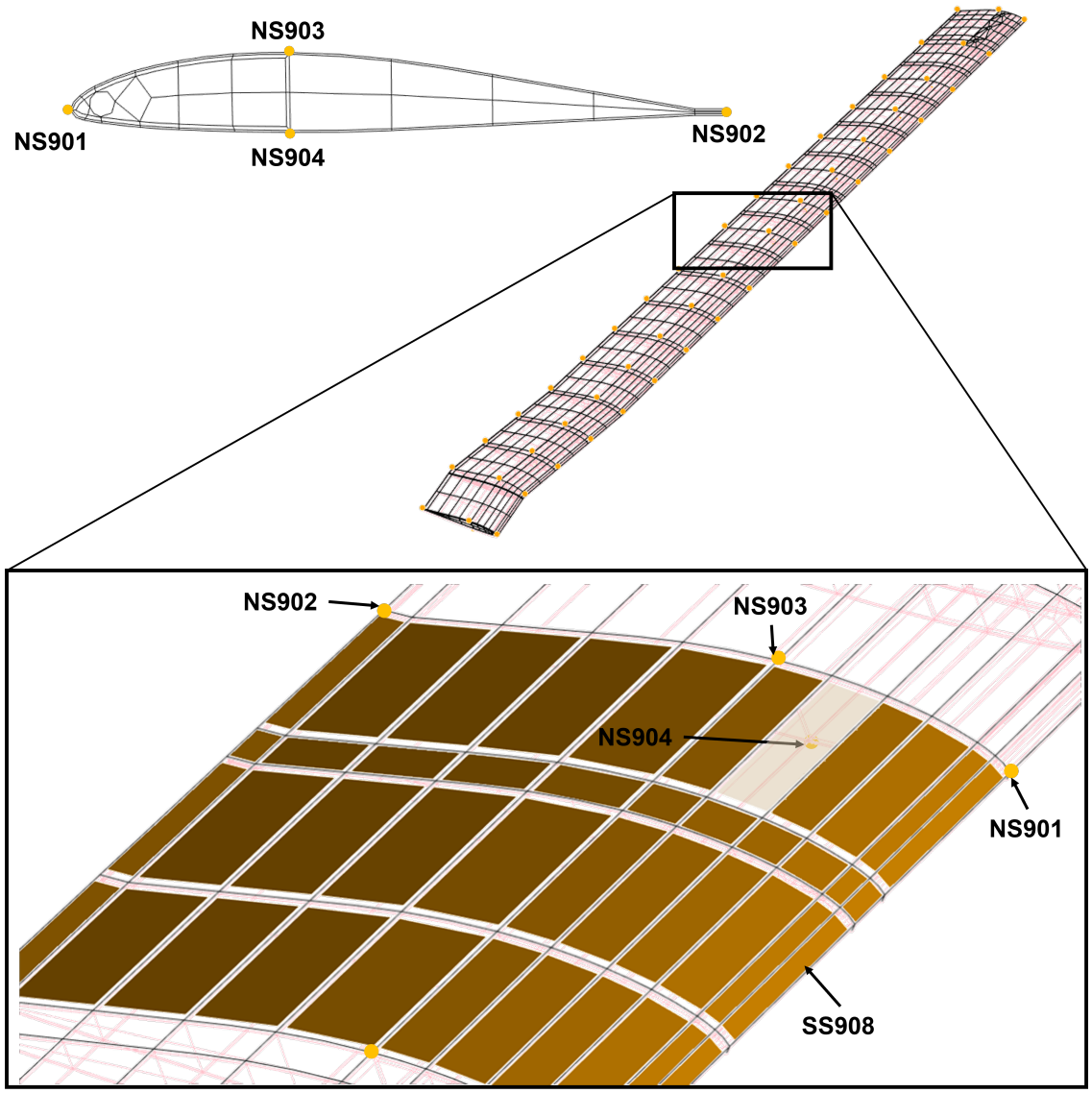

Figure 4.26: The 900 class nodesets.

Finally, the mesh is exported as an I-DEAS Universal (.unv) mesh file. Then a python code, SamBuilder, developed by Staruk [102] is used to convert the mesh file to X3D mesh data file (.dat), joint data files (.j.dat), and the Structural Analysis Model (SAM) input file. These are all readable ASCII files. The SAM is a Fortran namelist file. Material properties, ply orientations, blade orientations, blade position relative to hub, and joint properties are defined in the SAM input file. The SAM file, mesh file, and joint files are inputs to X3D.

4.3 Blade Aerodynamic Model

The built-in aerodynamic model in X3D is a lifting-line model with 2-D unsteady flow airfoil C81 tables and free wake. The free wake is a time-marching version of Maryland Free Wake [103]. For the present study, a single rolled-up vortex is used, released from the deformed blade tip quarter-chord. The vortex strength equals 55% maximum circulation outboard of 50% span, and the vortex core is 10% of the tip chord when formed with a growth factor of 0.05. These numbers are set empirically based on experience validation with single and coaxial rotors of a similar scale. In hover, 12 turns of wake with 15° azimuth angle discretization are used. A full span Weissinger-L near wake model [104] is used 30° behind each blade after which the wake rolls up. For edgewise flow, 4 turns of wake with 5° azimuth angle discretization are used. The near wake model is turned off for edgewise flight to avoid complications on the retreating side near the reverse flow boundary. A sample wake geometry in hover is shown in Figure 4.27.

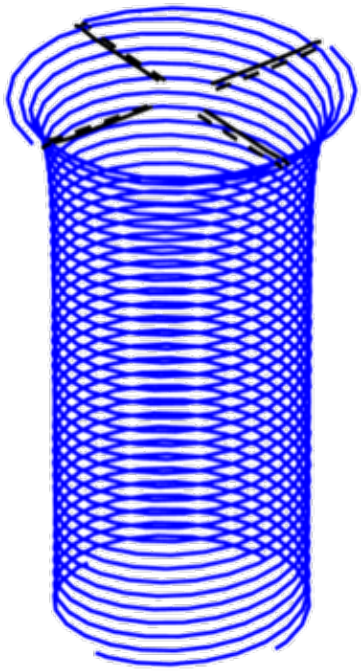

Figure 4.27: Hover free wake geometry.

An interface is needed to communicate between the aerodynamic and structural models. The sideset and nodesets described in the last section are essential for exchanging information. In the blade aerodynamic model, 23 aerodynamic panels are created as shown in Figure 4.28. Each aerodynamic panel has a corresponding aerodynamic segment on the mesh (900 class sideset), to which the aerodynamic forces and moments are supplied. More aerodynamic panels are assigned to the tip region. The aerodynamic segmental normal force F_N, chordwise force F_C, and pitch moment about the quarter chord $M_{1/4}$ on the lifting line are re-distributed over the surface to create nodal normal force f_N and chordwise force f_C. This re-distribution is ad hoc at present but ensures the net moment remains the same. This is a limitation of the lifting line model, not the structural model. Figure 4.29 shows the forces

and Equations (4.1) and (4.2) [99] give the re-distribution method. The variables ξ and η are the chordwise and normal coordinates of the surface nodes, and n is the number of surface nodes. α_0, α_1, and β_0 are the coefficients needed to solve to calculate f_N and f_C.

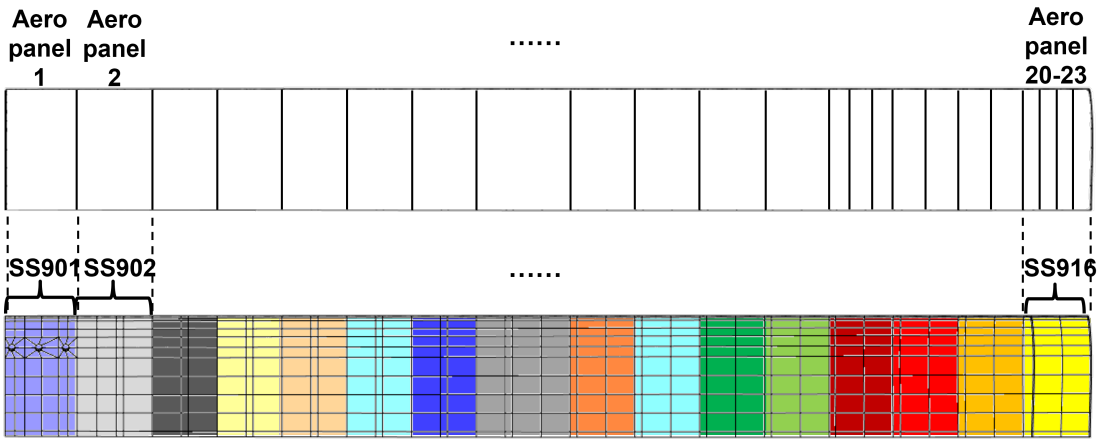

Figure 4.28: Aerodynamic panels corresponding to aerodynamic sideset.

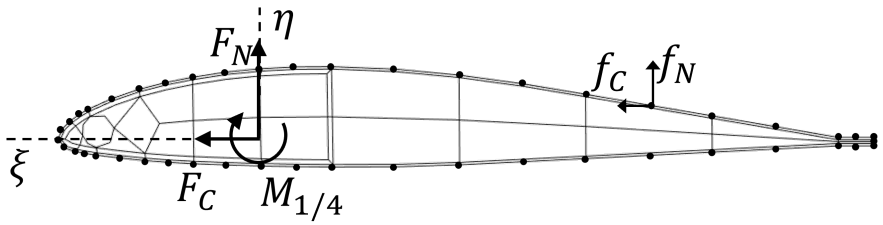

Figure 4.29: Aerodynamic node forces.

$$\begin{bmatrix} F_N \\ F_C \\ M_{1/4} \end{bmatrix} = \begin{bmatrix} n & \sum \xi & 0 \\ 0 & \sum \eta^2 & n \\ \sum \xi & \sum(\xi^2 - \eta^3) & -\sum \eta \end{bmatrix} \begin{bmatrix} \alpha_0 \\ \alpha_1 \\ \beta_0 \end{bmatrix} \tag{4.1}$$

$$f_N = \alpha_0 + \alpha_1 \xi$$
$$f_C = \beta_0 + \alpha_1 \eta^2 \tag{4.2}$$

4.4 Blade Structural Load Calculation

Unlike the force summation method or the deflection method in a 1-D beam model, a strain-based load calibration method is developed to extract structural loads from the 3-D model. This method mimics the strain-based load measurement method used during rotor tests. Instead of measured strains calculated strains are used. As in tests, pre and post-processing are needed. In pre-processing, known static loads (extension F_X, torsion (M_X), flap bending M_Y, and lag bending M_Z) of various magnitudes are applied to the structure one at a time. calculated strains are output from the 800 class node and grouped as in Equation (4.3). E_X, E_T, E_F, E_L are axial, torsional, flap bending, and lag bending strain groups. ϵ_{xx} and ϵ_{xy} are axial and in-plane shear strains. The blade structural loads can be calculated in post-processing based on these strain groups and a calibration matrix as shown by Equation (4.4). Since the strain groups and applied loads of each cross-section are known, the calibration matrix K for each section can be solved. K matrix is extracted row by row with F and M of various magnitudes, and least square inversion is used. Similar to the strain gauge circuit of the blade structural load sensor, this kind of strain group can enhance the strain magnitude of the correlated load.

$$\begin{bmatrix} E_X \\ E_T \\ E_F \\ E_L \end{bmatrix} = \begin{bmatrix} \epsilon xx_{NS801} + \epsilon xx_{NS802} + \epsilon xx_{NS803} + \epsilon xx_{NS804} \\ \gamma xy_{NS801} + \gamma xy_{NS802} - \gamma xy_{NS803} - \gamma xy_{NS804} \\ \epsilon xx_{NS801} + \epsilon xx_{NS802} - \epsilon xx_{NS803} - \epsilon xx_{NS804} \\ -\epsilon xx_{NS801} + \epsilon xx_{NS802} - \epsilon xx_{NS803} + \epsilon xx_{NS804} \end{bmatrix} \tag{4.3}$$

$$\begin{bmatrix} F_X \\ M_X \\ M_Y \\ M_Z \end{bmatrix} = K \begin{bmatrix} E_X \\ E_T \\ E_F \\ E_L \end{bmatrix} \tag{4.4}$$

The placement of the 800 class nodesets requires more discussion. As shown in Figure 4.30, consider a 3-D model of a twisted aluminum beam (20° twist, 1 m long, and 0.1 m wide) and two selection of 800 class nodesets: version-1 and version-2. Figure 4.31 and 4.32 show the axial strain and in-plane shear strain of the beam under a combination of all four tip loads ($F_X = 500N$, $M_X = 5Nm$, $M_Y = 5Nm$, $M_Z = 50Nm$). The extracted structural loads along the span are shown in Figure 4.33. It can be seen that two choices have a limited impact on structural load. This conclusion also holds for a rotating beam (RPM = 955), as shown in Figure 4.34-Figure 4.36.

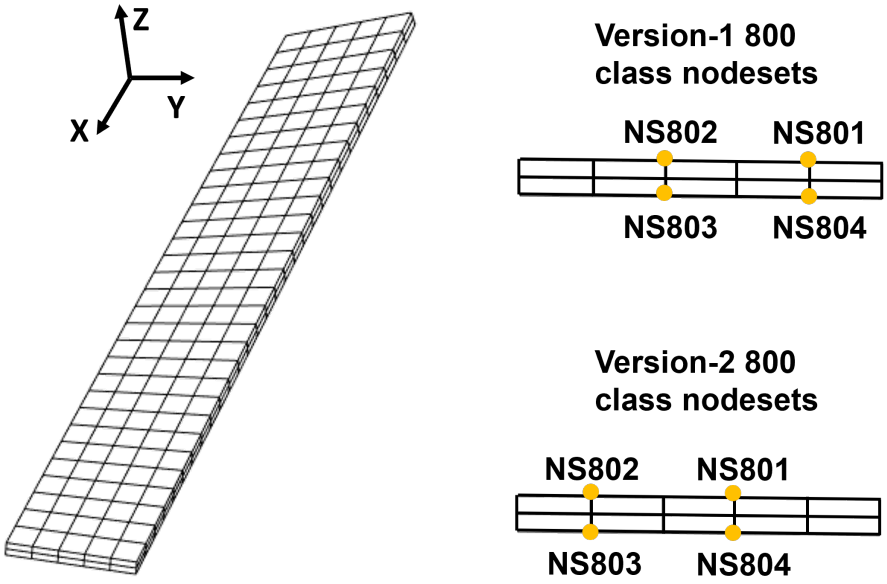

Figure 4.30: Mesh and 800 class nodesets of a twisted aluminum beam.

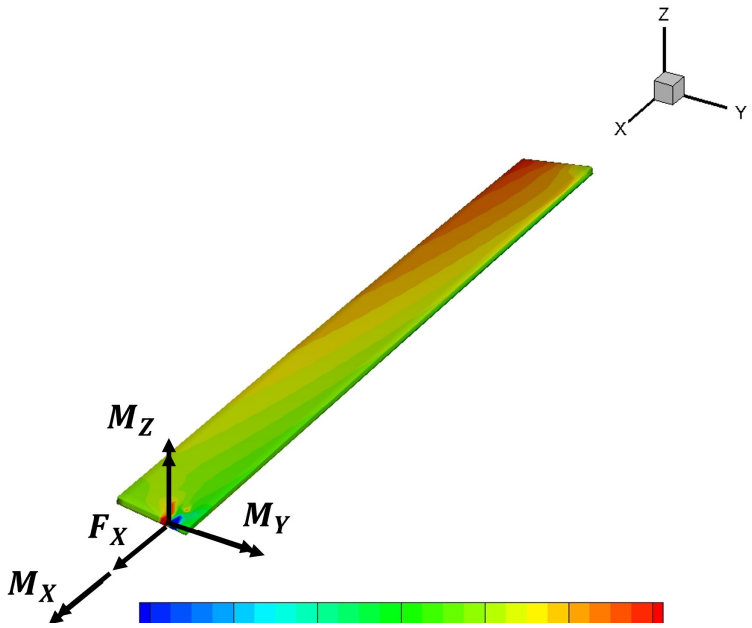

Figure 4.31: Axial strain on a twisted aluminum beam under tip loads.

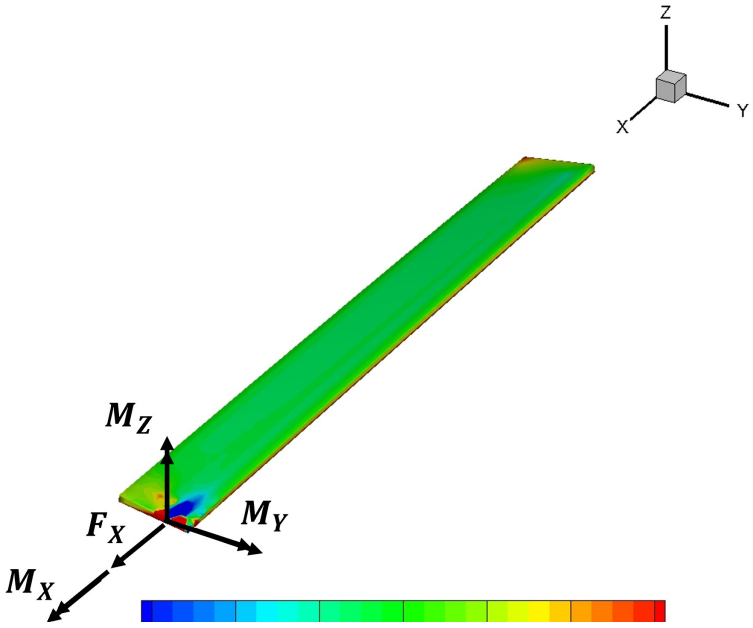

Figure 4.32: In-plane shear strain on a twisted aluminum beam under tip loads.

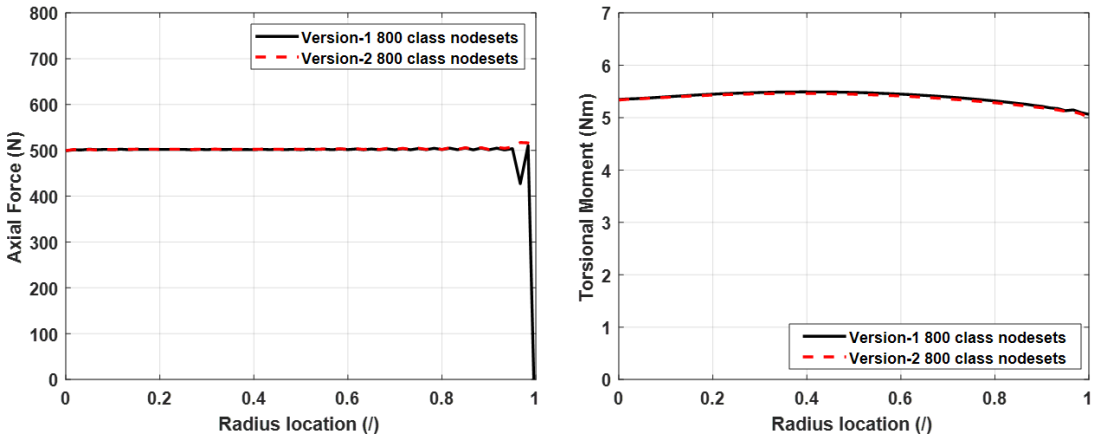

(a) Axial force.

(b) Torsional moment.

(c) Flap bending moment.

(d) Lag bending moment.

Figure 4.33: Structural loads of a twisted aluminum beam under tip loads.

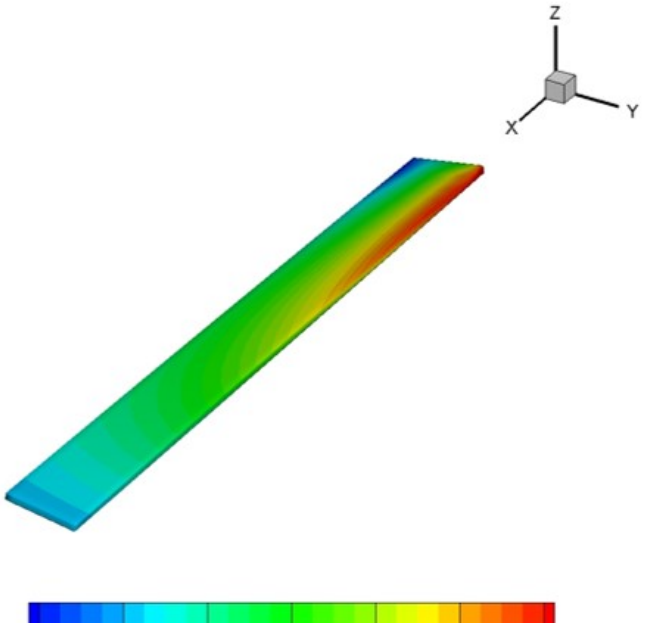

Figure 4.34: Axial strain on a rotating twisted aluminum beam.

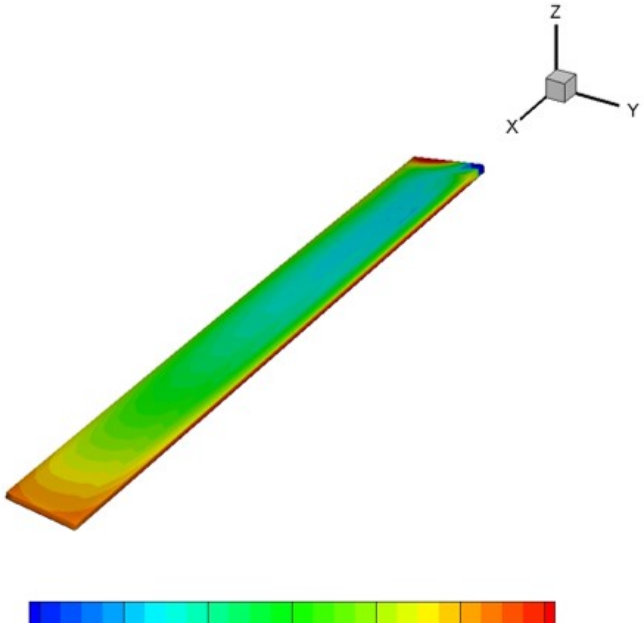

Figure 4.35: In-plane shear strain on a rotating twisted aluminum beam.

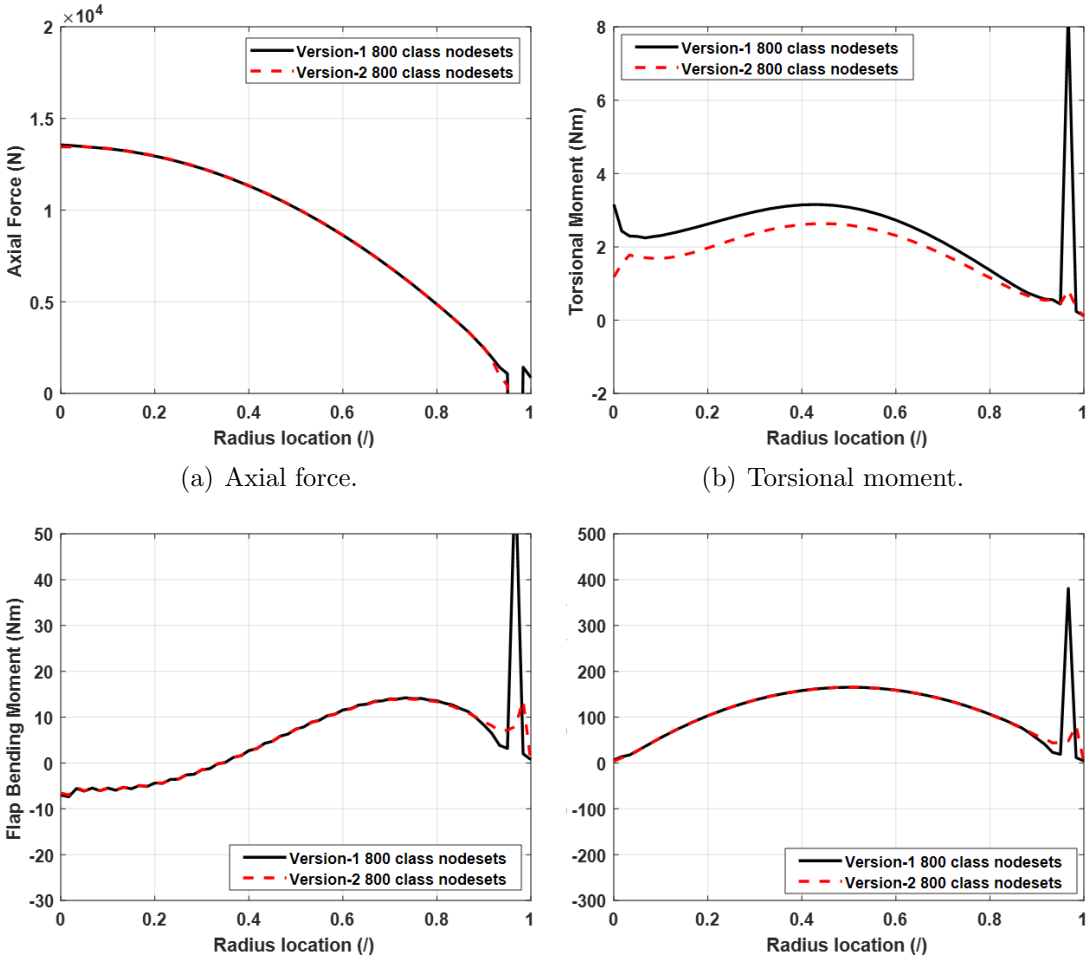

(a) Axial force.

(b) Torsional moment.

(c) Flap bending moment.

(d) Lag bending moment.

Figure 4.36: Structural loads of a rotating twisted aluminum beam.

Now consider the present blade. Figure 4.37 shows three versions of 800 class nodesets on the straight blade model. The third version is added to mimic precisely the strain gauge placement during tests. Furthermore, this third version in fact uses three distinct groups of nodesets. One each for flap, lag, and torsion.

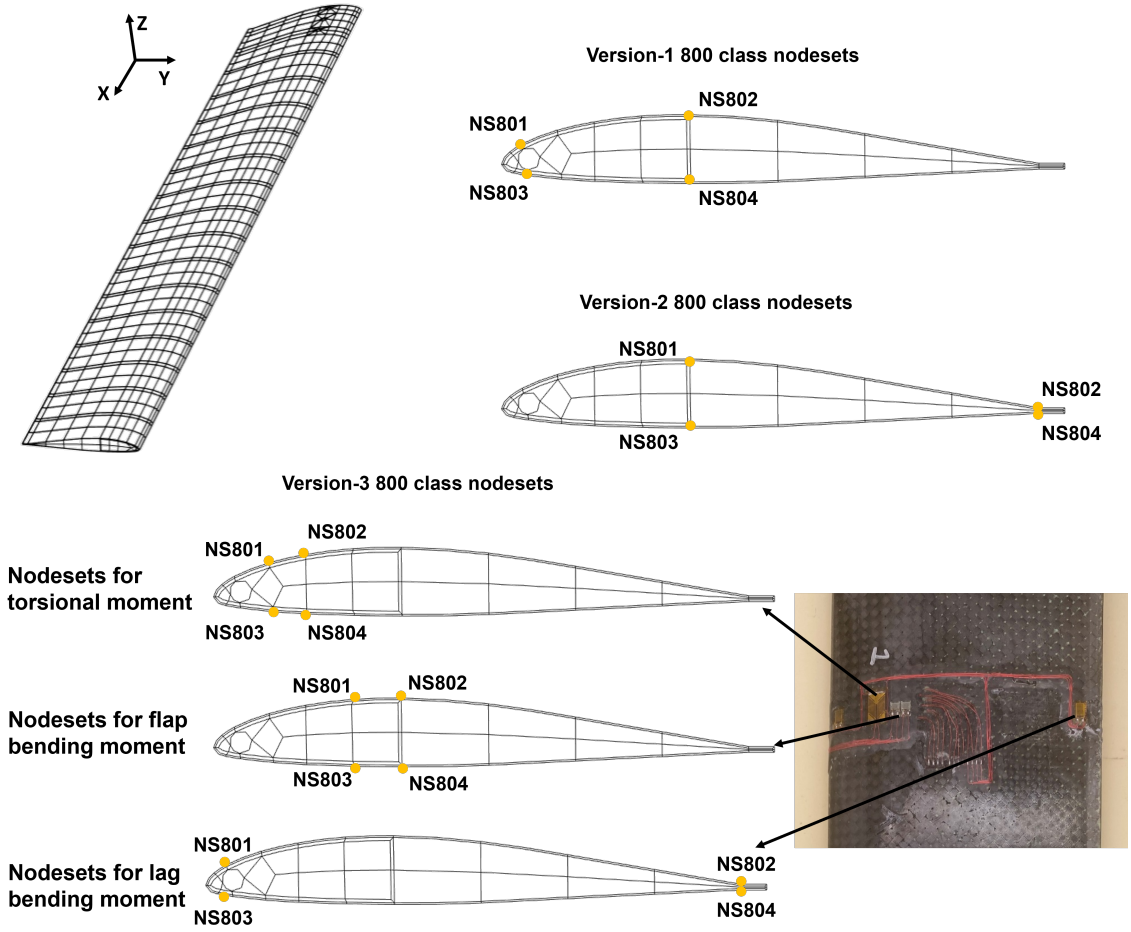

Figure 4.37: Mesh and 800 class nodesets of the straight twisted blade.

Figure 4.38 and 4.39 show the axial strain and in-plane shear strain of the blade under a combination of all four tip loads ($F_X = 500N$, $M_X = 5Nm$, $M_Y = 5Nm$, $M_Z = 50Nm$). The structural loads extracted using a different selection of nodesets (Figure 4.40) are still comparable except for the 3-D effects near the root and the

tip. However, the differences become marked in the rotating case. It can be seen in Figure 4.43 (RPM = 993, $\theta_{75} = 4°$) that the structural loads extracted from the third version of nodeset are very different from the other two versions, especially in axial force and lag bending moment. The jumps in version-1 and -3 are due to the presence of leading-edge weights. During pre-processing, the strain groups are calibrated against a tip axial force, not centrifugal force. For a uniform structure (twisted aluminum beam), the influence of centrifugal force can be captured by a tip axial force. But not for a blade with discrete weights inside. The axial force is applied only at the tip and then transferred to the rest of the structure, but the centrifugal force acts everywhere. The strain concentrations caused by the weights in presence of the centrifugal force cannot be accounted for with a static axial force calibration. The strain patterns under a tip axial force and centrifugal force are markedly different (Figure 4.38 and 4.41). This effect is more pronounced in the calculation of axial force and lag bending. Moreover, the structural loads that jump between positive and negative along the span is not physical but merely an artifact of local strain concentration. The problem can be solved by calibrating the strain against centrifugal force, but that is not feasible. The next best solution will be to avoid the region of strain concentration when selecting nodes. The version-2 nodeset is one of the solutions. The impact of these nodesets will be validated further later with test data.

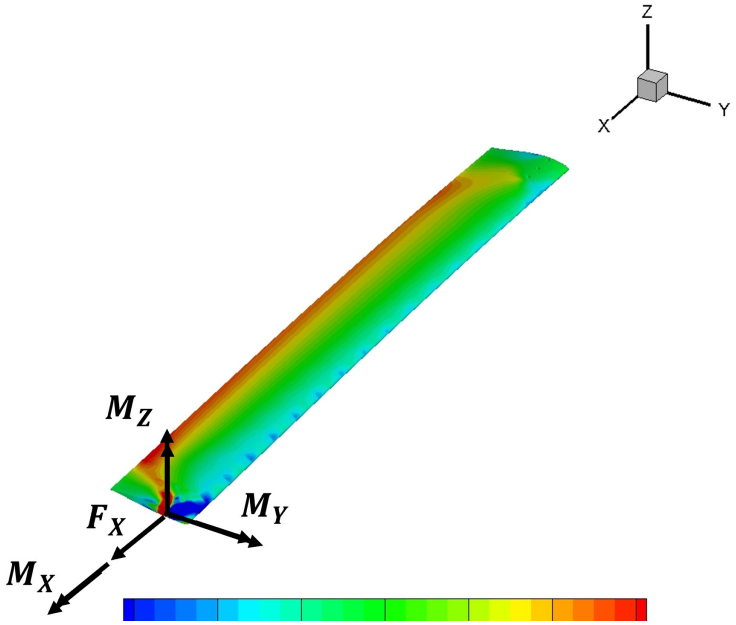

Figure 4.38: Axial strain on the straight blade under tip loads.

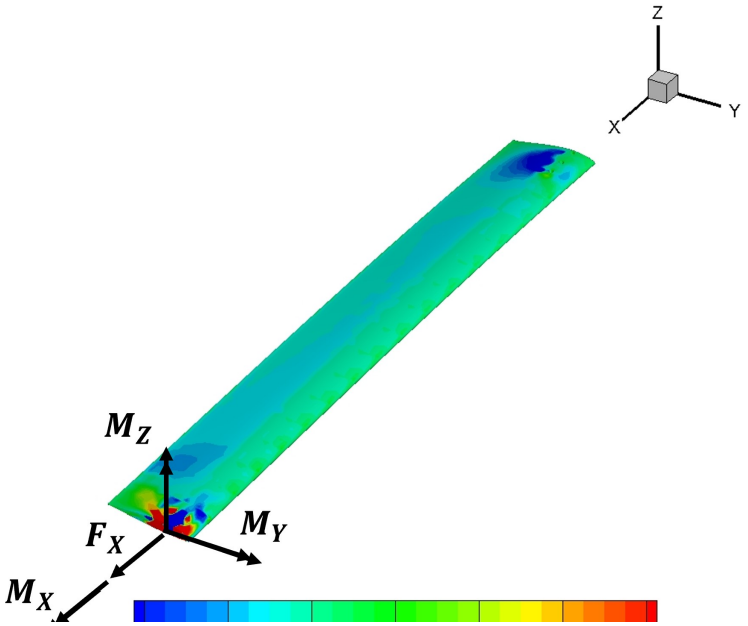

Figure 4.39: In-plane shear strain on the straight blade under tip loads.

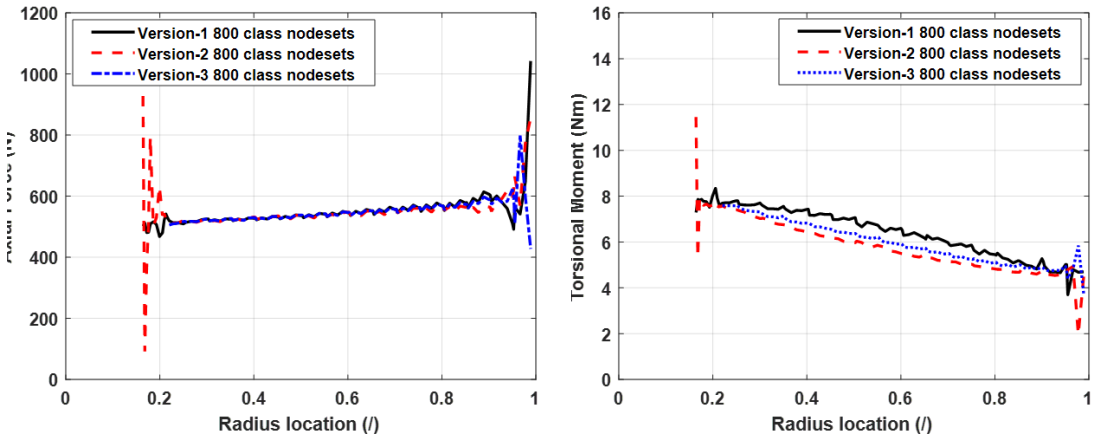

(a) Axial force.

(b) Torsional moment.

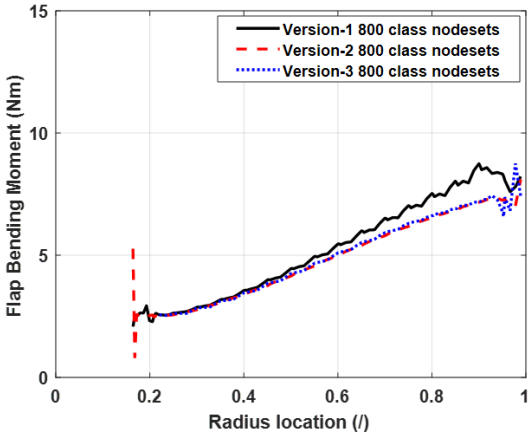

(c) Flap bending moment.

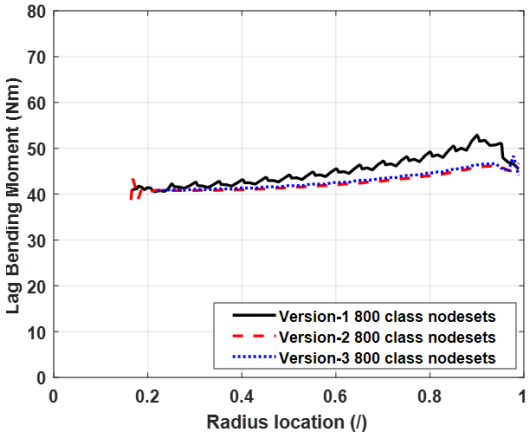

(d) Lag bending moment.

Figure 4.40: Structural loads of the straight blade under tip loads.

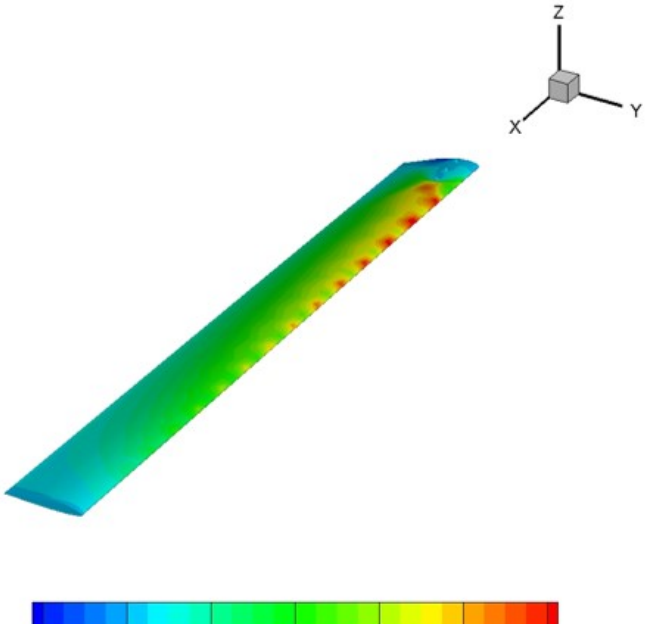

Figure 4.41: Axial strain on the rotating straight blade.

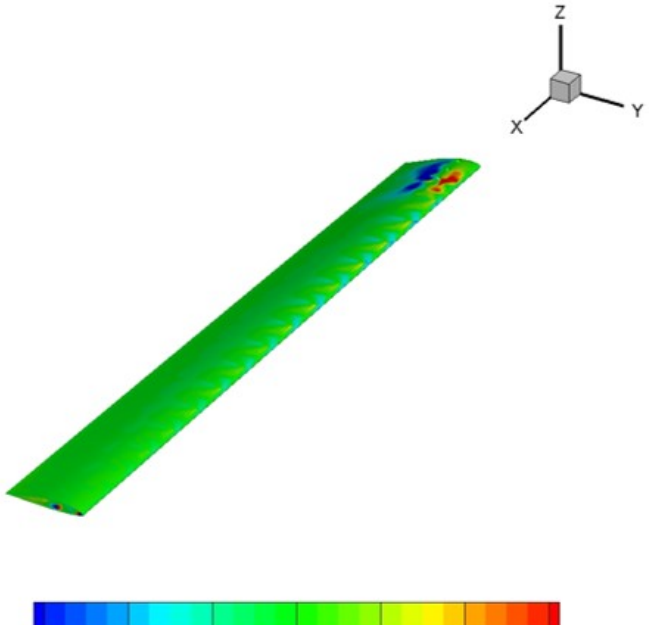

Figure 4.42: In-plane shear strain on the rotating straight blade.

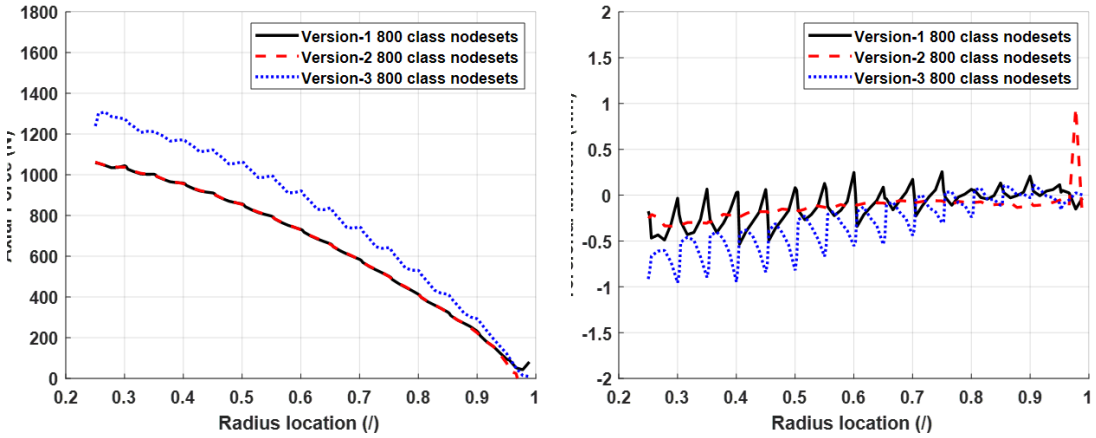

(a) Axial force.

(b) Torsional moment.

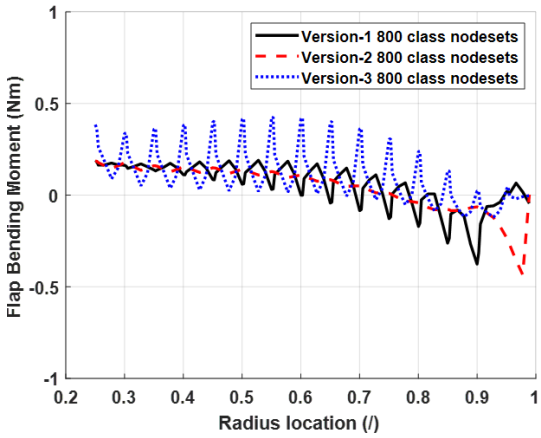

(c) Flap bending moment.

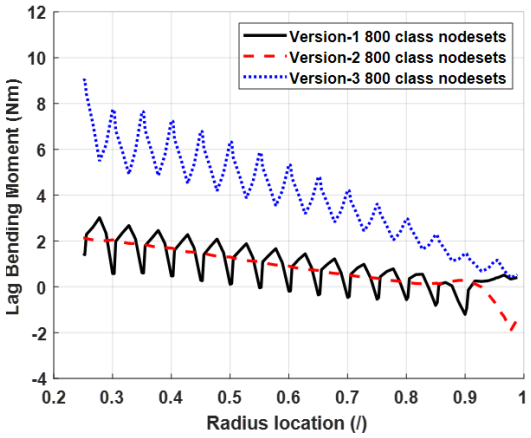

(d) Lag bending moment.

Figure 4.43: Structural loads of the rotating straight blade.

4.5 Summary

This chapter presented the development of the 3-D blade model. The special features in the geometric model needed for mesh generation were highlighted. The process for meshing the 3-D blade structural model was detailed. Structural models for the straight blade and the double anhedral blade were formulated. The lifting line model was set up for aerodynamic calculation. A structural load calibration method was described with several options of sensor placement and the best placement was identified.

Chapter 5: Rotor Tests and Model Validation

The 10-ft vacuum chamber was used to test the blades without aerodynamic effects. The objectives were to measure rotating natural frequencies and 3-D strains. This was followed by hover tests. The test procedures, post-processing, and the data acquired are detailed in this chapter. The data is used to validate the 3-D structural model, aerodynamic model, and aero-structural interface of the double anhedral blade systematically.

5.1 Vacuum Chamber Test

5.1.1 Test Procedure

The rotating blade natural frequencies and strains were measured with two test procedures. For the frequency test:

1. The vacuum chamber hub was mounted on the vacuum chamber shaft via four shoulder bolts, as shown in Figure 3.6. Then the slipring wires were connected to the PCB on both sides of the hub. A connectivity check was performed to the hub PCB terminals (Figure 3.26) and the slipring non-rotating end wires with a multimeter.

2. The hub strain gauge (Figure 3.26) and shaker were connected to the data acquisition system via the hub PCB terminals and the slipring. The hub strain gauge was checked at the slipring non-rotating end with a multimeter to see if the resistance value is as expected (350 Ω). Next, the function generator (Figure 3.27) was turned on and the excitation frequency was set. As the shaker operates, the frequencies were picked up by the hub strain gauge. This was a check of the frequency excitation system.

3. The slipring wires connected to the hub were secured with aluminum taps. Then the hub was spun up at a low speed. The rotational speed measured by the RPM sensor (Figure 3.4) was checked against a tachometer. Next, excitation frequency sweeps were performed. The sweeps were performed at multiple rotor speeds to check if the shaker, the hub strain gauge, and the data acquisition system work properly when the hub is spinning.

4. The blades were installed in the blade adapters with three shoulder bolts and locknuts (Figure 3.10). Then the blade root pitch was adjusted to zero degrees by changing the length of the pitch links (Figure 3.12).

5. The blade strain gauges were connected to the data acquisition system via the hub PCB terminals and the slipring. All of the blade strain gauges were checked at the slipring non-rotating end with a multimeter to see if the resistance value is as expected (350 Ω). Next, simple tip static load was applied to the blade to examine if the measured strain is as expected. The wires were secured on the hub with aluminum tapes. The final test setup is shown in

Figure 5.1.

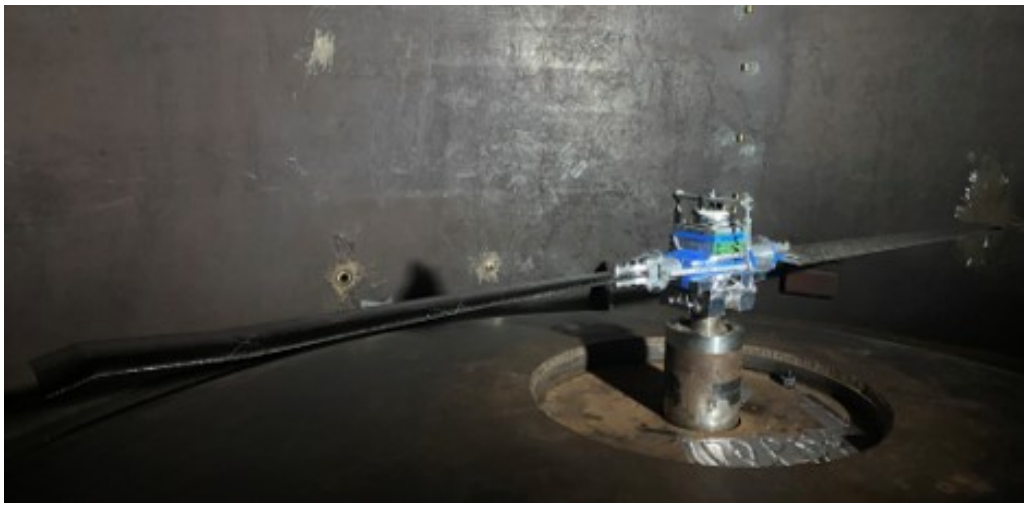

Figure 5.1: Final setup of the frequency test.

6. After the chamber entry and air outlet was sealed, the air pump was turned on to vacuum the chamber. The chamber was considered vacuumed when the chamber pressure indicated by the pressure gauge (Figure 3.3(b)) was below 0.3 inch Hg ($\geq$ 99% vacuum). This process took about 20 minutes. The low-pressure level can be maintained for at least 30 minutes, which was enough to perform multiple tests.

7. The rotor speed was adjusted to the target value via the motor controller (Figure 3.4). As the rotor speed became stable, an excitation frequency sweep was performed. Meanwhile, the time history of the hub strain and blade strains were recorded. This process was repeated for multiple rotor speeds, including zero rotor speed.

8. Only two blades can be tested in a test. So, steps 4-7 were repeated with the

other two blades to examine the repeatability of the test and the similarity of the blades.

For the strain test:

1. The shaker was replaced by the aluminum block (Figure 3.20), and the blade root pitch was fixed at 5.6°.

2. The blade installation and chamber vacuuming steps are the same as steps 3-6 in the frequency test.

3. After the chamber was vacuumed, the rotor was spun up at the lowest controllable speed. A baseline case was recorded at this rotor speed. Due to the rotation, the brush in the slipring might change the overall resistance of the strain measurement system. Hence, the strain signal at the lowest controllable rotor speed was used as the baseline. Because the rotor speed was low, the centrifugal force was negligible at this point.

4. Rotation speed sweep was performed. Once the rotor speed stabilized at the desired value, 3 seconds of strain data were recorded.

5. The position of two test blades was swapped, and then the test was repeated. All four blades were tested eventually.

5.1.2 Data Processing

The raw data from the frequency tests were strains versus time. The data was first passed through a low pass filter with the highest excitation frequency (300

Hz) as the threshold. Then frequencies were extracted using Fast Fourier Transform (FFT). In Figure 5.2, the frequency spectrum of a blade spinning at 200 RPM is shown as an example. The peaks at multiples of the excitation voltage (120 Hz and 240 Hz) were discarded. The remaining peaks were from blade dynamics.

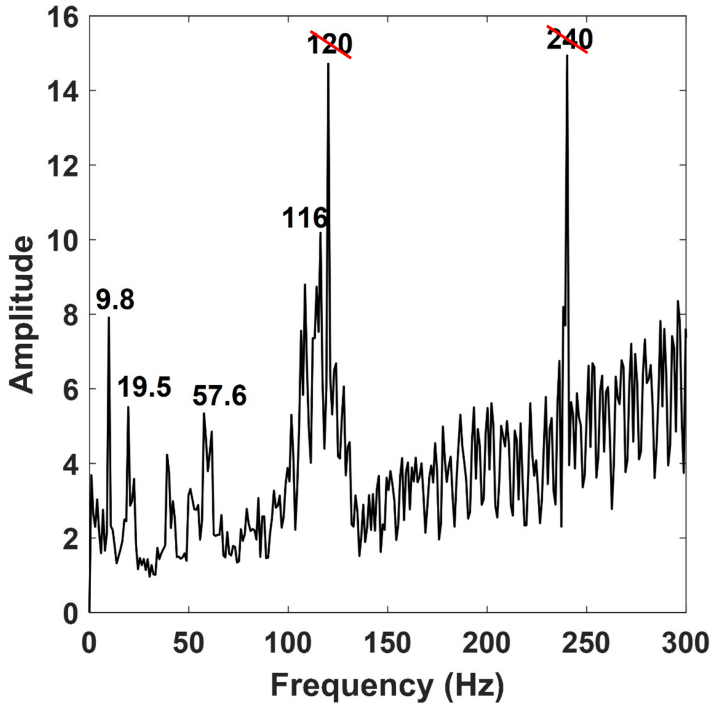

Figure 5.2: Frequency spectrum of strain signal at 200 RPM.

The data from the strain test was first subtracted by the strain of the baseline case. The subtracted raw strain data from the strain rosette at the top surface of 30%R are shown in Figure 5.3. These strain data of gauge 1-3 were measured in the local axis (Figure 5.4), then they were transformed to axial ϵ_{xx}, chordwise ϵ_{yy}, and in-plane shear γ_{xy} strain using Equation (2.3).

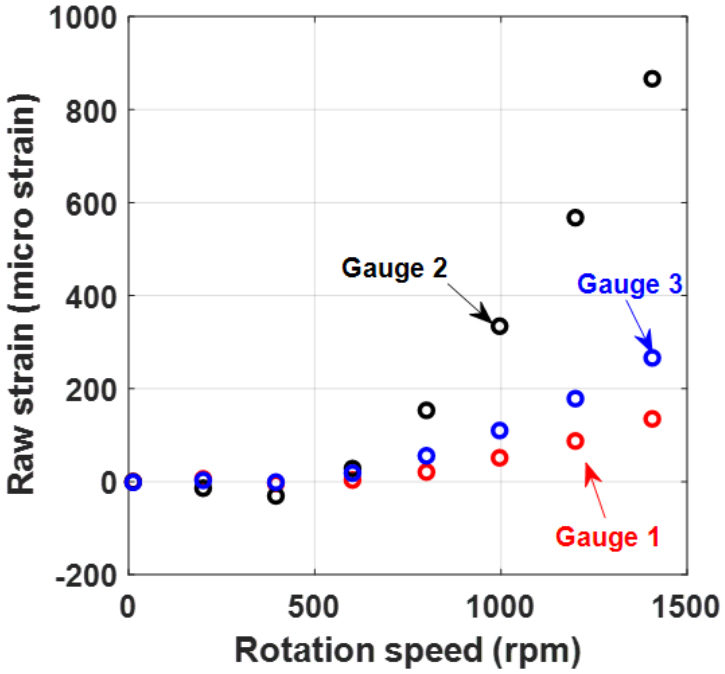

Figure 5.3: Raw strain signals.

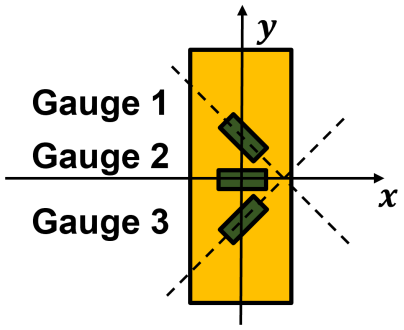

Figure 5.4: Strain rosette diagram.

5.1.3 Data Analysis and Model Validation

The measured frequencies and the X3D predictions are shown in Figure 5.5. The markers represent measured frequencies, and the different colors correspond to different blades. Up to seven non-rotating frequencies and six rotating frequencies were captured. The vacuum chamber motor limits the rotor speed range. The solid

lines are the predicted frequencies. The dashed lines are the constant per-revolution frequencies. The 900 Nm/rad flap and lag root stiffness and the 75 Nm/rad pitch stiffness were considered in the prediction. The predictions match well with the test data except for the highest mode. The cross-over of the first two modes is also observed. By analyzing the mode shape in X3D, each mode was identified. The second lag frequency could not be measured. Due to the high lag stiffness, the test could not excite the second lag mode. The test data is documented in Appendix B.1

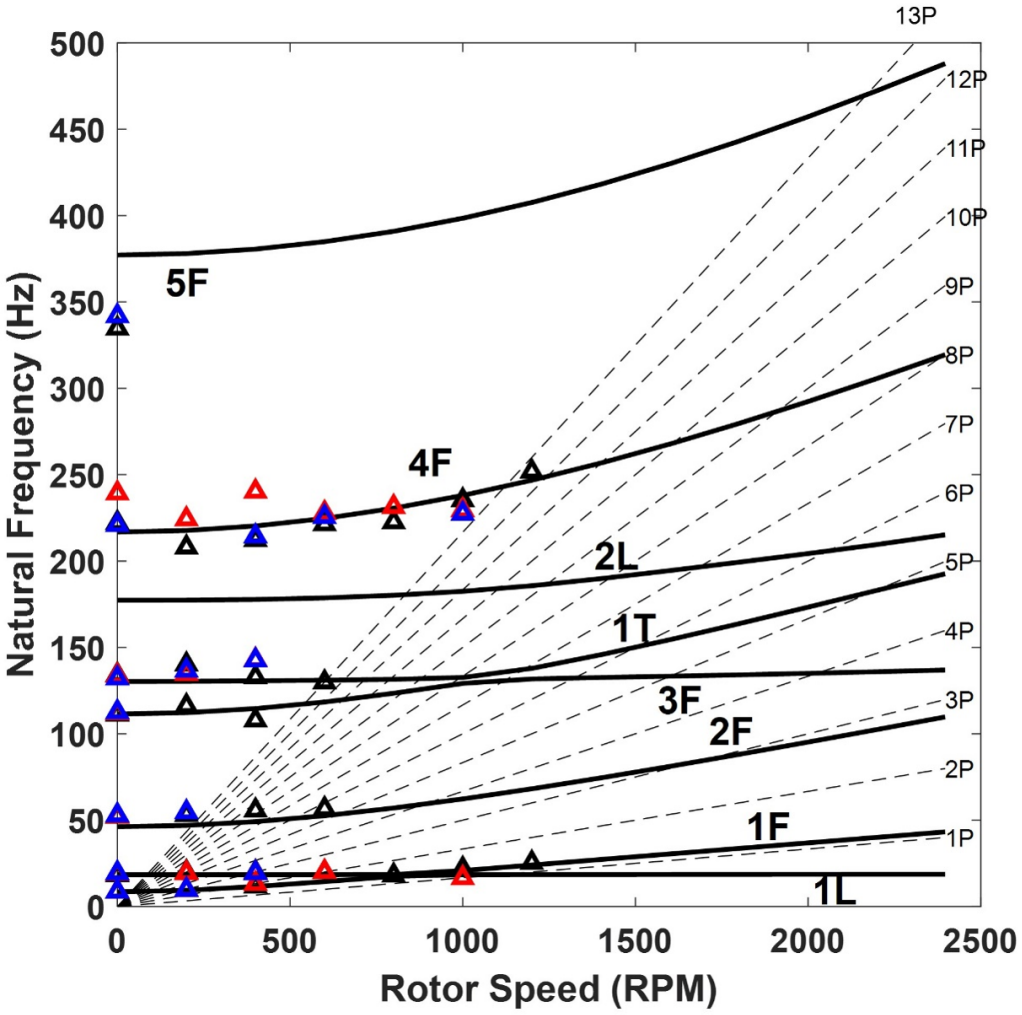

Figure 5.5: Fan plot of the double anhedral blade: symbols are measurements; solid lines are predictions.

The measured strains on the top surface at 30%R are shown in Figure 5.7. Axial ϵ_{xx}, chordwise ϵ_{yy}, and in-plane shear γ_{xy} strains were measured. Measurements from multiple blades are shown (markers). The error bars illustrate the differences introduced by $\pm 2^{\circ}$ of strain gauge misalignment. It can be seen that there is generally good repeatability between blades. However, large discrepancies are observed when comparing the data from the two arms (Figure 5.6). The X3D prediction is overlaid in the figure (lines). The solid lines are from the baseline model with no pre-cone angle. Examination of the discrepancies revealed that the vacuum chamber hub had in fact a -1° to -2° of pre-cone angle at the end block. When the pre-cone angle was included in the model (dash line), the agreement between test data and prediction became satisfactory. The predictions with pre-cones show that the 3-D structural model captures the impact of such un-intended imperfections.

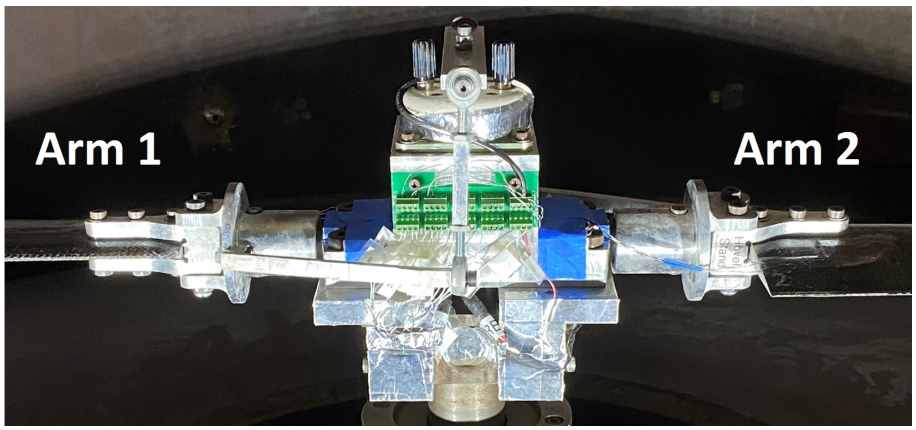

Figure 5.6: Arms of the vacuum chamber hub.

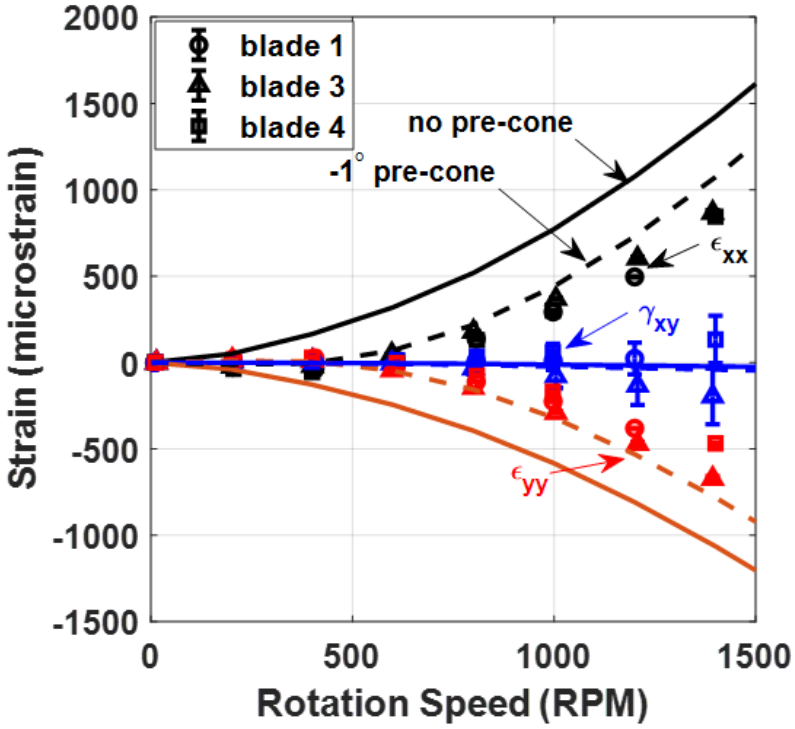

(a) Vacuum chamber hub arm 1.

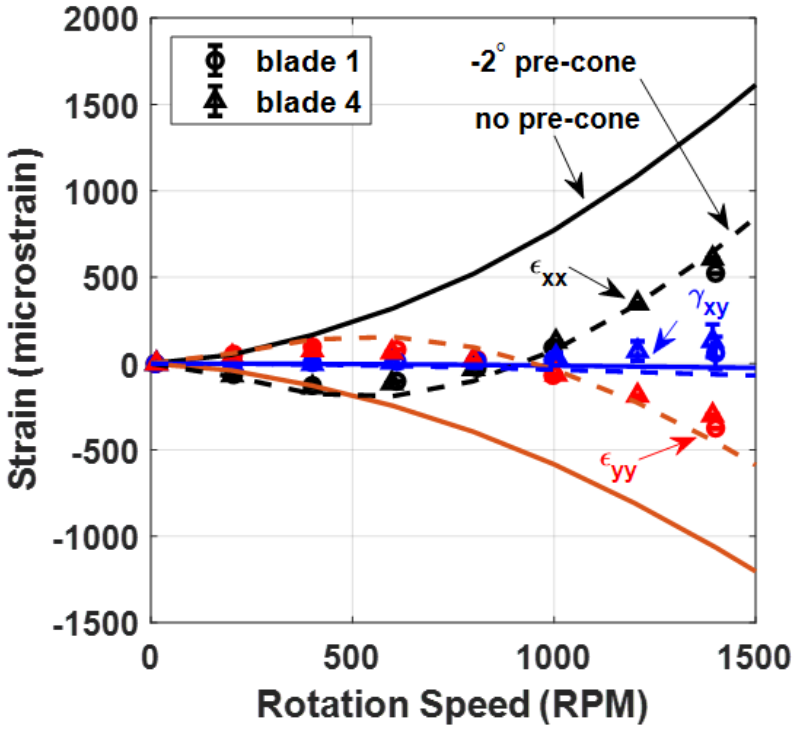

(b) Vacuum chamber hub arm 2.

Figure 5.7: Rotating strains on the top surface at 30%R: symbols are measurements; lines are predictions.

5.2 Hover Test

5.2.1 Test Procedure

The hover test procedure considers the following steps.

1. Stand sensors and actuators were connected directly to the National Instruments SCXI system. These stand sensors and actuators were a hub balance, a rotor speed sensor, an encoder, and three swashplate actuators. The rotating frame sensors were the four pitch sensors, four pitch link load cells, and a torque sensor. They were connected to the PCB in the hub cap. From these goes to the slipring and thereafter the data acquisition system. The encoder signal was calibrated against the azimuth angle by rotating the hub manually to acquire the relation shown in Figure 3.40. The hub cap was then closed and wires secured with tapes.

2. The motor hydraulic hoses were connected from the hydraulic pump to the hydraulic motor, the cooling inlet hose from the water tap to the hydraulic pump, and the cooling outlet hose from the hydraulic pump to the water sink. A simple motor check was performed. The hub (no blades yet) was spun up at the lowest controllable speed. The hydraulic pump temperature was monitored to see if the cooling system works properly. The temperature should remain below 100°F.

3. A rotor speed sweep from 300 to 2300 RPM was performed, and hub loads were recorded. The hub loads data was processed to look for the 1/rev component. Then counterweights were attached on the side of the hub cap to eliminate the 1/rev hub load. Tungsten alloy leading-edge weights were used as the counterweights (Figure 5.8). The counterweights must be secured carefully with aluminum tapes and superglue to withstand the enormous centrifugal force.

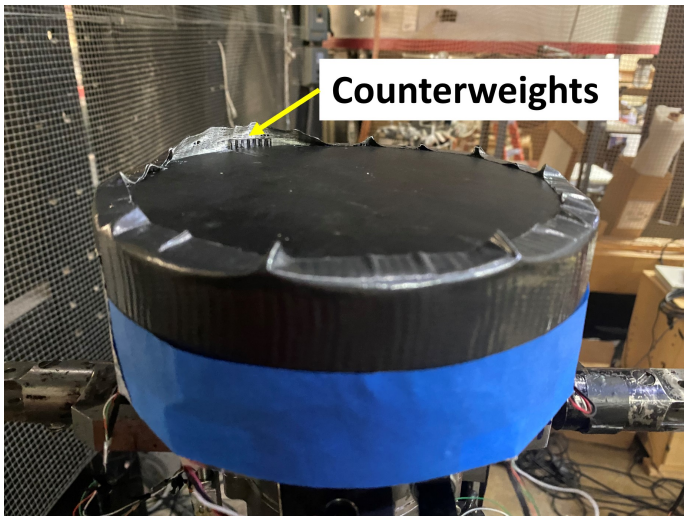

Figure 5.8: Hover stand hub balancing.

4. Tests to acquire hub tare data were performed. Hub tare data is hub loads of the isolated hub (no blades) at different rotor speeds. First, baseline hub load signals were saved. The baseline hub loads are the hub loads when the rotational speed is zero. Then the hub was spun up to a target rotor speed, and the hub loads were recorded. This step was repeated from 300 to 2300 RPM. The hub tare data was acquired by subtracting the baseline hub loads from the rotating hub loads.

5. The hover stand was moved up on the hover tower, which raised the rotor 12 ft (4.3R) about the ground out of the ground effect region. The high bay crane was used to lift the hover stand. Extra care should be taken in this step to keep the hover stand as well as the operators safe. Kevlar straps were lashed on the stand pole (near the center of gravity) and wrapped around the hub before being hooked on the crane. When the hover stand rested on the tower, the connection bolts were tightened.

6. The double anhedral blades were mounted on the blade grips with three shoulder bolts and locknuts with an external-tooth lock washer. Then the root pitch hall effect sensors were calibrated. The calibration method was described in section 3.2.2. After leveling the swashplate, the length of the pitch links was adjusted to equalize the pitch angles. The range of collective and cyclic angles is also determined by the length of the pitch links. Next, the blade sensors were connected to the hub cap PCB, and the signals were checked in the LabVIEW program before securing the sensor wires.

7. The blade tracking was performed. The objective of blade tracking is to ensure the aerodynamic similarity between blades. To this end, a tracking procedure was followed. Reflective tapes of different colors were attached to the blade tips, as shown in Figure 5.9. Then a high-intensity strobe light was placed on the outside frame in the hub rotating plane and pointed at the hub center. Due to the four-bladed configuration, the reflective tapes will appear to be frozen at a certain azimuth angle when the strobe frequency equals four times

the rotational frequency. As shown in Figure 5.10, four tapes overlap closely, indicating that the blades are well tracked. In other word, the tips are following the same path in space. Otherwise, adjustment of pitch link length is required, and the tracking process was repeated until all blades follow the same tip paths.

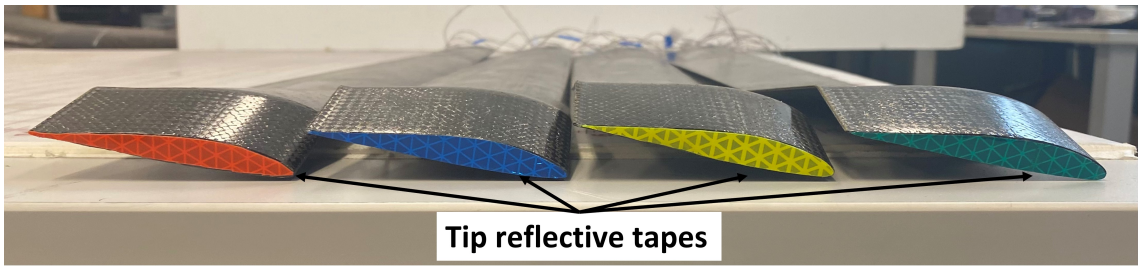

Figure 5.9: Reflective tapes for blade tracking.

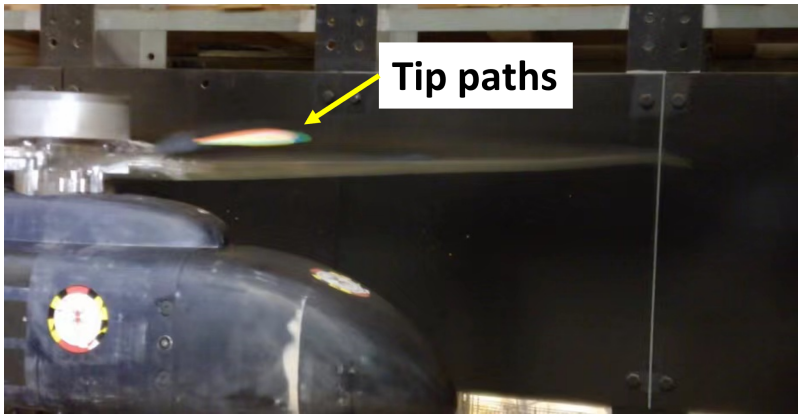

Figure 5.10: Blade tracking.

8. The last step before the rotor test was fuselage assembling. An existing 3D-printed fuselage was used as a fairing to shield the internal structure and improve the smoothness of the flow field. The fuselage was originally printed in four pieces: nose, two side panels, and tail, and at least two operators were needed to assemble it safely. The fabrication of the fuselage was not part of this research. The final hover test setup is shown in Figure 5.11.

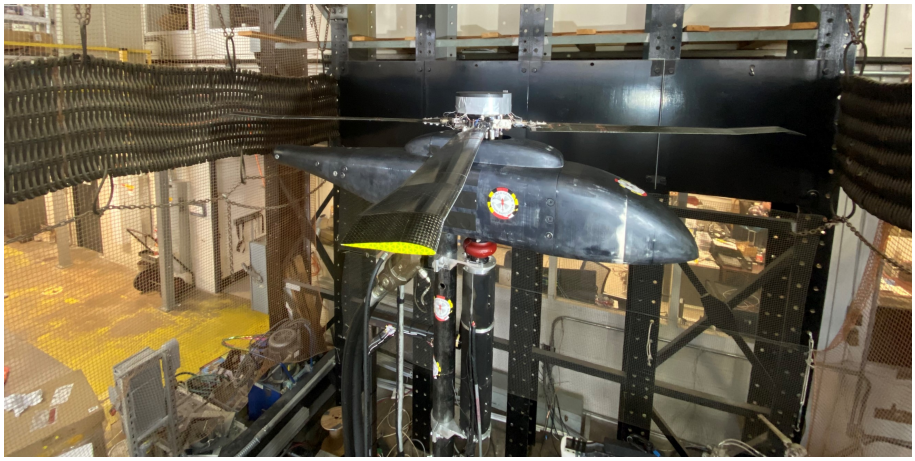

Figure 5.11: Final setup of the hover test.

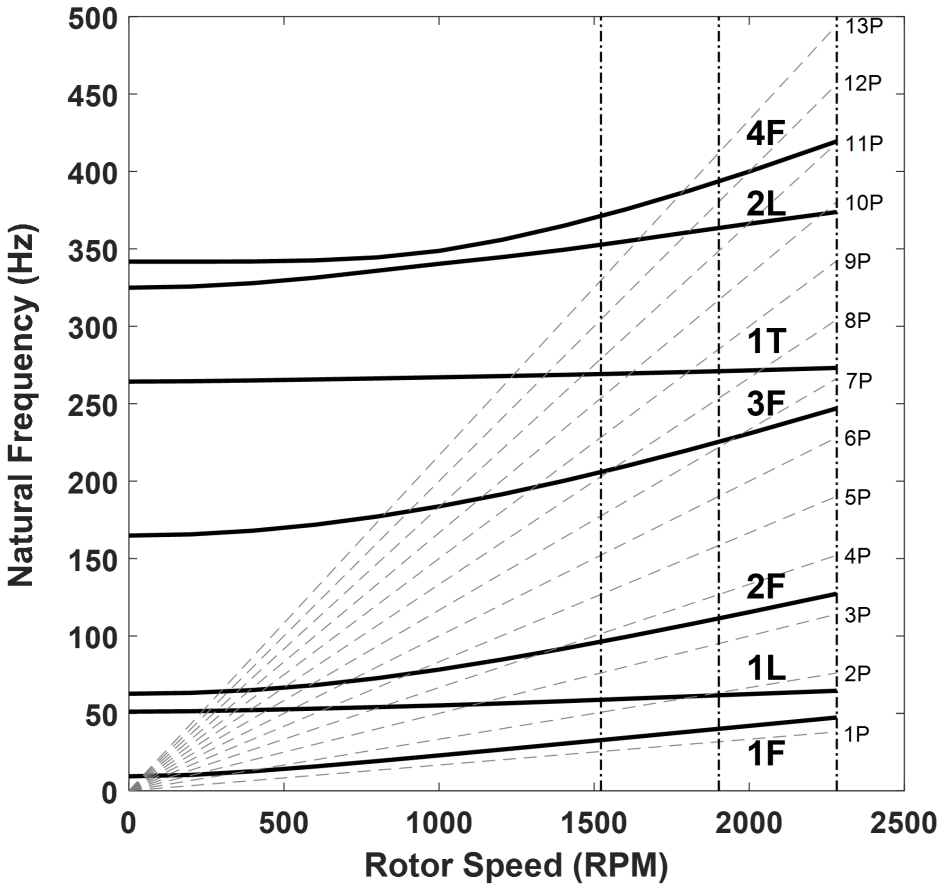

Figure 5.12: Fan plot of the hingeless rotor; the vertical lines are the RPM selected.

9. From the predicted fan plot (Figure 5.12), three rotor tip Mach numbers of 0.4, 0.5, and 0.6 were selected. The temperature and pressure were also measured.

10. Before the rotor was spun up, all of the sensor signals were recorded, and this case was used as a baseline. Then the rotor speed was increased to the target RPM. Once the rotor speed stabilized, the collective was adjusted to the desired value. While adjusting collective, the rotor speed might vary as well due to the change in rotor torque, hence, adjustment of the rotor speed was also needed. The rotor was trimmed with cyclic controls. For a hingeless rotor, it is hard to use blade flap motion as an indicator of rotor trim. In this test, the 1/rev flap bending moment was used as the trim target. The rotor was trimmed to minimize the 1/rev flap bending moment. Three seconds of data were saved before moving on to the next collective setting. During the test, the hydraulic pump temperature was kept below $140°F$.

5.2.2 Data Processing

The tip Mach number and blade loading envelope are shown in Figure 5.13. There are 80 test points in the collective sweep test. The raw data from each hover test point were stored in the form of voltage. The high-frequency harmonics ($\geq 100Hz$) were first removed by a low pass filter. There is a three-second time history record for each test point containing 76, 95, 114 revolutions for 0.4, 0.5, and 0.6 M_{tip} respectively. By clocking the signals to azimuth angles, multiple revolutions of data were merged to improve the signal-noise ratio. Then, the data from the

baseline case (the non-rotating case) were subtracted. The voltage signals were transferred to physical quantities by the calibration matrices. The hub tare data was subtracted from the hub loads, while an azimuth shift was performed for pitch link loads, blade loads, and blade stains.

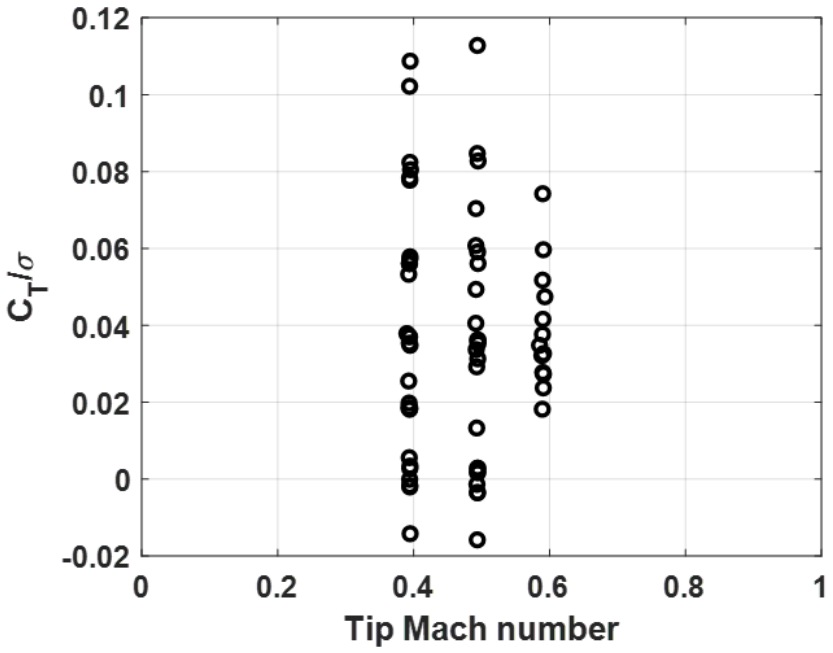

Figure 5.13: Hover test envelope.

5.2.3 Data Correlation with Prediction

The rotor hover performance is shown in terms of collective, thrust C_T/σ, and power C_P/σ. Figure of Merit (FM) is calculated from thrust and power. Figures 5.14 and 5.15 shown blade loading and power coefficient versus collective, respectively. The markers with different shapes are test data at different tip Mach numbers. The dashed lines are X3D predictions. It can be seen that the non-dimensional hover performance is not sensitive over this range of tip Mach numbers. The blade loading increases with collective linearly, and power grows quadratically.

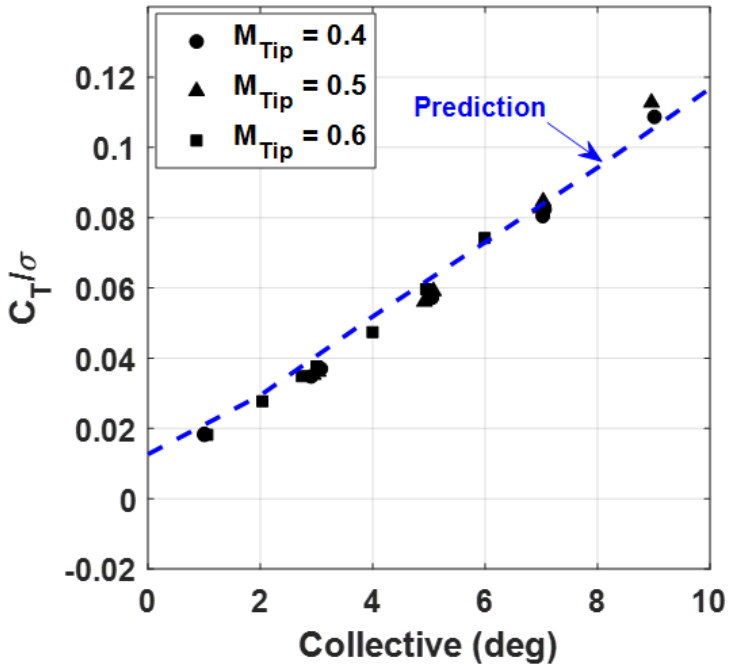

Figure 5.14: Blade loading vs. collective.

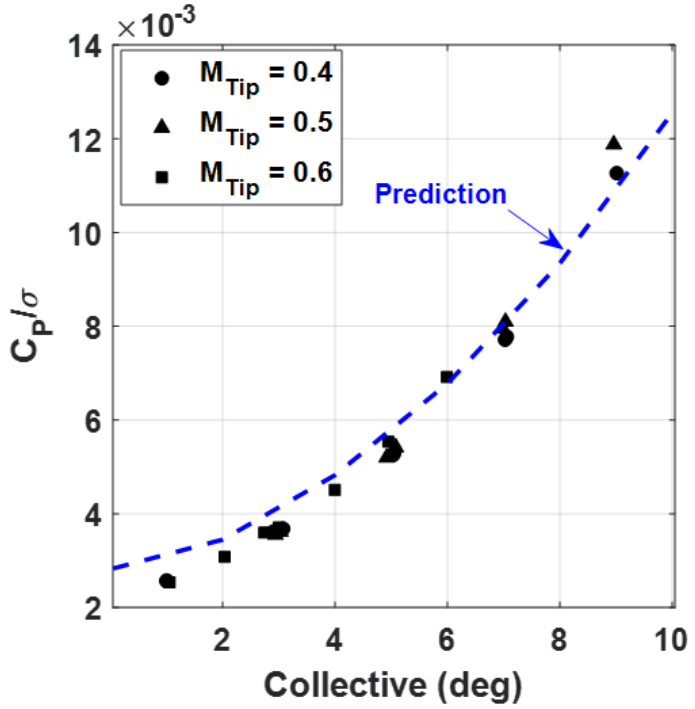

Figure 5.15: Power coefficient vs. collective.

Figure 5.16 plots power versus thrust, and the curve fit was used to acquire C_{d0} for analysis correction, which is 0.016. This model rotor is quite efficient as shown in Figure 5.17. There is no stall observed in the test range. And the maximum Figure of Merit (Equation (5.1)) is 0.713, which occurs at a blade loading of 0.117. Thus a high Figure of Merit can be achieved on a scale model rotor when properly designed. The agreement of test data and predictions is satisfactory. The test data is documented in Appendix B.2

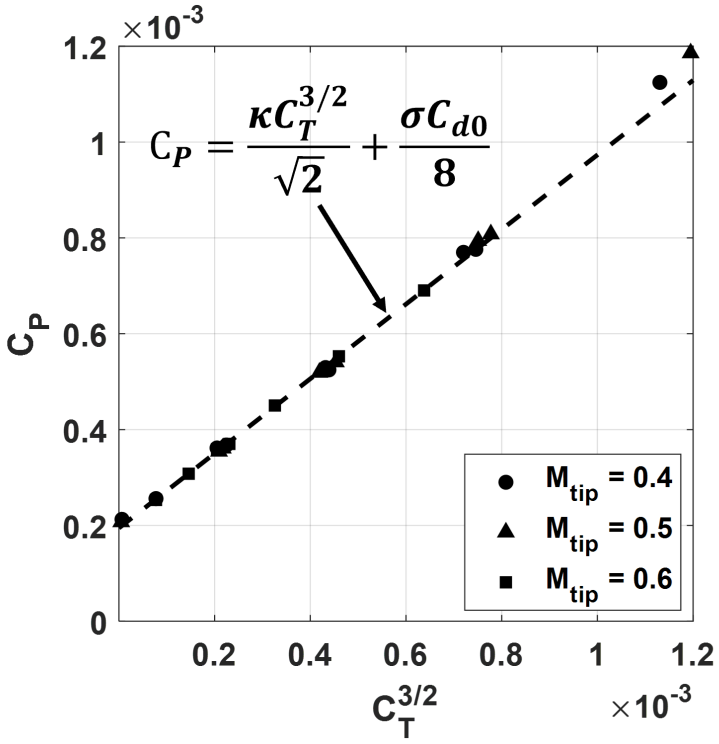

Figure 5.16: Power vs. Thrust.

$$FM = \frac{C_T^{3/2}/\sqrt{2}}{C_P} \tag{5.1}$$

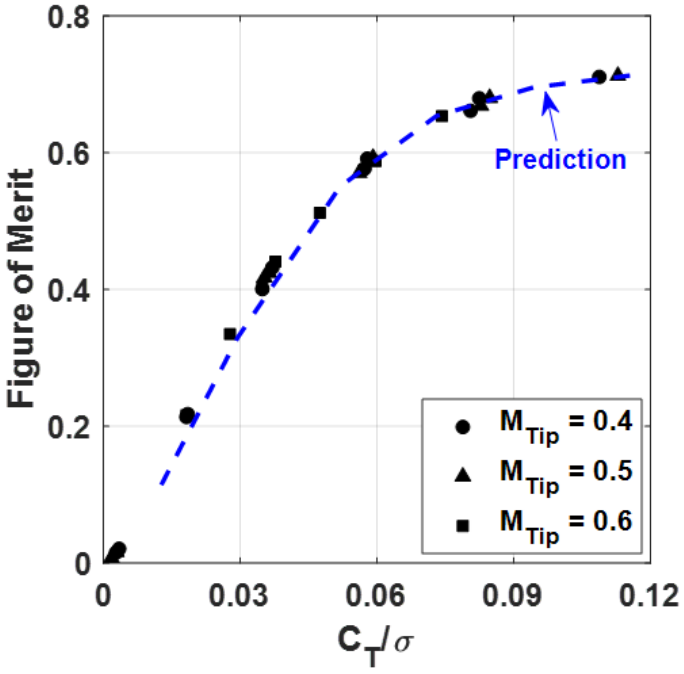

Figure 5.17: Figure of Merit vs. blade loading.

Blade flap bending moments measured at 40%R are shown in Figure 5.18. The test data is indicated by markers. Different colors represent different tip Mach numbers. The flap bending moment is positive when the blade bends up. The flap bending moment increases with collective due to the obvious increase in lift. But it decreases with tip Mach number due to an increase in the centrifugal force, which relieves the moment. The prediction captures the general trend. However, there is discrepancies in the magnitude.

Blade lag bending moments measured at 40%R are shown in Figure 5.19. Positive bending is toward the trailing edge. The magnitude of lag bending moment at 40%R shows no change with collective, but it increases with tip Mach number due

to increased drag. However, not significant enough to impact torque. The prediction of lag bending moments matches well with the measurements.

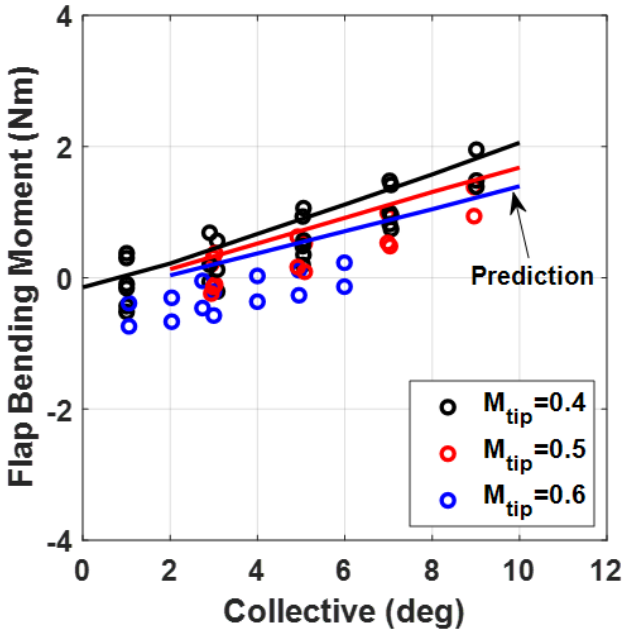

Figure 5.18: Flap bending moment at 40%R (test vs. prediction).

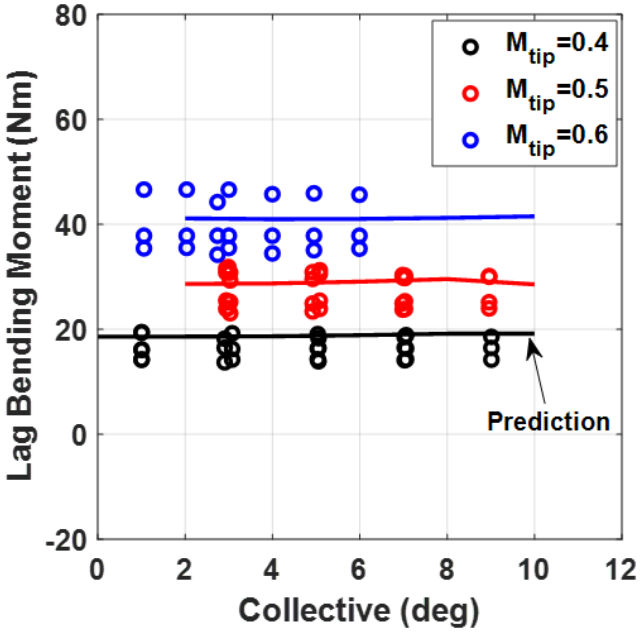

Figure 5.19: Lag bending moment at 40%R.

The torsional moment test data measured at 40%R, shown in Figure 5.20. It is also not sensitive to collective but grows with rotor speed. However, unlike lag, the prediction does not agree with the measurement. The absolute magnitudes are close, but the trend with tip Mach number is flipped. The positive values indicate a nose-up twist. Yet the pitch link loads are nose down in compression, as shown in Figure 5.21. Surprisingly the prediction here agrees with the measurement. The pitch link loads grow with both collective and Mach number. The agreement is reasonable, though not entirely satisfactory. Based on the agreement of flap, lag bending, and pitch link load, it is reasonable to assume the errors in torsional moment validation are from measurements, not prediction. There are discrepancies in the slope of the pitch link loads. More vacuum tests focused on torsion loads, and high-fidelity 3-D CFD aerodynamics is recommended to resolve the apparent mystery.

As discussed in section 4.4, the placement of 800 class nodesets had a large impact on the structural load extraction. The loads predicted in Figure 5.18-5.20 were extracted with the version-3 800 class nodesets shown in Figure 5.22 (same as version-3 Figure 4.37). These nodesets are intended to mimic the strain gauge placement in the test. However, as discussed in section 4.4, the loads calculated (test and prediction) based on strains extracted from these locations are contaminated with local strain concentration. Thus, though the extracted loads from version-3 nodesets have a satisfactory agreement with test data, this nodeset was not used in further analysis. The version-2 nodesets selected nodes avoiding concentration region was used instead, which give more physical structural loads.

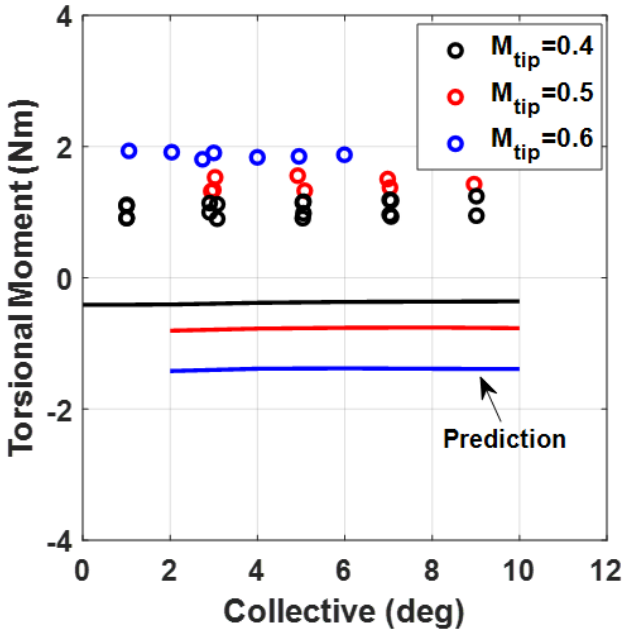

Figure 5.20: Torsional moment at 40%R.

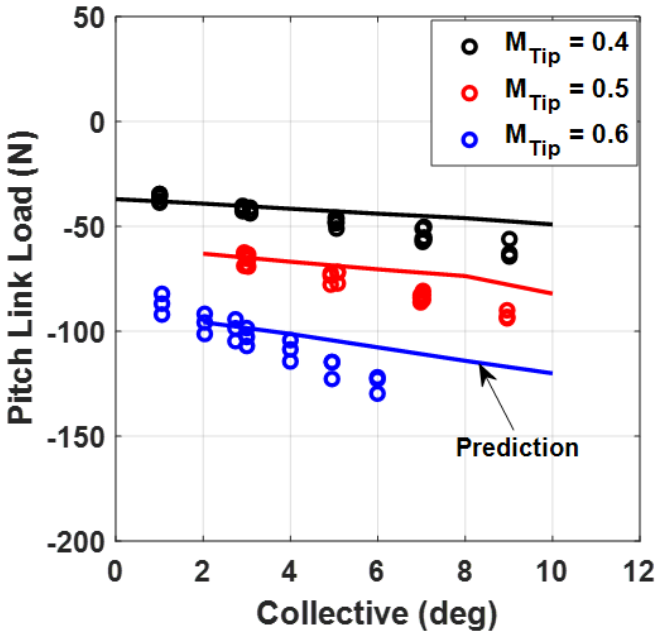

Figure 5.21: Pitch link load vs. collective.

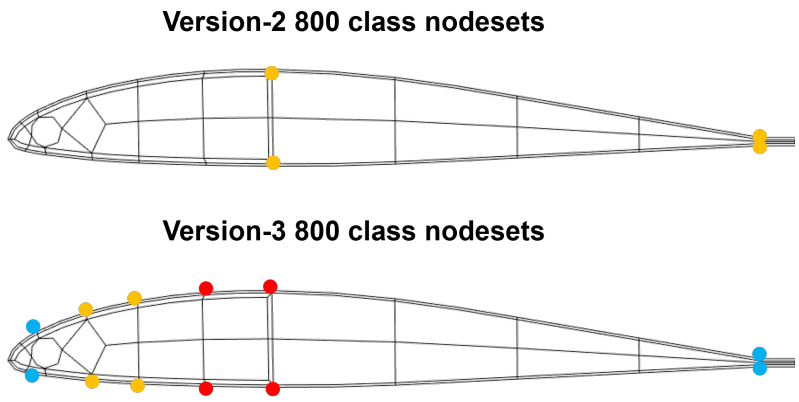

Figure 5.22: Two version of 800 class nodesets.

Measured Strains from the top surface at 30%R reveal a clear pattern (Figure 5.23). The axial strain ϵ_{xx} decreases as the collective angle increases. The extension generated by the centrifugal force is countered by the compression generated by the lift. As the tip Mach number increases, the centrifugal force outweighs that of the lift. Therefore, the axial strain increases. The chordwise strain behaves in the opposite fashion due to the local Poisson's ratio effect. The in-plane shear strain γ_{xy} always remains low. The solid and dash lines are predictions of two tip Mach numbers, respectively. The agreement is satisfactory as both magnitude and trends are captured.

Compared to the strain near the root, measured strains on the bottom surface at 80%R near the anhedral junction (Figure 5.24) are much lower and much harder to predict. The data is also more scattered due to the low magnitude. However, some trends can be identified. Both centrifugal force and the lift generate extension at this location, which of course, grows with the rotor speed. So the axial strain increases as the rotor speed increases. The magnitude of the in-plane shear is comparable to the normal strains. The agreement between prediction and test data degraded at

this location due to the generally low magnitude of strain. But the trend was still captured.

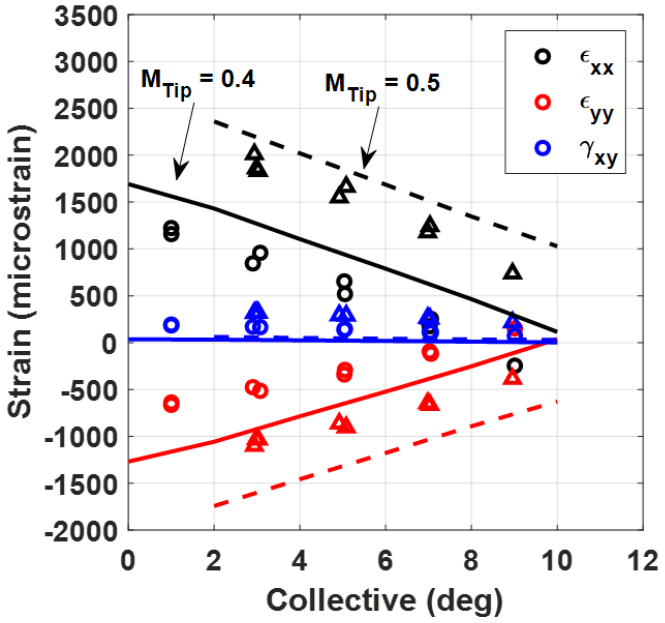

Figure 5.23: Mean Strain on the top surface of 30%R.

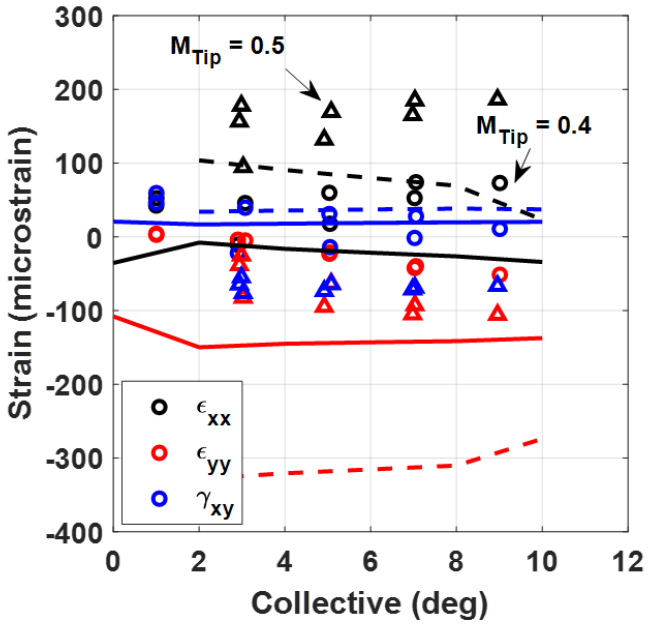

Figure 5.24: Mean Strain on the bottom surface of 80%R.

5.3 Summary

In this chapter, the vacuum chamber test and hover test results were described. The test procedure of the vacuum chamber test and hover test as well as the data processing method were described in detail. Blade natural frequencies and surface strains were measured in the vacuum chamber test. Rotor performance, structural loads, and strains were measured in the hover test. The test data was used to validate the 3-D blade model developed in Chapter 4. The 3-D blade structural model is validated with the measured fanplot and strains. The prediction of rotor performance, flap bending moment, lag bending moment, pitch link load, and surface strains are satisfactory. Strain-load calibration revealed the importance of sensor placement. Complex blades have regions of strain concentration and these are to be avoided. The torsional moment and pitch link load were inconsistent. More vacuum tests and 3-D CFD analyses are recommended to understand this behavior. At this point, the 3-D blade model is ready for further analysis of the influence of the double anhedral tip.

Chapter 6: Comparison of Straight and Double Anhedral Blades

The comparison of the straight and double anhedral rotor is analyzed in this chapter. Due to the lack of resources and the closure of the Glenn L. Martin wind tunnel, no straight blades could be built, and no forward flight tests could be carried out. So analysis remained the only option available for comparison. A straight rotor model is used as a baseline for comparison (Figure 6.1). Frequency, performance, structural loads, and strain/stress are studied.

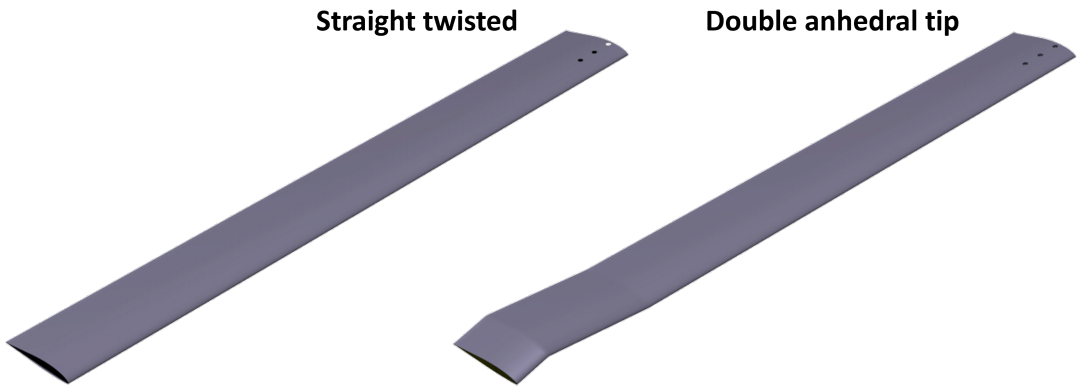

Figure 6.1: Straight and double anhedral blades; same twist of $-16°$

6.1 Blade Natural Frequencies and Mode Shapes

The influence of the double anhedral tip on natural frequencies is shown in Figure 6.2. These frequencies are generated using the 3-D structural model while assuming the blade roots are rigid and the collective pitch at 75%R is zero. The solid lines are the double anhedral blade frequencies, whereas the dotted lines are the straight blade frequencies. Both blades have the same twist. The thin dashed lines are constant per-revolution frequencies. There is a negligible difference in the first frequency. The effect of the tip geometry starts to show from the second frequency and becomes significant in all higher frequencies thereafter. The double anhedral blade frequencies are lower than the straight blade frequencies. The local center of gravity offset in the normal direction at the tip appears to make the blade softer.

The dominant motion in each mode can be identified by examining the mode shape. A comparison of the first five mode shapes at 1522 RPM is shown in Figures 6.3-6.12. The first frequency of the straight and double anhedral blades are 1.32/rev and 1.29/rev respectively. The mode shapes of both are dominated by flap bending. Due to the twist, there is also some lag motion in the first mode but it is small (Figure 6.3 and 6.4, see side view). Mode two is the first lag mode (Figure 6.5 and 6.6). Here the lag motion is clearly visible. Mode three is the second flap (Figure 6.7 and 6.8), and mode four is the third flap (Figure 6.9 and 6.10). Mode five is the first torsional mode (Figure 6.11 and 6.12). Since the magnitude of mode shape is arbitrary, the direction of twist is immaterial. The main conclusion is that the double anhedral tip does not appear to introduce any new mode or coupling. It is

the frequencies that differentiate the designs.

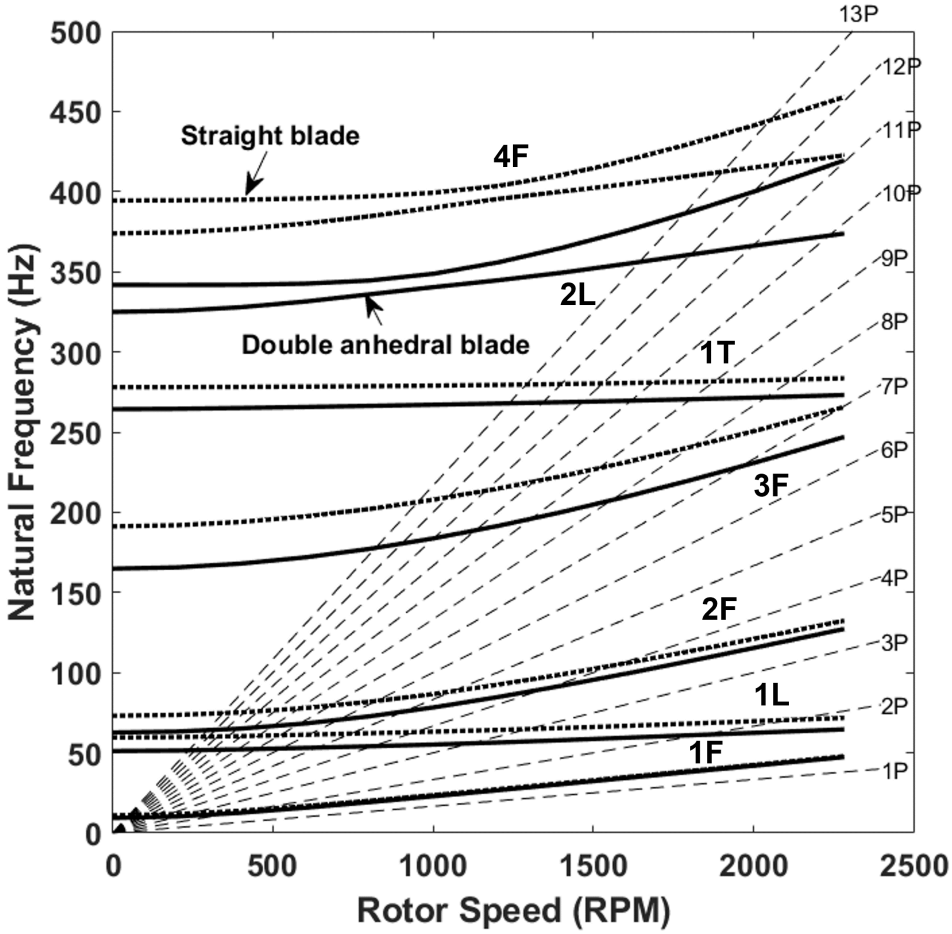

Figure 6.2: Fan plot of straight blade (solid lines) compared to double anhedral blade (dotted lines). Rigid root, $\theta_{75} = 0°$.

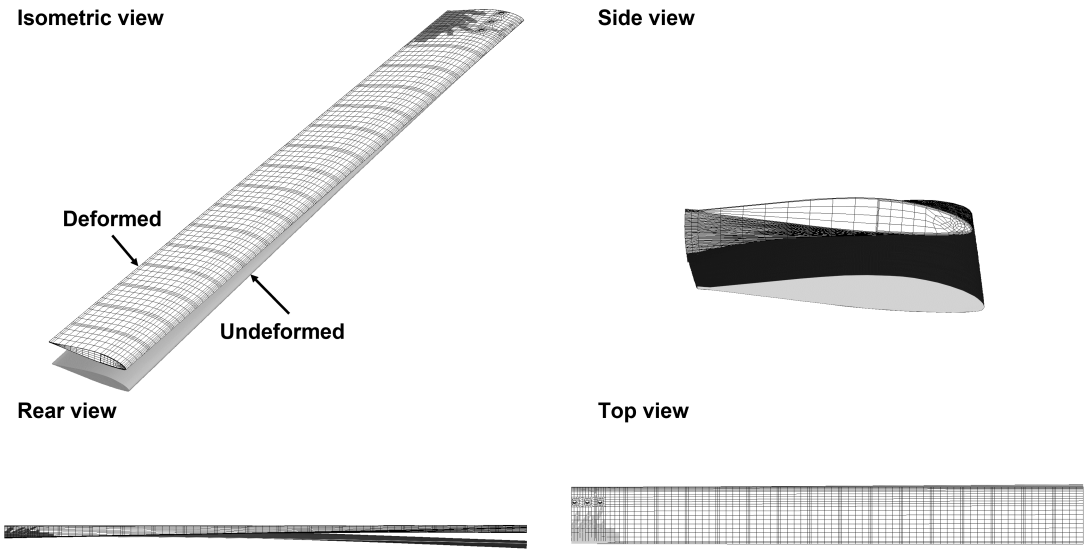

Figure 6.3: Straight blade mode 1; first flap (1.32/rev).

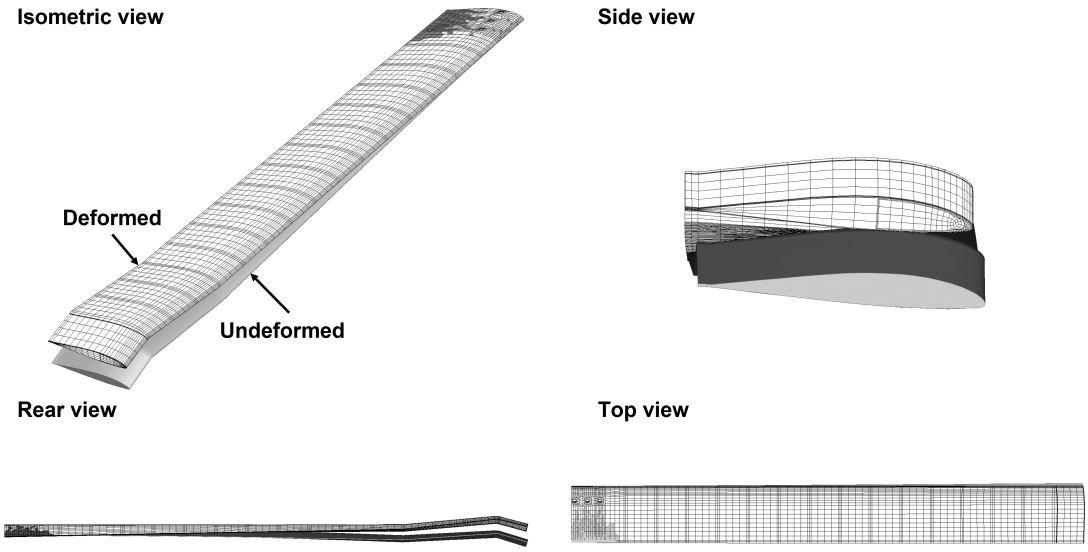

Figure 6.4: Double anhedral blade mode 1; first flap (1.29/rev).

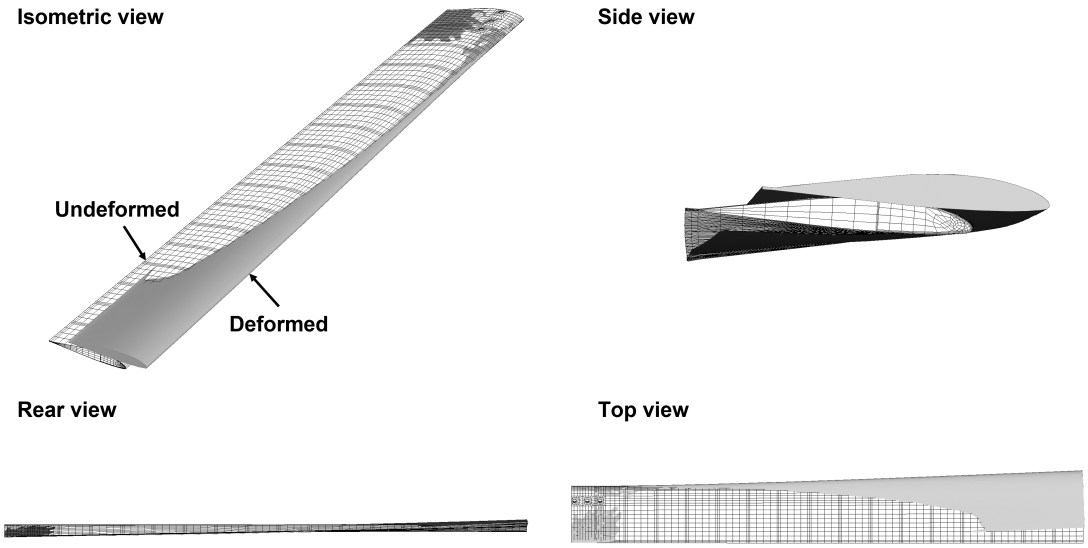

Figure 6.5: Straight blade mode 2; first lag (2.62/rev).

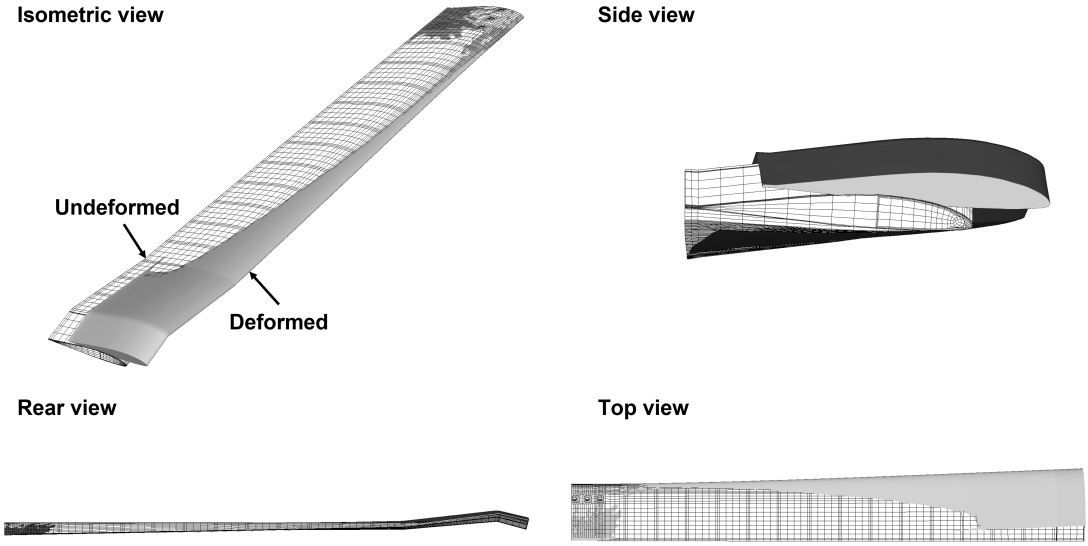

Figure 6.6: Double anhedral blade mode 2; first lag (2.32/rev).

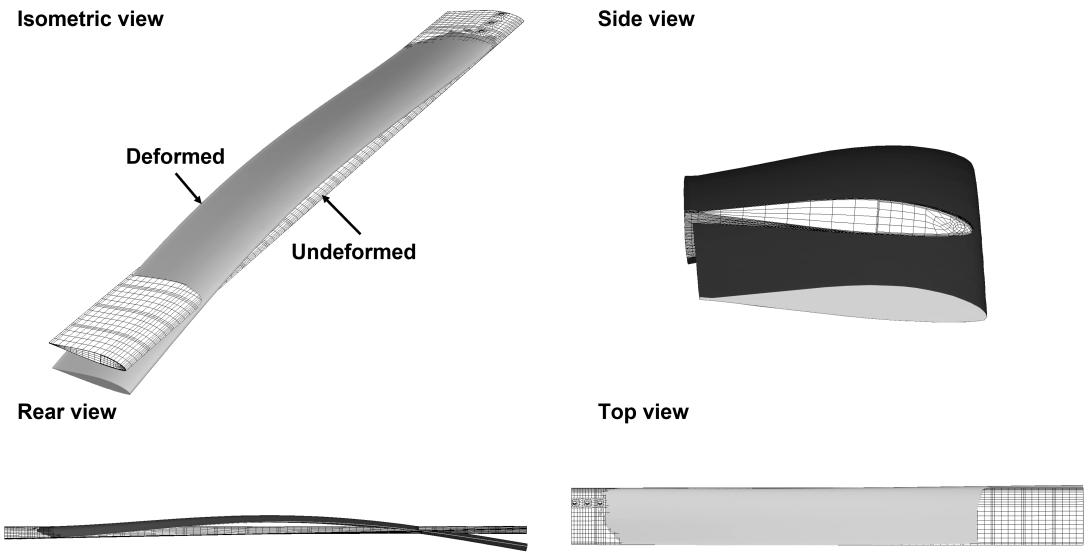

Figure 6.7: Straight blade mode 3; second flap (4.07/rev).

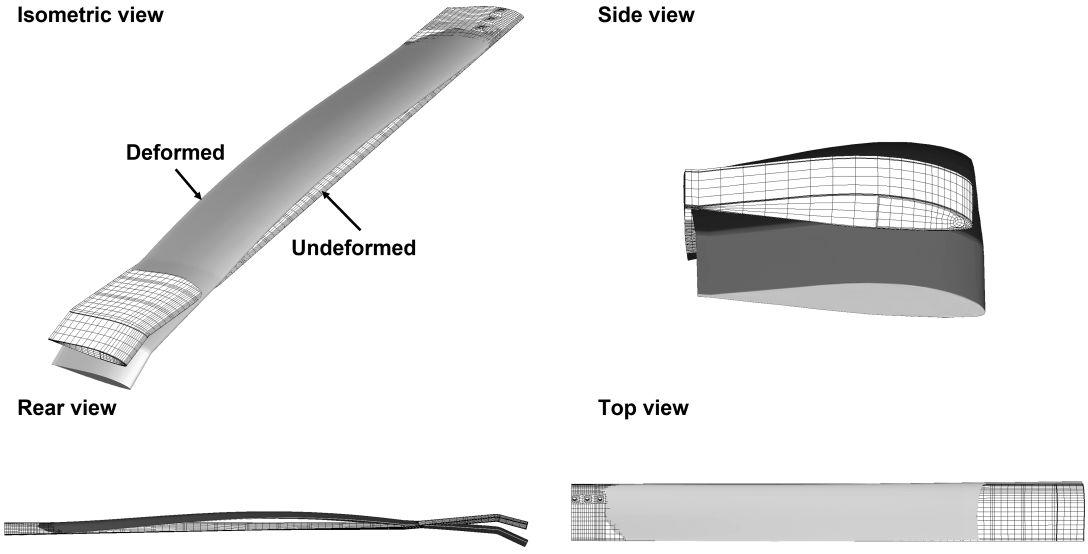

Figure 6.8: Double anhedral blade mode 3; second flap (3.8/rev).

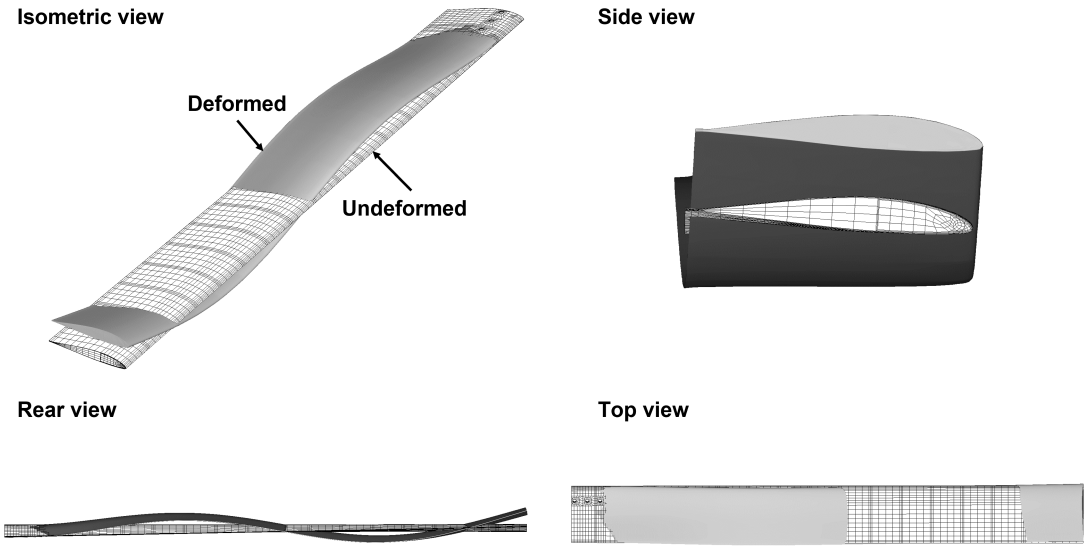

Figure 6.9: Straight blade mode 4; third flap (8.9/rev).

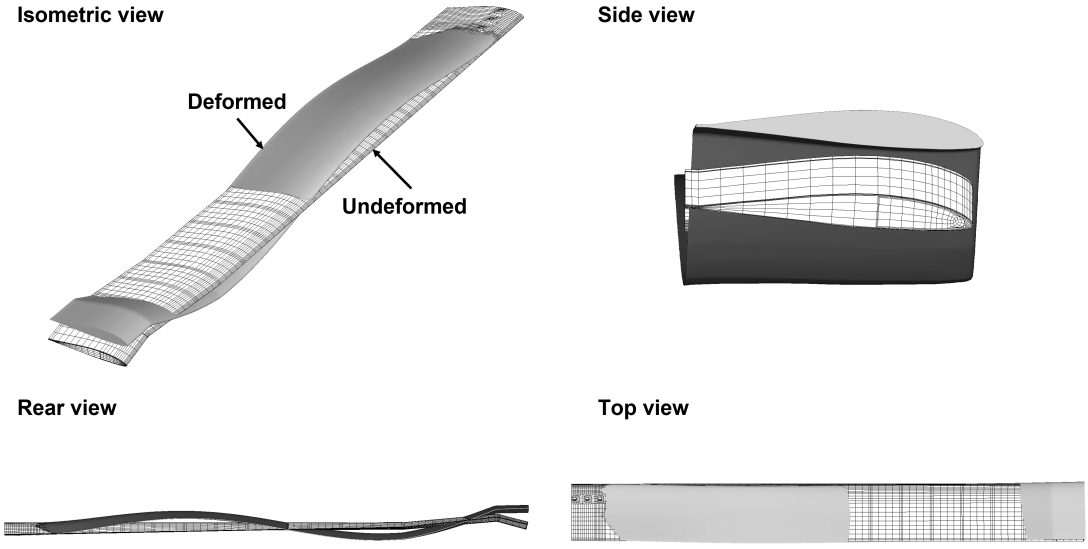

Figure 6.10: Double anhedral blade mode 4; third flap (8.12/rev).

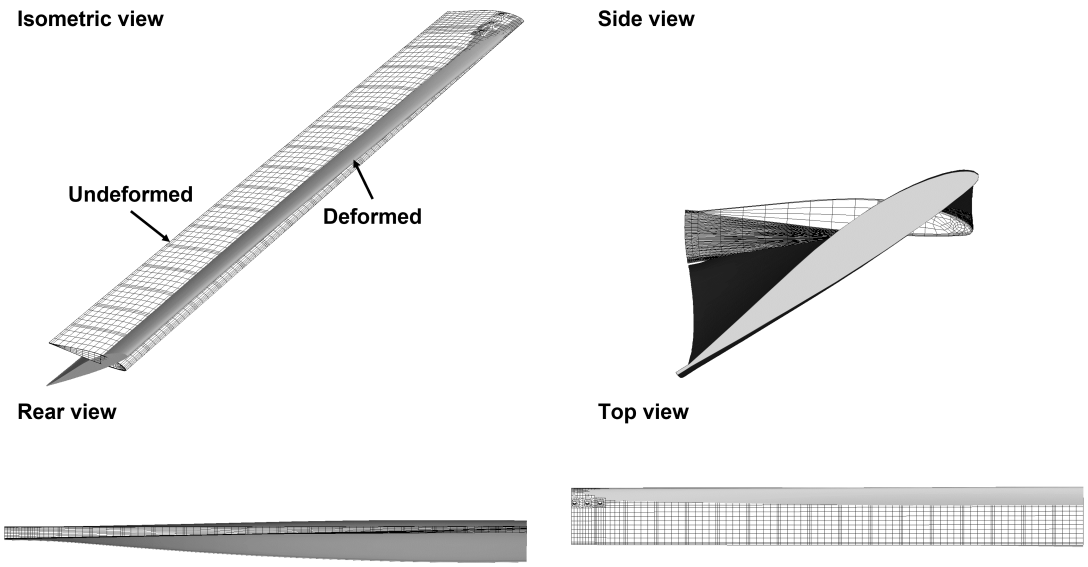

Figure 6.11: Straight blade mode 5; first torsion (11.07/rev).

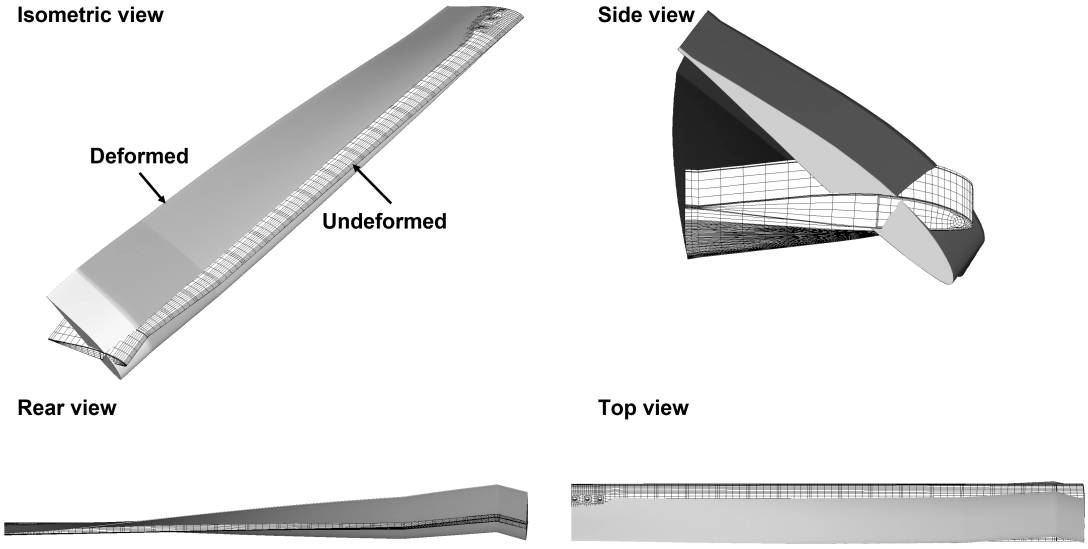

Figure 6.12: Double anhedral blade mode 5; first torsion (10.64/rev).

6.2 Strains in Vacuum

The straight and double anhedral blades have markedly different strain distributions. The strain distributions in vacuum at a speed of 1522 RPM and a collective of 0° are shown in Figures 6.13-6.17. The comparison of axial strain ϵ_{xx}, in-plane shear strain γ_{xy}, and out-of-plane strain ϵ_{zz} are presented. The indices refer to the rotating frame coordinate: the X-direction is oriented axially along the radius of the un-deformed blade and positive toward the tip, the Z-direction is pointing vertically upward in the direction of nominal thrust, and the Y-direction follows the right-hand rule, hence in the rotating plane pointing in the direction of the leading-edge. In each figure, the left-hand sub-figure shows the surface strain distribution, and the right-hand sub-figure shows the cross-section strains at 30%R, 50%R, 80%R, and 95%R along with the strains in the D-spar. It can be observed that there are strong 3-D patterns in the strains. Due to the centrifugal force, the axial strain decreases from the root toward the tip. The strain concentrations near the leading-edge are caused by the discrete leading-edge weights. The root axial strain of the double anhedral blade is much higher than the straight blade (Figure 6.13 and 6.14). The double anhedral blade also has a compression region at the dihedral junction. Both of these phenomena are caused by the vertical center of gravity (C.G.) offset of the double anhedral tip, which introduces an additional bending moment via centrifugal force.

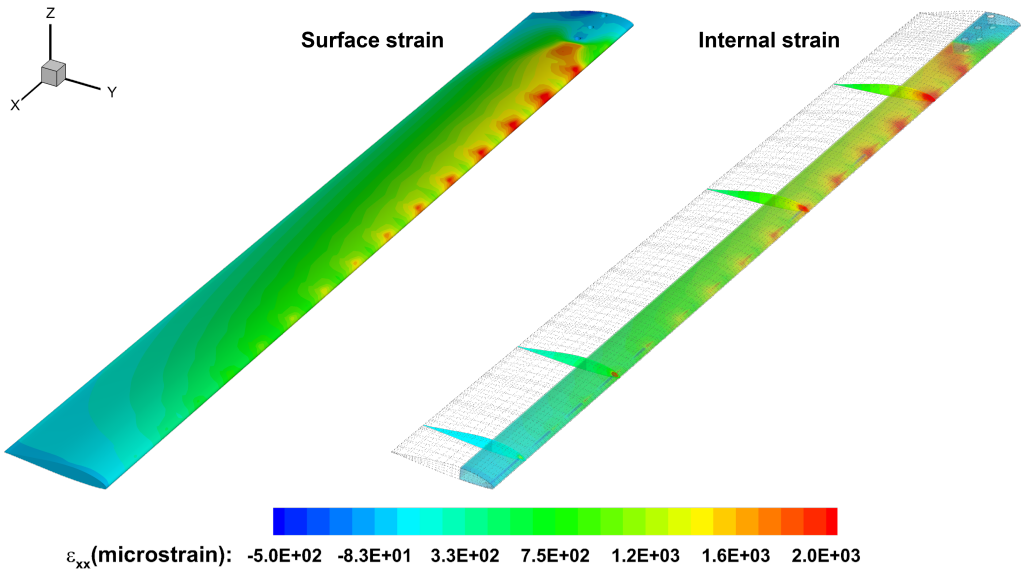

Figure 6.13: Predicted axial strain ϵ_{xx} distribution in vacuum for straight blade (1522 RPM).

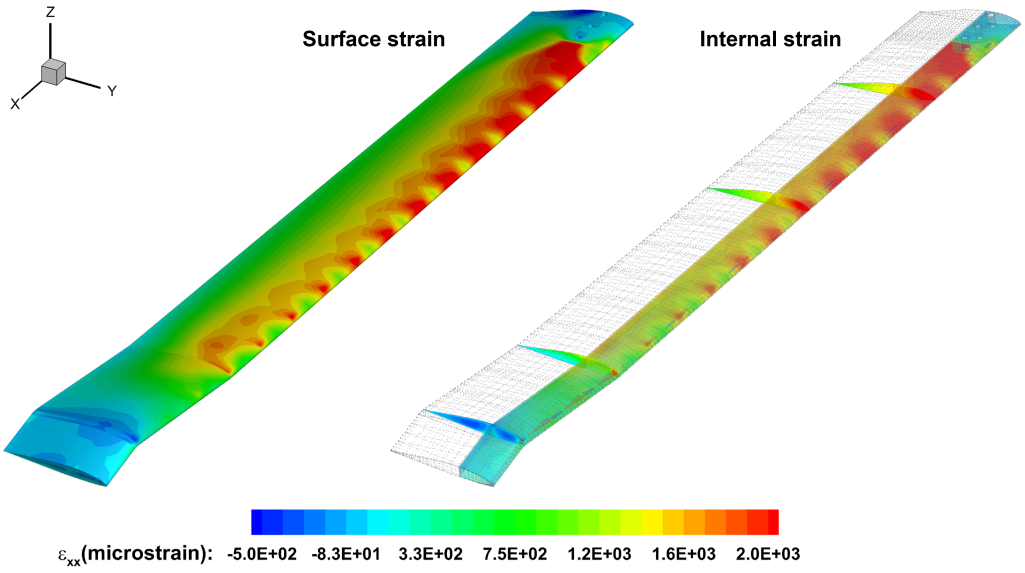

Figure 6.14: Predicted axial strain ϵ_{xx} distribution in vacuum for double anhedral blade (1522 RPM).

The in-plane shear strain (Figure 6.15 and 6.16) magnitudes are small in both blades. A pair of strain concentration zones occur at the top surface near the root of both blades. The shear strain reflects that there is a torsional moment near the root. This torsional moment is the propeller moment. Moving outboard, there is limited impact of the tip geometry on the strain patterns. From midspan to the tip, the D-spar carries most of the shear strain. At the tip of the double anhedral blade, strain concentrations appear in the dihedral portion. These concentrations indicate that the C.G. offset also introduces additional propeller moment. Figure 6.17 compares the out-of-plane strain distribution. Out-of-plane strain can represent inter-laminar strain to a certain extent. This type of strain is important in a composite material as it relates to delamination. There is no out-of-plane strain on the surface, naturally only the internal strain is shown. The out-of-plane strain only increases at the dihedral and anhedral junctions. The absolute magnitude is still too low to be of any concern.

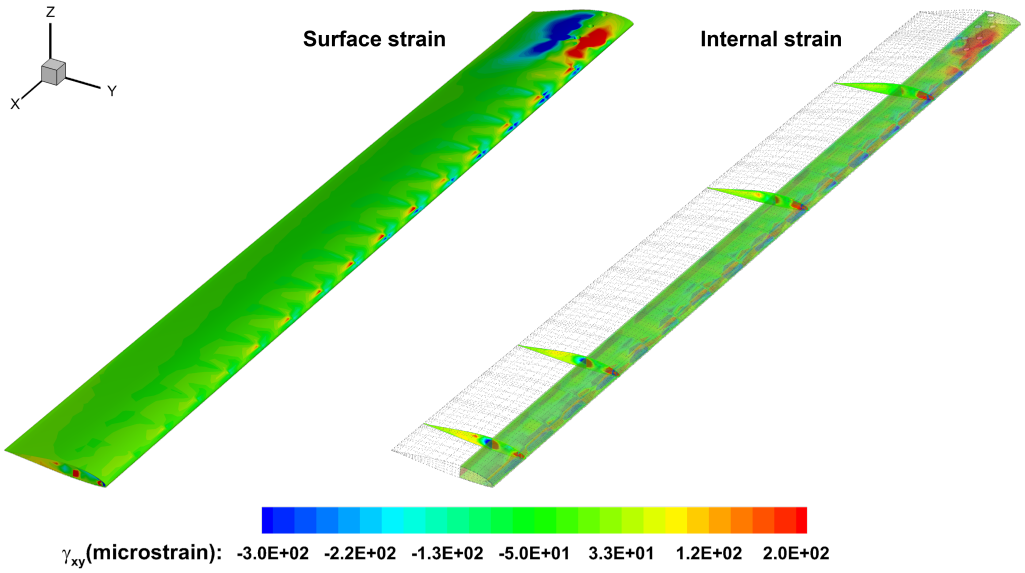

Figure 6.15: Predicted in-plane shear strain γ_{xy} distribution in vacuum for straight blade (1522 RPM).

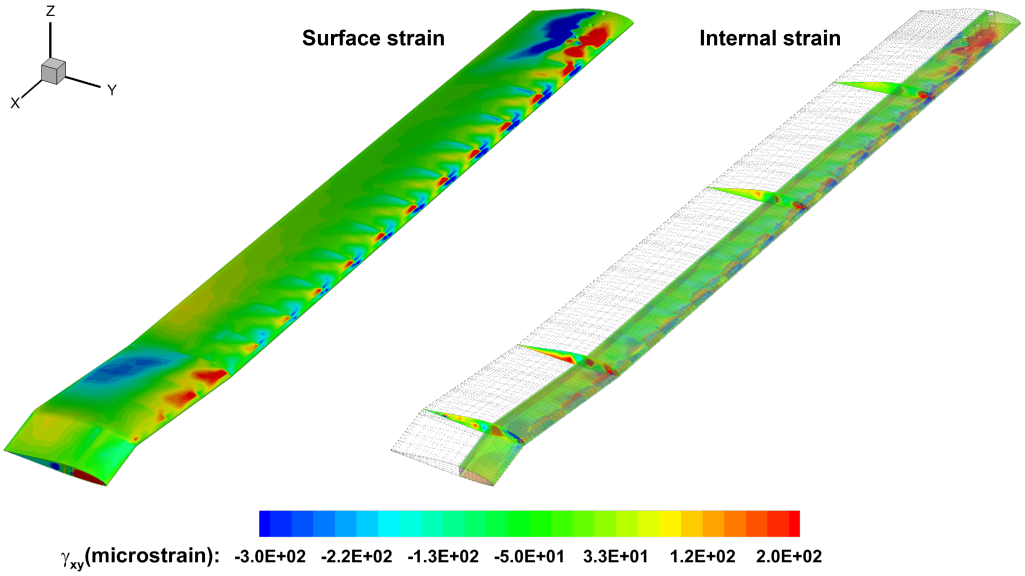

Figure 6.16: Predicted in-plane shear strain γ_{xy} distribution in vacuum for double anhedral blade (1522 RPM).

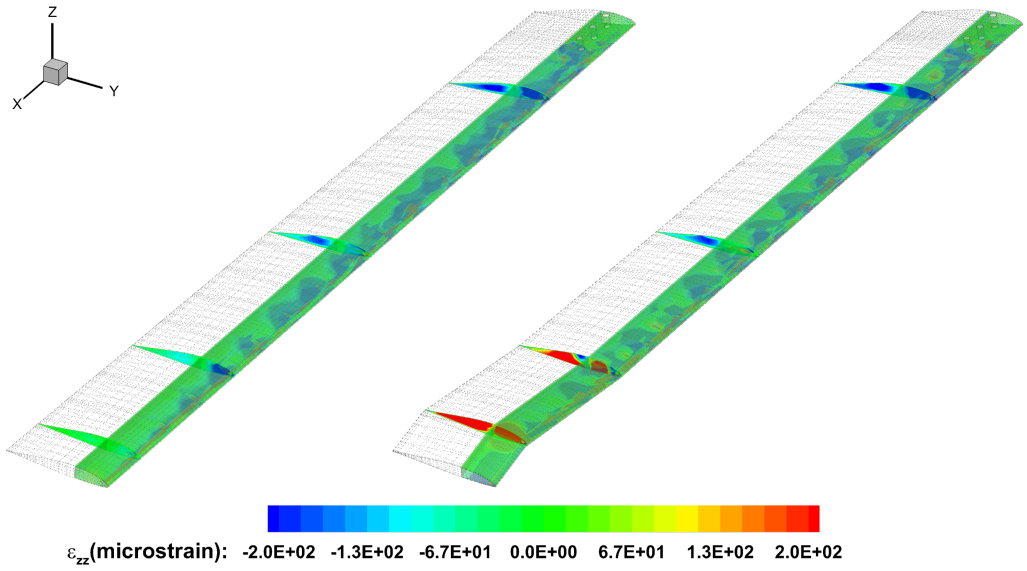

Figure 6.17: Predicted out-of-plane strain ϵ_{zz} distribution in vacuum (1522 RPM; left: straight blade; right: double anhedral blade).

6.3 Hover Analysis

6.3.1 Rotor Performance

Hover performance is presented as power coefficient (C_P/σ) and Figure of Merit (FM) variation with blade loading (C_T/σ). As shown in Figure 6.18 and 6.19, the influence of the double anhedral tip on the power coefficient is negligible, and the highest Figure of Merit is improved by a minuscule 0.7% near the blade loading of 0.117. This might simply be an artifact of the essentially 2D nature of the lifting line model. More differences might occur when 3D CFD is brought to bear instead of freewake model.

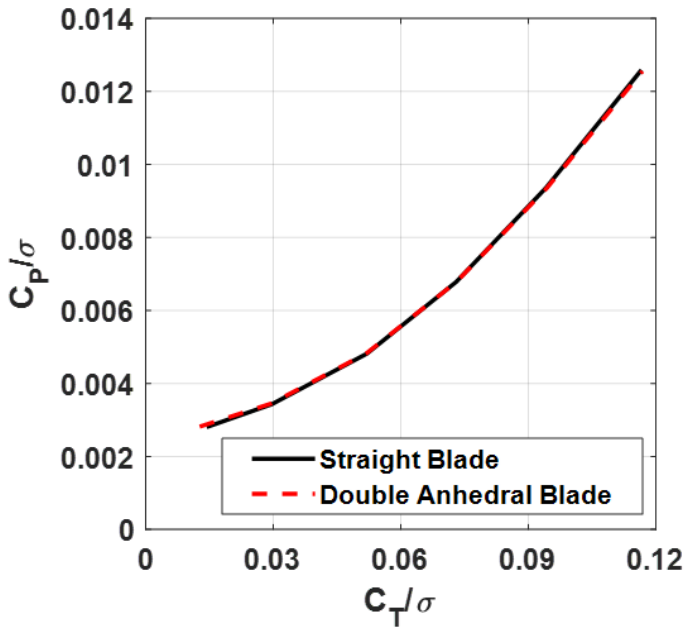

Figure 6.18: Power versus blade loading. $M_{tip} = 0.4$.

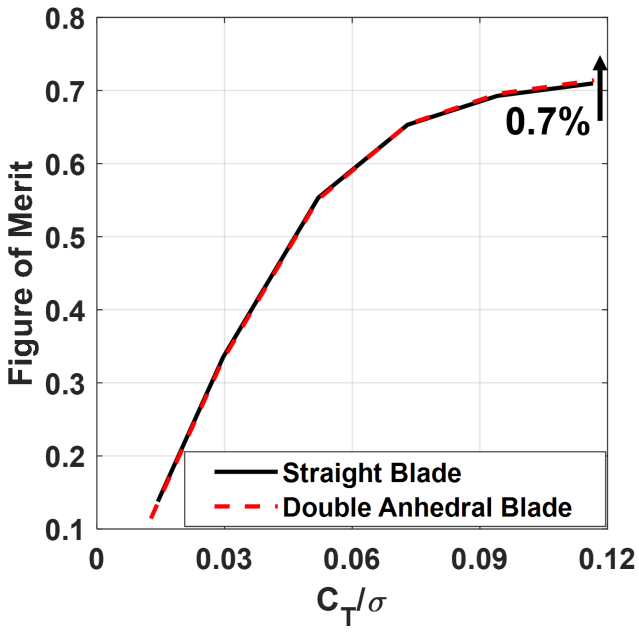

Figure 6.19: Figure of Merit versus blade loading. $M_{tip} = 0.4$.

6.3.2 Blade Structural Loads

Figure 6.20 shows the axial force at 30%R, 50%R, and 70%R. The solid lines represent the straight blade, while the dash lines represent the double anhedral blade. The axial force is mainly the centrifugal force, hence, it decreases from root to tip as expected, and it is not sensitive to the collective angle. The axial force on the double anhedral blade is slightly higher because the tip mass of the double anhedral blade is slightly higher.

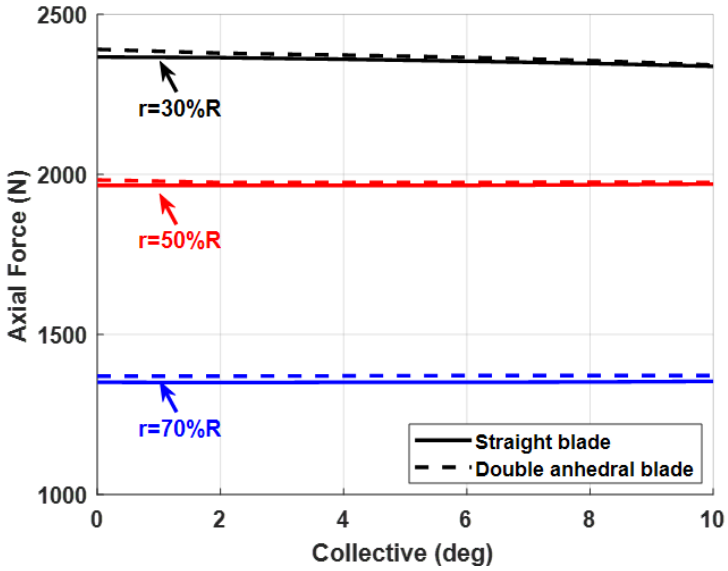

Figure 6.20: Comparison of axial force.$M_{tip} = 0.4$.

In Figure 6.21, the flap bending moment at inboard (30%R), midspan (50%R), and outboard (70%R) are compared. The positive flap bending moment indicates a bending up. The flap bending moments near the root increase with collective due to the obvious increase in lift. Moving outboard, the flap bending moment of the straight blade decreases, and the sensitivity to the collective also reduce.

For the double anhedral blade, the bending moment is always lower, and at the outboard portion significantly downward. The lack of variation with collective indicates that the difference is not due to aerodynamics, but centrifugal force. As shown in Figure 6.22, the vertical C.G. offset of the double anhedral portion generates a centrifugal force which generates a downward bending moment. The inboard and midspan flap bending moment is reduced by this downward bending moment. The outboard moment is dominated by this downward moment.

The lag bending moment comparison is shown in Figure 6.23. The positive lag bending moment means the blade is bending toward the trailing edge. Compared to the straight blade, the lag bending moment of the double anhedral blade decreases substantially throughout the span. The reduction decreases outboard. This reduction is also related to the out-of-plane C.G. offset. At positive collectives, the vertical C.G. offset generates an aft-C.G. offset, as shown in Figure 6.24. This aft-C.G. offset generates a lead-lag moment via the centrifugal force, which counters the lag moment from the drag.

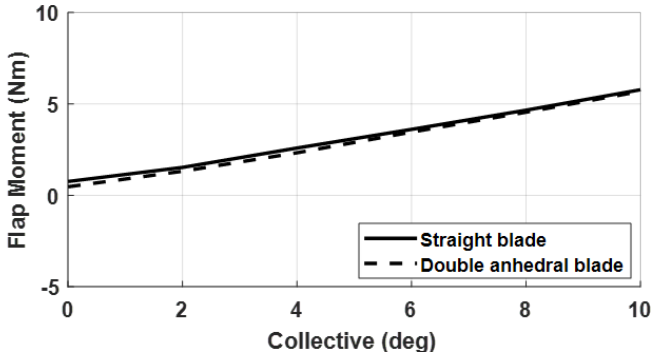

(a) Flap bending moment at 30%R.

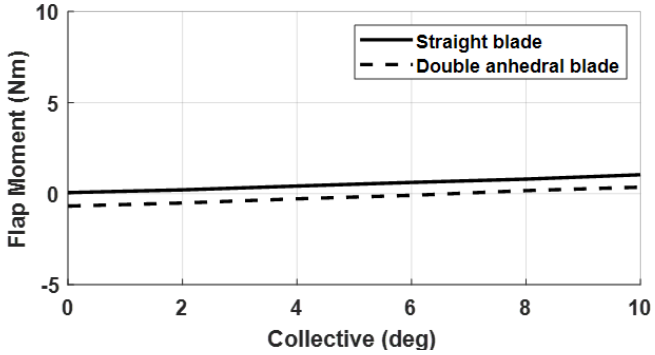

(b) Flap bending moment at 50%R.

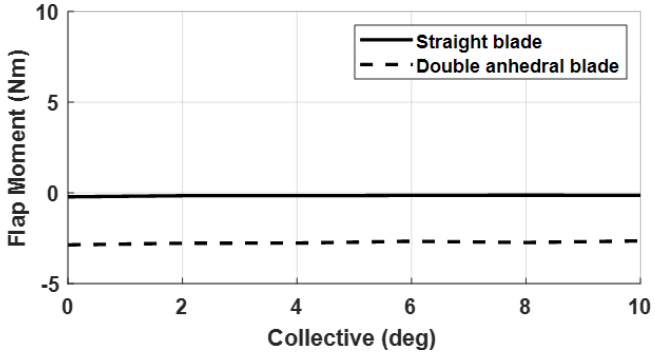

(c) Flap bending moment at 70%R.

Figure 6.21: Flap bending moment in hover. Straight blade versus double anhedral blade. $M_{tip} = 0.4$.

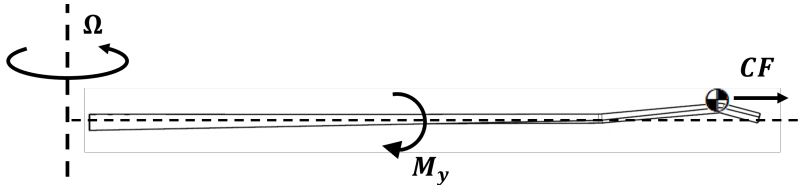

Figure 6.22: Diagram of flap bending moment on the double anhedral blade.

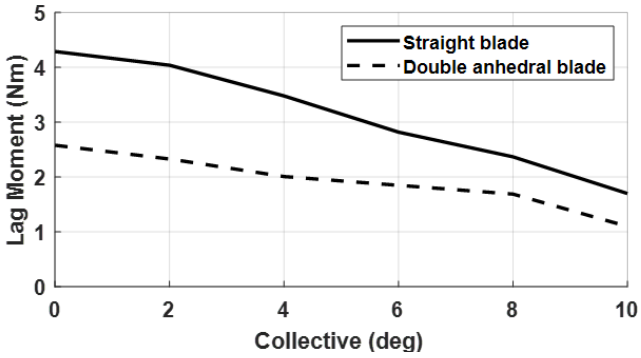

(a) Lag bending moment at 30%R.

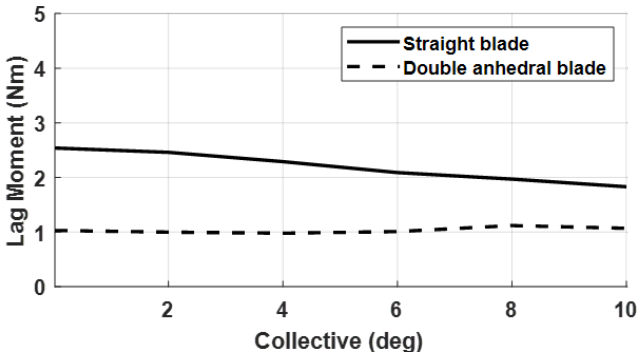

(b) Lag bending moment at 50%R.

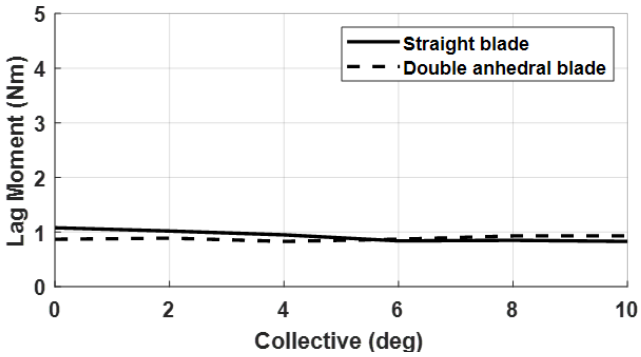

(c) Lag bending moment at 70%R.

Figure 6.23: Lag bending moment in hover: Straight blade versus double anhedral blade. $M_{tip} = 0.4$.

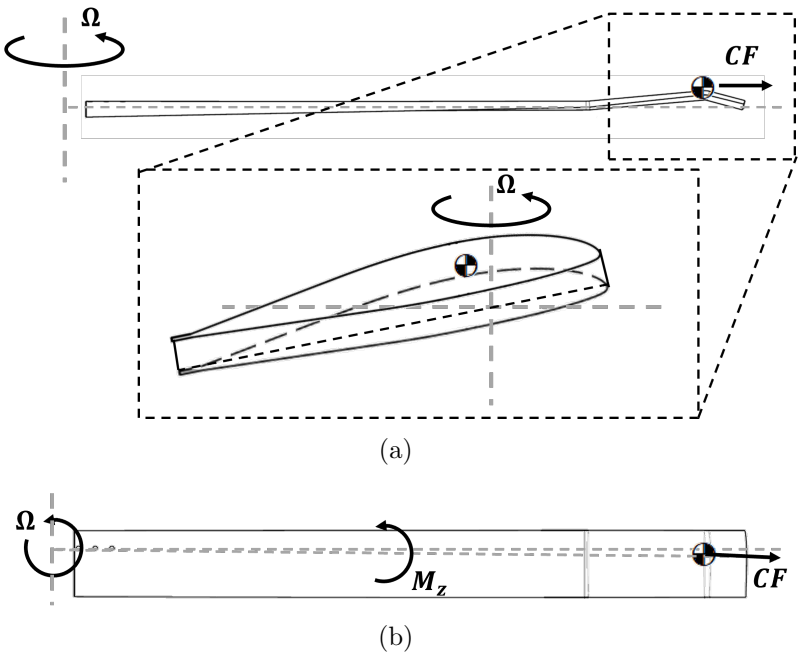

Figure 6.24: Diagrams of lag bending moment on the double anhedral blade.

The situation is different for torsion moment (Figure 6.25). Throughout the blade span, the torsion moment is nose down (negative) for both blades. In the inboard portion, both torsion moments grow with collective due to the increase in propeller moment. In this region, the torsion moment of the double anhedral blade is nose up compared to the straight blade. This can be explained by the additional propeller moment introduced by the double anhedral tip shown in Figure 6.26. Due to the C.G. offset, there is an additional propeller moment acting at the tip which is a nose up moment. While the rest of the blade generates a nose down propeller moment, this nose up moment reduces the torsion moment near the root. However, midspan out the torsion moment of the double anhedral blade is nose down compared to the straight blade. In this region, the opposite propeller moment from the tip and the straight portion further twist the blade, hence, increasing the blade torsion

moment.

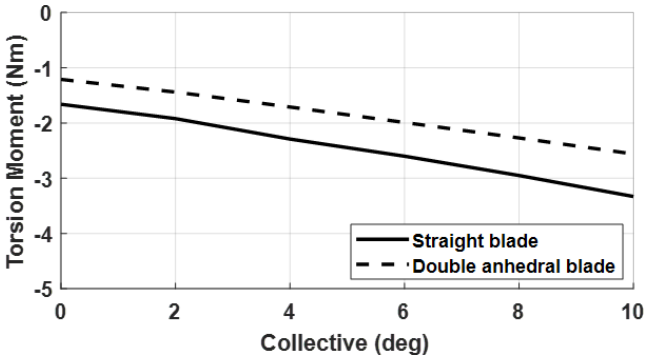

(a) Torsion moment at 30%R.

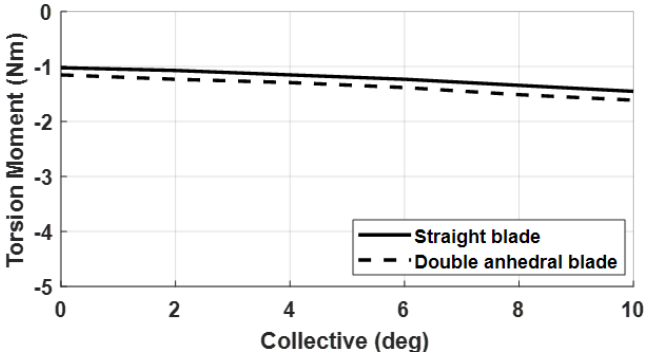

(b) Torsion moment at 50%R.

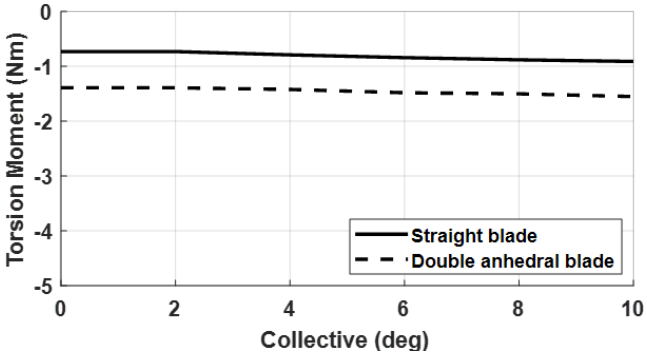

(c) Torsion moment at 70%R.

Figure 6.25: Torsion moment in hover. Straight blade versus double anhedral blade. $M_{tip} = 0.4$.

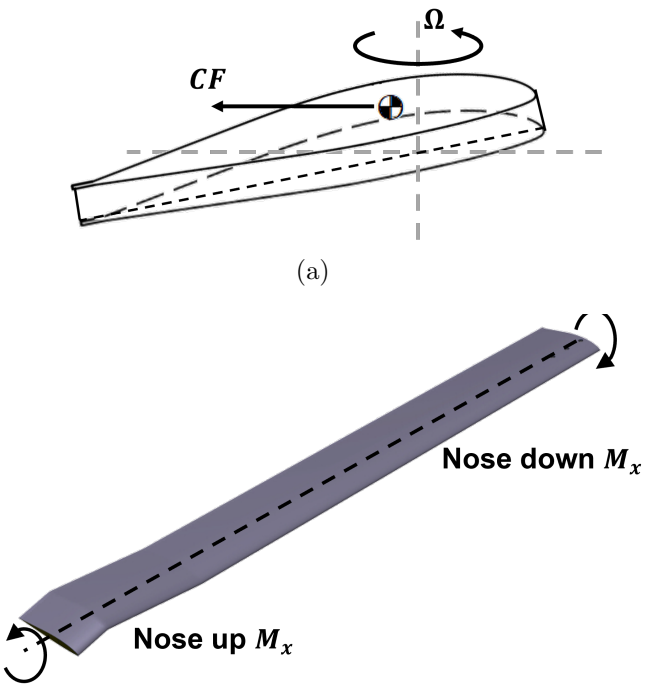

(a)

(b)

Figure 6.26: Diagrams of torsion moment on the double anhedral blade.

The impact of double anhedral on the blade torsion moment is reflected in the pitch link load (Figure 6.27). The double anhedral decrease the magnitude of pitch link load, and the reduction grows with the collective. This is also due to the nose up propeller moment at the tip countering the nominal nose down propeller moment from the rest of the blade (Figure 6.28).

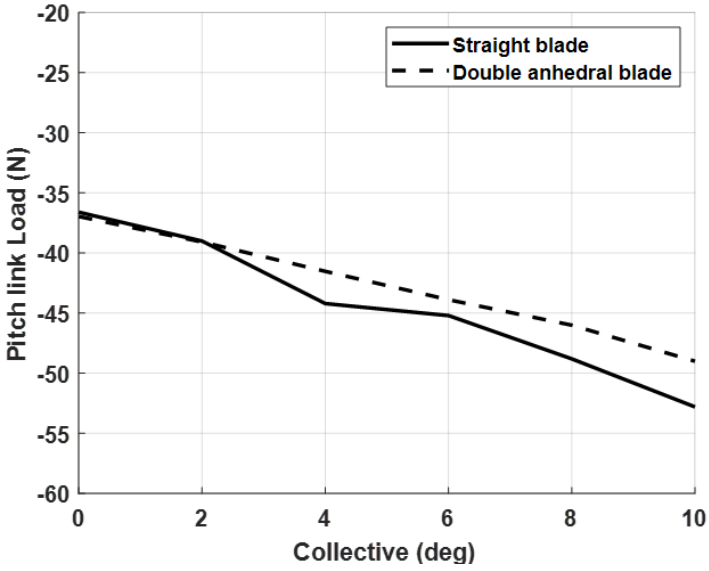

Figure 6.27: Pitch link load in hover. Straight blade versus double anhedral blade. $M_{tip} = 0.4$.

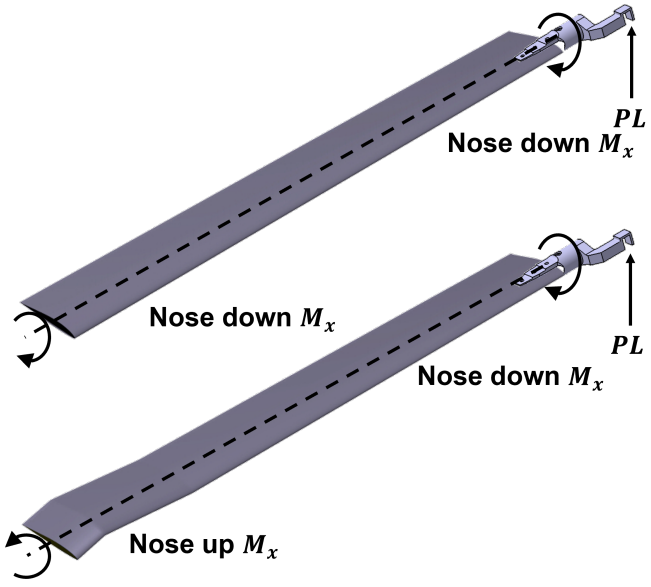

Figure 6.28: Propeller moment direction of the straight and double anhedral blades.

6.3.3 Blade Strain/stress

The prediction of blade axial strain ϵ_{xx} distributions in hover are shown in Figures 6.29 and 6.30. Both rotors are operating at 1522 RPM ($M_{tip} = 0.4$) and a collective of 10° ($C_T/\sigma = 0.117$). The left subfigures show the blade undeformed (dotted mesh) and deformed geometry and the surface strains. The right-hand subfigures show the internal strain at 30%R, 50%R, 80%R, and 95%R, along with the strains in the D-span. The main deformation is the bending up due to lift. Therefore, there are high negative and positive axial strains on the top and bottom surfaces respectively. Due to the drag, the positive strain at the leading-edge in the inboard-midspan region is much higher now compared to the vacuum strains. The double anhedral blade has a high positive axial strain region inboard of the dihedral junction. Figure 6.31 compares the internal axial stress σ_{xx}. In the inboard region, the loads are shared by the skin and spar for both blades. However, the load in the outboard portion of the double anhedral blade is mainly carried by the skin.

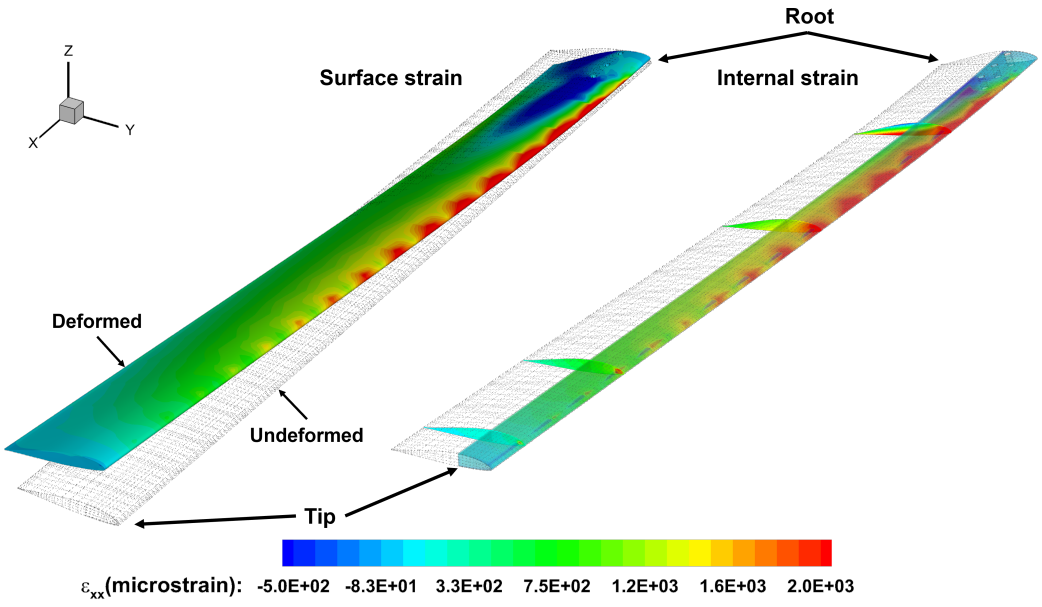

Figure 6.29: Axial strain ϵ_{xx} distribution of straight blade. $C_T/\sigma = 0.117$, $M_{tip} = 0.4$.

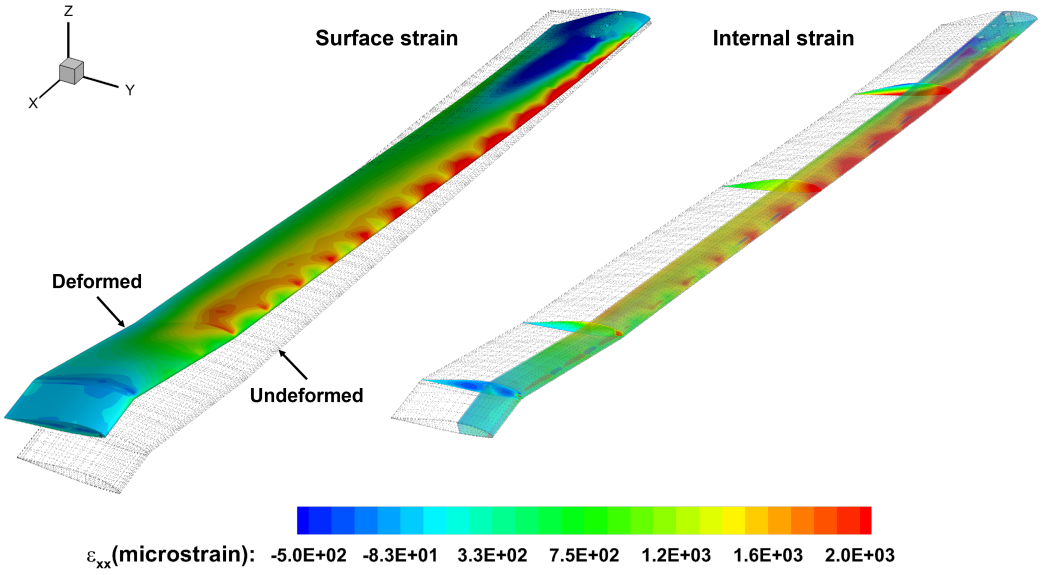

Figure 6.30: Axial strain ϵ_{xx} distribution of double anhedral blade. $C_T/\sigma = 0.117$, $M_{tip} = 0.4$.

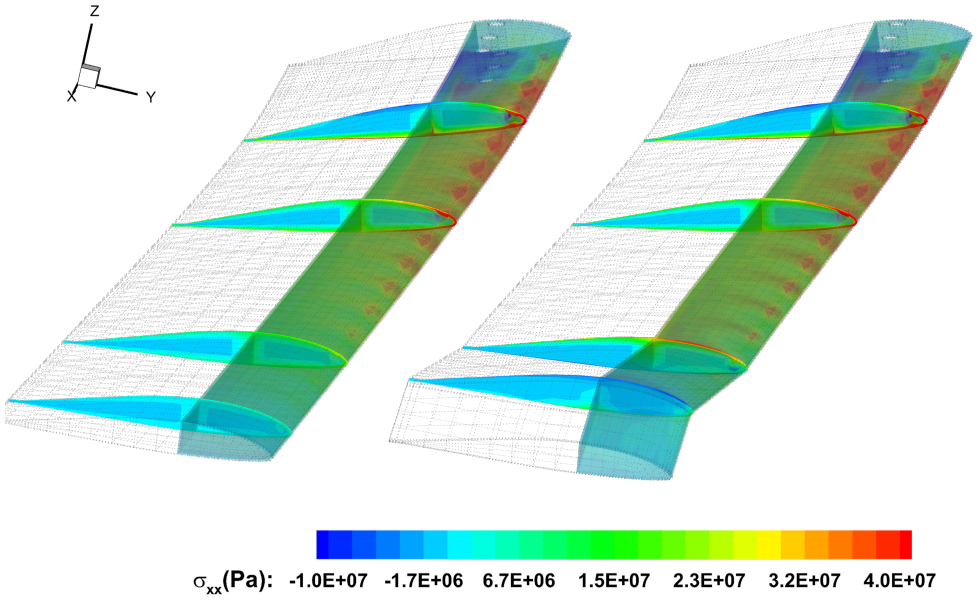

Figure 6.31: Internal axial stress σ_{xx} distribution. $C_T/\sigma = 0.117$, $M_{tip} = 0.4$.

Figures 6.32-6.34 show the in-plane shear strain γ_{xy} and stress σ_{xy}. These strain magnitudes are comparable to that of vacuum. But higher shear strains occur near the trailing edge in the inboard to midspan region for the straight blade, and this region expands to the outboard for the double anhedral blade. The strain pattern in the tip portion of the double anhedral blade is similar to the pattern in vacuum. The internal in-plane shear stress is shown in Figure 6.34. It is clear that the majority of shear stress is carried by the skin, especially for the dihedral and the anhedral junction. The out-of-plane strain ϵ_{zz} and stress σ_{zz} are examined in Figures 6.35 and 6.36. The double anhedral tip geometry increases the strain at the dihedral and anhedral junctions slightly, and the out-of-plane stresses are carried by the D-spar.

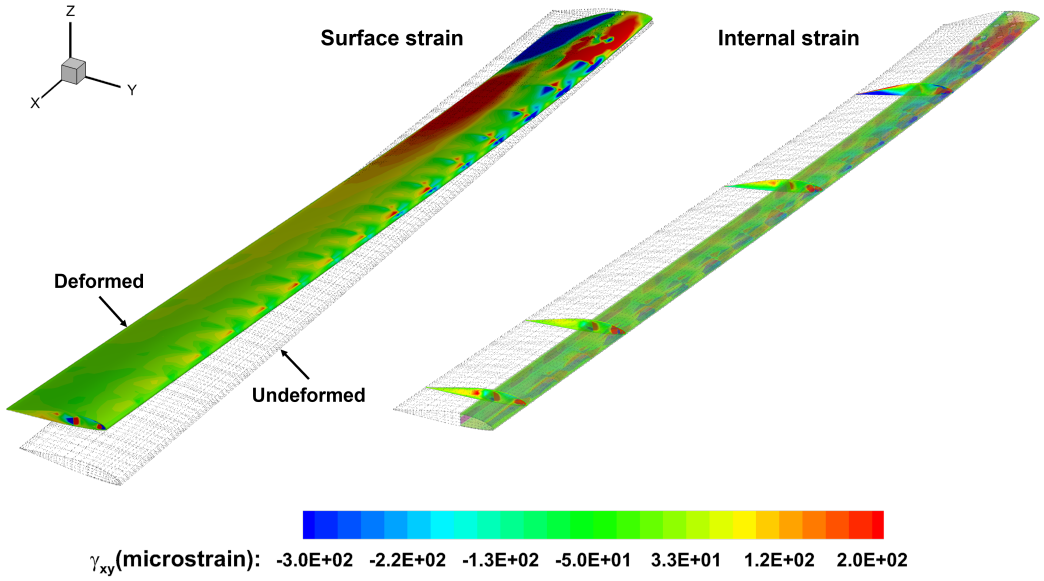

Figure 6.32: In-plane shear strain γ_{xy} distribution of straight blade. $C_T/\sigma = 0.117$, $M_{tip} = 0.4$.

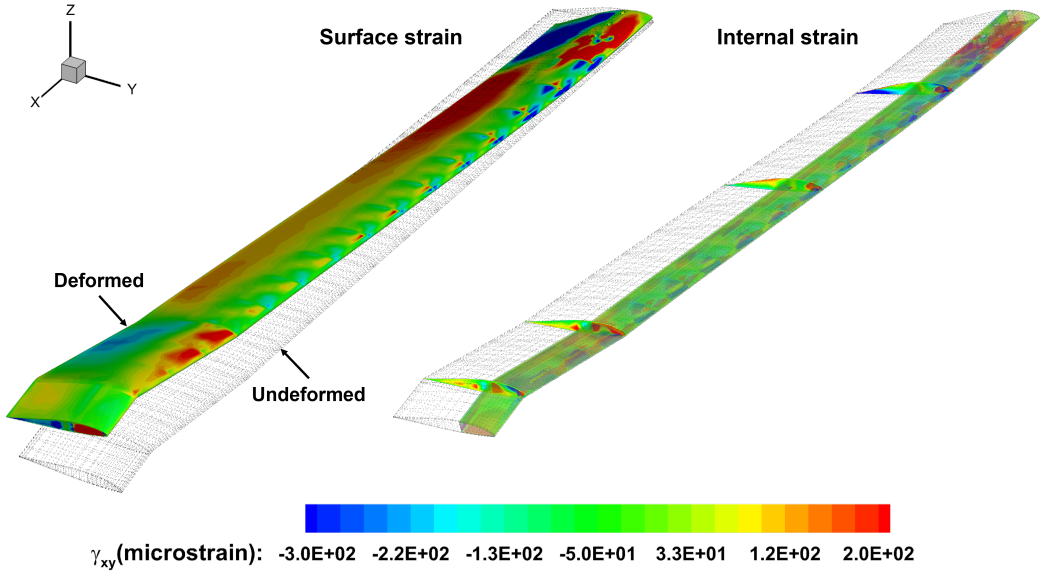

Figure 6.33: In-plane shear strain γ_{xy} distribution of double anhedral blade. $C_T/\sigma = 0.117$, $M_{tip} = 0.4$.

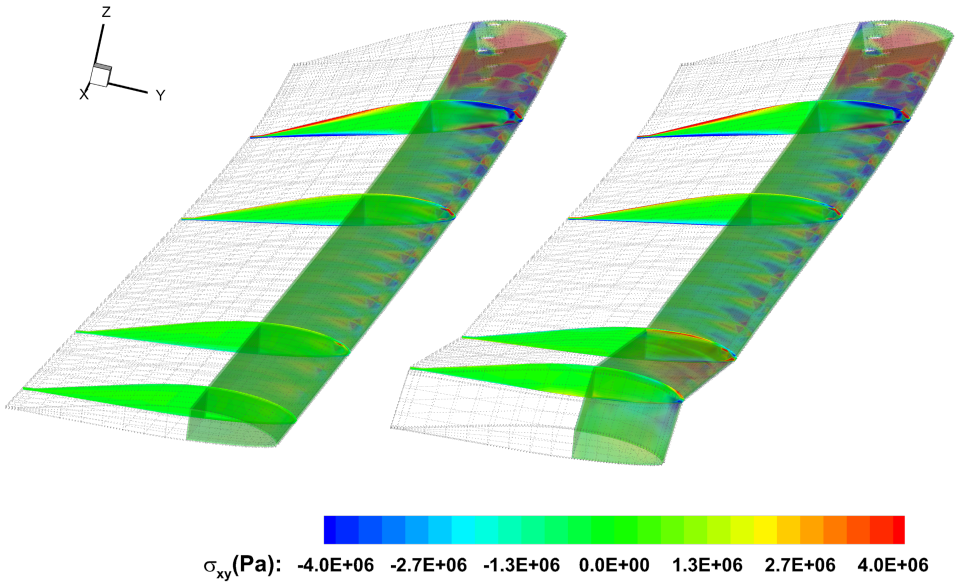

Figure 6.34: Internal in-plane shear stress σ_{xy} distribution. $C_T/\sigma = 0.117$, $M_{tip} = 0.4$.

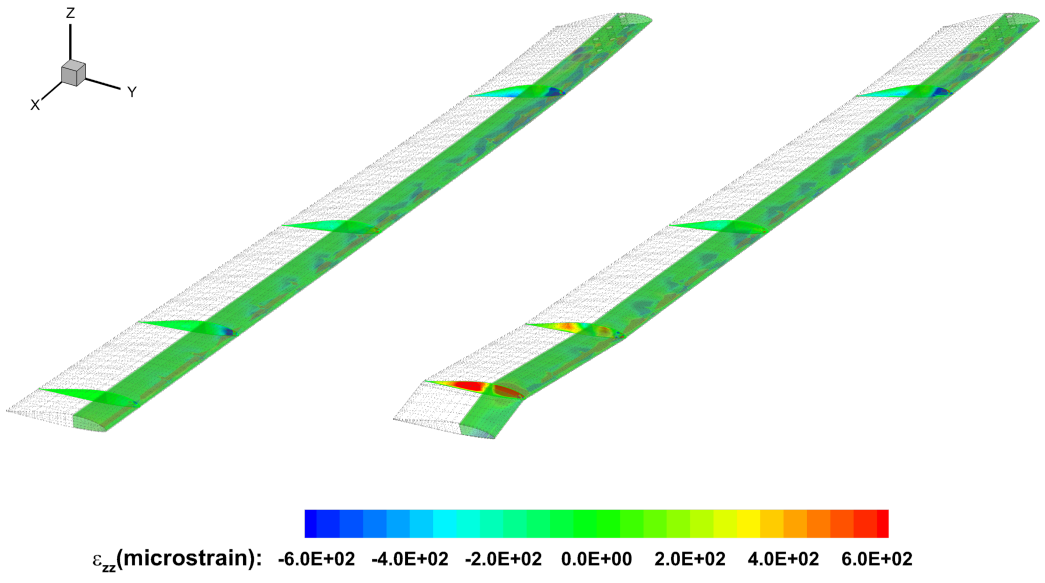

Figure 6.35: Out-of-plane strain ϵ_{zz} distribution of straight blade and double anhedral blade. $C_T/\sigma = 0.117$, $M_{tip} = 0.4$.

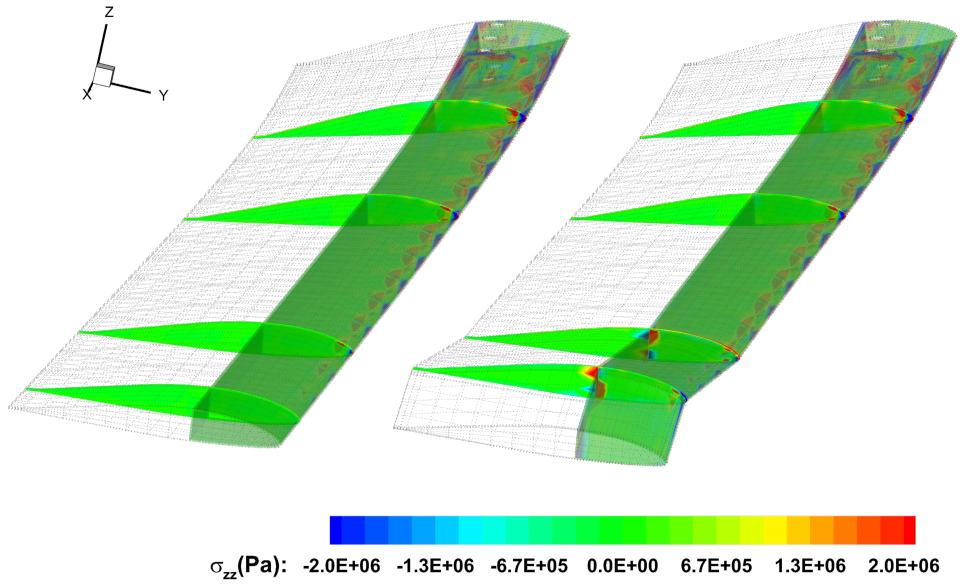

Figure 6.36: Out-of-plane stress σ_{zz} distribution of straight blade and double anhedral blade. $C_T/\sigma = 0.117$, $M_{tip} = 0.4$.

6.4 Forward Flight Analysis

The influence of double anhedral tip in forward flight is studied in this section. The rotors operate at 1522 RPM ($M_{tip} = 0.4$) with a forward shaft tilt of 4°. At each tip speed ratio ($\mu = V/\Omega R$), the trim target is blade loading (C_T/σ) of 0.1 and zero hub moments ($C_{MX}/\sigma = 0$, $C_{MY}/\sigma = 0$) accomplished by the collective (θ_{75}) and cyclic (θ_{1C}, θ_{1S}) angles.

6.4.1 Rotor Performance

The rotor power, drag, and trim controls are studied. The rotor performance metric in forward flight is the effective lift-to-drag ratio (L/D_e). The definition of this parameter is given by Equation (6.1).

$$L/D_e = \frac{\mu C_L}{C_Q - \mu C_X} \tag{6.1}$$

where C_L is lift coefficient, C_Q is torque coefficient, C_X is propulsive force coefficient, and $\mu = V_\infty/\Omega R$ is tip speed ratio (Figure 6.37).

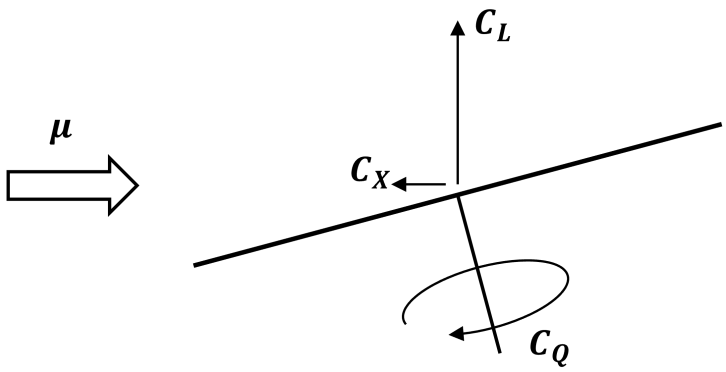

Figure 6.37: Diagram of rotor in forward flight.

Figure 6.38 presents the effective lift-to-drag ratio variation with advance ratio. The solid line is the straight rotor, while the dash line is the double anhedral rotor. In this range of tip speed ratio (0.05-0.3), the effective lift-to-drag ratio increases with forward flight speed as is typical of any rotor. The performance of the straight rotor is higher, and the difference worsens with tip speed ratio. At the tip speed ratio of 0.3, the L/D_e of the straight rotor is 16.7% higher. These differences is mainly due to the higher propulsive force of the straight rotor, as shown in Figure 6.39. The rotor torque between two rotors is very similar (Figure 6.40). The control angles needed to trim the rotors are shown in Figure 6.41. The control angles are very similar throughout the advance ratio range.

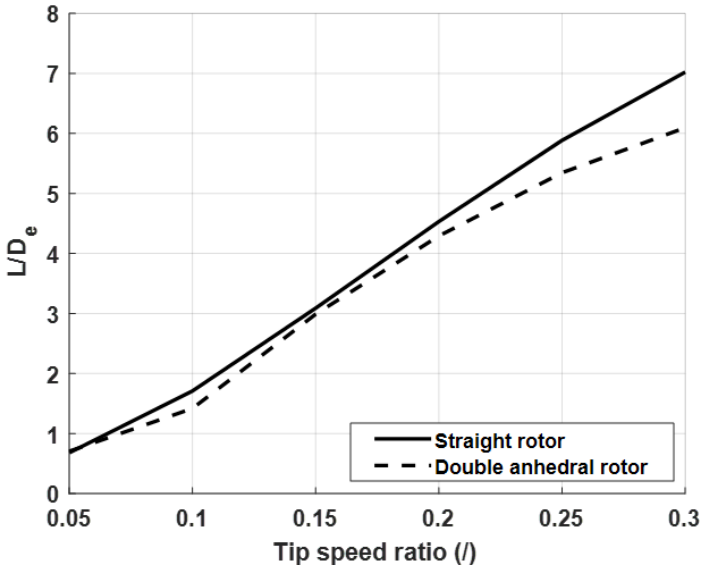

Figure 6.38: Rotor effective lift-to-drag ratio ($M_{tip} = 0.4$, $\alpha_s = 4°$, $C_T/\sigma = 0.1$).

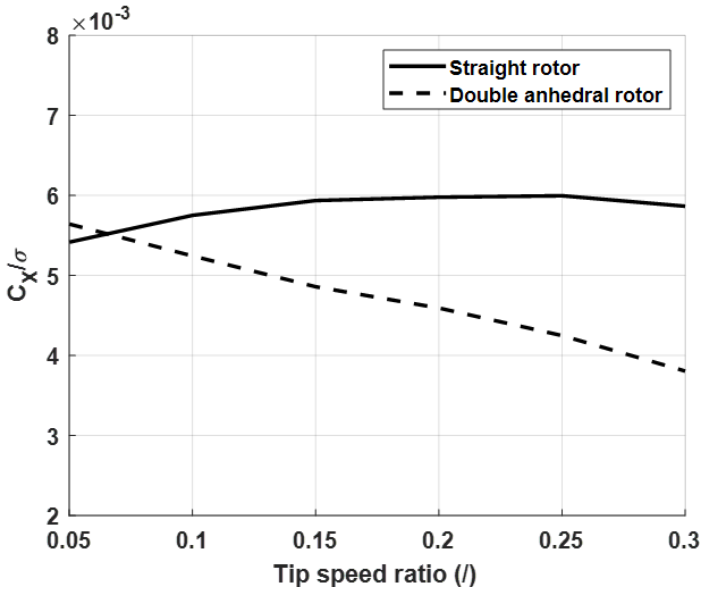

Figure 6.39: Rotor propulsive force coefficient ($M_{tip} = 0.4$, $\alpha_s = 4°$, $C_T/\sigma = 0.1$).

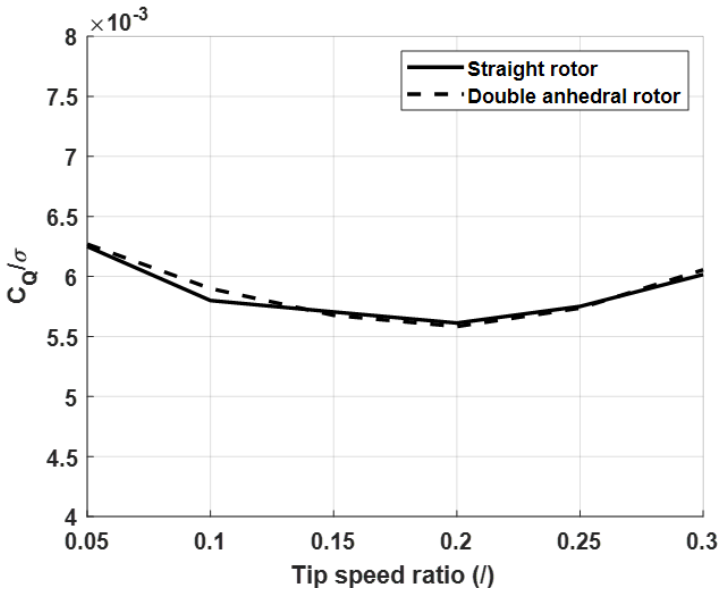

Figure 6.40: Rotor torque coefficient ($M_{tip} = 0.4$, $\alpha_s = 4°$, $C_T/\sigma = 0.1$).

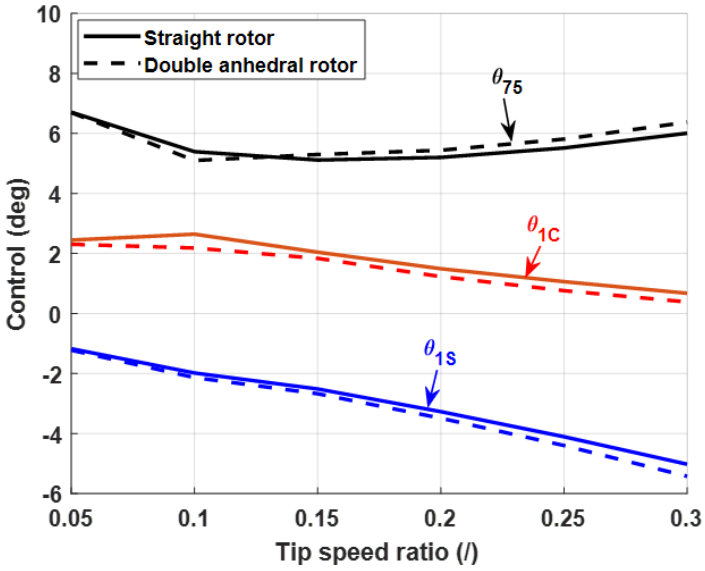

Figure 6.41: Trimmed forward flight control ($M_{tip} = 0.4$, $\alpha_s = 4°$, $C_T/\sigma = 0.1$).

6.4.2 Hub Vibratory Loads

The hub H force F_H and side force F_Y are combined into in-plane hub force F, and roll moment M_X and pitch moment M_Y into a net hub moment M as shown in Equations (6.2) and (6.3).

$$F(\psi) = \sqrt{F_H(\psi)^2 + F_Y(\psi)^2} \tag{6.2}$$

$$M(\psi) = \sqrt{M_X(\psi)^2 + M_Y(\psi)^2} \tag{6.3}$$

The dimensional and non-dimensional vibratory hub loads are shown in Figures 6.42 and 6.43. The hub loads are non-dimensionalized by the mean thrust. The solid and dash lines represent the straight rotor and the double anhedral rotor respectively. Since both rotors are four-bladed, only 4/rev (black lines) and 8/rev (red lines) hub loads are shown.

Figures 6.42(a) and 6.43(a) shows the in-plane vibratory hub force variation with tip speed ratio. Both rotors have the same trend of 4/rev and 8/rev components. The 4/rev in-plane vibratory hub force increase initially and reach a peak at the tip speed ratio of 0.1, then decrease with the tip speed ratio. As for the 8/rev component, it grows as the tip speed ratio increase, but the magnitude is negligible compared to the 4/rev component. The vertical vibratory hub force is given in Figure 6.42(b). The trend is similar to the in-plane force, but the magnitude is 5 times higher. This is typical of rotors. The 4/rev of the double anhedral rotor is

15% higher at the low tip speed ratio peak. Greater differences between two rotors appear in the vibratory hub moment (Figure 6.42(c)). At a tip speed ratio of 0.1, the 4/rev vibratory hub moment of the double anhedral rotor is twice as high as the straight rotor. Vibratory loads at a high tip speed ratio require 3-D tip transonic pitching moments which are beyond the capability of lifting line models. Nevertheless, the increase in θ_{1S} and consequent 3/rev lift gives rise to a 4/rev moment at high tip speed ratios. The trend of 4/rev vibratory torque typically follows the vertical force, which increases by 18% with the double anhedral tip.

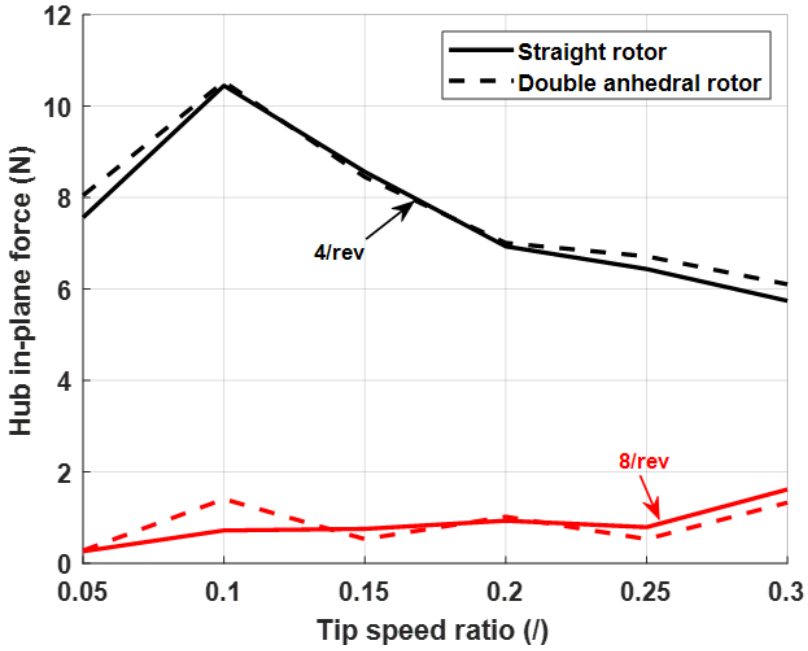

(a) In-plane force

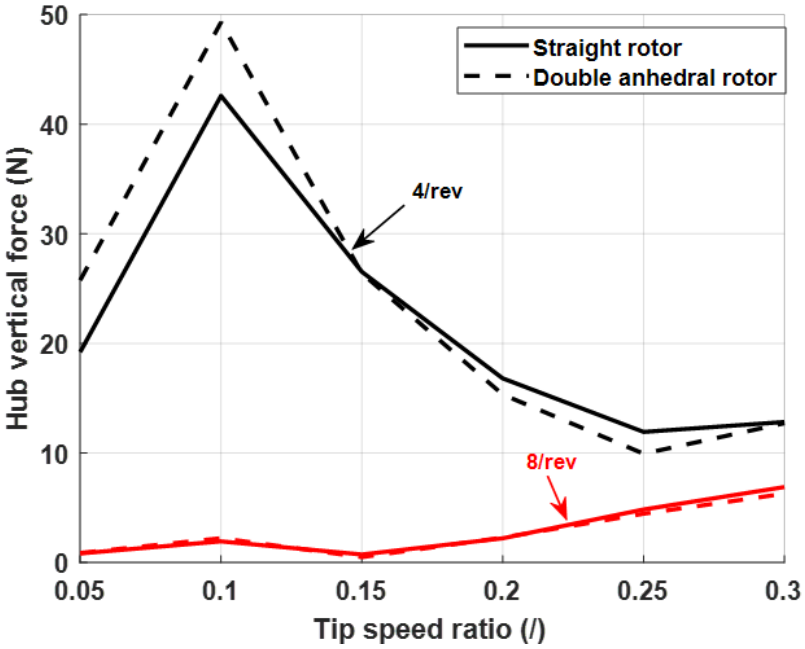

(b) Vertical force

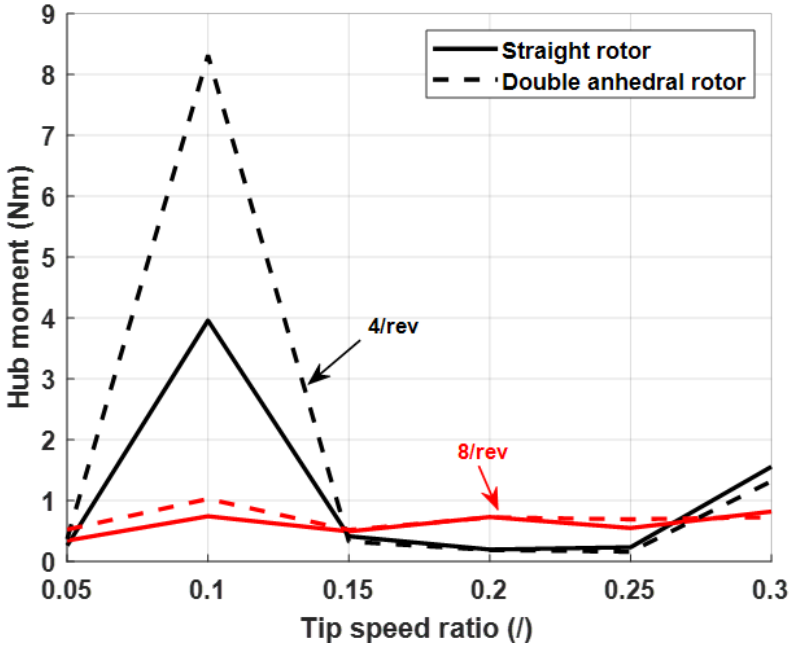

(c) Hub moment

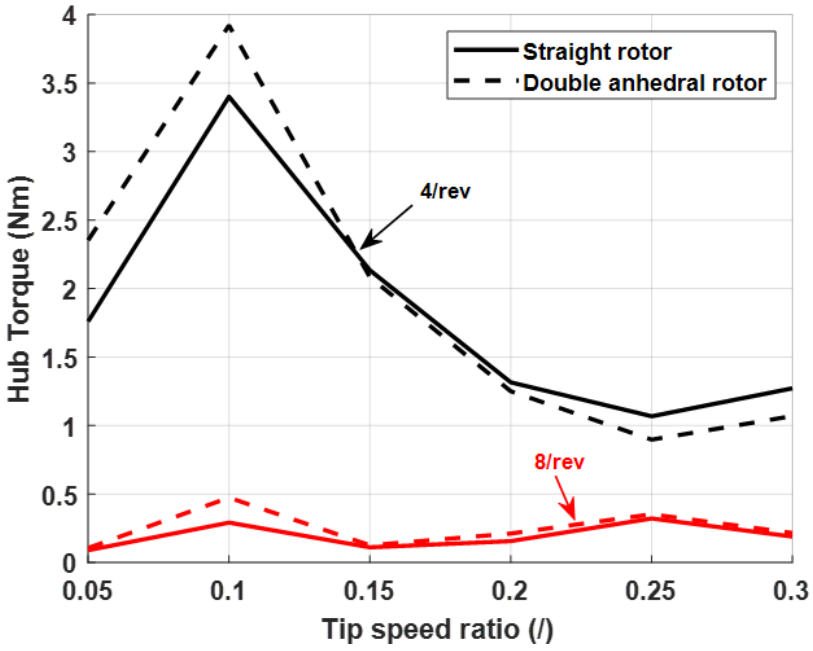

(d) Torque

Figure 6.42: Hub 4/rev and 8/rev vibratory loads ($M_{tip} = 0.4$, $\alpha_s = 4°$, $C_T/\sigma = 0.1$).

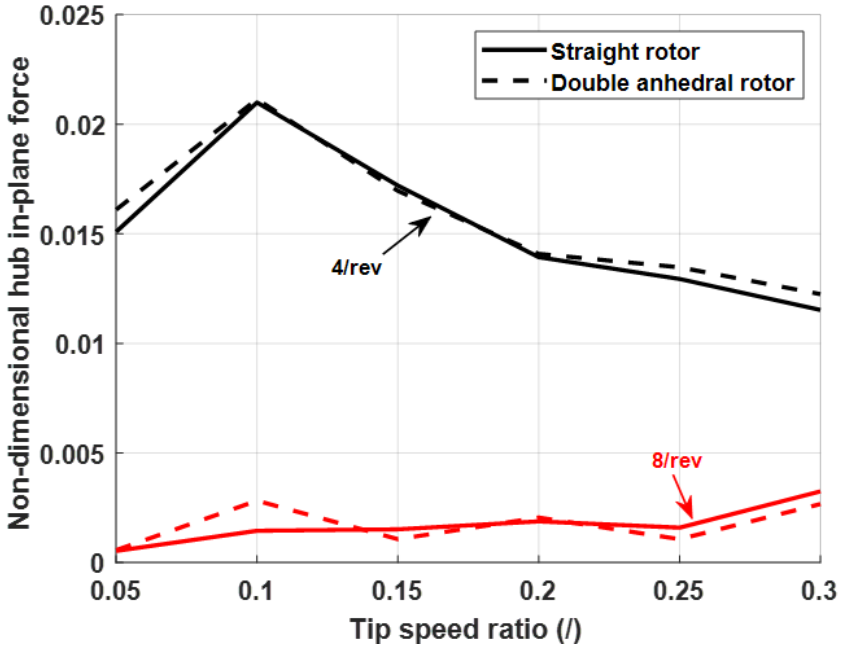

(a) Non-dimensional in-plane force

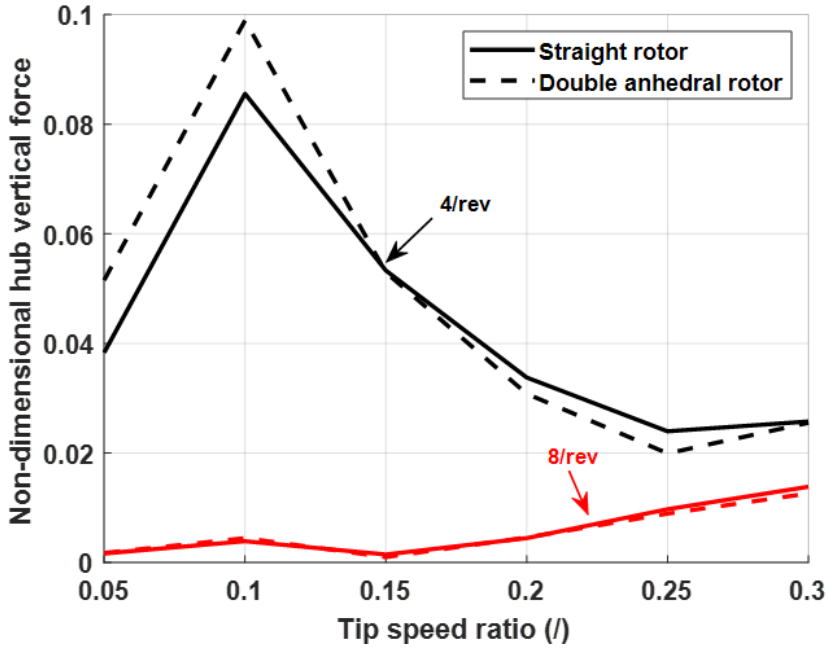

(b) Non-dimensional vertical force

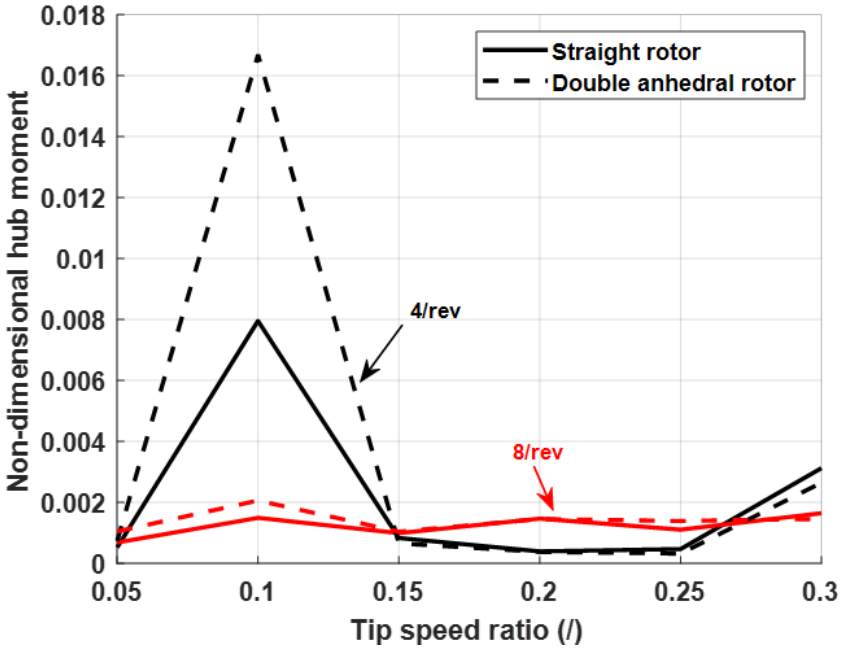

(c) Non-dimensional hub moment

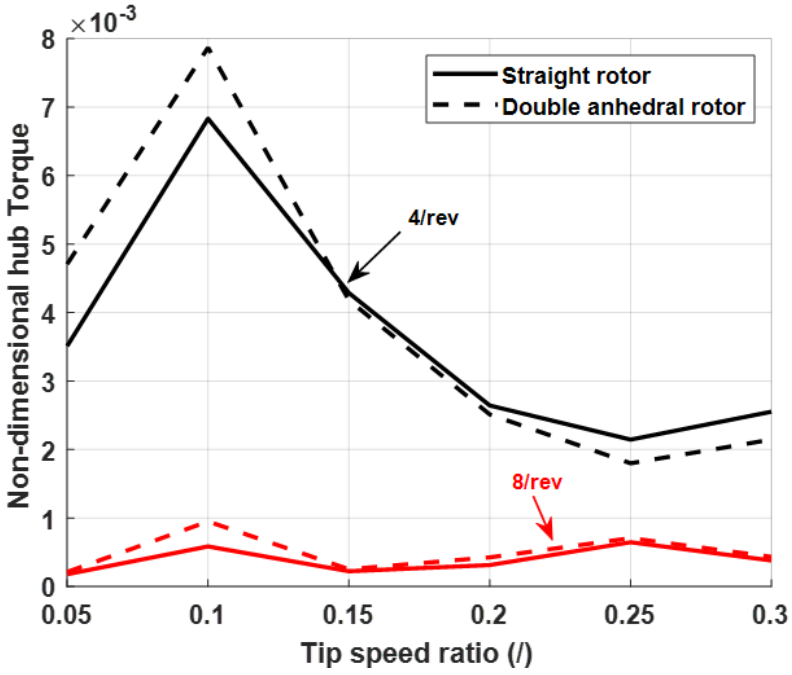

(d) Non-dimensional torque

Figure 6.43: Non-dimensional hub 4/rev and 8/rev vibratory loads ($M_{tip} = 0.4$, $\alpha_s = 4°$, $C_T/\sigma = 0.1$).

6.4.3 Blade Structural Loads

Structural load is an important aspect of design, especially for a hingeless rotor. The flap bending moment azimuthal variations in Figure 6.44 are extracted from 30%R (black lines) and 50%R (red lines). The solid lines are the straight blade, while the dash lines are the double anhedral blade. The mean flap bending moment of the double anhedral blade is lower than the straight blade at both 30%R and 50%R, which is consistent with the conclusion drawn from hover analysis.

The oscillatory flap moments at 30%R and 50%R variation with tip speed ratio are shown in Figures 6.45. The solid and dash lines are the straight blade and the double anhedral blade respectively. At 30%R, flap bending moments are dominated

by a 1/rev component when the tip speed ratio is low. The double anhedral blade 1/rev component is much stronger than the straight blade at $\mu = 0.1$. As the tip speed ratio increases, 1/rev and 2/rev components are comparable. The higher harmonics components (3/rev and 4/rev) always remain at a low level. At 50%R, the flap bending moments are dominated by the 1/rev component except for the lowest tip speed ratio case. The impact of the double anhedral tip is limited at this spanwise location. These indicate that the high vibratory hub load of the double anhedral blade at a tip speed ratio of 0.1 is due to the high 1/rev flap bending moment.

The legends used in Figures 6.46 and 6.47 are the same as in Figures 6.44 and 6.45. The peak-to-peak magnitude of lag bending moment increase with the tip speed ratio (Figure 6.46). Regardless of the spanwise location, the lag bending moments are dominated by the 2/rev component as shown in Figure 6.47. Its magnitude at 30%R first decreased by 20% when $\mu = 0.1$ then increased by 2.5 times when $\mu = 0.3$. The double anhedral blade always has a higher 2/rev oscillatory lag bending moment.

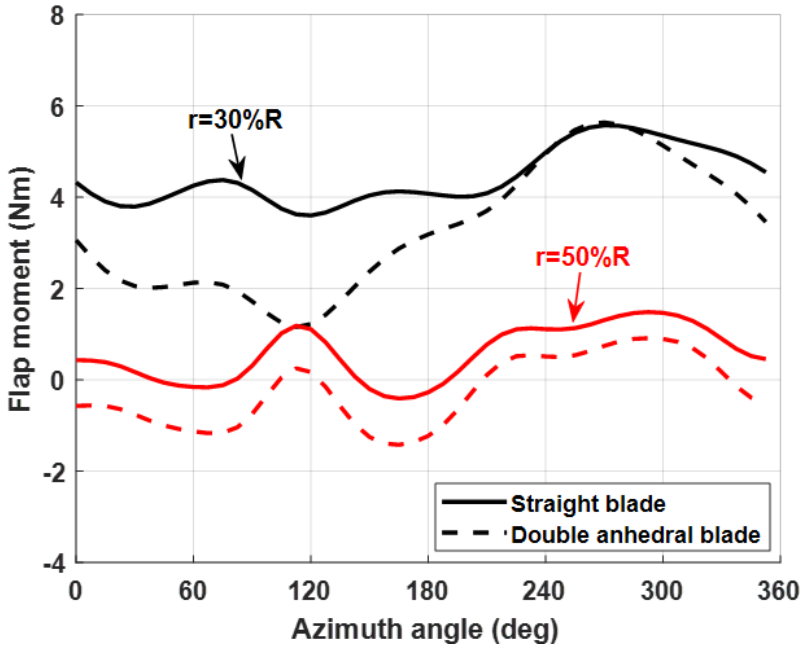

(a) $\mu = 0.1$

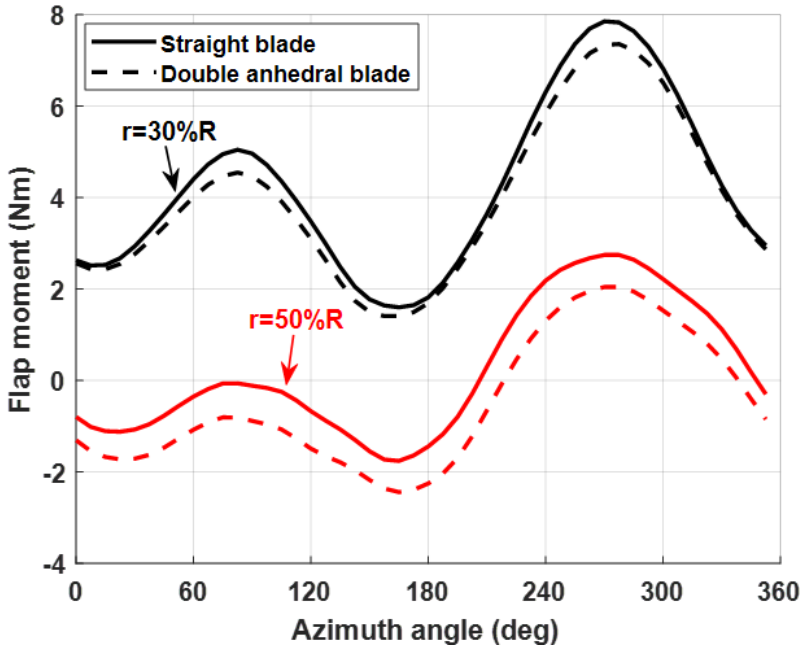

(b) $\mu = 0.3$

Figure 6.44: Flap bending moment versus azimuth ($M_{tip} = 0.4$, $\alpha_s = 4°$, $C_T/\sigma = 0.1$).

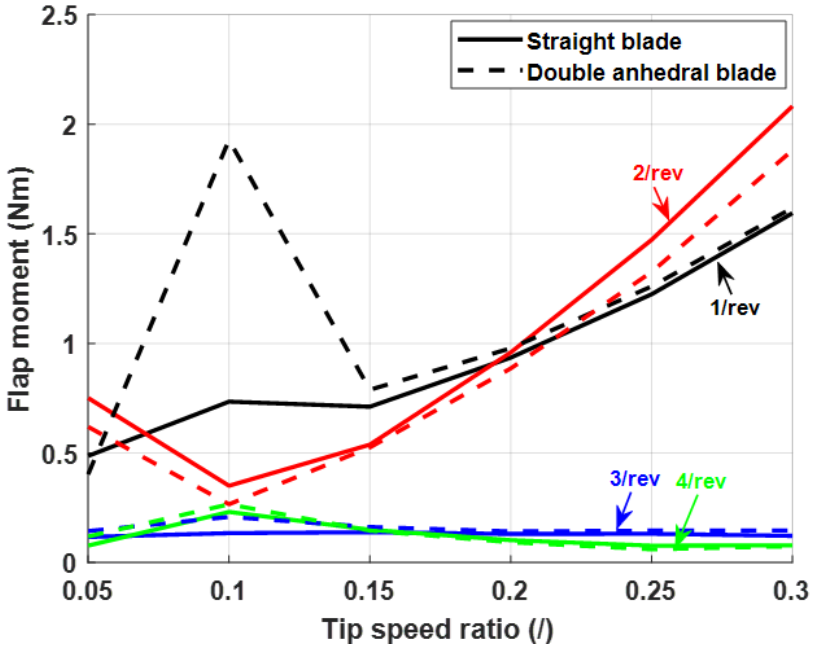

(a) $r = 30\%R$

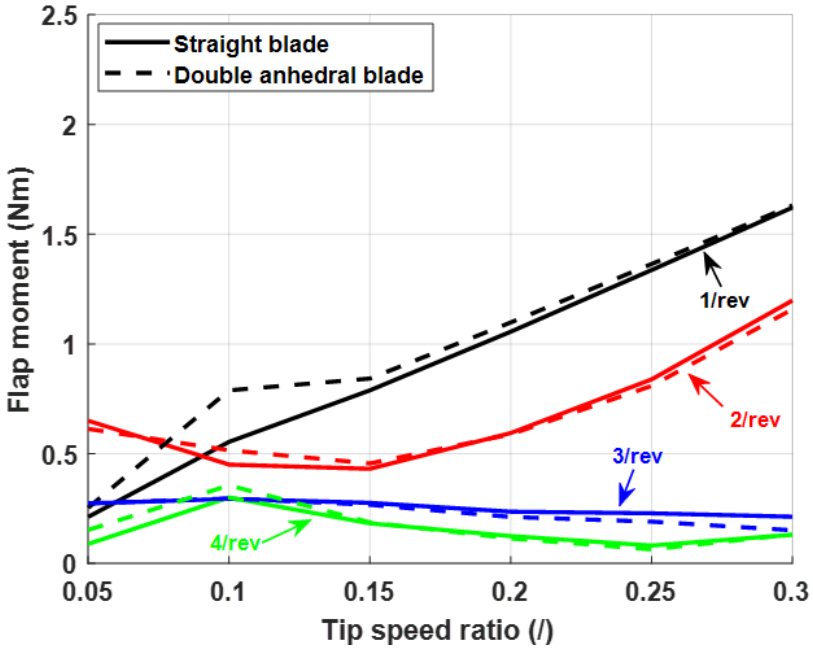

(b) $r = 50\%R$

Figure 6.45: Oscillatory flap bending moment versus tip speed ratio ($M_{tip} = 0.4$, $\alpha_s = 4°$, $C_T/\sigma = 0.1$).

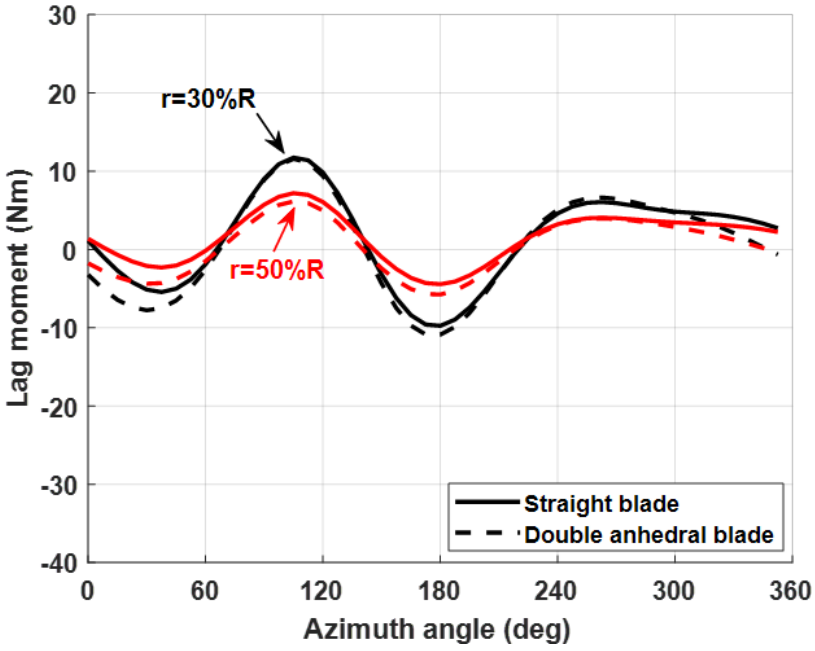

(a) $\mu = 0.1$

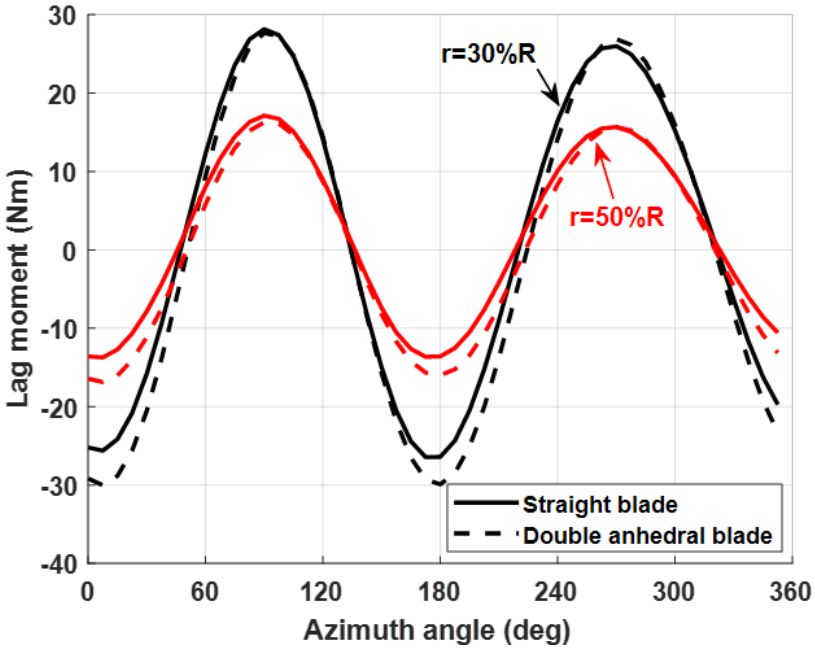

(b) $\mu = 0.3$

Figure 6.46: Lag bending moment versus azimuth ($M_{tip} = 0.4$, $\alpha_s = 4°$, $C_T/\sigma = 0.1$).

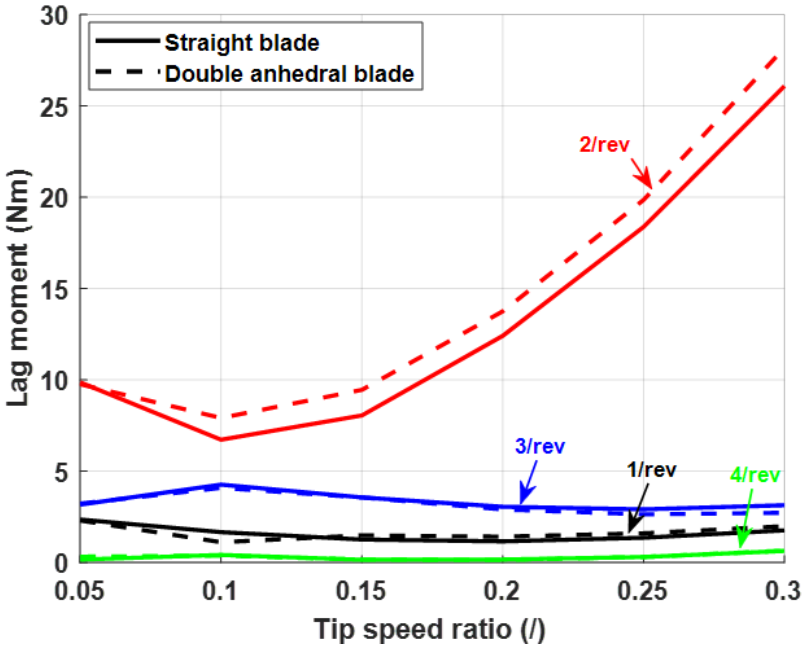

(a) $r = 30\%R$

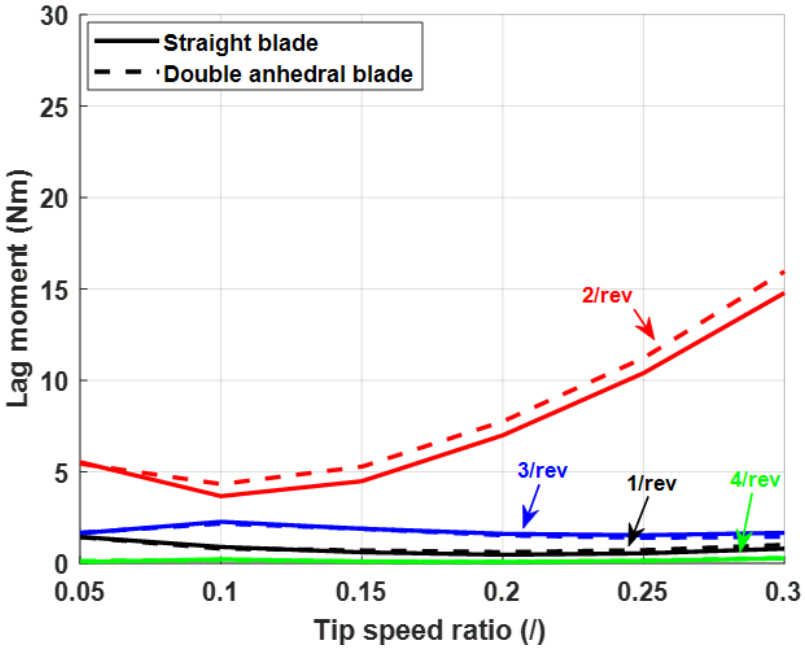

(b) $r = 50\%R$

Figure 6.47: Oscillatory lag bending moment versus tip speed ratio ($M_{tip} = 0.4$, $\alpha_s = 4°$, $C_T/\sigma = 0.1$).

Figure 6.48 shows the azimuthal variation of torsion moment. The double anhedral blade has a lower mean and peak-to-peak torsion moment. In Figure 6.49, the oscillatory torsion moments are from 30%R and 50%R. At 30%R, the straight blade torsion moment is dominated by the 2/rev component regardless of the tip speed ratio. The double anhedral blade is also dominated by the same harmonics component, however, the magnitude is much lower. At 50%R, the double anhedral blade has a much lower 2/rev component.

The pitch link loads are shown in Figure 6.50. The pitch link is always in compression while the tip speed ratio is low, and the highest magnitude occurs at an azimuth angle of 180°. At a 0.3 tip speed ratio, there is an extension pitch link load on the retreating side of the rotor. The 1/rev and 2/rev components have similar magnitudes. The double anhedral blade has a higher oscillatory pitch link load (Figure 6.51).

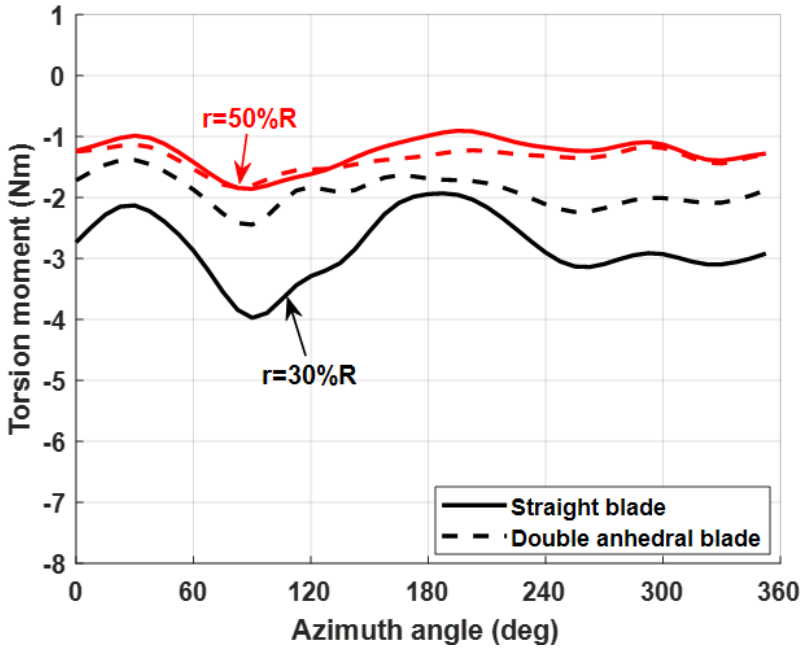

(a) $\mu = 0.1$

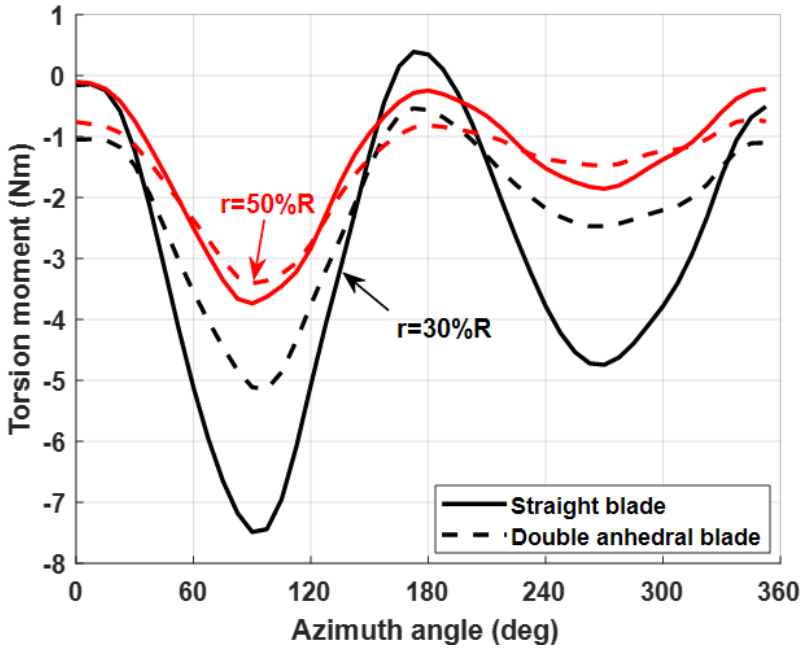

(b) $\mu = 0.3$

Figure 6.48: Torsion moment versus azimuth ($M_{tip} = 0.4$, $\alpha_s = 4°$, $C_T/\sigma = 0.1$).

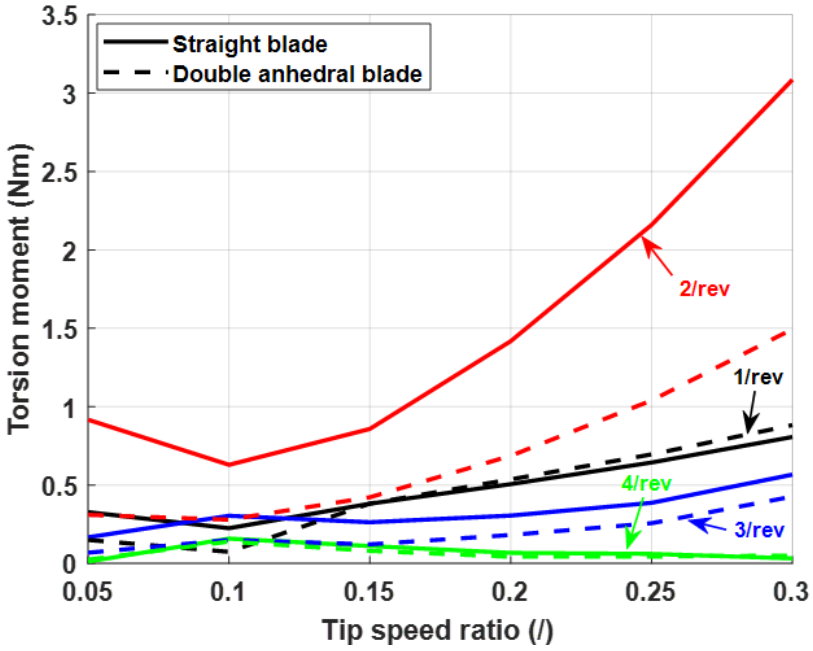

(a) $r = 30\%R$

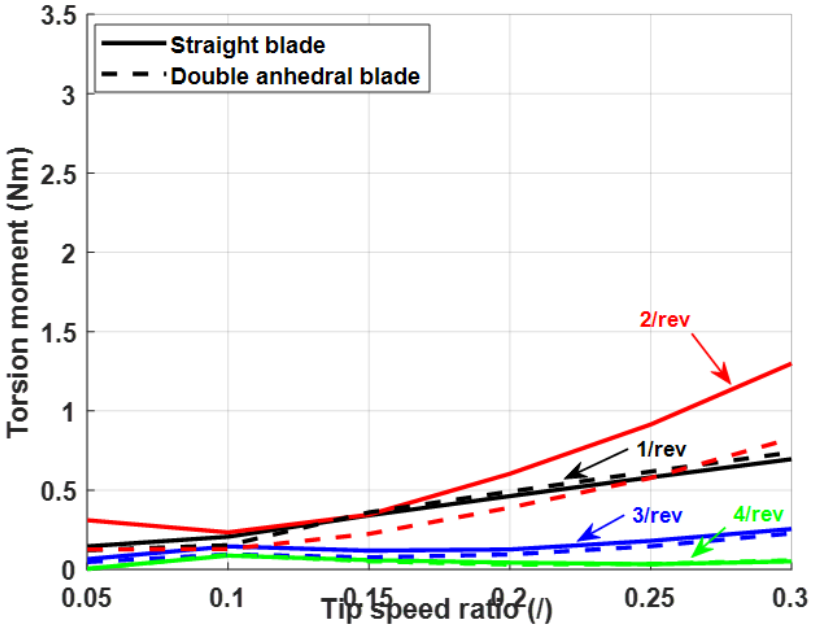

(b) $r = 50\%R$

Figure 6.49: Oscillatory torsion moment versus tip speed ratio ($M_{tip} = 0.4, \alpha_s = 4°, C_T/\sigma = 0.1$).

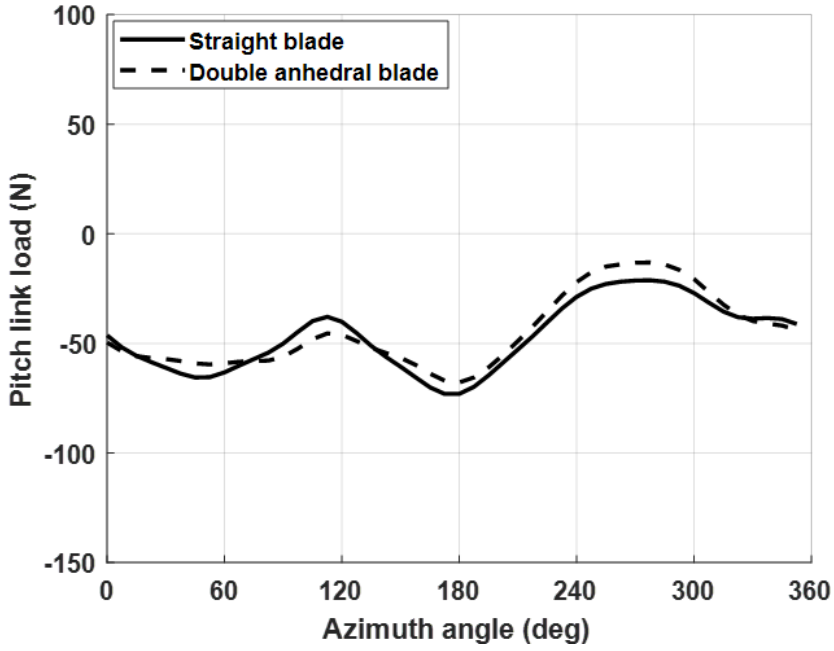

(a) $\mu = 0.1$

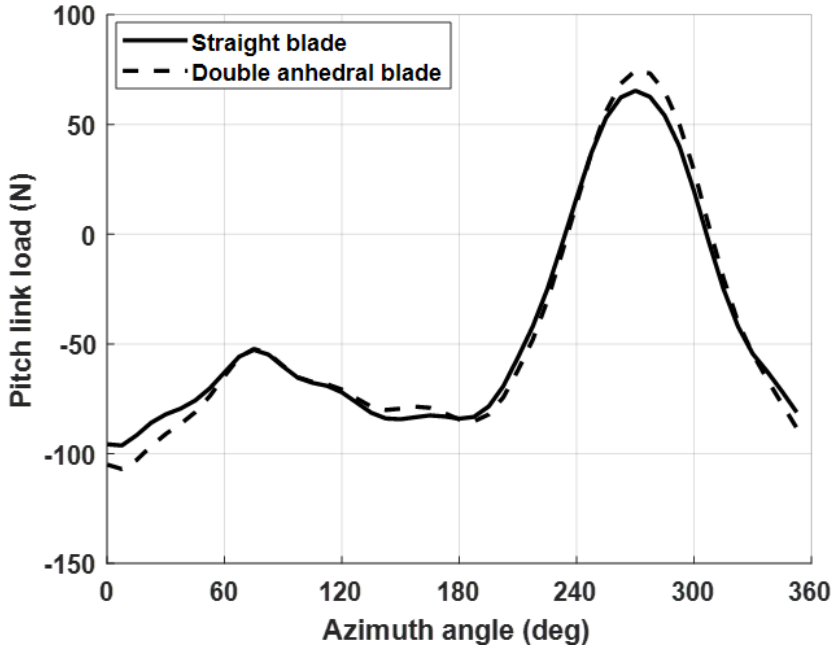

(b) $\mu = 0.3$

Figure 6.50: Pitch link load versus azimuth ($M_{tip} = 0.4$, $\alpha_s = 4°$, $C_T/\sigma = 0.1$).

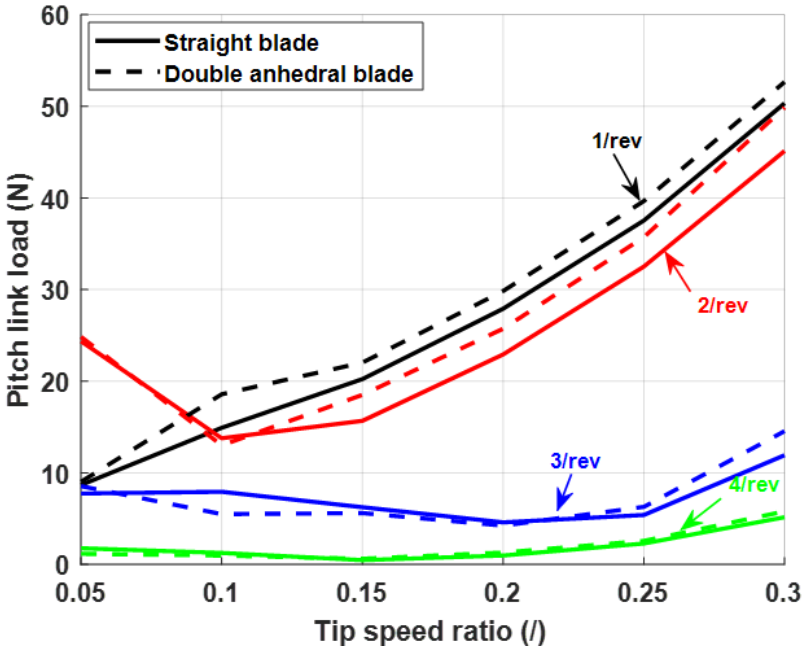

Figure 6.51: Oscillatory pitch link load versus tip speed ratio ($M_{tip} = 0.4$, $\alpha_s = 4°$, $C_T/\sigma = 0.1$).

6.4.4 Blade Strain/stress

The axial strain ϵ_{xx}, in-plane shear strain γ_{xy}, and out-of-plane strain ϵ_{zz} are examined in forward flight. There are a large amount of detailed data available, but only the strain distributions at 0°, 90°, 180°, and 270° of the 0.3 tip speed ratio case are shown.

Figures 6.52 and 6.53 show the axial strain of the straight blade and the double anhedral blade at various azimuth angles. In each subfigure, the left side shows the undeformed (dotted mesh) and deformed geometry as well as the surface strains. The right side shows the internal strains at 30%R, 50%R, 80%R, and 95%R along with the strains in the D-span. At 0° and 180° azimuth, both blades have high positive axial strains near the root at the trailing edge. At 90° and 270° azimuth,

high negative axial strains appear near the root at the trailing edge, while high positive axial strain present at the leading-edge. These strain patterns are consistent with the flap and lag bending moment. The double anhedral tip expands all of the high axial strain regions at the trailing edge and leading-edge. Meanwhile, the tip geometry introduces strain concentrations near the anhedral and dihedral junction at 90° and 270° azimuth respectively.

The in-plane shear strain distributions are shown in Figures 6.54 and 6.55. The in-plane shear strain is mainly carried by the skin. The leading-edge weights introduce shear strain concentrations near the leading-edge. And the highest concentrations near the root occur at 90° and 270° azimuth for both blades. The double anhedral tip changes the in-plane shear strain patterns in the tip portion. And the magnitude in the tip region is comparable to the root region, which is quite high.

As shown in Figure 6.56, the pattern of the internal out-of-plane strain of two blades is compared. The variations of strain near the root for the two blades are similar. The only difference resulting from the tip geometry occurs at the anhedral junction which is the same as in hover.

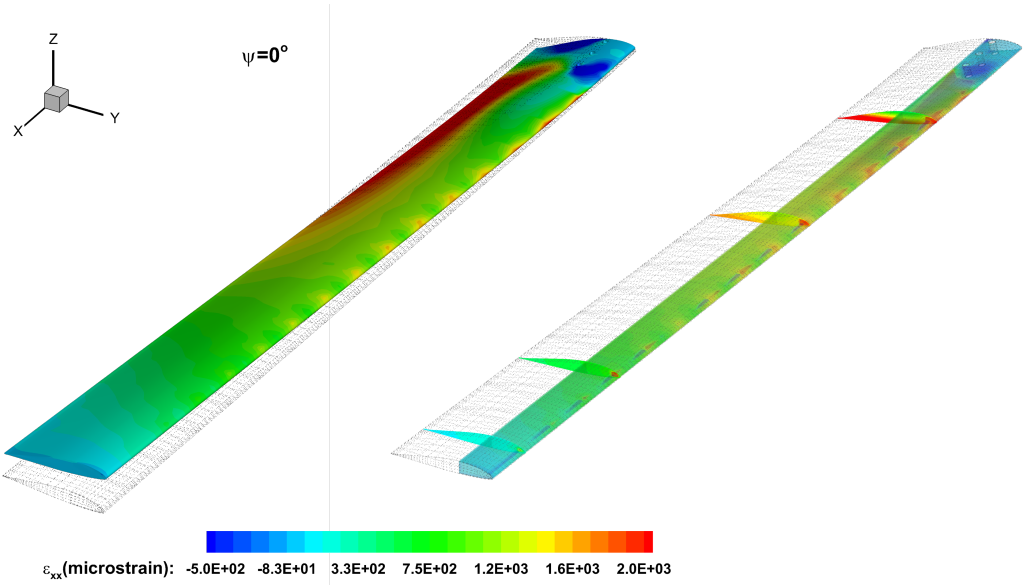

(a) $\psi = 0°$

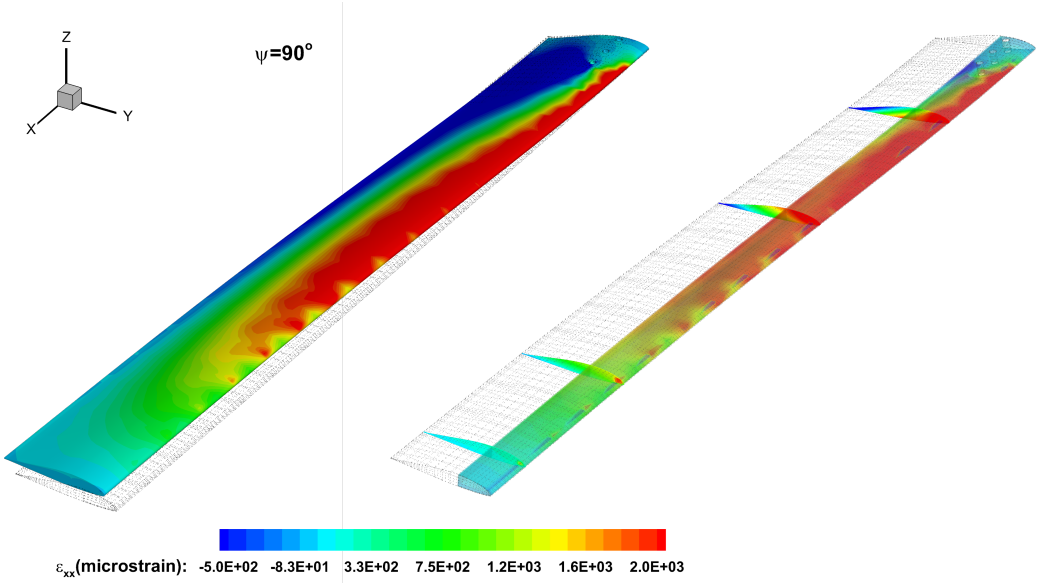

(b) $\psi = 90°$

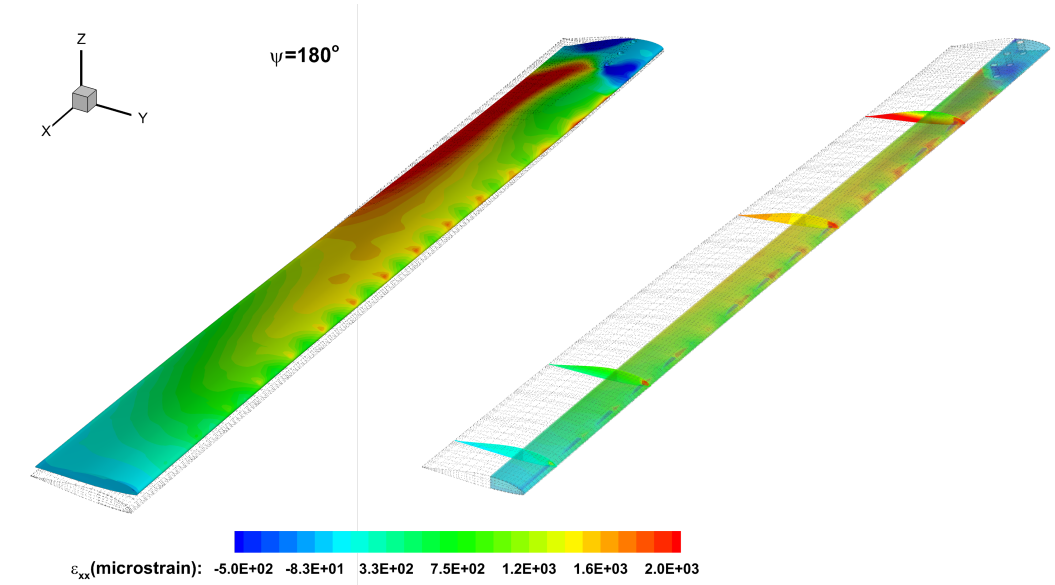

(c) $\psi = 180°$

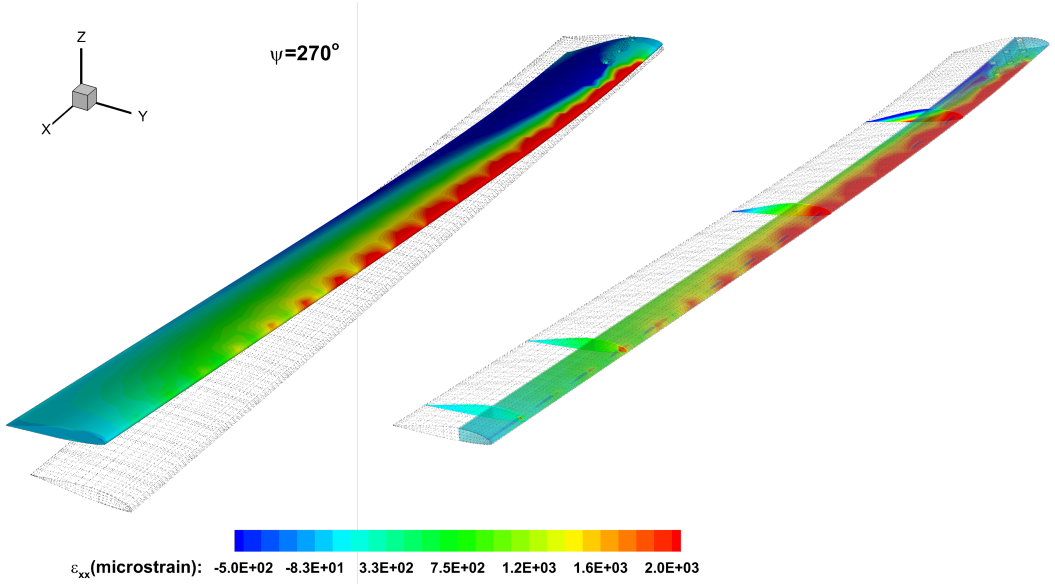

(d) $\psi = 270°$

Figure 6.52: Axial strain ϵ_{xx} distribution of straight blade ($M_{tip} = 0.4$, $\alpha_s = 4°$, $C_T/\sigma = 0.1$, $\mu = 0.3$).

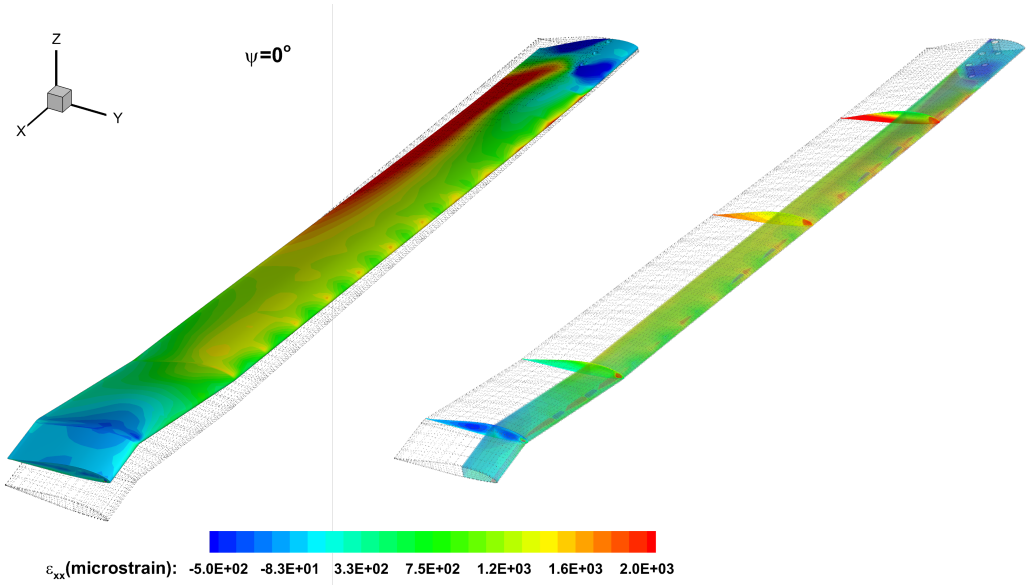

(a) $\psi = 0°$

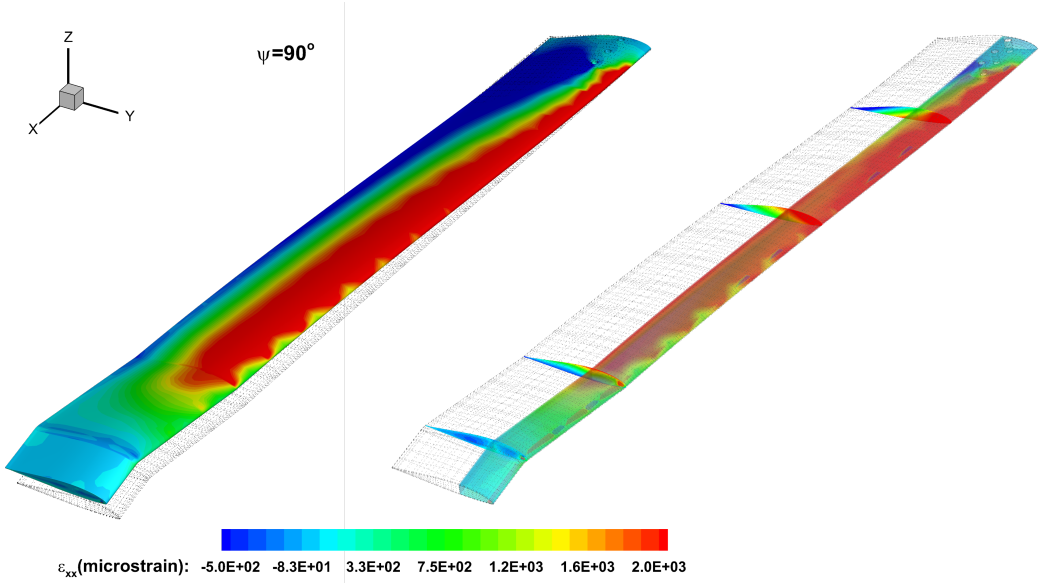

(b) $\psi = 90°$

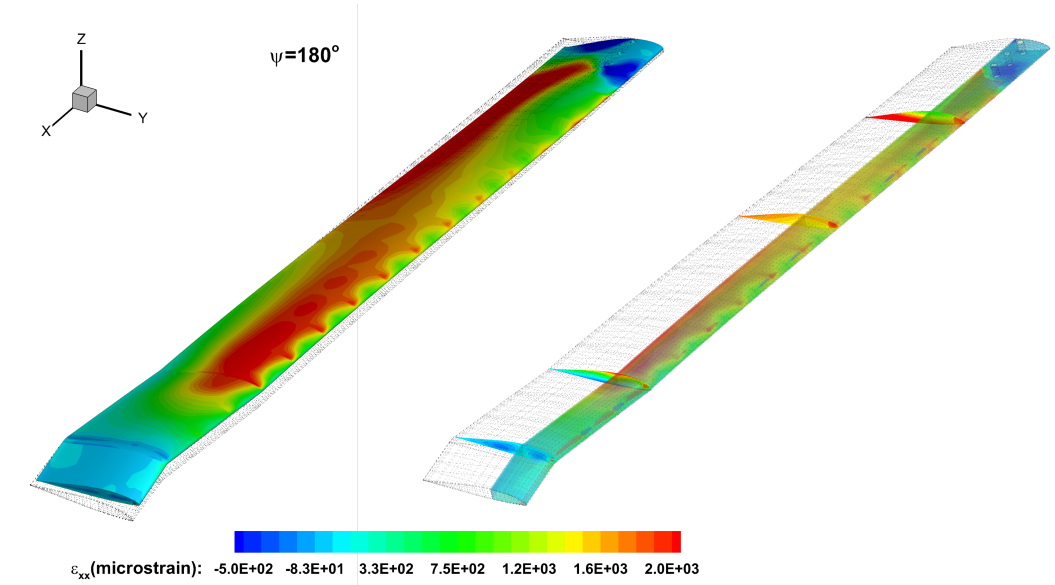

(c) $\psi = 180°$

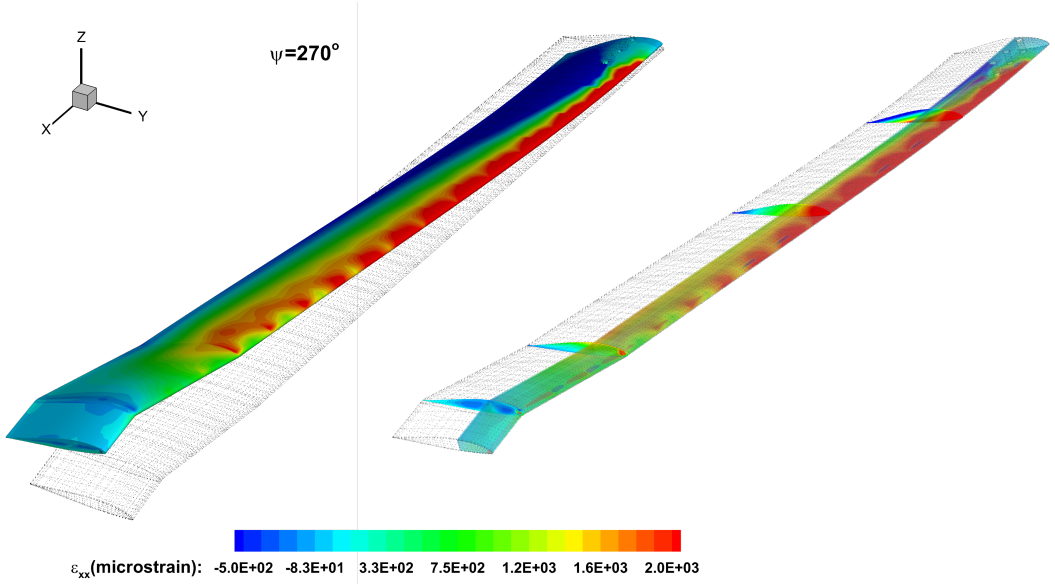

(d) $\psi = 270°$

Figure 6.53: Axial strain ϵ_{xx} distribution of double anhedral blade ($M_{tip} = 0.4$, $\alpha_s = 4°$, $C_T/\sigma = 0.1$, $\mu = 0.3$).

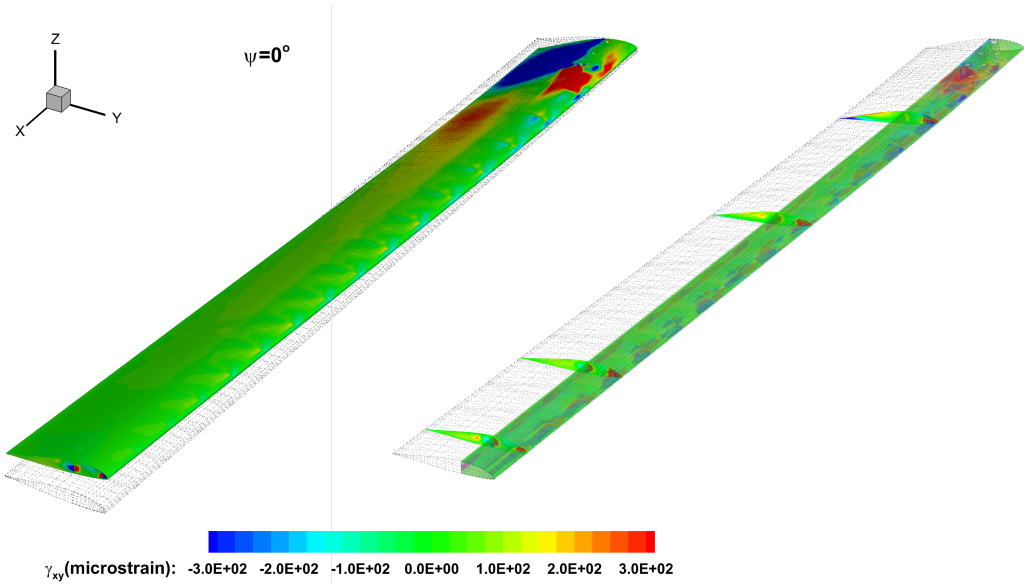

(a) $\psi = 0°$

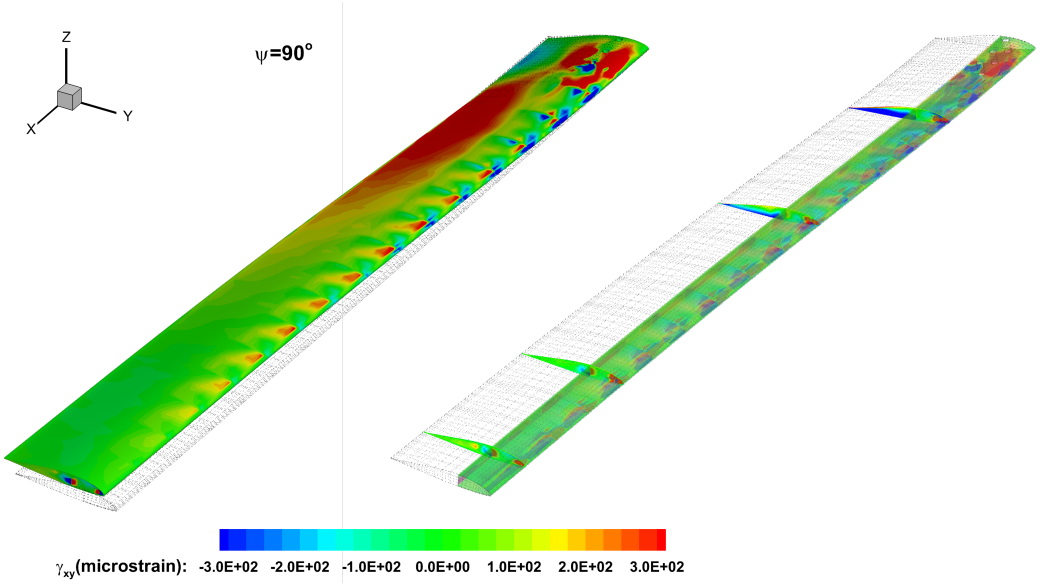

(b) $\psi = 90°$

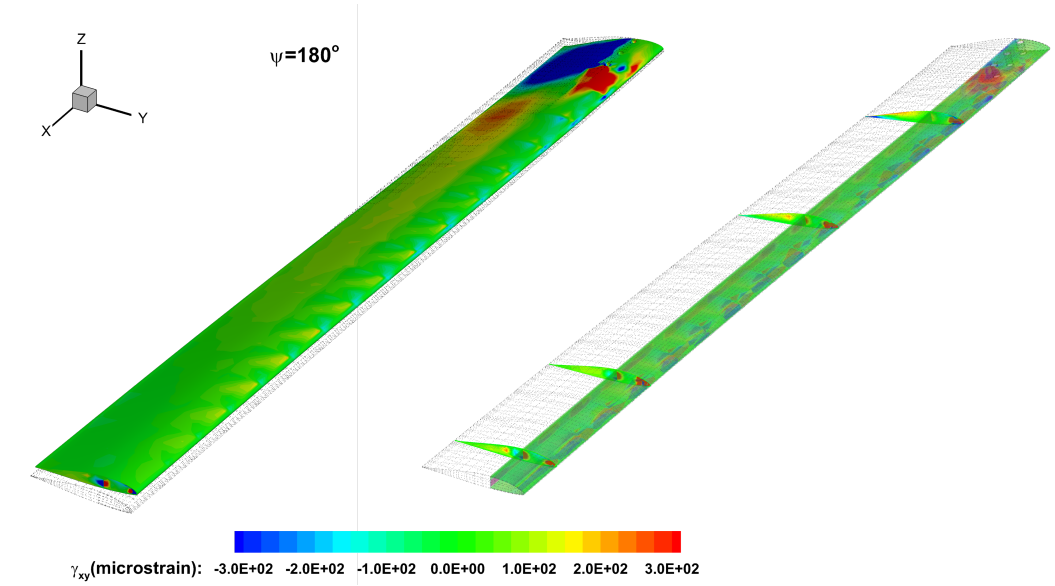

(c) $\psi = 180°$

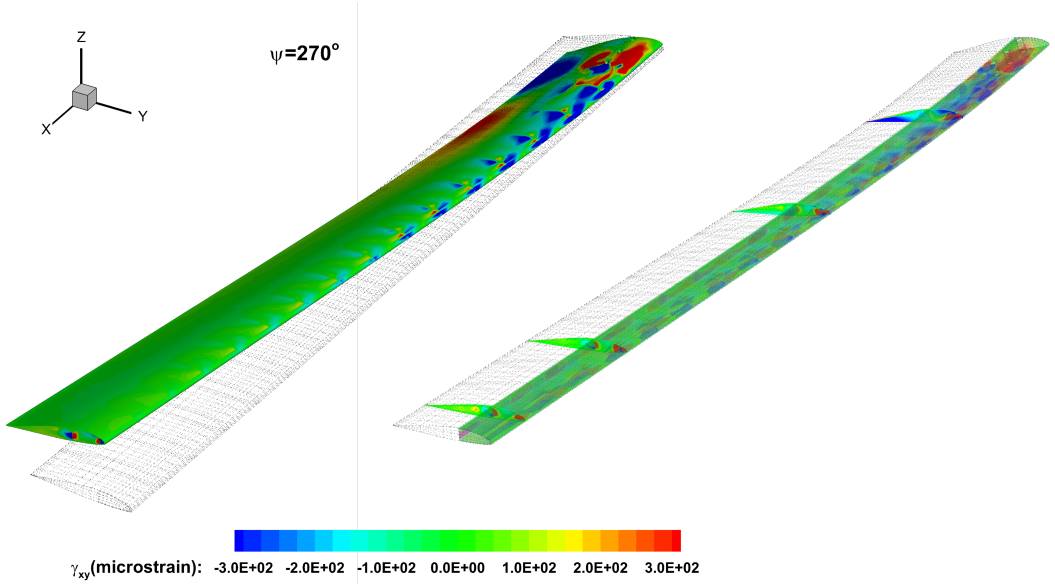

(d) $\psi = 270°$

Figure 6.54: In-plane shear strain γ_{xy} distribution of straight blade ($M_{tip} = 0.4$, $\alpha_s = 4°$, $C_T/\sigma = 0.1$, $\mu = 0.3$).

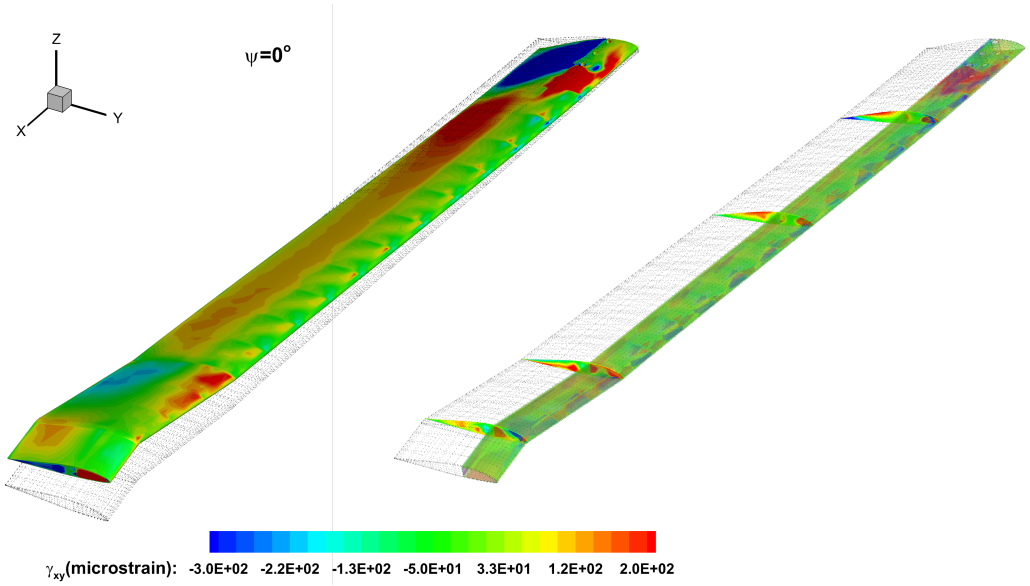

(a) $\psi = 0°$

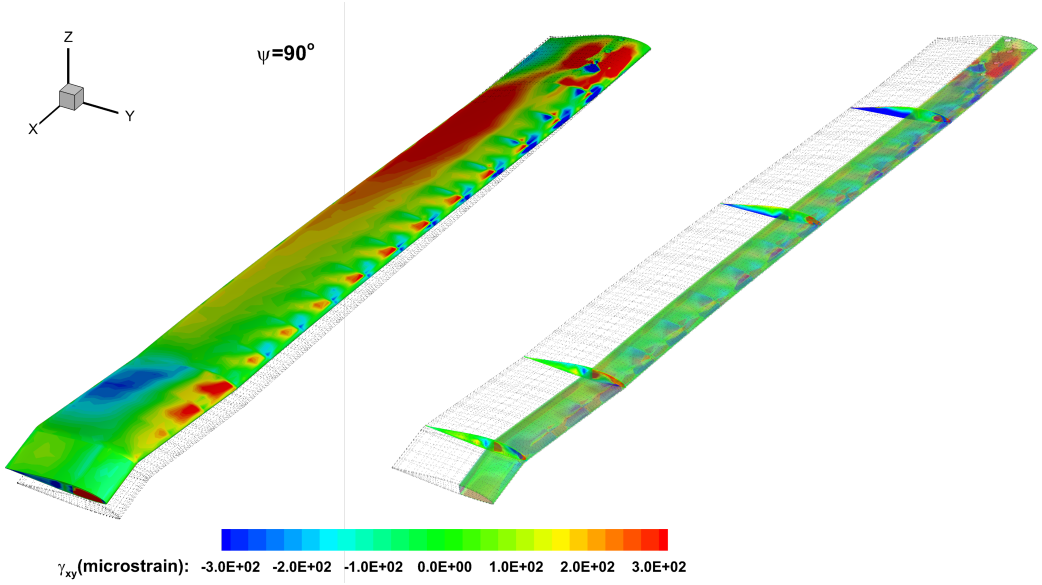

(b) $\psi = 90°$

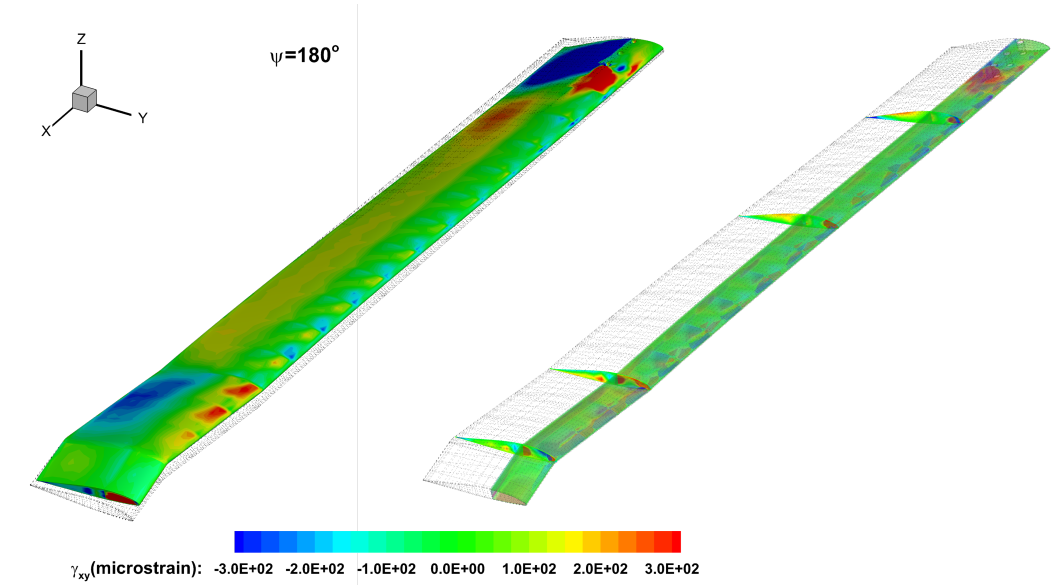

(c) $\psi = 180°$

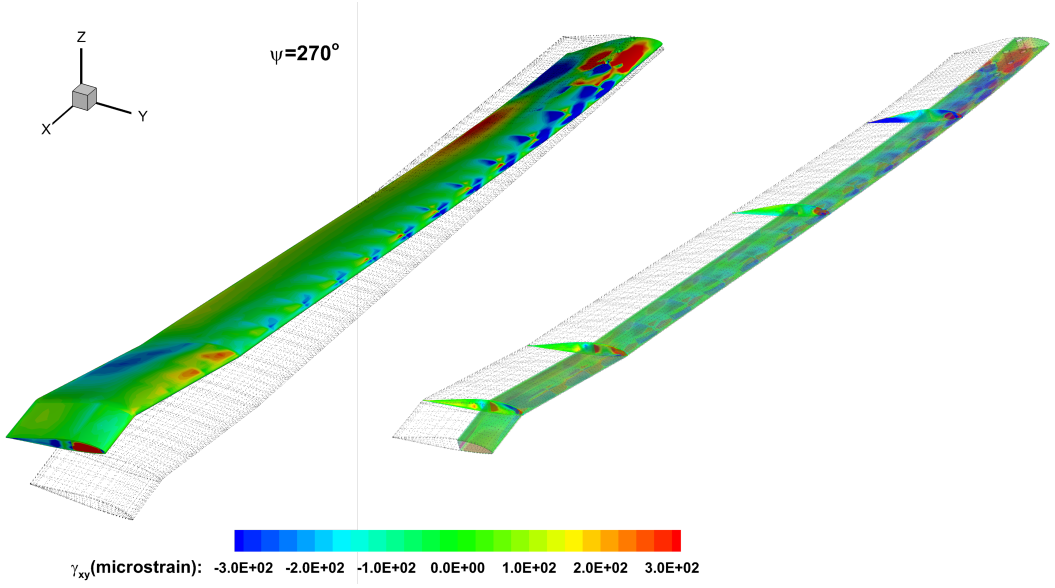

(d) $\psi = 270°$

Figure 6.55: In-plane shear strain γ_{xy} distribution of double anhedral blade ($M_{tip} = 0.4$, $\alpha_s = 4°$, $C_T/\sigma = 0.1$, $\mu = 0.3$).

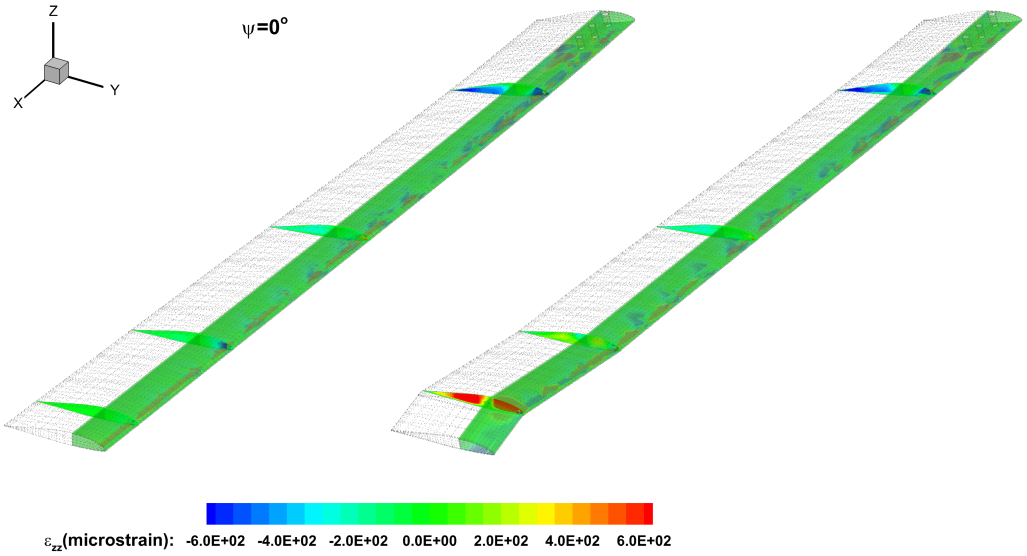

(a) $\psi = 0°$

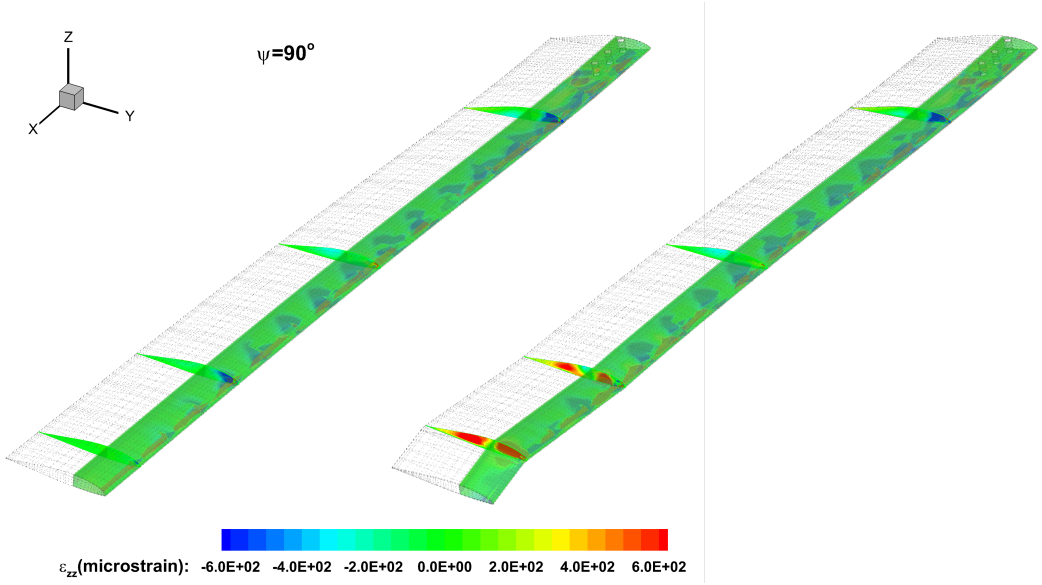

(b) $\psi = 90°$

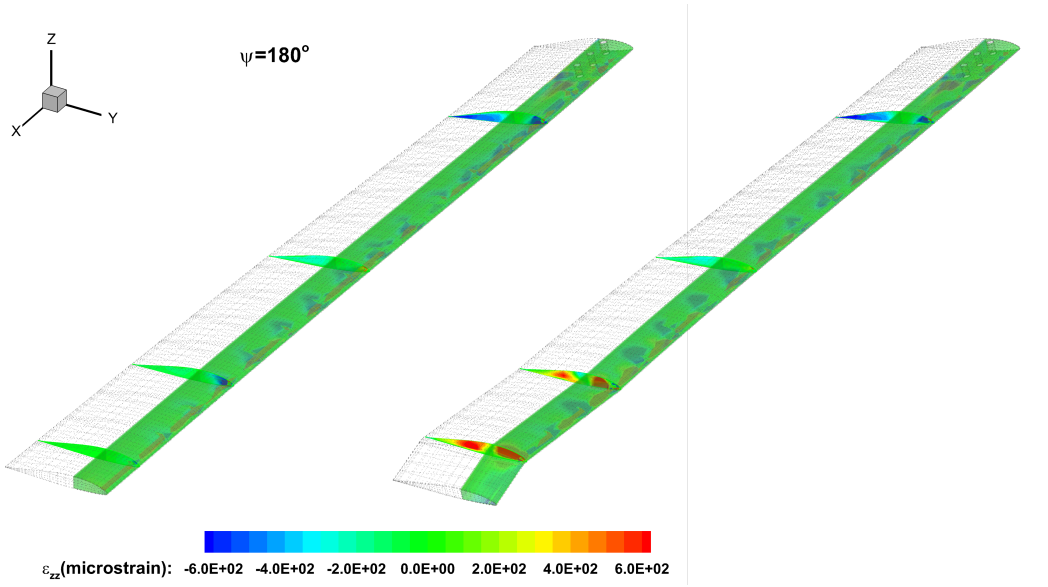

(c) $\psi = 180°$

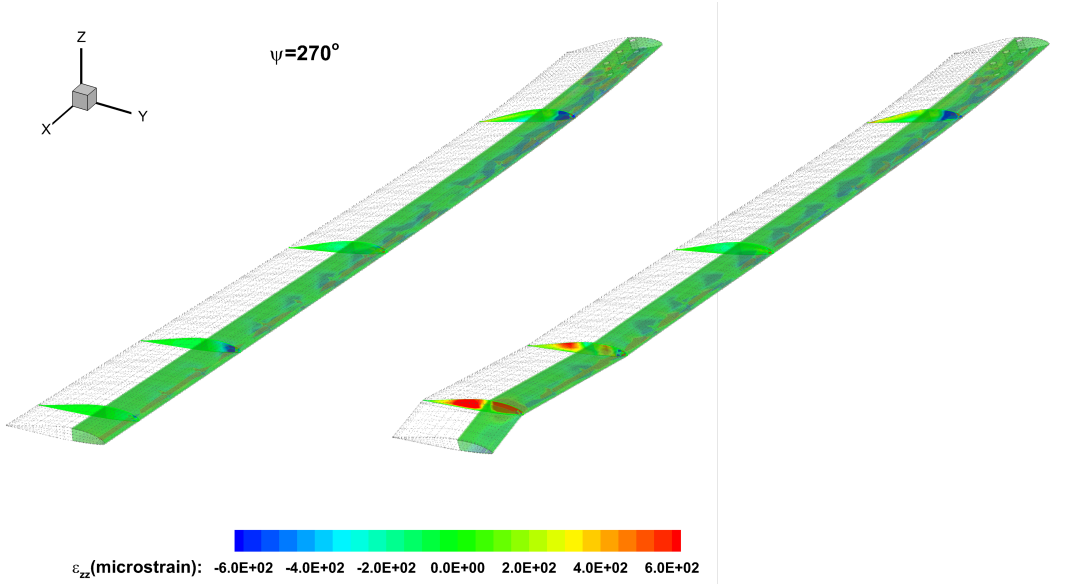

(d) $\psi = 270°$

Figure 6.56: Out-of-plane strain ϵ_{zz} distribution comparison ($M_{tip} = 0.4$, $\alpha_s = 4°$, $C_T/\sigma = 0.1$, $\mu = 0.3$).

6.5 Summary

In this chapter, the 3-D models of the straight blade and the double anhedral blade are used to study the impacts of the double anhedral tip. Analysis of frequencies and strains in vacuum, performance, vibration, loads, and strain/stress in hover and forward flight were conducted. Based on this investigation, the following conclusions are drawn:

1. For a hingeless rotor, the effect of the double anhedral tip starts to show from the second frequency and becomes significant in all higher frequencies. The double anhedral blade frequencies are lower due to the tip center of gravity offset appearing to make the blade softer.

2. In vacuum, the vertical center of gravity offset of the double anhedral blade introduces additional bending moment via centrifugal force which increases the root axial strain magnitude and strain compression concentration at the dihedral junction. Meanwhile, a pair of in-plane shear strain concentrations in the dihedral portion also result from the additional propeller moment generated by the tip geometry.

3. In hover, the influence of the double anhedral tip on rotor performance is limited. The highest Figure of Merit only increased by 0.7%.

4. The tip center of gravity offset of the double anhedral tip reduces the root flap, lag, and torsion moment in hover.

5. In forward flight, the straight rotor has a higher effective lift-to-drag ratio due to its higher propulsive force.

6. At a tip speed ratio of 0.1, the strong 1/rev flap bending moment of the double anhedral blade causes a 15% higher 4/rev vibratory hub vertical load.

7. Regardless of the spanwise location, the lag bending moments are dominated by 2/rev components in forward flight. And the double anhedral blade always has a higher oscillatory lag bending moment. As for torsional moment and pitch link load, the double anhedral blade also has more oscillatory loads.

Chapter 7: Summary and Conclusions

7.1 Summary

This study investigated the aeromechanics behavior of a Mach-scaled double anhedral composite rotor. Both experimental and analytical methods were employed to investigate the subject systematically. Double anhedral tips are a recent introduction in rotors with no research data available for understanding their behavior or modeling them adequately. The objectives were to bridge these gaps.

Double anhedral blades of 5.6-ft diameter were designed and fabricated. The blade has a D-spar, and there is a 5° dihedral portion from 80%R to 95%R and a 15° anhedral portion from 95%R to the tip. They were instrumented for strains and structural loads. A two-bladed hingeless hub was designed and fabricated for the vacuum chamber to measure rotating frequencies (fanplot). The hover tests were performed on the AGRC Mach-scaled hingeless rig. And the tests were carried out up to tip Mach number of 0.6, collective range of 0°-10°. The rotor performance, hub loads, blade structural loads, pitch link loads, and surface strains were measured.

A double anhedral tip is a 3-D structure. Accordingly, a 3-D model was developed with CATIA (CAD), Cubit (hexahedral meshing), and X3D (aeromechanics). The 3-D CAD was constructed jointly with Boeing to ensure the geometry was

representative of a modern rotor yet generic enough to be open source for U.S. Gov-industry-academia joint study. The meshing used 27-node solid hexahedral elements, as needed by X3D. The pitch bearing was modeled with a joint commanded by a control input. In total there were 3427 elements and $\approx 100,000$ degrees of freedom. Properties of the composite plies were acquired through in-house four-point bending coupon tests. The aerodynamic model used C-81 decks and a lifting line with a refined free wake. The data acquired from tests were used to validate the model.

A 3-D model of a straight blade was also developed as a baseline for comparison. This model had the same external and internal structure except for the tip. Ideally, such a model should be fabricated, but fabrication was not pursued due to the lack of resources. By comparing the behavior of the analytical models, important insights could be gained. The models were also used to study forward flight loads. Wind-tunnel tests were planned but were shelved due to the prolonged shut-down of the tunnel.

7.2 Key Conclusions

This thesis is one of the first systematic studies of a double anhedral tip composite rotor in the public domain. Based on the study, the following key conclusions were drawn. The conclusions are given in the order they were learned, not importance.

1. Composite blades with double anhedral tip were successfully fabricated using

mold pressure alone. There is no additional treatment needed for the skin and the spar, but the foam core should be carefully separated at the tip junctions and assembled separately. The fabrication process documented in this study allows all test blades to have a high degree of similarity ($\pm 0.3\%$ of mass).

2. The strain-load static calibration for blade structural loads can be contaminated by the strain concentration from the segmented leading-edge weights. Therefore, some points should be avoided for strain gauge placement. The location of strain sensors in the 3-D model should also avoid these strain concentration regions accordingly.

3. There were seven non-rotating frequencies and six rotating frequencies captured in the vacuum chamber from $0 - 1200$ RPM. These frequency data were limited only by the motor RPM, yet the cross-over of the first flap and lag modes were captured. The second lag frequency was missed. The 3-D model predictions had a satisfactory agreement with the measured frequencies.

4. The 3-D model was validated with blade surface strains measured in vacuum. The agreement was satisfactory once the pre-cone angle of the vacuum chamber hub was taken into account. The pre-cone angle was small, approximately -1 to -2°, and a small deviation from the intended design. This activity demonstrated that 3-D was capable of capturing the true behavior of the rotor, as-built, including un-intended imperfections of the test setup.

5. In the hover test, a maximum Figure of Merit of 0.713 was observed at all M_{tip}

(0.4-0.6) near a blade loading of $C_T/\sigma = 0.117$. This indicated that relatively high hover performance can be achieved for a model-scale rotor when designed properly. A proper design has smooth leading and trailing edges, smooth transition region, identical blade weight, and center of gravity location. The 3-D model had a satisfactory agreement with performance data.

6. The prediction of the flap and lag bending moments at $40\%R$, pitch link loads, and surface strains at $30\%R$ and $80\%R$ captured the trends generally, over the collective and tip Mach number range. The prediction of the torsional moment at $40\%R$ does not agree with the measurement. Based on the comparison with pitch link load and the simplicity of the control system, it might be reasonable to assume the measurement was incorrect. But the reasons were not clear, so this remains to be resolved in the future.

7. When compared with the predicted fanplot of the straight blades, only the first frequency of the double anhedral blade was identical. The frequencies were all different from the second to the higher modes. The double anhedral blade frequencies were lower. The local center of gravity offset at the tip appears to make the blade softer.

8. Limited improvement in hover performance was predicted by the double anhedral blade. The maximum Figure of Merit was increased by a negligible 0.7% at a blade loading of 0.12. The lifting line model with a single tip vortex wake is not expected to capture any 3-D tip flow effect precisely. The data acquired however would provide CFD researchers a baseline to pursue this

problem.

9. In hover, the inboard and midspan flap bending moments decrease for the double anhedral blade. The double anhedral tip also leads to a reduction in lag bending moment though out the span. In the inboard region, the torsional moment of the double anhedral blade is lower. However, it is higher at the midspan. The double anhedral tip also decreases the pitch link load, and the reduction grows with the collective. The main source of these effects is the vertical center of gravity offset of the tip, which generates additional bending moments and propeller moments with significant ramification inboard.

10. Strong 3-D patterns are observed in predicted strain on the double anhedral blade. In hover, midspan axial strain can be higher both externally and internally. There is also a compression zone at the tip dihedral junction. In-plane shear strain concentrations also appear in the dihedral region, due to an additional propeller moment introduced by the C.G. offset there. Out-of-plane strains increase at the dihedral and anhedral junctions.

11. In forward flight, the performance of the straight rotor is higher, and the difference worsens with the tip speed ratio. At the tip speed ratio of 0.3, the effective lift-to-drag ratio of the straight rotor is higher by 16.7%. However, the controls needed to trim the rotor remain the same with or without the double anhedral tip.

12. The vibratory hub loads in forward flight are significantly influenced by the

double anhedral tip. Of the two high vibration regions, the one at low speed, near the $\mu = 0.1$ transition, can be predicted by lifting line with free wake. At that tip speed ratio, the 4/rev vibratory vertical hub force, hub moment, and hub torque increase by 15%, 100%, and 18% respectively with the double anhedral tip.

13. The inboard oscillatory flap bending moment in forward flight is dominated by the 1/rev component at a low advance ratio, and the double anhedral blade has a high magnitude. As the tip speed ratio reached 0.3, the inboard 2/rev component outweighs the 1/rev. The double anhedral blade has a lower 2/rev moment.

14. Regardless of the spanwise location, the lag bending moments in forward flight are dominated by the 2/rev component. Its magnitude at 30%R first decreased by 20% when $\mu = 0.1$ then increased by 2.5 times when $\mu = 0.3$. The double anhedral blade always has a higher 2/rev lag bending moment.

15. The double anhedral blade has a lower mean and peak-to-peak torsion moment. At 30%R, the straight blade torsion moment is dominated by the 2/rev component regardless of the tip speed ratio. The double anhedral blade is also dominated by 2/rev, however, the magnitude is much lower.

7.3 Contributions

The main contributions of this thesis are the following.

1. The successful development of a double anhedral Mach-scaled rotor model. It is a joint industry-academia open-source model. The design and fabrication method for advanced geometry blades, such as double anhedral tip, was developed in Maryland.

2. A vacuum chamber hub was developed that would allow the measurement of rotating frequencies. The excitation mechanism was designed specially and fabricated in-house. Combined with pressure control, the test system can be used for vacuum, seal-level, high-altitude, and even Mars conditions. This facility is new in Maryland and unique in academia.

3. A unique set of test data on a double anhedral tip was acquired. Including frequencies, strains, rotor performance, structural loads, and strains well documented and freely available to U.S. Government, industry, and academia. These data will be used by Boeing to insert X3D into their workflow. This data will also be used by U.S. Army Helios to understand double anhedral tip flow.

4. The data will support the exploration of advanced 3-D CFD/CSD fluid-structure interface mythologies of the future.

7.4 Recommendations for Future Work

This investigation is the first step in understanding the aeromechanics behaviors of double anhedral tip composite rotor. Important works remain for the future.

The source of high vibration in forward flight and its potential remedy remain to be resolved. The current rotor provides a suitable base for launching into that endeavor. The roadmap for that task ahead is listed below.

1. First, the forward flight tests that have been postponed by the Glenn L. Martin wind tunnel closure must be carried out as soon as possible. It remains a crucial part of this project. The performance, blade structural loads, pitch link loads, surface strains, and hub vibratory loads must be measured. In addition, significant effort must be devoted to measure aerodynamic pressures and airloads near the tip. Airloads would require the placement of at least 5 surface taps on either side of the airfoil.

2. The current tests and analysis were all carried out for a hingeless rotor. It is recommended to repeat the same investigation on an articulated hub. This would be a good training exercise for a new student. The same blades can be used only the hub will need to be changed.

3. The high fidelity 3-D structural model should be coupled with a 3-D CFD model to perform an Integrated 3-D (I3D) analysis. The true flow field of the double anhedral tip particularly in forward flight required 3-D CFD for precise resolution of the surface pressures and shear stresses.

4. Once the vibratory loading problem is resolved, attention should be paid to stability measurements, particularly at slowed RPM, and high-speed/high-μ conditions.

Appendix A: Engineering Drawings

List of engineering drawings:

A.1 Vacuum Chamber Hub Central Block

A.2 Vacuum Chamber Hub End Block

A.3 Vacuum Chamber Hub Blade grip

A.4 Vacuum Chamber Hub Blade Adaptor

A.5 Vacuum Chamber Hub Pitch Horn

A.6 Vacuum Chamber Hub Pitch Link

A.7 Vacuum Chamber Hub Pitch arm

A.8 Vacuum Chamber Hub Shaker Housing

A.1 Vacuum Chamber Hub Central Block

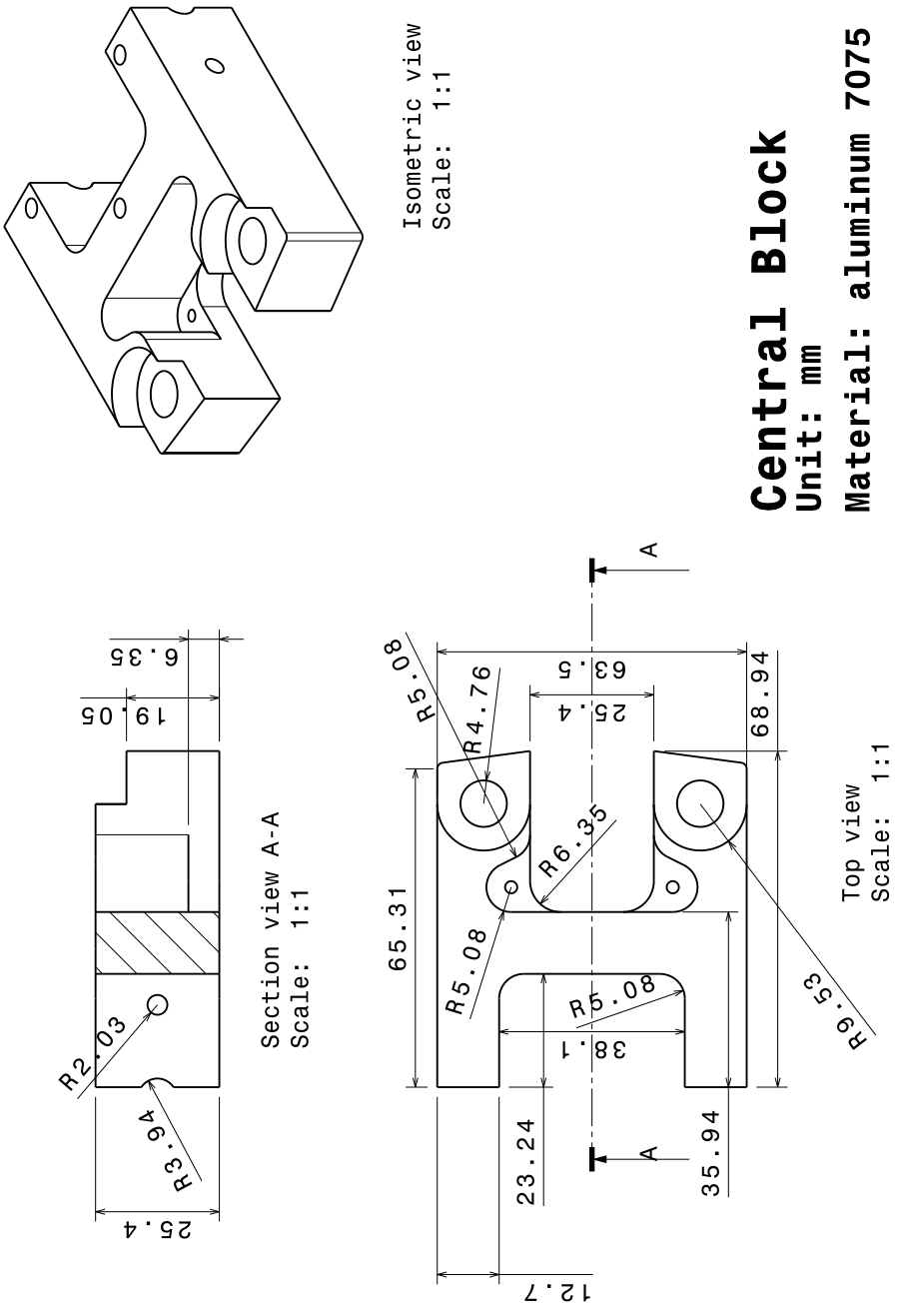

A.2 Vacuum Chamber Hub End Block

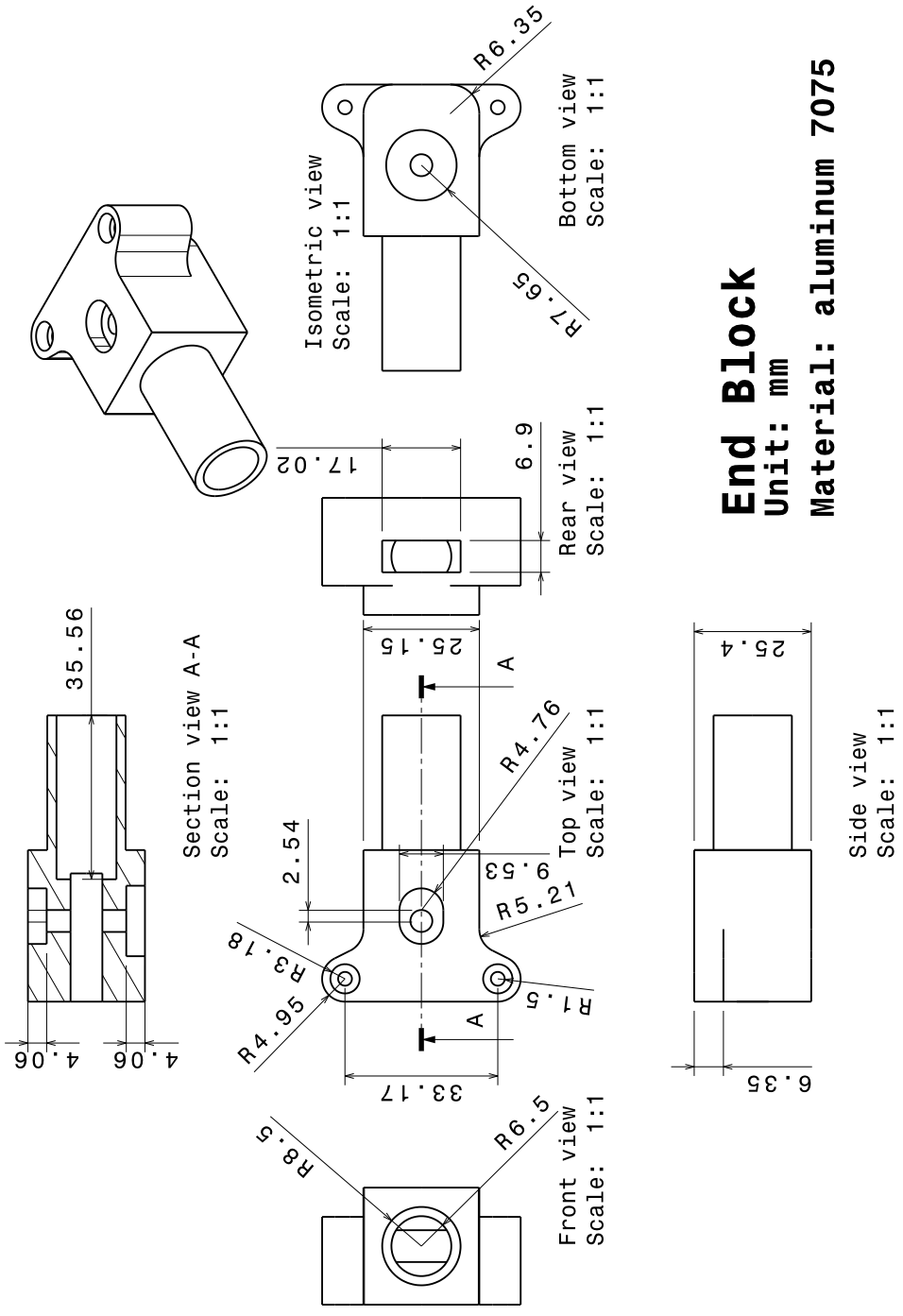

A.3 Vacuum Chamber Hub Blade grip

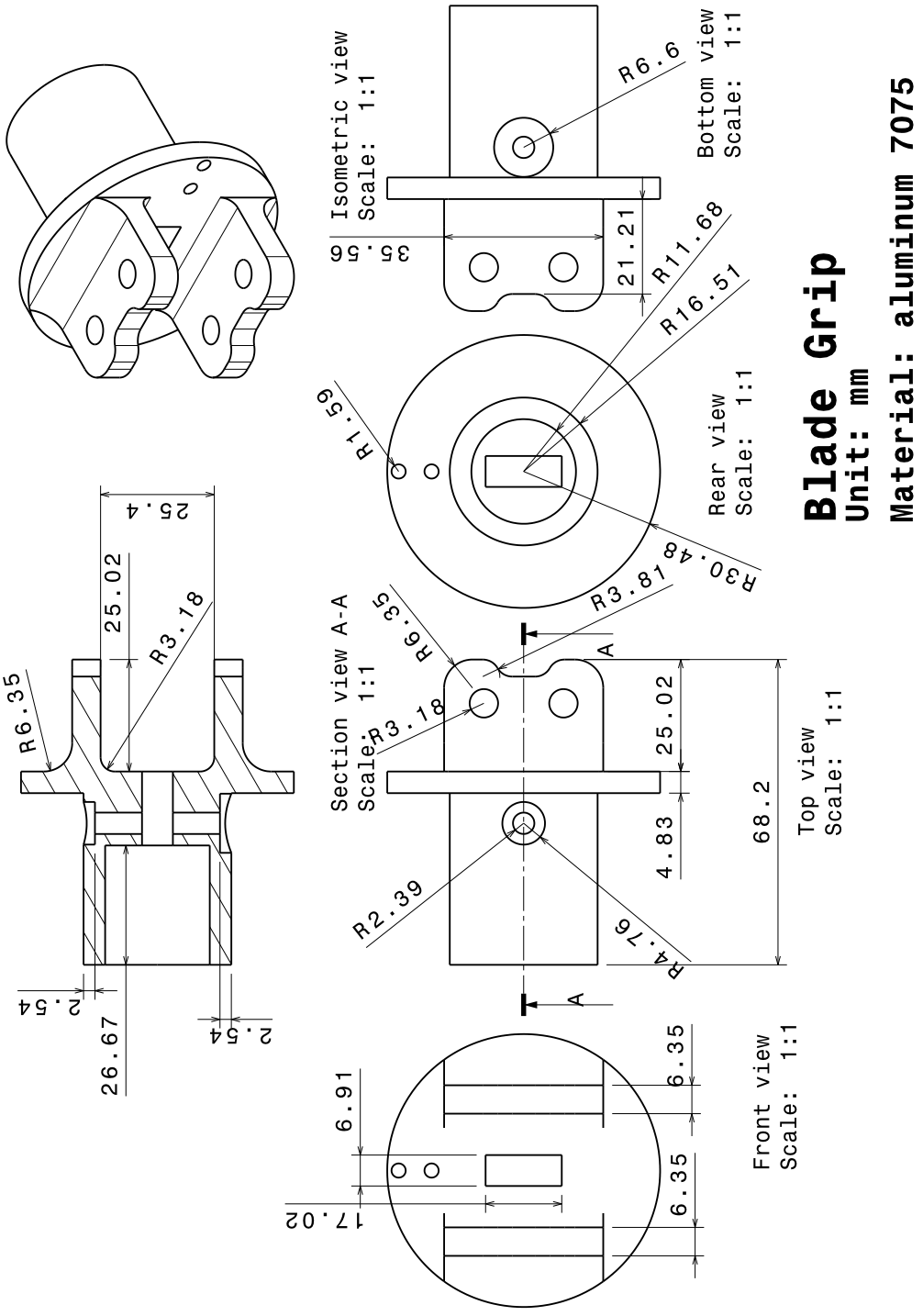

A.4 Vacuum Chamber Hub Blade Adaptor

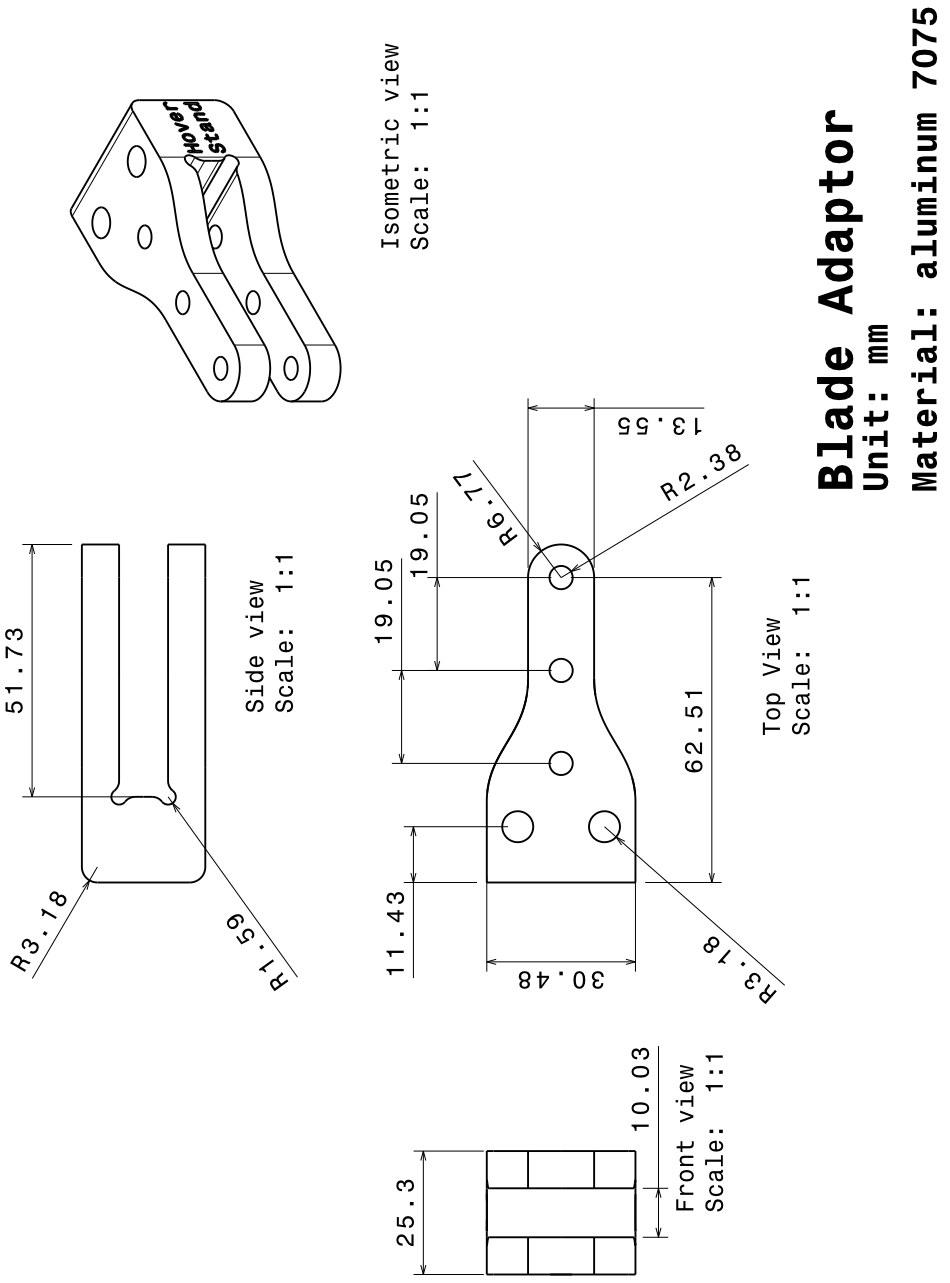

A.5 Vacuum Chamber Hub Pitch Horn

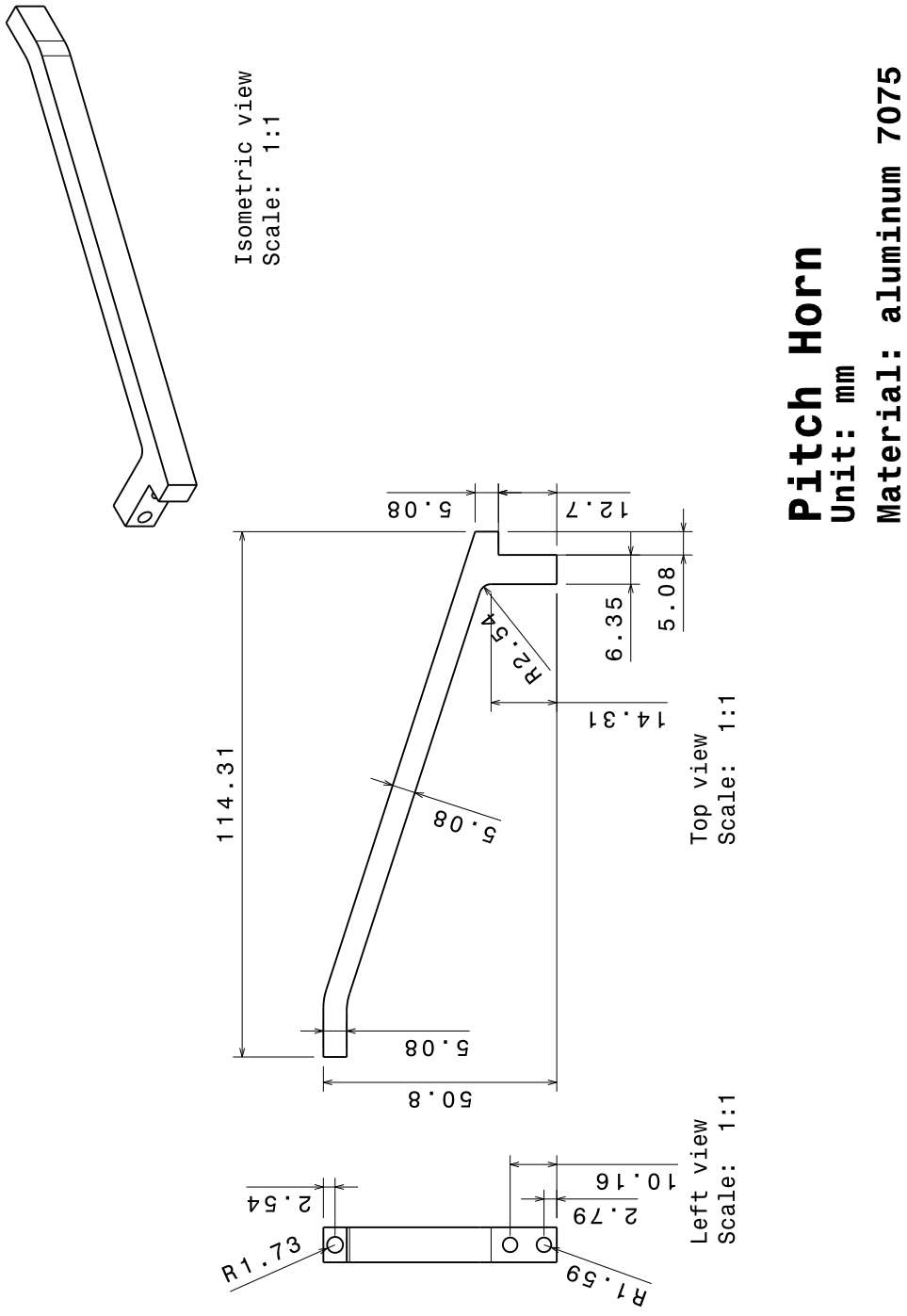

A.6 Vacuum Chamber Hub Pitch Link

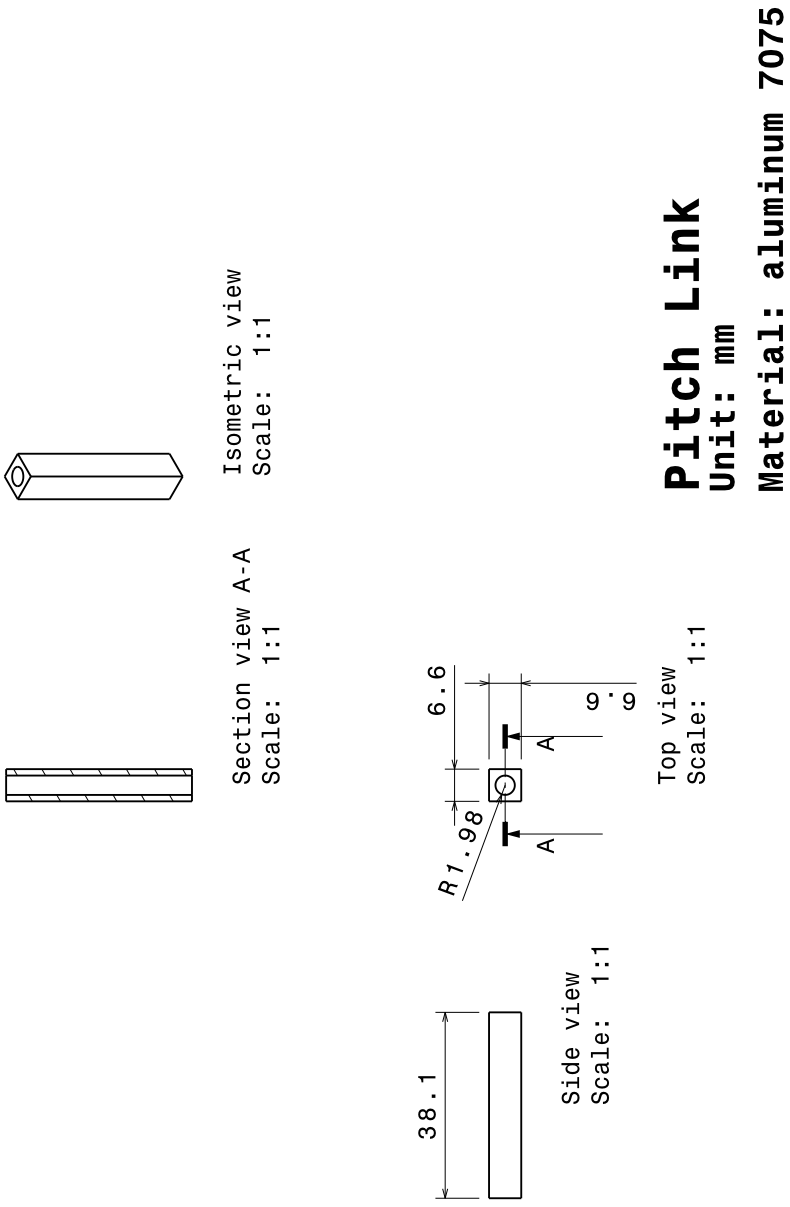

A.7 Vacuum Chamber Hub Pitch arm

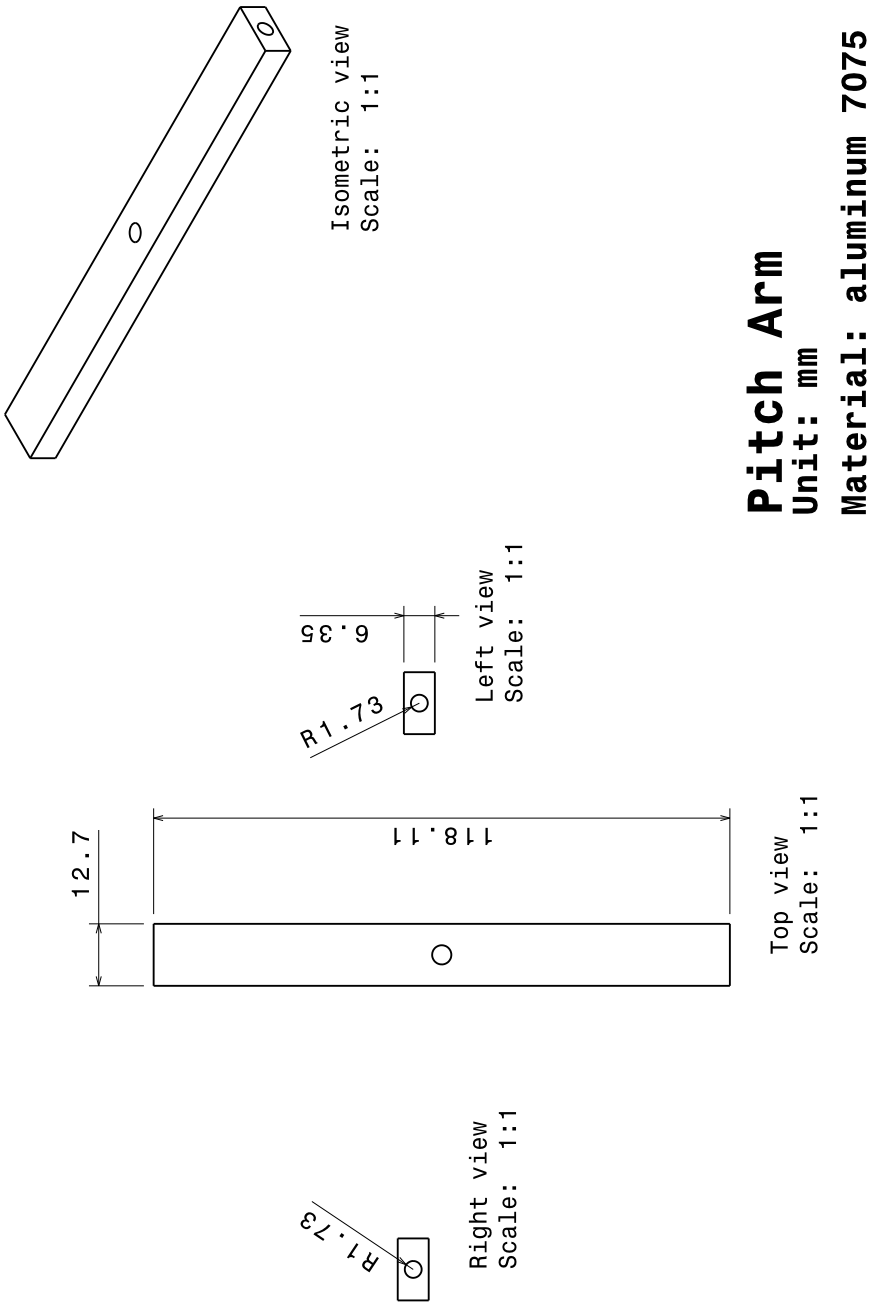

A.8 Vacuum Chamber Hub Shaker Housing

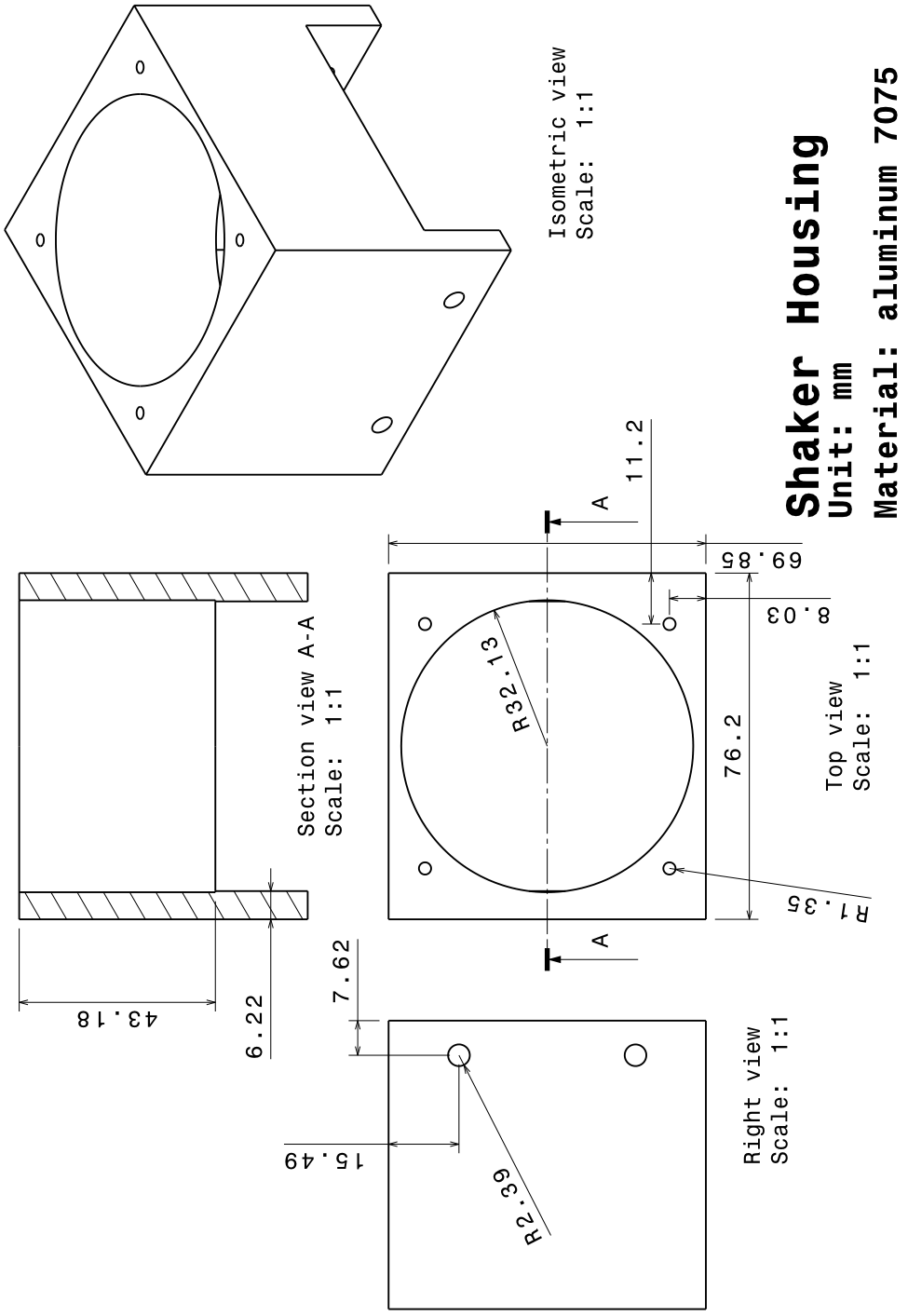

Appendix B: Test Data

B.1 Vacuum Frequency Test Data

Table B.1: Frequency test data.

RPM	Frequency (Hz)
0	8.7
0	8.8
0	8.9
0	18.3
0	19.2
0	19.5
0	52.2
0	52.4
0	53
0	111.2
0	112.1
0	112.7
0	132.2
0	133.8
0	134.2
0	221

RPM	Frequency (Hz)
0	222.2
0	239.3
0	334.7
0	341.9
200	9.8
200	9.8
200	9.8
200	19.5
200	20
200	53.1
200	54.7
200	116.2
200	134.8
200	136.7
200	140.2
200	208

RPM	Frequency (Hz)
200	224.3
400	11.7
400	13.2
400	19.5
400	19.5
400	20
400	55.7
400	107.9
400	132.8
400	142.6
400	142.9
400	212.3
400	214.4
400	240.3
600	20
600	20.2

RPM	Frequency (Hz)
600	56.6
600	129.9
600	221.4
600	225.6
600	227.9
800	18.1
800	222.6
800	231.4
1000	16.6
1000	21.9
1000	227.5
1000	229.5
1000	235.3
1200	25.4
1200	251.9

B.2 Hover Performance Test Data

Table B.2: Hover performance test data ($M_{tip} = 0.4$).

θ_{75}	C_T/σ	C_P/σ	FM
1	0.0182	0.002565	0.2138
1	0.0185	0.002578	0.2179
2.9	0.0348	0.003624	0.4008
3.1	0.037	0.003684	0.432
5	0.0572	0.0057	0.59
5	0.0578	0.00526	0.577
7	0.08	0.0077	0.66
7	0.082	0.0078	0.68
9	0.1087	0.0113	0.711

Table B.3: Hover performance test data ($M_{tip} = 0.5$).

θ_{75}	C_T/σ	C_P/σ	FM
2.9	0.0353	0.00355	0.417
2.98	0.0362	0.00362	0.4248
3	0.0362	0.00361	0.4252
4.9	0.0561	0.0052	0.5707
5.08	0.0591	0.00542	0.5926
6.98	0.0827	0.00795	0.6685
7.03	0.0847	0.0081	0.6802
8.9	0.1128	0.01188	0.7126

Table B.4: Hover performance test data ($M_{tip} = 0.6$).

θ_{75}	C_T/σ	C_P/σ	FM
1	0.0182	0.00254	0.216
2	0.0277	0.0031	0.335
2.7	0.0348	0.0036	0.404
3	0.0377	0.0037	0.441
4	0.0474	0.00451	0.512
4.9	0.0596	0.00554	0.5879
6	0.0742	0.00691	0.6534

Bibliography

[1] Leishman, J. G., Principles of Helicopter Aerodynamics, second edition, Cambridge University Press, 2006.

[2] Stroub, R. H., Rabbott, J. P. and Niebanck, C. F., "Rotor Blade Tip Shape Effects on Performance and Control Loads from Full-Scale Wind Tunnel Testing", *Journal of the American Helicopter Society* Vol. 24,No. 4, 1979, pp. 28–35.

[3] McVeigh, M. A. and McHugh, F. J., "Influence of Tip Shape, Chord, Blade number, and Airfoil on Advanced Rotor Performance", *Journal of the American Helicopter Society* Vol. 29,No. 4, 1984, pp. 55–62.

[4] Althoff, S. L. and Noonan, K. W., "Effect of Blade Planform Variation on a Small-scale Hovering Rotor," NASA Technical Memorandum 4164, 1990.

[5] Bingham G. J., "The Aerodynamic Influences of Rotor Blade Airfoils, Twist, Taper and Solidity on Hover and Forward Flight Performance", The 37th annual forum of the American Helicopter Society, New Orleans, LA, May 1981. pp. 37–50.

[6] Berry J. D., "Quarter-scale Testing of An Advanced Rotor System for the UH-1 Helicopter", The 37th annual forum of the American Helicopter Society, New Orleans, LA, May 1981. pp. 456–62.

[7] Prouty, R., Helicopter Aerodynamics Volume I, Lulu. com., 2009.

[8] Spivey, R. F., "Blade Tip Aerodynamics—profile and Planform Effects", The 24th annual national forum of the American Helicopter Society, Washington, DC, 1968. p. 205.

[9] Spivey, W. A. and Morehouse, G. G., "New Insights into the Design of Swept-tip Rotor Blades", The 26th annual national forum of the American Helicopter Society, Washington, DC, 1970.

[10] Wilby, P. G. and Philippe, J. J., "An Investigation of the Aerodynamics of an RAE Swept Tip using a Model Rotor", The 8th European rotorcraft Forum, Aix-en-Provence, France, Aug 1982, TP no. 1982-76, 1982. 15 p.

[11] Mantay, W. R. and Yeager Jr, W. T., "Parametric Tip Effects for Conformable Rotor Applications", The 9th European rotorcraft Forum, Stresa, Italy, 1983. p. 53.1–29.

[12] Riley, M. J., "Measurements of the Performance of a Helicopter Swept Tip Rotor in Flight", The 12th European rotorcraft Forum, Garmisch-Partenkirchen, West Germany, 1986.

[13] Kim, K. C. and Chopra, I., "Aeroelastic Analysis of Swept, Anhedral, and Tapered Tip Rotor Blades", *Journal of the American Helicopter Society* Vol. 37, No. 1, 1992, pp. 15–30.

[14] Epps, J. J. and Chandra, R., "The Natural Frequencies of Rotating Composite Beams with Tip Sweep", *Journal of the American Helicopter Society* Vol. 41, No. 1, 1996, pp. 29–36.

[15] Weller, W. H., "Experimental Investigation of Effects of Blade Tip Geometry on Loads and Performance for an Articulated Rotor System," NASA TP-1303. AVRADCOM TR 78-53, 1979.

[16] Mueller, R., "The Influence of Winglets on Rotor Aerodynamics", The 12th European rotorcraft Forum, Garmisch-Partenkirchen, West Germany, 1986. p. 34.1–34.15.

[17] Mueller, R., "Winglets on Rotorblades in Forward Flight—a Theoretical and Experimental Investigation", The 14th European rotorcraft Forum, Milano, Italy, 1988.

[18] Nagel, F., "Wings With End Plates", Memo. Rep. 130, Eng. Div., McCook Field, Nov. 4, 1924.

[19] Hemke, P. E., "Drag of Wings with End Plates", NACA-TR-267, 1928.

[20] Mangler, W., "The Lift Distribution of Wings with End Plates", NACA-TM-856, 1938.

[21] Whitcomb, R. T., "A Design Approach and Selected Wind Tunnel Results at High Subsonic Speeds for Wing-tip Mounted Winglets", NASA Technical Note L-10908, 1976.

[22] Whitcomb, R. T., "Methods for Reducing Aerodynamic Drag", NASA Conference Publication 2211, Proceedings of Dryden Symposium, Edwards, California, 16 September 1981.

[23] Jones, R. T. and Lasinski, T. A., "Effects of winglets on the induced drag of ideal wing shapes", NASA Technical Memorandum A-8329, 1980.

[24] Eppler, R., "Induced drag and winglets", *Aerospace science and Technology* Vol. 1, No. 1, 1997, pp. 3–15.

[25] Al Sidairi, K. A. and Rameshkumar, G., "Design of winglet device for aircraft", *International Journal of Multidisciplinary Sciences and Engineering* Vol. 7, No. 1, 2016, pp. 23–30.

[26] Faye, R., Laprete, R. and Winter, M., "Blended winglets", Aero, Boeing (17), January. 2002.

[27] Johansen, J. and Sørensen, N. N., "Numerical Analysis of Winglets on Wind Turbine Blades using CFD", In European Wind Energy Congress. Milano: EWEA, 2007.

[28] Herrick, L. L., et al., "Blunt-leading-edge raked wingtips," ed: Google Patents, 2000.

[29] Halpert, J., Prescott, D., Yechout, T. and Arndt, M., "Aerodynamic optimization and evaluation of KC-135R winglets, raked wingtips, and a wingspan extension", The 48th AIAA Aerospace Sciences Meeting Including the New Horizons Forum and Aerospace Exposition, Orlando, Florida, January, 2010.

[30] McLean, D., "Wingtip Devices: What they Do and How They Do it", the Boeing Performance and Flight Operations Engineering Conferncee, 20075.

[31] Guerrero, J. E., Wittkowski, K. and Sanguineti, M, "Variable Cant Single Winglets for Improvement of Aircraft Flight Performance", 2019.

[32] Muller, R., "Special Vortices at a Helicopter Rotor Blade", *Journal of the American Helicopter Society* Vol. 35, No. 4, 1990, pp. 16–22.

[33] Desopper, A., Lafon, P., Ceroni, P. and Philippe, J. J., "10 Years of Rotor Flows Studies at ONERA - State of the Art and Future Studies", ONERA, TP, 1986, p.12.

[34] Desopper, A., Lafon, P., Philippe, J. J. and Prieur, J., "Effect of an Anhedral Sweptback Tip on the Performance of a Helicopter Rotor", *VERTICA* Vol. 12, No. 3, 1988, pp. 345-355.

[35] Vuillet, A., Allongue, M., Philippe, J. J. and Desopper, A., "Performance and Aerodynamic Development of the Super Puma MK II Main Rotor with New SPP 8 Blade Tip Design", The 15th European rotorcraft Forum, Amsterdam, Netherlands, 1989.

[36] Tung, C. and Lee, S., "Evaluation of Hover Performance Prediction Codes", The 50th annual forum of the American Helicopter Society, Washington, DC, May 1994.

[37] McAlister K. W., Tung, C. and Heinech, J. T., "Forced Diffusion of Trailing Vorticity from a Hovering Rotor", The 57th annual forum of the American Helicopter Society, Washington, DC, May 2001.

[38] Srinivas, V., Chopra, I. and Nixon, M. W., "Aeroelastic Analysis of Advanced Geometry Tiltrotor Aircraft", *Journal of the American Helicopter Society* Vol. 43, No. 3, 1998, pp. 212–221.

[39] Strawn, R. C., Caradonna, F. X. and Duque, E. P., "30 years of rotorcraft computational fluid dynamics research and development", *Journal of the American Helicopter Society*, Vol. 51, No. 1, 2006, pp. 5-21.

[40] Datta, A., Nixon, M. and Chopra, I., "Review of rotor loads prediction with the emergence of rotorcraft CFD", *Journal of the American Helicopter Society*, Vol. 52, No. 4, 2007, pp. 287-317.

[41] Le Pape, A. and Beaumier, P., "Numerical Optimization of Helicopter Rotor Aerodynamic Performance in Hover", The 29th European rotorcraft Forum, Friedrichshafen, Germany, 2003.

[42] Aiken, E. .W, Ormiston, R. A. and Young, L. A., "Future Directions in Rotorcraft Technology at NASA Ames Research Center", The 56th annual forum of the American Helicopter Society, Virginia Beach, VA, May 2000.

[43] Imiela, M., "High Fidelity Optimisation Framework for Helicopter Rotors", The 35th European rotorcraft Forum, Hamburg, Germany, 2009.

[44] Imiela, M., "Investigation of Aeroelastic Effects for a Helicopter Main Rotor in Hover", The 36th European rotorcraft Forum, Paris, France, 2010.

[45] Kumar, M. R. and Venkatesan, C., "Effects of Rotor Blade-tip Geometry on Helicopter Trim and Control Response", *The Aeronautical Journal* Vol. 121, No. 1239, 2017, pp. 637–659.

[46] Huang, S., Fan, F., Yuan, M. and Sun, W., "Aerodynamic Performance and Aeroacoustic Characteristics of Model Rotor with Anhedral Blade Tip in Hover", *Transactions of Nanjing University of Aeronautics and Astronautics* Vol. 35, No. 1, 2018, pp. 162–169.

[47] Iswahyudi, S. and Wibowo, S. B., "Effect of Blade Tip Shapes on the Performance of a Small HAWT: An investigation in a wind tunnel", *Case Studies in Thermal Engineering* Vol. 19, 2020, p. 100634.

[48] Uluocak, S., Perçin, M. and Uzol, O., "Experimental Investigation of Tip Anhedral Effects on the Aerodynamics of a Model Helicopter Rotor in Hover", *Aerospace Science and Technology* Vol. 113, 2021, p. 106671.

[49] Bousman, W. G., "Rotorcraft Airloads Measurements: Extraordinary Costs, Extraordinary Benefits the 31st Alexander Nikolsky Honorary Lecture", *Journal of the American Helicopter Society* Vol. 59, No. 3, 2014, pp. 1–30.

[50] Rabbott, Jr, R. P. and Churchill, G. B., "Experimental Investigation of the Aerodynamic Loading on a Helicopter Rotor Blade in Forward Flight", NACA-RM-L56I07, 1956.

[51] Norman, T. R., Shinoda, P., Peterson, R. L. and Datta A., "Full-Scale Wind Tunnel Test of the UH-60A Airloads Rotor", American Helicopter Society 67th Annual Forum Proceedings, Virginia Beach, VA, May 3–5, 2011.

[52] Flax, A. H., "The bending of rotor blades", *Journal of the Aeronautical Sciences* Vol. 14, No. 1, 1947, pp. 42-50.

[53] Yuan, S. W., "Bending of Rotor Blades in the Plane of Rotation", *Journal of the Aeronautical Sciences* Vol. 14, No. 5, 1947, pp. 285-293.

[54] DiPrima, R. C. and Handelman, G. H., "Vibrations of Twisted Beams", *Quarterly of Applied Mathematics* Vol. 7, No. 3, 1954, pp. 241-259.

[55] Houbolt, J. C. and Brooks, G. W., "Differential Equations of Motion for Combined Flapwise Bending, Chordwise Bending, and Torsion of Twisted Nonuniform Rotor Blades", NACA, TR-1346, 1957.

[56] Hodges, D. H. and Dowell, E. H., "Nonlinear Equations of Motion for the Elastic Bending and Torsion of Twisted Nonuniform Rotor Blades", NASA, TN-D-7818, 1974.

[57] Kvaternik, R. G. and Kaza, K. R., "Nonlinear Curvature Expressions for Combined Flapwise Bending, Chordwise Bending, Torsion, and Extension of Twisted Rotor Blades", NASA, TM-X-73, 1976.

[58] Johnson, W., "Aeroelastic Analysis for Rotorcraft in Flight or in a Wind Tunnel", NASA, TN-D-8515, 1977.

[59] Rosen, A. and Friedmann, P. P., "Nonlinear Equations of Equilibrium for Elastic Helicopter or Wind Turbine Blades Undergoing Moderate Deformation", NASA, CR-159478, 1978.

[60] Bir, G., Chopra, I. and Nguyen, K., 'Development of UMARC (University of Maryland Advanced Rotor Code)", The 46th annual forum of the American Helicopter Society, Washington, DC, May 1990.

[61] Crespo da Silva, M. R. M., "Flap-Lag-Torsional Dynamic Modelling of Rotor Blades in Hover and in Forward Flight, Including the Effects of Cubic Non-Linearities", NASA, CR-166194, 1981.

[62] Hodges, D. H., "Nonlinear Equations for Dynamics of Pretwisted Beams Undergoing Small Strains and Large Rotations", NASA, TP-2470, 1985.

[63] Johnson, W., 'Rotorcraft Aerodynamics Models for a Comprehensive Analysis", The 54th annual forum of the American Helicopter Society, Washington, DC, May 1998.

[64] Hong, C. H. and Chopra, I., "Aeroelastic Stability Analysis of a Composite Rotor Blade", *Journal of the American Helicopter Society* Vol. 30, No. 2, 1985, pp. 57–67.

[65] Bauchau, O. A., "A Beam Theory for Anisotropic Materials", *Journal of Applied Mechanics* Vol. 5, 1985, pp. 416–422.

[66] Bauchau, O. A. and Hong, C. H., "Large Displacement Analysis of Naturally Curved and Twisted Composite Beams", *AIAA Journal* Vol. 25, No. 11, 1987, pp. 1469–1475.

[67] Bauchau, O. A. and Hong, C. H., "Nonlinear Composite Beam Theory", *Journal of Applied Mechanics* Vol. 55, 1988, pp. 156–163.

[68] Hong, C. H. and Chopra, I., "Aeroelastic Stability Analysis of a Composite Bearingless Rotor Blade", *Journal of the American Helicopter Society* Vol. 31, No. 4, 1986, pp. 29–35.

[69] Smith, E. C. and Chopra, I., "Aeroelastic Response, Loads, and Stability of a Composite Rotor in Forward Flight", *AIAA Journal* Vol. 31, No. 7, 1993, pp. 1265–1273.

[70] Benquet, P. and Chopra, I., "Calculated Dynamic Response and Loads for an Advanced Tip Rotor in Forward Flight", The 15th European rotorcraft Forum, Amsterdam, Netherland, Sep. 1989.

[71] Celi, R. and Friedmann, P. P., "Structural Optimization with Aeroelastic Constraints of Rotor Blades with Straight and Swept Tips", *AIAA Journal* Vol. 28, No. 5, 1992, pp. 928-936.

[72] Bir, G. and Chopra, I., "Aeromechanical Stability of Rotorcraft with Advanced Geometry Blades", AIAA 34th Structures, Structural Dynamics and Materials Conference, La Jolla, California, April 1993.

[73] Ganguli, R. and Chopra, I., "Aeroelastic Optimization of an Advanced Geometry Helicopter Rotor", *Journal of the American Helicopter Society* Vol. 41, No. 1, 1996, pp. 18-28.

[74] Bauchau, O. A. and Kang, N. K., "A Multibody Formulation for Helicopter Structural Dynamic Analysis", *Journal of the American Helicopter Society* Vol. 38, No. 2, 1993, pp. 3-14.

[75] Ghiringhelli, G. L., Masarati, P., Mantegazza, P. and Nixon, M. W., "Multi-Body Analysis of the 1/5 scale Wind Tunnel Model of the V-22 Tiltrotor", The 55th annual forum of the American Helicopter Society, Montreal, Canada, May 1999.

[76] Saberi, H., Khoshlahjeh, M., Ormiston, R. A. and Rutkowski, M. J., "Overview of RCAS and Application to Advanced Rotorcraft Problems", The 4th AHS Decennial Specialist's Conference on Aeromechanics, San Francisco, California, January 2004.

[77] Truong, V. K., "Dynamics Studies of the ERATO Blade, Based on Finite Element Analysis", Proceedings of the 31st European Rotorcraft Forum, Florence, Italy, Sept. 2005.

[78] Yeo, H., Truong, K. V. and Chandra, R., "Comparison of One-dimensional and Three-dimensional Structural Dynamics Modeling of Advanced Geometry Blades", *Journal of Aircraft* Vol. 51, No. 1, 2014, pp. 226-235.

[79] Johnson, W. and Datta, A., "Requirement for Next Generation Comprehensive Analysis of Rotorcraft", AHS Specialist's Conference on Aeromechanics, San Francisco, CA, January 2008.

[80] Datta, A. and Johnson, W., "Three-Dimensional Finite Element Formulation and Scalable Domain Decomposition for High Fidelity Rotor Dynamic Analysis", The 65th annual forum of the American Helicopter Society, Grapevine, TX, May 2009.

[81] Datta, A. and Johnson, W., "A Multibody Formulation for Three Dimensional Brick Finite Element Based Parallel and Scalable Rotor Dynamic Analysis", ELORET CORP MOFFETT FIELD CA NASA AMES RESEARCH CENTER, May, 2010.

[82] Staruk, W., Chopra, I. and Datta, A., "Three-Dimensional CAD-Based Structural Modeling for Next Generation Rotor Dynamic Analysis", The 70th annual forum of the American Helicopter Society, Quebec, Canada, May 2014.

[83] Staruk, W., Datta, A., Chopra, I. and Jayaraman, B., "An Integrated Three-dimensional Aeromechanics Analysis of the NASA tilt Rotor Aeroacoustic Model", *Journal of the American Helicopter Society* Vol. 63, No. 3, 2018, pp. 1-12.

[84] Ward, E., Chopra, I., and Datta, A., "Rotation-frequency-driven Extension–torsion Coupled Self-twisting Rotor Blades", *Journal of Aircraft*, Vol. 55, No. 5 , 2018, pp. 1929-1941.

[85] Chi, C., Datta, A., Chopra, I., and Chen, R., "Three-Dimensional Strains on Twisted and Swept Composite Rotor Blades in Vacuum", *Journal of Aircraft*, Vol. 58, No. 1, 2021, pp. 1-16.

[86] Lumba, R. T. and Datta, A., "Scalable Domain Decomposition for Large-Scale Multibody-3D Finite Element Structures", In AIAA Scitech 2021 Forum, p. 1078.

[87] Patil, M., and Datta, A., "A Scalable Time-Parallel Solution of Periodic Rotor Dynamics in X3D", *Journal of the American Helicopter Society*, Vol. 66, No. 4, 2021, pp. 1-16.

[88] Luther G. Jones, CH-47 Cargo Helicopters, Army Aviation Sustainment Summit,October 5, 2017.

[89] Sandford, R. W. and Belko, R. P., "CH-47 Fiberglass Rotor Blade Design and Fabrication", *Journal of the American Helicopter Society* Vol. 27, No. 2, 1982, pp. 43–50.

[90] Bao, J., Nagaraj, V. T., Chopra, I. and Bernhard, A. P., "Wind Tunnel Test of Five Sets of Mach Scale Composite Tailored Rotor with Flap-Bending/Torsion Couplings for Vibration Reduction", *Journal of the American Helicopter Society* Vol. 53, No. 3, 2008, pp. 215–225.

[91] SprutCAM, *sprutcam.com*, 2022

[92] Tormach, *tormach.com*, 2022

[93] ROHACELL, *www.rohacell.com*, 2022

[94] Cytec Engineered Materials, FM 300 High Shear Strength Modified Epoxy Adhesive, *www.cytec.com/*, 2022.

[95] Hexcel Composites, IM7/8552 Weave Product Data, *www.hexcel.com/*, 2022.

[96] ASTM, D7264, Standard Test Method for Flexural Properties of Polymer Matrix cComposite Materials. *American Society for Testing and Materials Annual Book of ASTM Standards*, 2007.

[97] Saxena, A., Primary Control of a Mach Scale Swashplateless Rotor using Brushless DC Motor Actuated Trailing Edge Flaps. PhD thesis, University of Maryland, College Park MD, 2015.

[98] Wang, X., Wind Tunnel Test on Slowed Rotor Aeromechanis at High Advance Ratios. PhD thesis, University of Maryland, College Park MD, 2020.

[99] Datta, A., "X3D—A 3D Solid Finite Element Multibody Dynamic Analysis for Rotorcraft", American Helicopter Society Technical Meeting on Aeromechanics Design for Vertical Lift, San Francisco, CA, Jan. 2016, pp.20-22.

[100] Staruk, W., CAD-Based Modeling of Advanced Rotary Wing Structures for Integrated 3-D Aeromechanis Analysis. PhD thesis, University of Maryland, College Park MD, 2017.

[101] T. Blacker, S. Owen, M. Staten, R. Quadros, B. Hanks and et al., "CUBIT Geometry and Mesh Generation Toolkit 15.2 User Documentation", *Sandia National Laboratories*, SAND2016-1649 R, Albuquerque, New Mexico, May, 2016.

[102] Staruk, W., "Instructions for Using samBuilder", *U.S. ARMY*, Feb., 2018.

[103] Shastry, A., and Datta, A., "Predicting Wake and Structural Loads in RPM Controlled Multirotor Aircraft", Vertical Flight Society Transformative Vertical Flight Technical Meeting, San Jose, California, January 21–23, 2020

[104] Weissinger, J., The Lift Distribution of Swept-Back Wings. Technical Report NACA-TM-1120, National Advisory Committee for Aeronautics, Langley Aeronautical Lab, March, 1947.